39. Rylands, H. D.: Some Data on the Effects of Thrust on Drag at Subsonic Speeds. Aeroplane and Armament Experimental Estab., Gr. Brit. AAEE/Res/309, 1962. (U)

40. Salmi, R. J.: Effects of Jet Billowing on Stability of Missile-Type Bodies at Mach 3.85. NASA TN D-284, 1960. (U)

41 Salmi, R. J., and Klann, J. L.: Interference Effects at Mach 1.9 on a Horizontal Tail Due to Trailing Shock Waves From an Axisymmetric Body With an Exiting Jet. NACA RM E55J13a, 1956. (U)

42. Smelt, R., and Davies, H.: Estimation of Increase in Lift Due to Slipstream. ARC R&M 1788, 1937. (U)

43. Smith, R. D.: The Effect of Free Stream Turbulence and Vorticity on the Field of a Free Jet. MIT ASRL TR 1013, 1963. (U)

44. Squire, H. B., and Trouncer, J.: Round Jets in a General Stream. ARC R&M 1974, 1944. (U)

45. Sweberg, H. H., and Dingeldein, R. C.: Summary of Measurements in Langley Full-Scale Tunnel of Maximum Lift Coefficients and Stalling Characteristics of Airplanes. NACA WR L-145, 1945. (U)

46. Swihart, J. M., and Crabill, N. L.: Steady Loads Due to Jet Interference on Wings, Tails, and Fuselages at Transonic Speeds. NACA RM L57D24b, 1957. (U)

47. Tomlinson, B. N.: A Brief Note on the Effect of an Offset Thrust Line on the Longitudinal Static Stability of an Aeroplane. Jour. Royal Aeron. Soc., Vol. 59, Aug. 1965. (U)

48. Vidal, R. J., Curtis, J. T., and Hilton, J. H.: The Influence of Two-Dimensional Stream Shear on Airfoil Maximum Lift. Cornell Aeron. Lab., Report A1-1190-A-7, 1961. (U)

49. Vidal, R. J., Hilton, J. H., and Curtis, J. T.: The Two-Dimensional Effects of Slipstream Shear on Airfoil Characteristics. Cornell Aeron. Lab., Report A1-1109-A-5, 1960. (U)

50. Weiberg, J. A., Griffin, R. N., Jr., and Florman, G. L.: Large-Scale Wind-Tunnel Tests of an Airplane Model With an Unswept, Aspect-Ratio-10 Wing, Two Propellers, and Area-Suction Flaps. NACA TN 4365, 1958. (U)

51. Weil, J., and Sleeman, W. C., Jr.: Prediction of the Effects of Propeller Operation on the Static Longitudinal Stability of Single-Engine Tractor Monoplanes With Flaps Retracted. NACA TN 1722, 1948. (U)

52. Weil, J., and Wells, E. G.: Wind-Tunnel Tests of the 1/8-Scale Powered Model of the Curtiss XBTC-2 Airplane. I-Preliminary Investigation of Longitudinal Stability. NACA WR L-667, 1944. (U)

53. Weil, J., and Boykin, R. I.: Wind-Tunnel Tests of the 0.15-Scale Powered Model of the Fleetwings XBTK-1 Airplane Longitudinal Stability and Control. NACA WR L-785, 1945. (U)

54. Wu, J. C., Mosher, D. K., and Wright, M. A.: Experimental and Analytical Investigations of Jets Exhausting Into a Deflecting Stream. AIAA P-69-0223, 1969. (U)

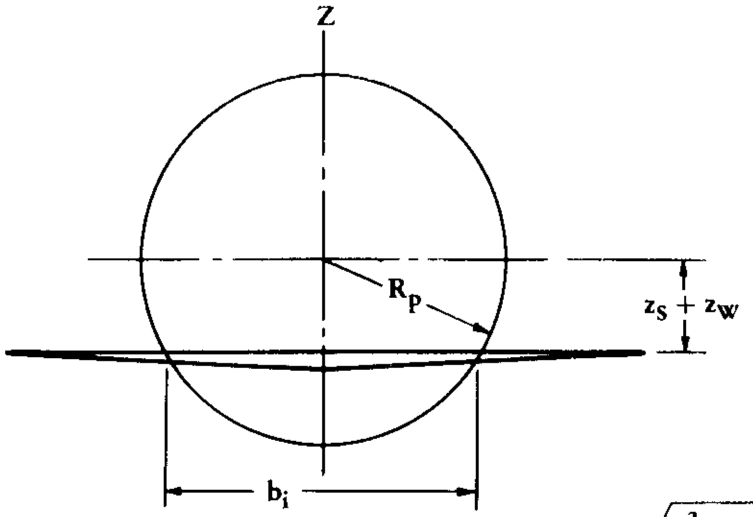

$$b_i = 2\sqrt{R_p^2 - (z_S + z_W)^2}$$

Cross section taken at quarter-chord of wing MAC for S_i (S_{H_i} is found in an identical manner as S_i with the cross section taken at the quarter-chord of the tail MAC.)

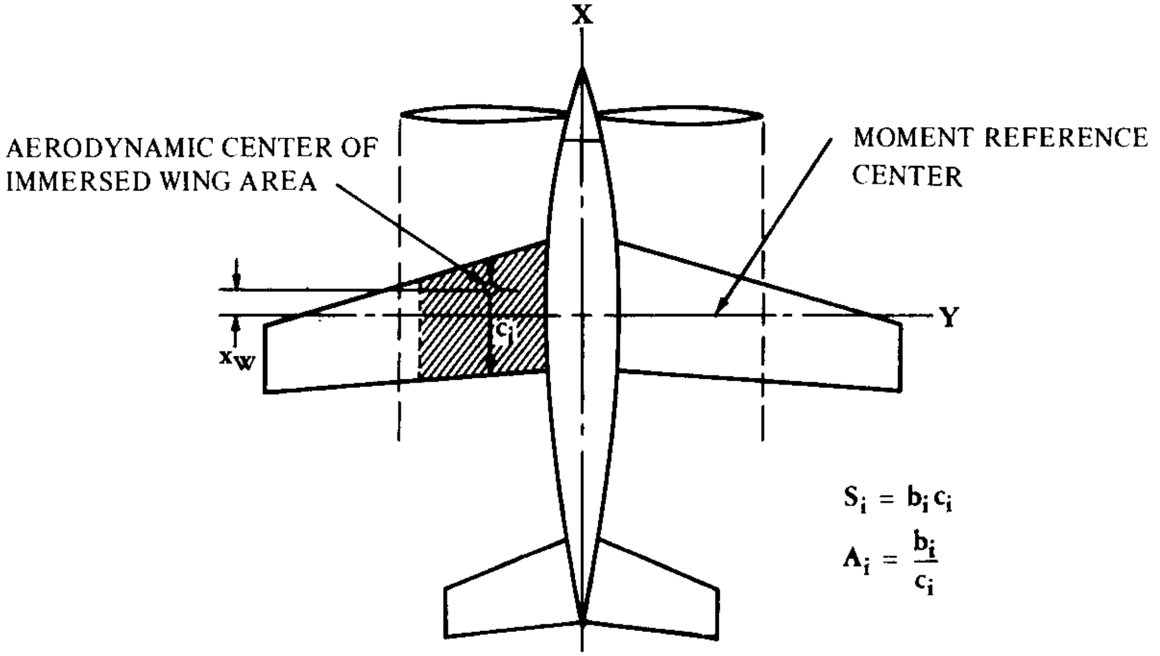

$$S_i = b_i c_i$$

$$A_i = \frac{b_i}{c_i}$$

FIGURE 4.6-12 DEFINITION SKETCH FOR CALCULATION OF IMMERSED WING AREA

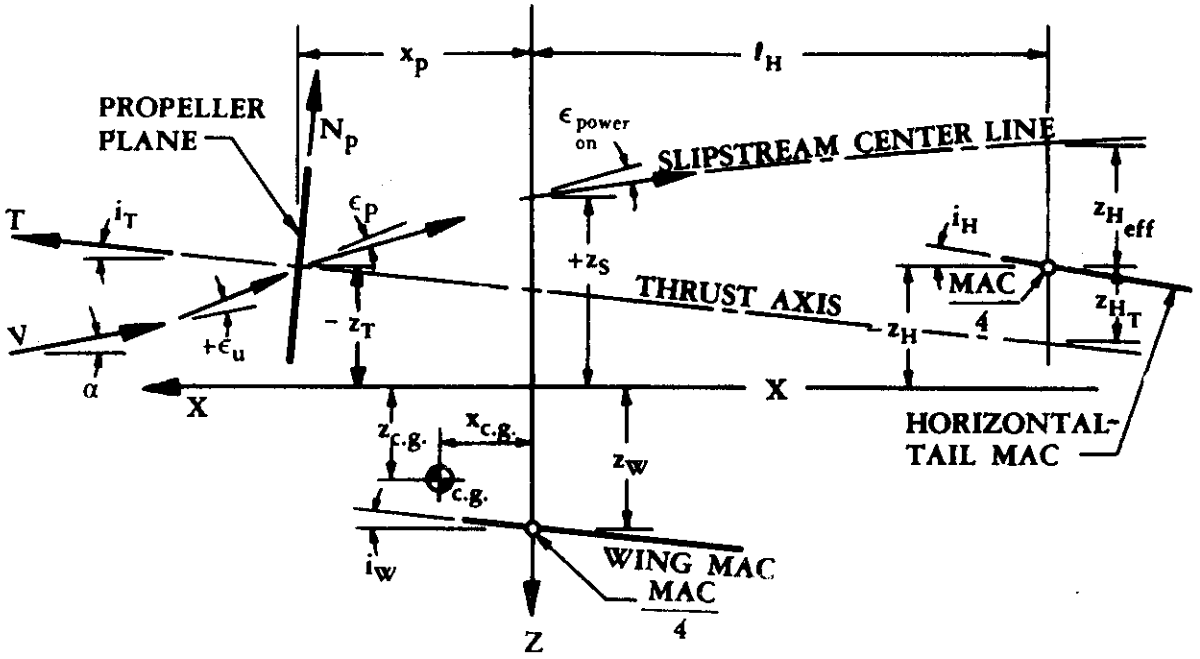

FIGURE 4.6-13a DEFINITION SKETCH FOR PROPELLER POWER EFFECTS CALCULATIONS

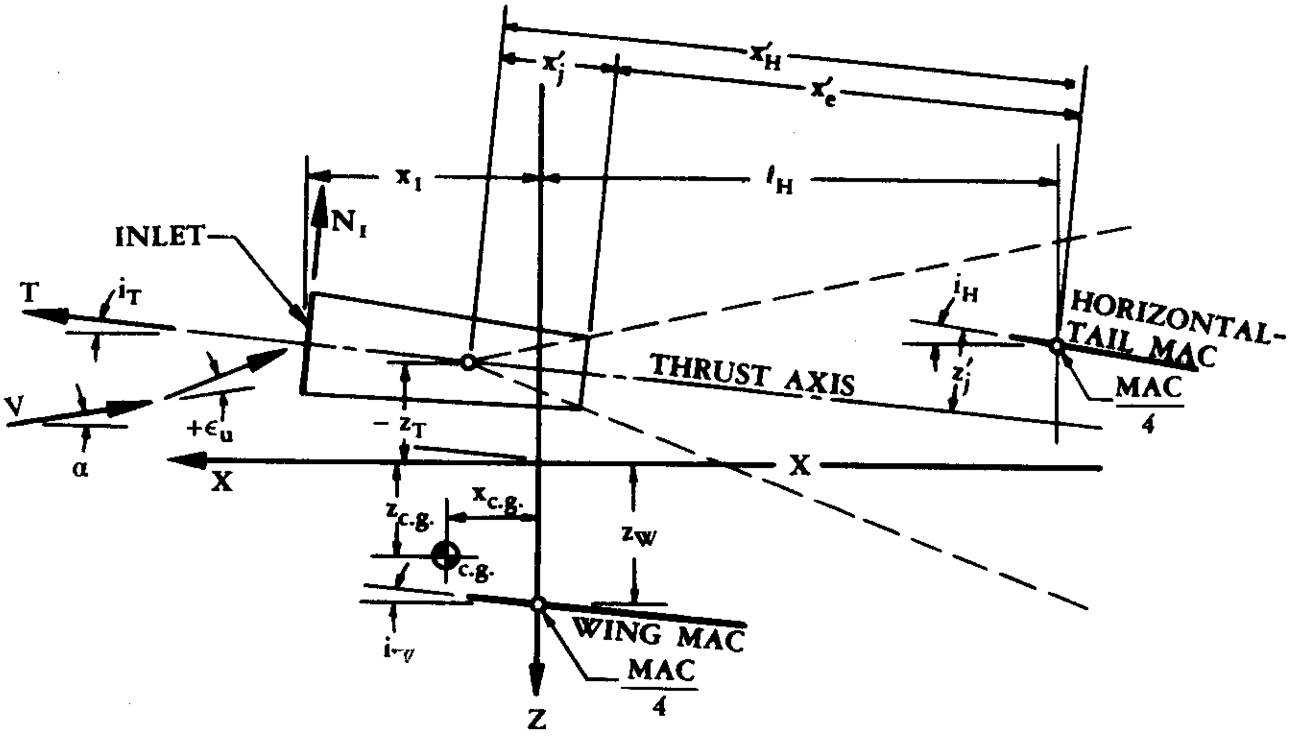

FIGURE 4.6-13b DEFINITION SKETCH FOR JET POWER EFFECTS CALCULATIONS

4.6.1 POWER EFFECTS ON LIFT VARIATION WITH ANGLE OF ATTACK

A. PROPELLER POWER EFFECTS ON LIFT

The primary purpose of a propeller is to develop thrust. In performing this function, the propeller often causes pronounced changes in the aerodynamic characteristics of a vehicle.

The effects of a propeller on the forces and moments acting on a vehicle may be divided into two groups, those due to the direct action of the propeller forces and those due to the propeller slipstream.

The first group includes the forces and moments due to the thrust vector and the forces and moments acting on the propeller as a result of its inclination to the oncoming stream. When a propeller is placed at an angle of attack, a force results normal to the thrust axis in the vertical plane. A pitching moment and a yawing moment also result. These forces and moments act on the propeller because of the unsymmetrical loading on the blades as a function of their rotational position. For counterrotating propellers the normal forces and pitching moments are additive, but the yawing moments cancel. These forces and moments are generally functions of propeller geometry.

The second group, those due to slipstream effects, depends greatly upon the component arrangement of the vehicle. However, the following generalizations can be made.

> The dynamic pressure behind the propeller may be greater or less than the free-stream dynamic pressure, depending upon whether the propeller is delivering positive or negative thrust, respectively. The forces and moments acting on airframe components immersed in the slipstream are directly proportional to the slipstream dynamic pressure.
>
> Because of the normal force acting on a propeller at angle of attack, a downwash field is generated behind the propeller plane. This downwash field changes the angle of attack of the airframe components operating in the propeller slipstream.

The method presented in this section for estimating propeller power effects on lift is based on a tail-last configuration. The method was taken from reference 1, which was developed from reference 2. The method predicts increments of lift for given values of thrust coefficient and angle of attack in the linear range. The effect of power on maximum lift is given in Section 4.6.2.

DATCOM METHOD

The Datcom method estimates the power-on lift curves based on power-off lift curves as a function of angle of attack, thrust coefficient, and lift coefficient.

This method analyzes the increments of lift coefficient due to propeller power effects in the following order:

1. Lift component of the thrust
2. Lift component of the propeller normal force
3. Change in angle of attack of the section of the wing in the propeller slipstream, due to the downwash flow field behind the propeller
4. Change in dynamic pressure over the section of the wing in the propeller slipstream
5. Change in lift due to downwash and changes in dynamic pressure acting on the horizontal tail

After the above lift increments for a given angle of attack have been calculated, the accumulated total is then applied to the power-off lift curve to obtain a point on the power-on lift curve. After several points have been generated (by considering several angles of attack), the linear section of the power-on lift curve is obtained for a given thrust coefficient.

The above increments in lift can be determined by the following steps. (Reference should be made to figure 4.6-13a for geometric definitions. In all cases the lift increments are based on the wing reference area.)

Step 1. Calculate the lift component of thrust as follows:

a. Calculate the angle of attack of the thrust axis α_T measured from the free-stream direction by

$$\alpha_T = i_T + \alpha \qquad \text{4.6.1-a}$$

b. Calculate the thrust coefficient per engine T_c' (if not given or assumed) by

$$T_c' = \frac{T}{q_\infty S_W} \qquad \text{4.6.1-b}$$

where the thrust per engine T is a given or chosen quantity.

c. Calculate the lift component of thrust by

$$\left(\Delta C_L\right)_T = nT_c' \sin \alpha_T \qquad \text{4.6.1-c}$$

where n is the number of engines. This equation is valid only when the thrust coefficients and the angles of attack of the thrust axis to the free stream are equal for all n engines.

Step 2. Calculate the lift component of propeller normal force per engine as follows:

a. Calculate the empirical normal-force factor K_N per blade (usually supplied by the propeller manufacturer) by

$$K_N = 262\left(\frac{b_p}{R_p}\right)_{.3R_p} + 262\left(\frac{b_p}{R_p}\right)_{.6R_p} + 135\left(\frac{b_p}{R_p}\right)_{.9R_p} \qquad 4.6.1\text{-d}$$

where the subscript indicates the radial position from the center of the propeller where the blade width b_p is to be evaluated.

b. From figure 4.6.1-25a (taken from reference 3) obtain a value for the propeller normal-force coefficient $\left[\left(C_{N_\alpha}\right)_p\right]_{K_N = 80.7}$, based on $K_N = 80.7$, as a function of propeller blade angle and type of propeller.

c. Calculate the true propeller normal-force coefficient $\left(C_{N_\alpha}\right)_p$ by

$$\left(C_{N_\alpha}\right)_p = \left[\left(C_{N_\alpha}\right)_p\right]_{K_N = 80.7}\left[1 + 0.8\left(\frac{K_N}{80.7} - 1\right)\right] \text{ (per radian)} \qquad 4.6.1\text{-e}$$

d. Evaluate the propeller correlation parameter defined as

$$\frac{S_W T_c'}{8R_p^2}$$

e. From figure 4.6.1-25b (taken from reference 3) obtain a value for the propeller-inflow factor f as a function of the propeller correlation parameter evaluated above (step 2.d).

f. Calculate the propeller disk area S_p by

$$S_p = \pi R_p^2 \qquad 4.6.1\text{-f}$$

g. Calculate the angle of attack of the propeller plane (local airstream to thrust axis) α_p by

$$\alpha_p = \alpha_T + \frac{\partial \epsilon_u}{\partial \alpha}\left(\alpha_W - \alpha_0\right) \qquad 4.6.1\text{-g}$$

where the upwash gradient $\partial \epsilon_u / \partial \alpha$ at the propeller may be obtained in Section 4.4.1 and

$$\alpha_W = \alpha + i_W \qquad \text{4.6.1-h}$$

h. Calculate the lift component of the propeller normal force by

$$\left(\Delta C_L\right)_{N_p} = f \left(C_{N_\alpha}\right)_p \frac{\alpha_p}{57.3} \frac{S_p}{S_W} \cos \alpha_T \qquad \text{4.6.1-i}$$

For multiple-engine configurations the total lift component of the propeller normal force is found by summing the single components due to each engine.

Step 3. Calculate the increment of lift due to the change in angle of attack on the wing induced by the propeller flow field per engine as follows:

a. Calculate the upwash gradient $\partial \epsilon_p / \partial \alpha_p$ by

$$\frac{\partial \epsilon_p}{\partial \alpha_p} = C_1 + C_2 \left(C_{N_\alpha}\right)_p \qquad \text{4.6.1-j}$$

where the constants C_1 and C_2 are obtained from figure 4.6.1-26 as a function of the propeller correlation parameter. The parameter $\left(C_{N_\alpha}\right)_p$ is obtained from step 2.c.

b. Calculate the downwash ϵ_p behind the propeller by

$$\epsilon_p = \frac{\partial \epsilon_p}{\partial \alpha_p} \alpha_p \qquad \text{4.6.1-k}$$

where the angle of attack of the propeller plane α_p is determined in step 2.g.

c. Calculate the change in the wing angle of attack $\Delta \alpha_W$ ahead of or behind the propeller by

$$\Delta \alpha_W = \frac{-\epsilon_p}{1 + \partial \epsilon_u / \partial \alpha} \qquad \text{4.6.1-}\ell$$

d. Calculate the angle of upwash ϵ_u at the propeller by

$$\epsilon_u = \frac{\partial \epsilon_u}{\partial \alpha} \left(\alpha_W - \alpha_0\right) \qquad \text{4.6.1-m}$$

e. Calculate the vertical distance from the X-axis to the propeller slipstream center line at the quarter-chord of the wing MAC by

$$z_s = x_p \tan(\alpha_T + \epsilon_u - \epsilon_p) - z_T \qquad 4.6.1\text{-n}$$

It should be noted that this equation is based on the assumption that the upwash and downwash are constant from the propeller to the quarter-chord of the MAC.

f. Calculate the span of the immersed wing b_i by

$$b_i = 2\left[R_p^2 - (z_s + z_W)^2\right]^{1/2} \qquad 4.6.1\text{-o}$$

g. Calculate the immersed wing area S_i by

$$S_i = b_i c_i \qquad 4.6.1\text{-p}$$

h. Calculate the effective aspect ratio A_i of the wing immersed in the slipstream (see figure 4.6-12) by

$$A_i = \frac{b_i}{c_i} \qquad 4.6.1\text{-q}$$

i. From figure 4.6.1-27 obtain a value for the empirical constant K_1 accounting for a nacelle or fuselage as a function of the wing and immersed-wing aspect ratio and the propeller correlation parameter (step 2.d).

j. Calculate the gain or loss in slipstream dynamic pressure $\Delta q_s/q_\infty$ by

$$\frac{\Delta q_s}{q_\infty} = \frac{S_W T_c'}{\pi R_p^2} \text{ (per engine)} \qquad 4.6.1\text{-r}$$

k. Calculate the change in wing lift due to the upwash or downwash of the propeller flow field per engine by

$$\left(\Delta C_L\right)_{\Delta\alpha_W} = \left(1 + \frac{\Delta q_s}{q_\infty}\right) \frac{S_i}{S_W} C_{L_\alpha} \Delta\alpha_W K_1 \qquad 4.6.1\text{-s}$$

where C_{L_α} is the lift-curve slope of the power-off lift curve, obtained by using the method of Section 4.1.3.2.

For multiple-engine configurations, the total lift component due to the change in angle of attack on the wing is found by summing the single components due to each engine.

Step 4. Calculate the increment of lift per engine due to the change in slipstream dynamic pressure on the wing by

$$\left(\Delta C_L\right)_q = K_1 \frac{\Delta q_s}{q_\infty} \frac{S_i}{S_W} \left(C_L\right)_{\substack{\text{power}\\\text{off}}} \qquad 4.6.1\text{-t}$$

where $\left(C_L\right)_{\substack{\text{power}\\\text{off}}}$ must be obtained from the power-off lift curve at the given angle of attack. For multiple-engine configurations, the total lift component due to the change in slipstream dynamic pressure acting on the wing is found by summing the single components due to each engine.

Step 5. Calculate the increment of lift on the horizontal tail due to the change in dynamic pressure and angle of attack as follows:

a. Calculate the total change in pitching-moment coefficient of the horizontal tail $\left(\Delta C_m\right)_H$ by

$$\left(\Delta C_m\right)_H = \left(\Delta C_{m_H}\right)_\epsilon + \left(\Delta C_{m_H}\right)_q \qquad 4.6.1\text{-u}$$

where $\left(\Delta C_{m_H}\right)_\epsilon$ and $\left(\Delta C_{m_H}\right)_q$ are calculated in Section 4.6.3.

b. Calculate the lift due to the horizontal tail by

$$\left(\Delta C_L\right)_H = -\left(\Delta C_m\right)_H \frac{\bar{c}}{\ell_H} \qquad 4.6.1\text{-v}$$

Step 6. Calculate the total change of lift due to the propeller power effects by summing the previously calculated elements as follows:

$$\left(\Delta C_L\right)_{\substack{\text{power}\\\text{on}}} = \left(\Delta C_L\right)_T + \left(\Delta C_L\right)_{N_p} + \left(\Delta C_L\right)_{\Delta\alpha_W} + \left(\Delta C_L\right)_q + \left(\Delta C_L\right)_H \qquad 4.6.1\text{-w}$$

This equation is computed for a range of angles of attack and thrust coefficients, and the lift curves are constructed. These curves are valid only in the linear-lift range.

Sample Problem

The following example is based on the single-engine test configuration of reference 3. The example is presented for one value of α and one value of T_c' .

Given:

Wing Parameters:

$S_W = 380\ \text{ft}^2$ $\quad A = 6.23$ $\quad i_W = 2.0°$ $\quad \bar{c} = 8.17\ \text{ft}$

$c_i = 9.17\ \text{ft}$ $\quad z_W = 1.4\ \text{ft}$ $\quad$ Wing root section: NACA 2416

Wing tip section: NACA 4412

$$\left.\begin{array}{l} C_{L_\alpha} = 0.08 \text{ per deg} \\ C_{L_{\substack{\text{power}\\\text{off}}}} = 0.50 \end{array}\right\} \begin{array}{l}\text{use test data or}\\ \text{Sections 4.1.3.2}\\ \text{and 4.1.3.3}\end{array}$$

Angles:

$\alpha = 4.0°$ (assumed) $\quad \alpha_0 = -2.8°$ $\quad \partial\epsilon_u/\partial\alpha = 0.13$ (Section 4.4.1)

Propeller Parameters:

Four-bladed propeller $\quad R_p = 6.79\ \text{ft}$ $\quad \beta = 18°$ (at $0.75\ R_p$) $\quad K_N = 65.8$

Engine Parameters:

$T_c' = 0.150$ per engine (assumed)

$n = 1$ $\quad i_T = 0$ $\quad z_T = 0$ $\quad x_p = 10.9\ \text{ft}$

Horizontal-Tail Parameters:

$S_H = 80\ \text{ft}^2$ $\quad \ell_H = 20.4\ \text{ft}$ $\quad (\Delta C_m)_H = 0.0218$ (Section 4.6.3)

Compute:

Determine the lift component of thrust

$$\alpha_T = i_T + \alpha \quad \text{(equation 4.6.1-a)}$$

$$= 0 + 4 = 4°$$

$T_c' = 0.150$ (given)

$$\left(\Delta C_L\right)_T = n\, T_c' \sin \alpha_T \qquad \text{(equation 4.6.1-c)}$$

$$= (1)\,(0.15)\,(0.0698) = 0.0105$$

Determine the lift component of propeller normal force

$$K_N = 65.8 \text{ (given)}$$

$$\left[\left(C_{N_\alpha}\right)_p\right]_{K_N = 80.7} = 0.165 \qquad \text{(figure 4.6.1-25a)}$$

$$\left(C_{N_\alpha}\right)_p = \left[\left(C_{N_\alpha}\right)_p\right]_{K_N = 80.7} \left[1 + 0.8\left(\frac{K_N}{80.7} - 1\right)\right] \qquad \text{(equation 4.6.1-e)}$$

$$= 0.165 \left[1 + 0.8\left(\frac{65.8}{80.7} - 1\right)\right]$$

$$= 0.141$$

The propeller correlation parameter is

$$\frac{S_W T_c'}{8R_p^2} = \frac{(380)\,(0.15)}{(8)\,(6.79)^2} = 0.155$$

$$f = 1.1 \qquad \text{(figure 4.6.1-25b)}$$

$$S_p = \pi R_p^2 \qquad \text{(equation 4.6.1-f)}$$

$$= (3.14)\,(6.79)^2 = 144.8 \text{ ft}^2$$

$$\frac{\partial \epsilon_u}{\partial \alpha} = 0.13 \text{ (given)}$$

$$\alpha_W = \alpha + i_W \qquad \text{(equation 4.6.1-h)}$$

$$= 4.0 + 2.0 = 6.0^\circ$$

$$\alpha_p = \alpha_T + \frac{\partial \epsilon_u}{\partial \alpha}\left(\alpha_W - \alpha_0\right) \qquad \text{(equation 4.6.1-g)}$$

$$= 4.0 + 0.13\,(6.0 + 2.8)$$

$$= 5.14^\circ$$

$$\left(\Delta C_L\right)_{N_p} = f\left(C_{N_\alpha}\right)_p \frac{\alpha_p}{57.3} \frac{S_p}{S_W} \cos \alpha_T \quad \text{(equation 4.6.1-i)}$$

$$= (1.1)(0.141) \frac{5.14}{57.3} \frac{144.8}{380} (0.998)$$

$$= 0.00529$$

Determine the increment of lift due to the change in angle of attack on the wing induced by the propeller flow field

$$\frac{\partial \epsilon_p}{\partial \alpha_p} = C_1 + C_2 \left(C_{N_\alpha}\right)_p \quad \text{(equation 4.6.1-j)}$$

$$\left.\begin{aligned} C_1 &= 0.08 \\ C_2 &= 0.25 \end{aligned}\right\} \text{(figure 4.6.1-26)}$$

$$\frac{\partial \epsilon_p}{\partial \alpha_p} = 0.08 + (0.25)(0.141) = 0.115$$

$$\epsilon_p = \frac{\partial \epsilon_p}{\partial \alpha_p} \alpha_p \quad \text{(equation 4.6.1-k)}$$

$$= (0.115)(5.14) = 0.59^\circ$$

$$\Delta \alpha_W = \frac{-\epsilon_p}{1 + \partial \epsilon_u / \partial \alpha} \quad \text{(equation 4.6.1-}\ell\text{)}$$

$$= \frac{-0.59}{1 + 0.13} = -0.522^\circ$$

$$\epsilon_u = \frac{\partial \epsilon_u}{\partial \alpha} (\alpha_W - \alpha_0) \quad \text{(equation 4.6.1-m)}$$

$$= 0.13\,(6.0 + 2.8) = 1.14^\circ$$

$$z_s = x_p \tan(\alpha_T + \epsilon_u - \epsilon_p) - z_T \quad \text{(equation 4.6.1-n)}$$

Using the small-angle approximation,

$$z_s = \frac{x_p}{57.3}(\alpha_T + \epsilon_u - \epsilon_p) + 0$$

$$= \frac{10.9}{57.3}(4.0 + 1.14 - 0.59) = 0.866 \text{ ft}$$

$$b_i = 2\left[R_p^2 - (z_s + z_W)^2\right]^{1/2} \qquad \text{(equation 4.6.1-o)}$$

$$= 2\left[(6.79)^2 - (0.866 + 1.4)^2\right]^{1/2}$$

$$= 12.8 \text{ ft}$$

$$S_i = b_i c_i \qquad \text{(equation 4.6.1-p)}$$

$$= (12.8)(9.17) = 117.4 \text{ ft}^2$$

$$A_i = \frac{b_i}{c_i} \qquad \text{(equation 4.6.1-q)}$$

$$= \frac{12.8}{9.17} = 1.40$$

$$K_1 = 0.96 \quad \text{(figure 4.6.1-27)}$$

$$\frac{\Delta q_s}{q_\infty} = \frac{S_W T_c'}{\pi R_p^2} \qquad \text{(equation 4.6.1-r)}$$

$$= \frac{(380)(0.15)}{(3.14)(6.79)^2}$$

$$= 0.394$$

$$\left(\Delta C_L\right)_{\Delta\alpha_W} = \left(1 + \frac{\Delta q_s}{q_\infty}\right)\frac{S_i}{S_W} C_{L_\alpha} \Delta\alpha_W \, K_1 \qquad \text{(equation 4.6.1-s)}$$

$$= (1 + 0.394)\,\frac{117.4}{380}\,(0.08)(-0.522)(0.96)$$

$$= -0.0173$$

Determine the increment of lift due to the change in slipstream dynamic pressure

$$\left(\Delta C_L\right)_q = K_1 \frac{\Delta q_s}{q_\infty} \frac{S_i}{S_W} \left(C_L\right)_{\substack{\text{power}\\\text{off}}} \qquad \text{(equation 4.6.1-t)}$$

$$= (0.96)\,(0.394)\; \frac{117.4}{380}\; (0.50)$$

$$= 0.0584$$

Determine the increment of lift on the horizontal tail due to the change in dynamic pressure and angle of attack

$$\left(\Delta C_m\right)_H = \left(\Delta C_{m_H}\right)_\epsilon + \left(\Delta C_{m_H}\right)_q \qquad \text{(equation 4.6.1-u)}$$

$$\left.\begin{aligned}\left(\Delta C_{m_H}\right)_\epsilon &= 0.0218\\ \left(\Delta C_{m_H}\right)_q &= 0\end{aligned}\right\} \text{(sample problem, Section 4.6.3)}$$

$$\left(\Delta C_m\right)_H = 0.0218$$

$$\left(\Delta C_L\right)_H = -\left(\Delta C_m\right)_H \frac{\bar{c}}{\ell_H} \qquad \text{(equation 4.6.1-v)}$$

$$= -(0.0218)\left(\frac{8.17}{20.4}\right)$$

$$= -0.00873$$

Determine the total change of lift due to the propeller power effects

$$\left(\Delta C_L\right)_{\substack{\text{power}\\\text{on}}} = \left(\Delta C_L\right)_T + \left(\Delta C_L\right)_{N_p} + \left(\Delta C_L\right)_{\Delta\alpha_W} + \left(\Delta C_L\right)_q + \left(\Delta C_L\right)_H$$

(equation 4.6.1-w)

$$= 0.0105 + 0.00529 - 0.0173 + 0.0584 - 0.00873$$

$$= 0.0482$$

The value of $\left(\Delta C_L\right)_{\substack{\text{power}\\\text{on}}}$ from reference 4 at $\alpha = 4.0^\circ$ and $T_c' = 0.15$ is 0.080.

B. JET POWER EFFECTS ON LIFT

The effects of jets on the aerodynamic characteristics of vehicles are generally of smaller magnitude than the effects of propellers. There are three effects of jets on the lift of a vehicle. The first is a contribution to the lift due to the thrust component. The second is a force acting at the engine inlet duct in a direction normal to the thrust axis. This force is due to the turning of the free stream in a direction parallel to the thrust axis. The third is the induced effect of the jet on wing or tail surfaces, i.e., that caused by the jets on the surrounding flow.

The first two effects are analyzed by the methods of reference 1 at both subsonic and supersonic speeds. The third effect requires special treatment.

The following discussion on jet flow fields will help clarify some of the important distinctions between subsonic and supersonic jets operating in subsonic and supersonic flows.

Subsonic Jets in Subsonic Flow

The velocity profile across a jet exit is nearly uniform. Mixing of the jet flow and the local free-stream flow starts at the lip of the jet and propagates laterally in the downstream direction. The velocity profile is modified by this viscous mixing action, and at some distance downstream of the apex of the core the velocity profiles become similar. This usually occurs at approximately eight exit-diameters from the nozzle. The region of flow less than approximately eight exit-diameters downstream is referred to as the transition region, and the region beyond this point is referred to as the fully developed region (see sketch (a)).

AXIAL VELOCITY COMPONENT

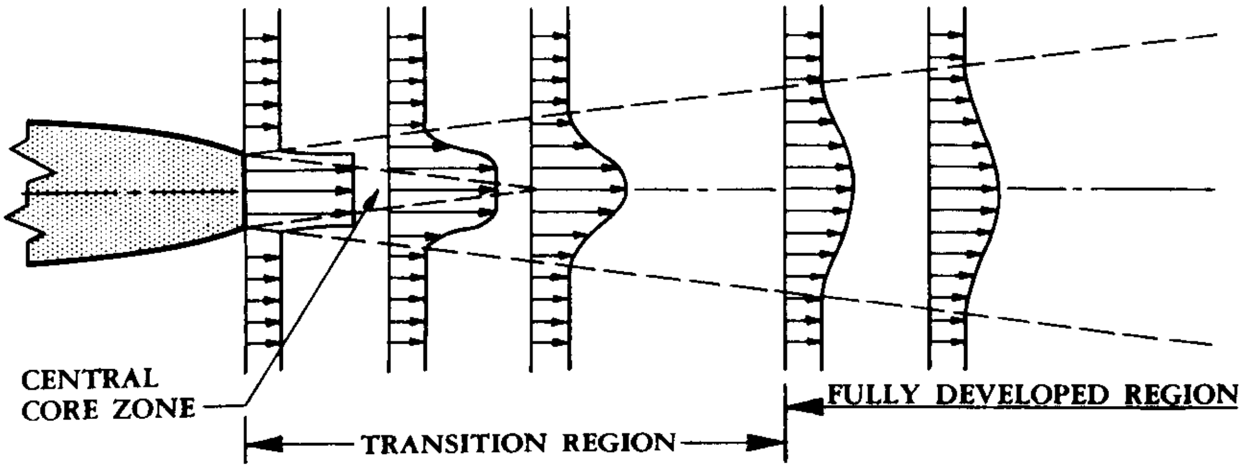

SKETCH (a)

Existing within the transition region is the central core zone of uniform flow, which dissipates downstream. The remaining segment of the two regions is made up of the mixing zone, which lies between the central core and the external flow.

The external flow is entrained by the jet, causing a radial inflow velocity component in the external flow as shown in sketch (b).

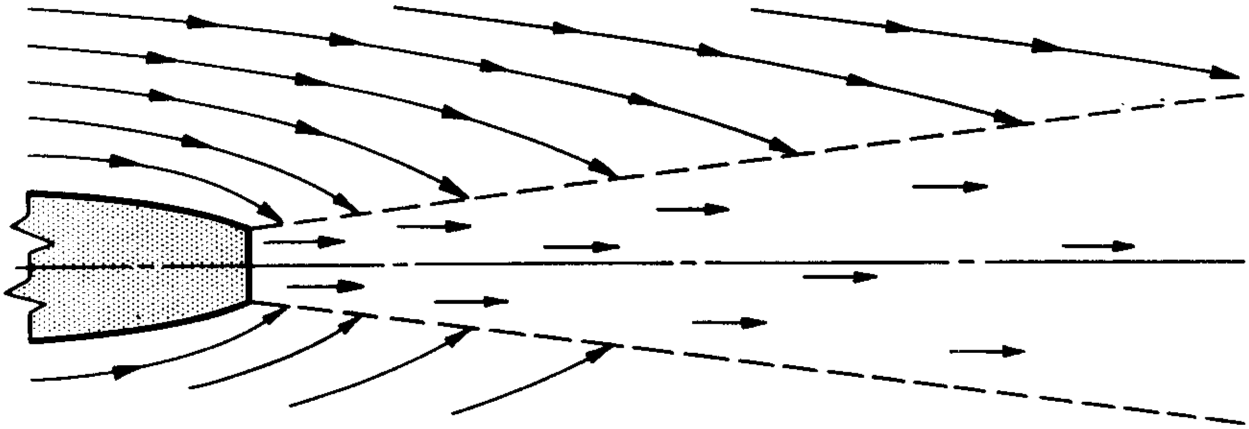

SKETCH (b)

Airframe components immersed in this external flow field experience changes in forces and moments due to these induced angle-of-attack changes.

Two methods are presented for calculating the interference effects of subsonic jets in a subsonic free stream. The first method is valid for downstream distances less than eight exit-diameters. This method incorporates a technique presented in reference 5 with a temperature-ratio correction from reference 6 and a span correction factor from reference 7.

The second method is valid for downstream distances greater than eight exit-diameters. This method is based on a technique from reference 7.

Supersonic Jet in Subsonic Flow

If the jet pressure ratio becomes sufficiently large, the jet expands supersonically beyond the exit. The jet will "plume" or bulge, as shown in sketch (c).

At some station downstream, the jet reaches a condition where it is expanded to atmospheric pressure. This station is termed the equivalent jet exit station. The external flow in the region of the jet plume can cause either inflow- or outflow-radial-velocity components. In general, large jet-pressure ratios and high free-stream velocities cause outflow velocities, and lower jet-pressure ratios and low free-stream velocities cause inflow velocities resulting from the entrainment of the external flow. A quantitative evaluation of these effects is not available. The external flow downstream of the equivalent jet exit station always has an inflow velocity component and is similar in this respect to subsonic jets.

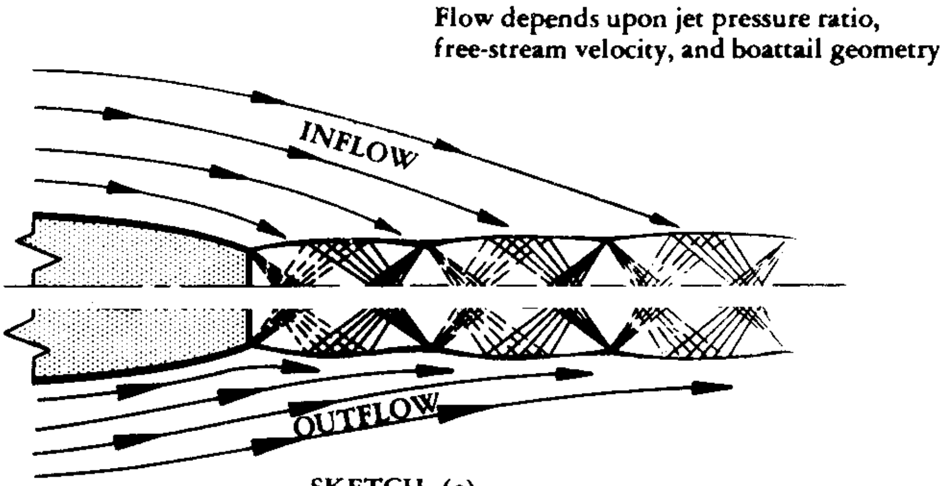

SKETCH (c)

No accurate flow model is available for predicting the jet interference effects of a supersonic jet exhausting into a subsonic flow. However, an approximate method is presented that is based on the method for analyzing subsonic jets in subsonic flow. The accuracy of this method has not been established.

Supersonic Jets in Supersonic Flow

At supersonic speeds the exhaust from supersonic jets causes strong disturbances in the external flow field in the form of shock and expansion waves. A typical flow pattern is shown in sketch (d).

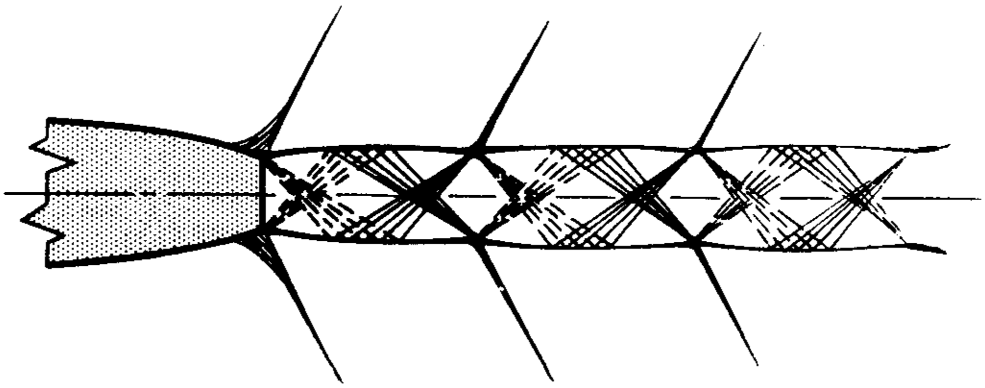

SKETCH (d)

Jets become greatly underexpanded at extreme altitudes, a phenomenon that results in strong effects on the flow upstream of the jet exit. Some limited data on this problem are available in reference 8.

The correct approach for analyzing the lift increment should consider the change in pressure distribution on the wing or tail due to the presence of the jet. The surface pressure distribution is a function of the free-stream Mach number and jet pressure ratio. Unfortunately, insufficient test data are available to provide complete charts for this estimation procedure. Test data at $M_\infty = 2.0$ and a jet pressure ratio of 7.0 from reference 9 are presented in figure 4.6.1-33 as representative data. The chart shows pressure contours at the vertical plane of symmetry of the jet. It is intended that these limited data, together with a description of the procedure, will provide some feeling for the problem.

DATCOM METHOD

The Datcom method estimates the power-on lift curves, based on power-off lift curves, as a function of angle of attack, thrust coefficient, engine-inlet area, and horizontal-tail parameters.

This method analyzes the increments of lift coefficient due to jet power effects in the following order:

1. Lift component of thrust
2. Lift component due to the turning of the free-stream flow parallel to the thrust axis
3. Lift component due to jet interference effects

After the above lift increments for a given angle of attack have been calculated, the accumulated total is then applied to the power-off lift curve to obtain a point on the power-on lift curve. After several points have been generated (by considering several angles of attack), the linear section of the power-on lift curve is obtained for a given thrust coefficient.

The above increments in lift can be determined by the following steps. (Reference should be made to figure 4.6-13b for geometric definitions. In all cases the lift increments are based on the wing reference area.)

Step 1. Calculate the lift component of thrust as follows:

a. Calculate the angle of attack of the thrust axis to the free stream α_T by

$$\alpha_T = i_T + \alpha \qquad 4.6.1\text{-a}$$

b. Calculate the thrust coefficient per engine T_c' (if not given or assumed) by

$$T_c' = \frac{T}{q_\infty S_W} \qquad 4.6.1\text{-b}$$

where the thrust per engine T is a given or chosen quantity.

c. Calculate the lift component of thrust by

$$\left(\Delta C_L\right)_T = n\, T_c' \sin \alpha_T \qquad 4.6.1\text{-c}$$

where n is the number of engines. This equation is valid only when the thrust coefficients and the angles of attack of the thrust axis to the free stream are equal for all n engines.

Step 2. Calculate the lift component per engine due to the turning of the free-stream flow in a direction parallel to the thrust axis as follows:

a. Calculate the angle between the thrust axis and the local velocity α_j at the engine inlet by

$$\alpha_j = \alpha_T + \epsilon_u \qquad 4.6.1\text{-x}$$

where the upwash ahead of the wing ϵ_u is obtained by

$$\epsilon_u = \frac{\partial \epsilon_u}{\partial \alpha} \left(\alpha_W - \alpha_0\right) \qquad 4.6.1\text{-m}$$

and the downwash gradient $\frac{\partial \epsilon_u}{\partial \alpha}$ is obtained from Section 4.4.1.

b. Calculate the turning component of lift by

$$\left(\Delta C_L\right)_{N_j} = \frac{2A_I \sin \alpha_j}{S_W} \qquad 4.6.1\text{-y}$$

For multiple-engine configurations, the total lift component due to the turning of the free-stream flow is found by summing the individual lift increments due to each engine.

Step 3. Calculate the lift component per engine due to the jet interference effects.

The various possible combinations of Mach number for the free-stream and nozzle exit conditions require different combinations to be analyzed separately. Methods for calculating four different jet interaction cases are presented. The surface affected is assumed to be a horizontal tail. Application to other lifting surfaces and to other bodies is similar.

Case I. Subsonic Free Stream – Subsonic Jet – Downstream Distance Less than Eight Exit-Diameters

a. Obtain the lift-curve slope of the horizontal tail $C_{L_{\alpha_H}}$ from Section 4.1.3.2.

b. Obtain the ratio of the horizontal-tail to free-stream dynamic pressure q_H/q_∞ at the quarter-chord of the horizontal-tail MAC from wind-tunnel-test data or Section 4.4.1.

c. From figure 4.6.1-28 obtain a value for the mean-effective-downwash ratio $\Delta\bar{\epsilon}/\Delta\epsilon$ as a function of aircraft geometry.

d. From figure 4.6.1-29 obtain the equivalent-jet-velocity ratio V_j'/V_∞ as a function of the actual-jet-velocity ratio V_j/V_∞ and the ratio of ambient temperature to jet static temperature.

e. From figures 4.6.1-30a through -30c obtain a value for the downwash increment $\Delta\epsilon$ as a function of aircraft geometry and equivalent-jet-velocity ratio.

f. Calculate the mean-effective-downwash increment $\Delta\bar{\epsilon}$ by

$$\Delta\bar{\epsilon} = \left(\frac{\Delta\bar{\epsilon}}{\Delta\epsilon}\right)\Delta\epsilon \qquad 4.6.1\text{-z}$$

g. Calculate the increment in lift per engine due to jet interference effects by

$$\left(\Delta C_L\right)_\epsilon = -C_{L_{\alpha_H}} \frac{S_H}{S_W} \frac{q_H}{q_\infty} \Delta\bar{\epsilon} \qquad 4.6.1\text{-aa}$$

For multiple-engine configurations, the total lift component due to jet interference effects is found by summing the individual lift increments due to each engine.

Case II. Subsonic Free Stream – Subsonic Jet – Downstream Distances Greater than Eight Exit-Diameters

a. Obtain the lift-curve slope of the horizontal tail $C_{L_{\alpha_H}}$ from Section 4.1.3.2.

b. Obtain the ratio of the horizontal-tail to free-stream dynamic pressure q_H/q_∞ at the quarter-chord of the horizontal-tail MAC from wind-tunnel-test data or Section 4.4.1.

c. From figure 4.6.1-28 obtain a value for the mean-effective-downwash ratio $\Delta\bar{\epsilon}/\Delta\epsilon$ as a function of aircraft geometry.

d. From figure 4.6.1-31 obtain a value for $z_j'\Delta\epsilon/x_H$ as a function of aircraft geometry and thrust coefficient.

e. Calculate the jet-induced downwash angle $\Delta\epsilon$ by

$$\Delta\epsilon = \frac{z_j'\Delta\epsilon}{x_H'} \frac{x_H'}{z_j'} \qquad 4.6.1\text{-bb}$$

where $x_H' = x_j' + x_e'$ 4.6.1-cc

and x_j' is usually expressed as

$$x_j' = 4.6\ R_j \qquad 4.6.1\text{-dd}$$

f. Calculate the mean-effective-downwash increment $\Delta\bar{\epsilon}$ by

$$\Delta\bar{\epsilon} = \left(\frac{\Delta\bar{\epsilon}}{\Delta\epsilon}\right)\Delta\epsilon \qquad 4.6.1\text{-z}$$

g. Calculate the increment in lift per engine due to jet interference effects by

$$\left(\Delta C_L\right)_\epsilon = -C_{L_{\alpha_H}} \frac{S_H}{S_W} \frac{q_H}{q_\infty} \Delta\bar{\epsilon} \qquad 4.6.1\text{-aa}$$

For multiple-engine configurations, the total lift component due to jet interference effects is found by summing the individual lift increments due to each engine.

Case III. Subsonic Free Stream – Supersonic Jet – Distances Downstream of the Fully Expanded Flow

a. From figure 4.6.1-32a obtain a value for the equivalent-jet orifice radius ratio R_j'/R_j as a function of the jet-exit total-pressure ratio.

b. From figure 4.6.1-32b obtain a value for the downstream displacement of the equivalent-jet orifice as a function of the equivalent-jet orifice radius.

The downstream displacement distance corresponds to the point at which the supersonic-jet flow has expanded to ambient pressure. The corresponding jet ratio at this station is the equivalent radius R_j'. These values are used in lieu of the actual jet radius and jet location in approximating the inflow velocities of the surrounding flow downstream of this equivalent jet-exit station.

Depending on the location of the surface of interest, the remaining steps are identical to those of case I (less than eight exit-diameters downstream) or case II (greater than eight exit-diameters downstream). For locations upstream of the fully expanded flow no method is available.

As pointed out in the discussion, the accuracy of this method is not known.

Case IV. Supersonic Free Stream – Supersonic Jet

A complete method is not presented because of a lack of wind-tunnel test data required for the formulation of design charts. However, if wind-tunnel data are available the following procedure is suggested:

a. Divide the surface under consideration into incremental areas ΔS_H.

b. Calculate the respective axial and radial locations of the incremental areas relative to the jet exit.

c. Construct a pressure-coefficient-contour chart from available data (see figure 4.6.1-33).

d. Obtain values of $\Delta p/q_\infty$ for each incremental area from the pressure-coefficient-contour chart as a function of their relative locations.

e. Sum the incremental forces acting over the surfaces to obtain the total change in lift coefficient by

$$\Delta C_L = \frac{1}{S_W} \Sigma \left[\Delta S_H \frac{\Delta p}{q_\infty}\right] \qquad 4.6.1\text{-ee}$$

By using the above procedure, several increments in horizontal-tail lift coefficient were calculated for the configuration tested in reference 10. The calculations were computed from the data of figure 4.6.1-33 for a variety of tail positions at Mach number of 1.9 and a jet pressure ratio of 6.66. The results of the calculations revealed errors ranging from 15 to 133 percent.

The total change in aircraft lift due to jet power effects is obtained by summing all lift components, i.e.,

$$\left(\Delta C_L\right)_{\substack{\text{power}\\ \text{on}}} = \left(\Delta C_L\right)_T + \left(\Delta C_L\right)_{N_j} + \left(\Delta C_L\right)_\epsilon \qquad 4.6.1\text{-ff}$$

Sample Problem

The following example is based on the four-engine DC-8 configuration. The example is presented for one value of α and one value of T_c'. The lift due to jet-interference effects is calculated by using the methods of case II, since the downstream distance of the horizontal tail is greater than eight engine exit-diameters.

Given:

Wing Parameters:

$S_W = 2930 \text{ ft}^2$ $\bar{c} = 272.8$ in. $A = 7.52$

$i_W = 0$ $\alpha = 5°$ $\alpha_0 = -2.5°$ (flaps up)

Horizontal-Tail Parameters:

$S_H = 560 \text{ ft}^2$ $\bar{c}_H$ 153.2 in. $C_{L_{\alpha_H}} = 0.0627$/deg (Section 4.1.3.2)

$q_H/q_\infty = 0.968$ (Section 4.4.1) $\ell_H = 855.0$ in. $b_H = 570.0$ in.

Engine Parameters:

Outboard Engines (2) $z_T = 53.0$ in. $z_j' = 175.7$ in.

$x_I = 145.2$ in. $x_e' = 788.0$ in. $y_T = 44.6$ ft

$\partial\epsilon_u/\partial\alpha = 0.17$ (Section 4.4.1) $R_j = 20$ in. $A_I = 13.64 \text{ ft}^2$

$i_T = 3.6°$ $T = 12{,}500$ lb

Inboard Engines (2) $z_T = 70.8$ in. $z_j' = 201.7$ in.

$x_I = 283.8$ in. $x_e' = 927.0$ in. $y_T = 25.7$ ft

$\partial\epsilon_u/\partial\alpha = 0.24$ (Section 4.4.1) $R_j = 20$ in. $A_I = 13.64 \text{ ft}^2$

$i_T = 3.6°$ $T = 12{,}500$ lb

Additional Parameters:

$M = 0.2$ $q_\infty = 57.2$ psf $h = 1000$ ft

Compute:

Determine the lift component of thrust

$$\alpha_T = i_T + \alpha \qquad \text{(equation 4.6.1-a)}$$

$$= 3.6 + 5 = 8.6^\circ$$

$$T_c' = \frac{T}{q_\infty S_W} \qquad \text{(equation 4.6.1-b)}$$

$$= \frac{12{,}500}{(57.2)\,(2930)} = 0.0746 \text{ (per engine)}$$

$$\left(\Delta C_L\right)_T = n\,T_c' \sin\alpha_T \qquad \text{(equation 4.6.1-c)}$$

$$= (4)\,(0.0746)\,(0.1495)$$

$$= 0.0446$$

Determine the lift component due to the turning of the free stream

$$\alpha_W = \alpha + i_W \qquad \text{(equation 4.6.1-h)}$$

$$= 5 + 0 = 5^\circ$$

$$\epsilon_u = \frac{\partial \epsilon_u}{\partial \alpha}\,(\alpha_W - \alpha_0) \qquad \text{(equation 4.6.1-m)}$$

$$\left(\epsilon_u\right)_{\substack{\text{outboard}\\\text{engine}}} = (0.17)\,(5 + 2.5) = 1.27^\circ$$

$$\left(\epsilon_u\right)_{\substack{\text{inboard}\\\text{engine}}} = (0.24)\,(5 + 2.5) = 1.80^\circ$$

$$\alpha_j = \alpha_T + \epsilon_u \qquad \text{(equation 4.6.1-x)}$$

$$\left(\alpha_j\right)_{\substack{\text{outboard}\\\text{engine}}} = 8.6 + 1.27 = 9.87^\circ$$

$$\left(\alpha_j\right)_{\substack{\text{inboard}\\\text{engine}}} = 8.6 + 1.80 = 10.4^\circ$$

$$\left(\Delta C_L\right)_{N_j} = \frac{2A_I \sin \alpha_j}{S_W} \qquad \text{(equation 4.6.1-y)}$$

Considering the lift increment due to both outboard engines

$$\left[\left(\Delta C_L\right)_{N_j}\right]_{\substack{\text{outboard}\\ \text{engines}}} = \frac{(2)\ (13.64)\ (0.1714)\ (2)}{2930} = 0.00319$$

Considering the lift increment due to both inboard engines

$$\left[\left(\Delta C_L\right)_{N_j}\right]_{\substack{\text{inboard}\\ \text{engines}}} = \frac{(2)\ (13.64)\ (0.1805)\ (2)}{2930} = 0.00336$$

The total lift component due to the turning of the free stream is

$$\begin{aligned}\left(\Delta C_L\right)_{N_j} &= \left[\left(\Delta C_L\right)_{N_j}\right]_{\substack{\text{outboard}\\ \text{engines}}} + \left[\left(\Delta C_L\right)_{N_j}\right]_{\substack{\text{inboard}\\ \text{engines}}}\\ &= 0.00319 + 0.00336\\ &= 0.00655\end{aligned}$$

Determine the lift component due to jet interference effects on the horizontal tail. The method of case II will be used to evaluate the jet interference effects, since $(\ell_H/R_j) > 8$.

$$\left.\frac{\Delta\bar{\epsilon}}{\Delta\epsilon}\right|_{\substack{\text{inboard}\\ \text{engines}}} = 0.37 \qquad \text{(figure 4.6.1-28)}$$

$$\left.\frac{\Delta\bar{\epsilon}}{\Delta\epsilon}\right|_{\substack{\text{outboard}\\ \text{engines}}} = 0.10 \qquad \text{(figure 4.6.1-28)}$$

$$\left.\frac{z_j'\Delta\epsilon}{x_H'}\right|_{\substack{\text{inboard}\\ \text{engines}}} = 0.07 \qquad \text{(figure 4.6.1-31)}$$

$$\left.\frac{z_j'\Delta\epsilon}{x_H'}\right|_{\substack{\text{outboard}\\ \text{engine}}} = 0.08 \qquad \text{(figure 4.6.1-31)}$$

$$x_H' = x_j' + x_e' \qquad \text{(equation 4.6.1-cc)}$$

$$x_j' = 4.6\ R_j \qquad \text{(equation 4.6.1-dd)}$$

$$\left(x_H'\right)_{\substack{\text{inboard}\\ \text{engine}}} = (4.6)\ (20) + 927$$

$$= 1019 \text{ in.}$$

$$\left(x_H'\right)_{\substack{\text{outboard}\\ \text{engine}}} = (4.6)\ (20) + 788$$

$$= 880 \text{ in.}$$

$$\Delta\epsilon = \frac{z_j'\Delta\epsilon}{x_H'}\ \frac{x_H'}{z_j'} \qquad \text{(equation 4.6.1-bb)}$$

$$\left(\Delta\epsilon\right)_{\substack{\text{inboard}\\ \text{engine}}} = (0.07)\ \frac{(1019)}{(201.7)}$$

$$= 0.354$$

$$\left(\Delta\epsilon\right)_{\substack{\text{outboard}\\ \text{engine}}} = (0.08)\ \frac{(880)}{175.7}$$

$$= 0.40$$

$$\Delta\bar{\epsilon} = \left(\frac{\Delta\bar{\epsilon}}{\Delta\epsilon}\right)\Delta\epsilon \qquad \text{(equation 4.6.1-z)}$$

$$\left(\Delta\bar{\epsilon}\right)_{\substack{\text{inboard}\\ \text{engines}}} = (0.37)\ (0.354)$$

$$= 0.131$$

$$\left(\Delta\bar{\epsilon}\right)_{\substack{\text{outboard}\\ \text{engines}}} = (0.10)\ (0.40)$$

$$= 0.04$$

$$\left(\Delta C_L\right)_\epsilon = -C_{L_{\alpha_H}}\ \frac{S_H}{S_W}\ \frac{q_H}{q_\infty}\ \Delta\bar{\epsilon} \qquad \text{(equation 4.6.1-aa)}$$

$$\left[\left(\Delta C_L\right)_\epsilon\right]_{\substack{\text{inboard}\\\text{engines}}} = -(0.0627)\ \frac{560}{2930}\ (0.968)\ (0.131)$$

$$= -0.00152$$

$$\left[\left(\Delta C_L\right)_\epsilon\right]_{\substack{\text{outboard}\\\text{engines}}} = -(0.0627)\ \frac{560}{2930}\ (0.968)\ (0.04)$$

$$= 0.00046$$

The total lift component due to jet interference effects on the horizontal tail is

$$\left(\Delta C_L\right)_\epsilon = -0.00152 - 0.00046$$

$$= -0.0020$$

$$\left(\Delta C_L\right)_{\substack{\text{power}\\\text{on}}} = \left(\Delta C_L\right)_T + \left(\Delta C_L\right)_{N_j} + \left(\Delta C_L\right)_\epsilon \qquad \text{(equation 4.6.1-ff)}$$

$$= (0.0446) + (0.00655) + (-0.0020)$$

$$= 0.049$$

REFERENCES

1. Decker, J., et al: USAF Stability and Control Handbook. M-3671, 1956. (U)
2. Ribner, H. S.: Notes on the Propeller and Slipstream in Relation to Stability. NACA WR L-25, 1944. (U)
3. Weil, J., and Sleeman, W. C., Jr.: Prediction of the Effects of Propeller Operation on the Static Longitudinal Stability of Single-Engine Tractor Monoplanes With Flaps Retracted. NACA TN 1722, 1948. (U)
4. Weil, J., and Boykin, R. I.: Wind-Tunnel Tests of the 0.15-Scale Powered Model of the Fleetwings XBTK-1 Airplane Longitudinal Stability and Control. NACA WR L-785, 1945. (U)
5. Squire, H. B., and Trouncer, J.: Round Jets in a General Stream. RAE Report Aero 1974, 1944. (U)
6. Abzug, M. J.: Effect of Jet and Rocket Operation on Static Longitudinal and Directional Stability. BuAer ADR Report M-35, 1945. (U)
7. Ribner, H. S.: Field of Flow About a Jet and Effect of Jets on Stability of Jet-Propelled Airplanes. NACA WR L-213, 1946. (U)
8. Salmi, R. J.: Effects of Jet Billowing on Missile-Type Bodies at Mach 3.85. NASA TN D-284, 1960. (U)
9. Bressette, W. E.: Investigation of the Jet Effects on a Flat Surface Downstream of the Exit of a Simulated Turbojet Nacelle at a Free-Stream Mach Number of 2.02. NACA RM L54E05a, 1954. (U)
10. Salmi, R. J., and Klann, J. L.: Interference Effects at Mach 1.9 on a Horizontal Tail Due to Trailing Shock Waves From an Axisymmetric Body With an Exiting Jet. NACA RM E55J13a, 1956. (U)

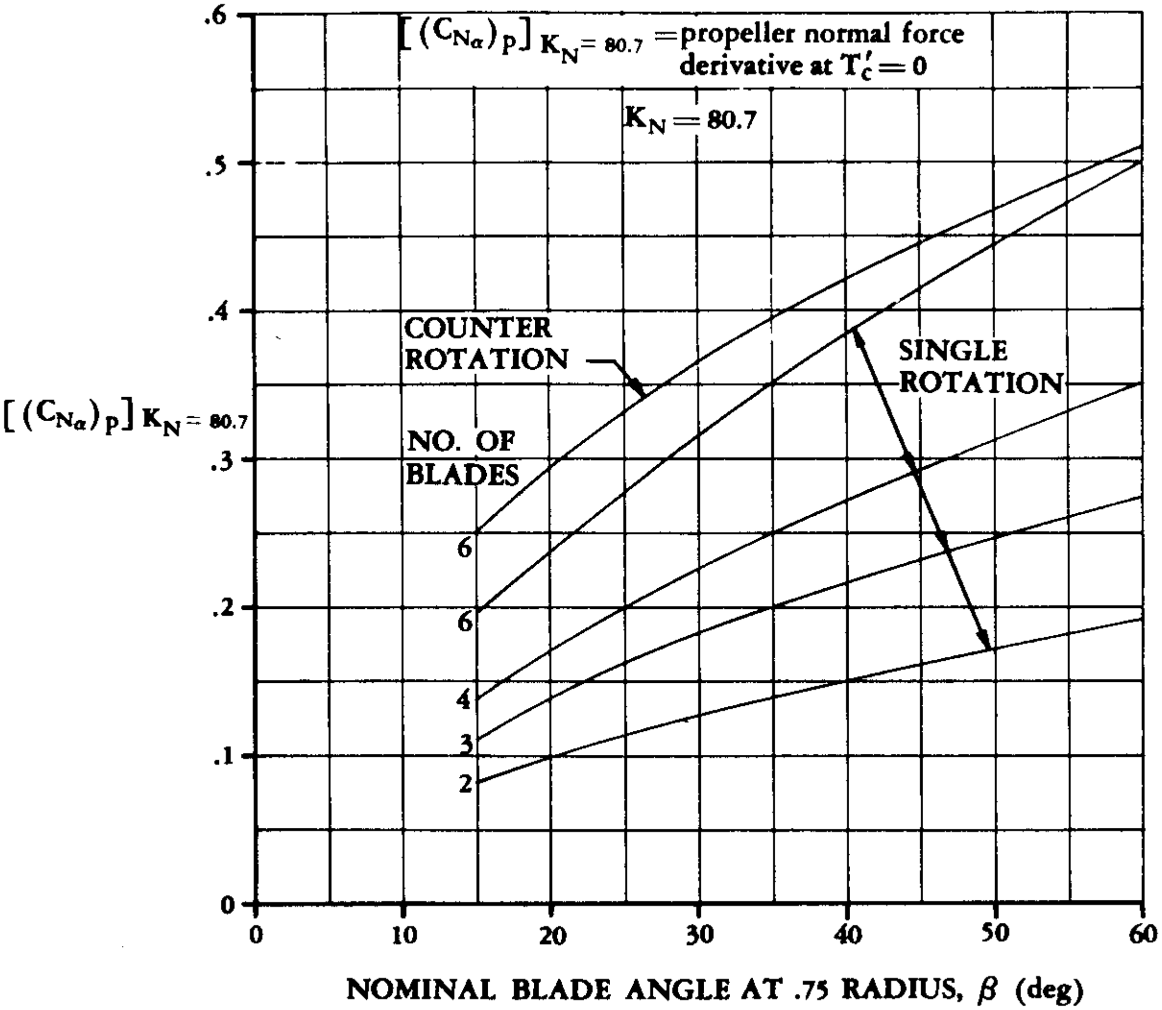

FIGURE 4.6.1-25a PROPELLER NORMAL-FORCE PARAMETER

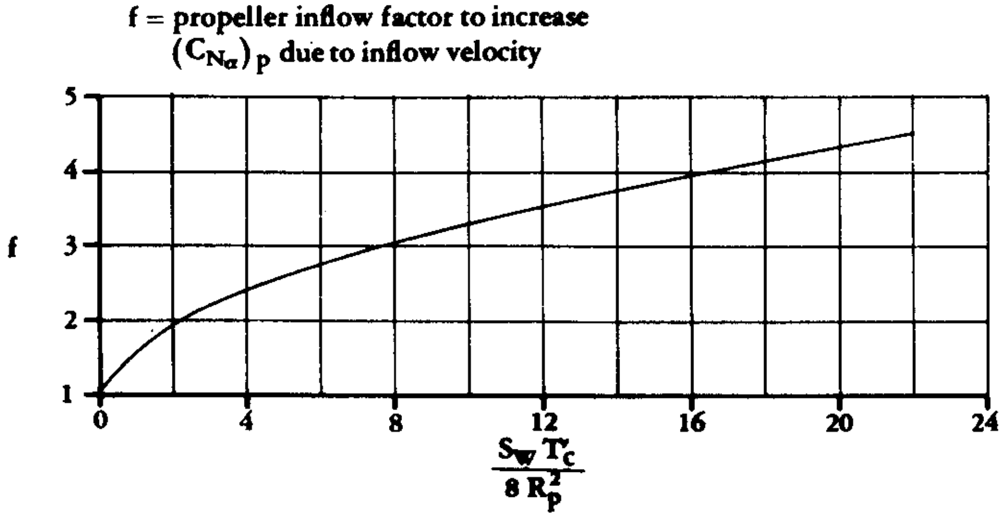

FIGURE 4.6.1-25b PROPELLER INFLOW FACTOR

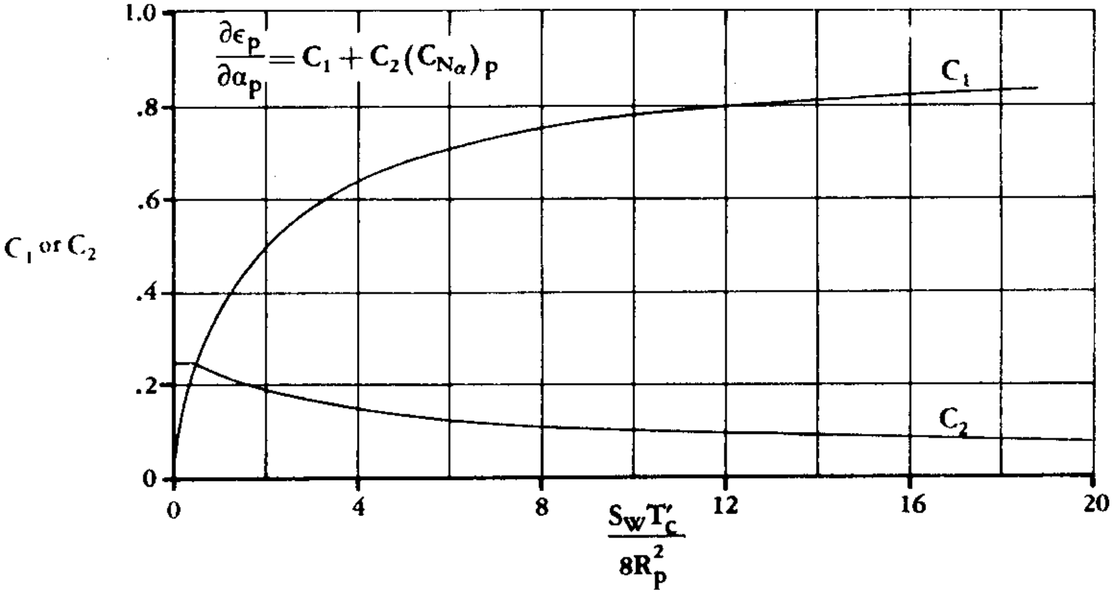

FIGURE 4.6.1-26 FACTORS FOR DETERMINING DOWNWASH DUE TO PROPELLERS

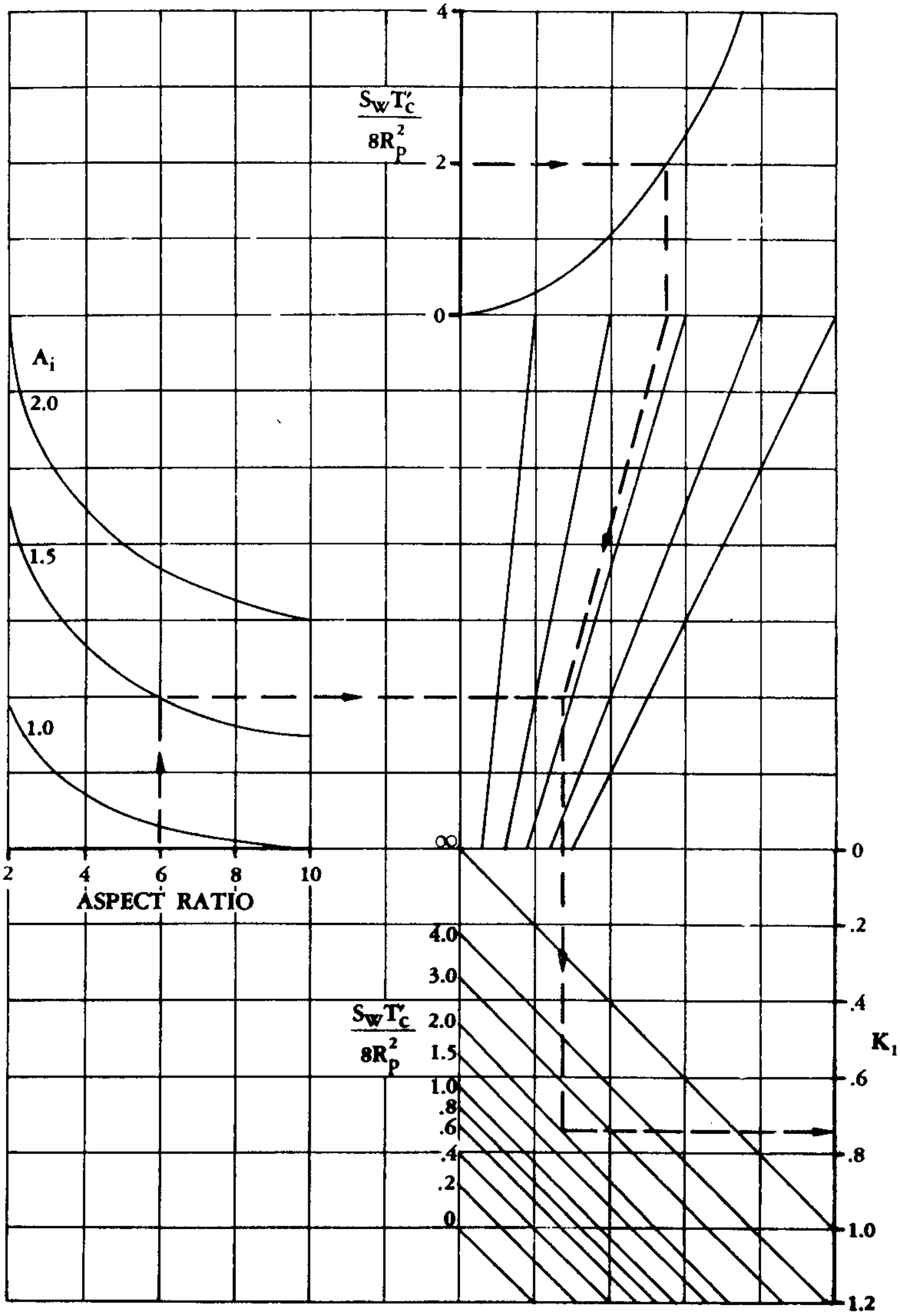

FIGURE 4.6.1-27 CORRELATION PARAMETER FOR ADDITIONAL WING LIFT DUE TO PROPELLER POWER

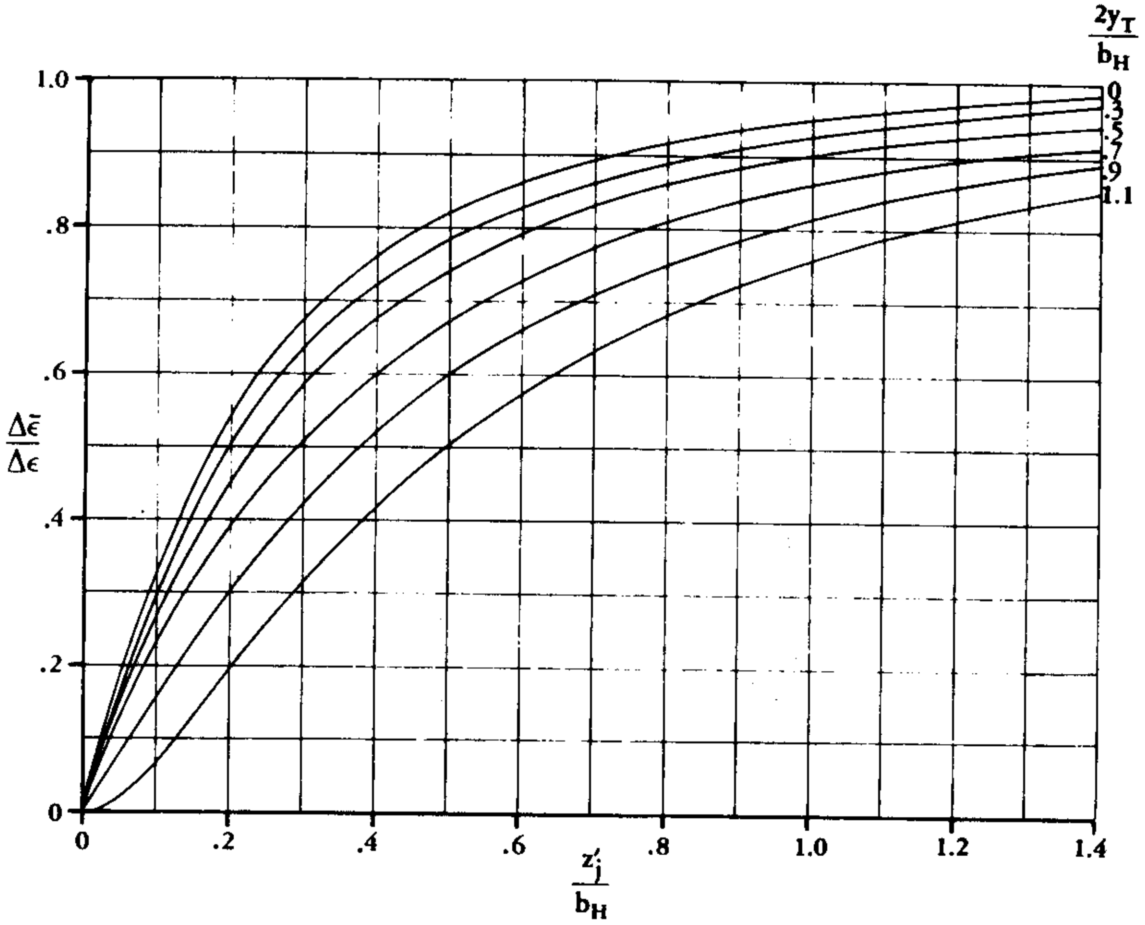

FIGURE 4.6.1-28 MEAN EFFECTIVE DOWNWASH ACTING ON HORIZONTAL TAIL

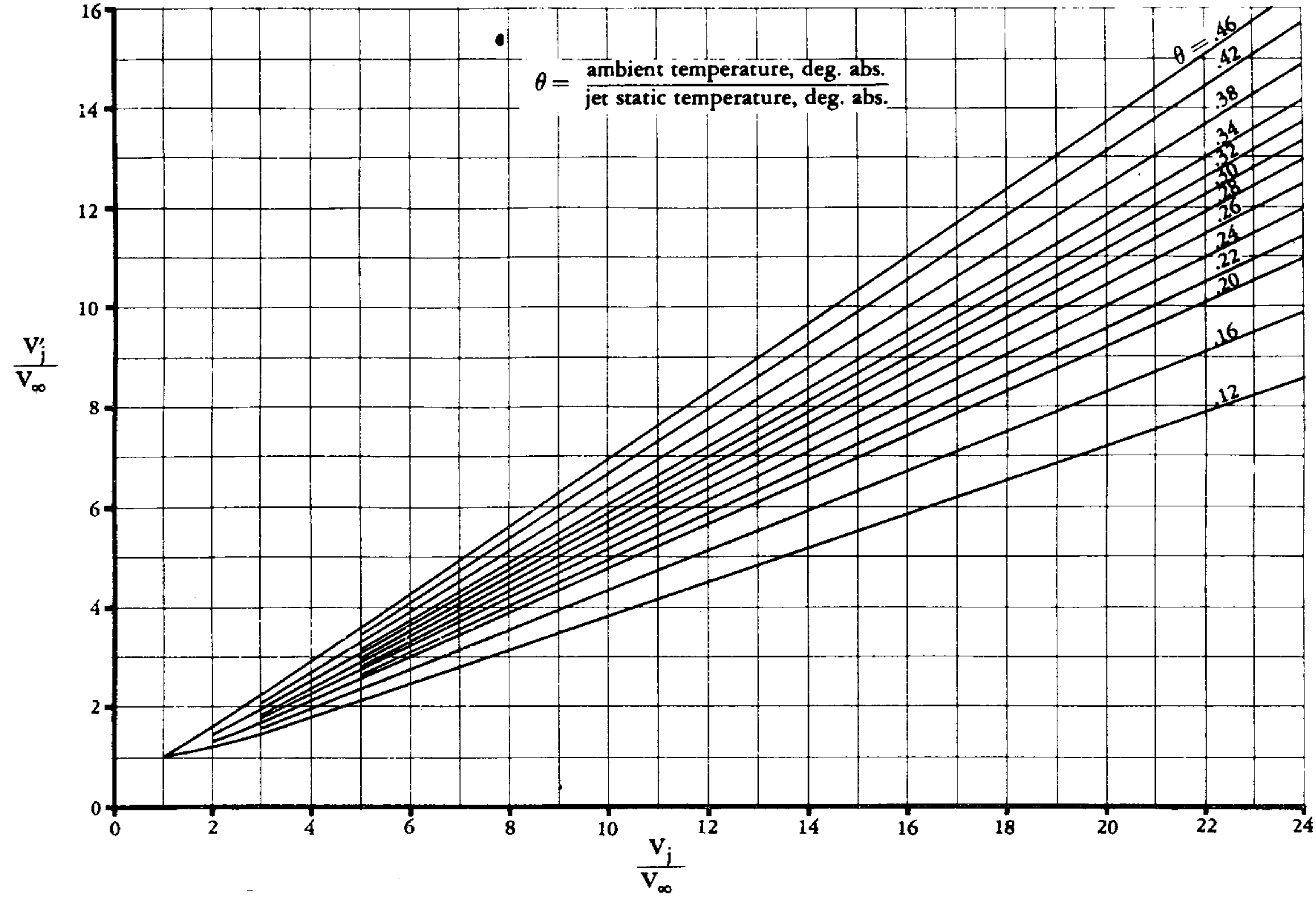

FIGURE 4.6.1-29 VARIATION OF EQUIVALENT VELOCITY RATIO, $\frac{V'_j}{V_\infty}$, WITH VELOCITY RATIO, $\frac{V_j}{V_\infty}$

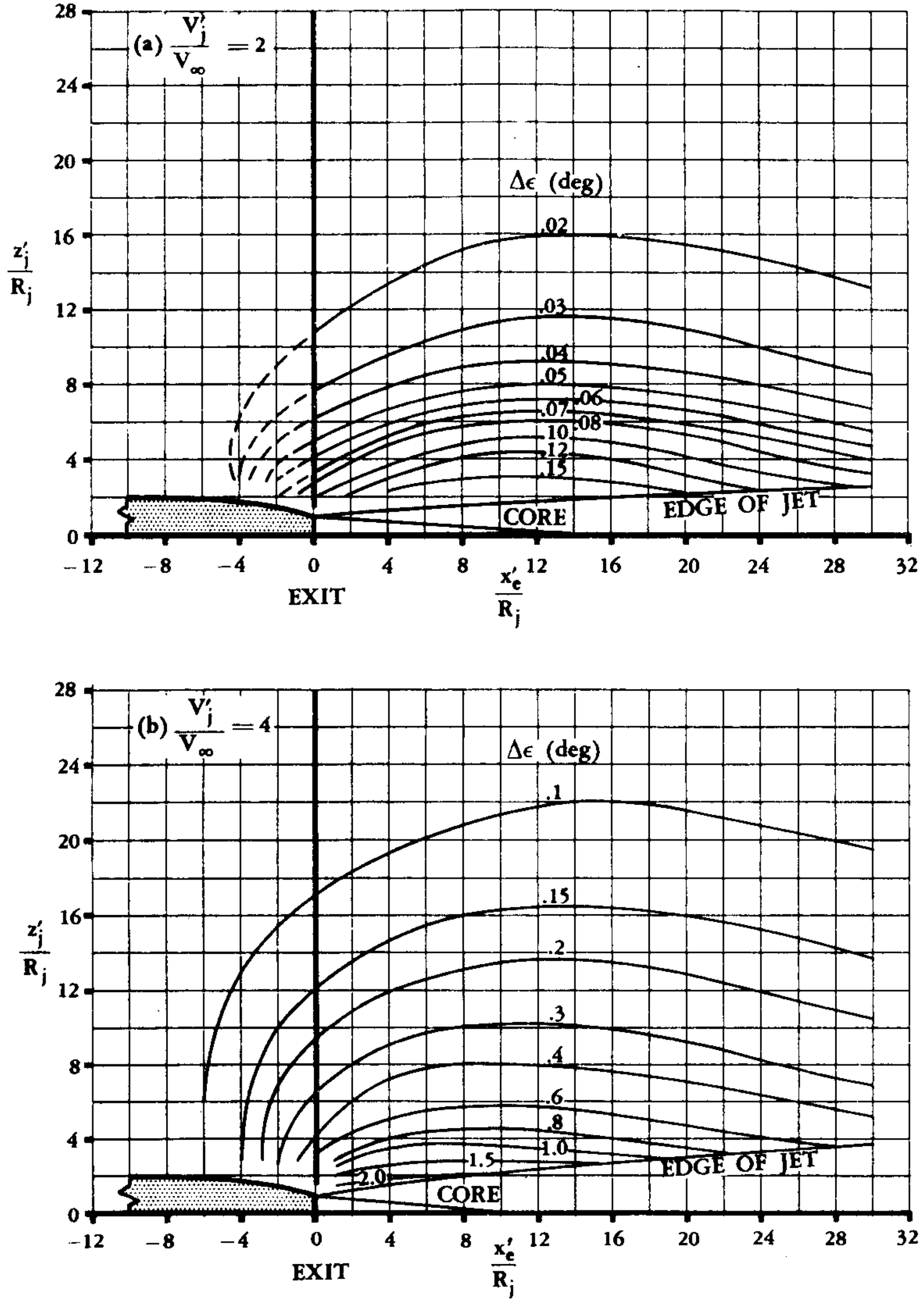

FIGURE 4.6.1-30 DOWNWASH INCREMENT DUE TO SUBSONIC JET IN A SUBSONIC STREAM

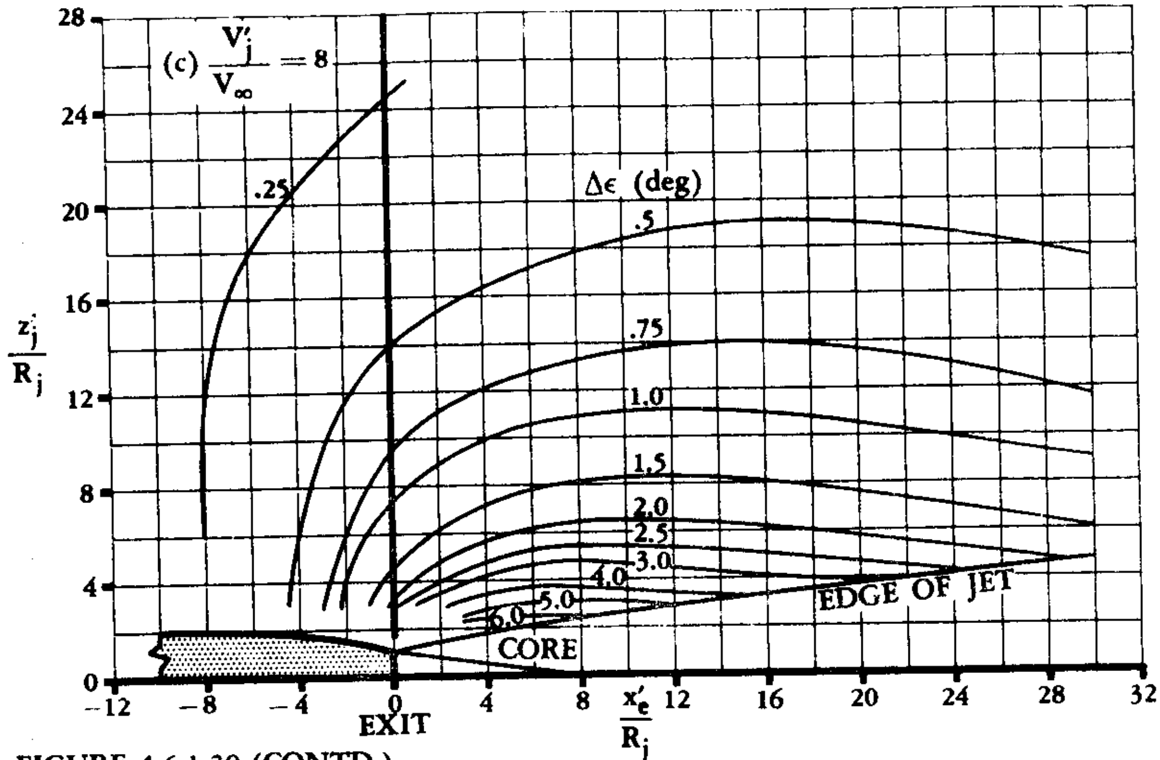

FIGURE 4.6.1-30 (CONTD)

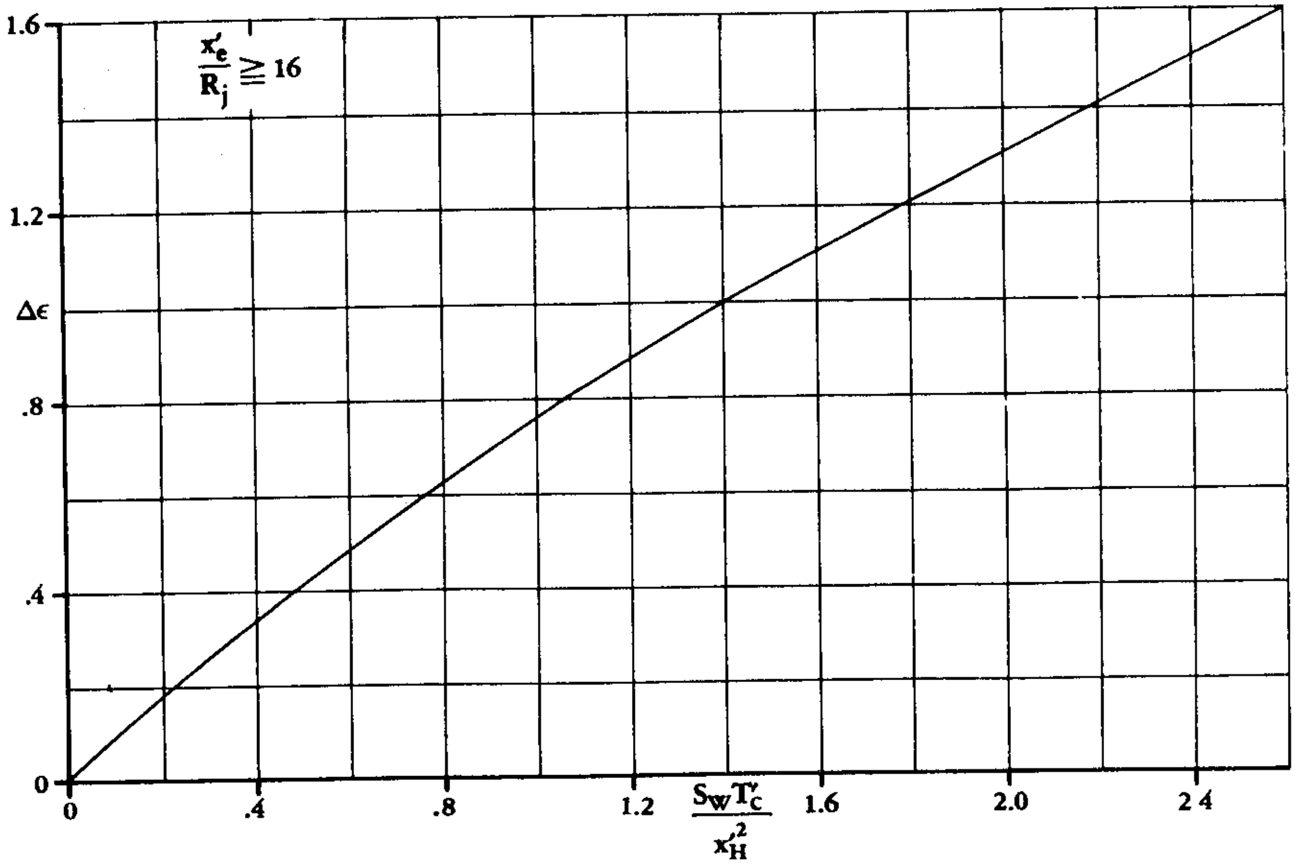

FIGURE 4.6.1-31 DOWNWASH INCREMENT DUE TO A SUBSONIC JET IN A SUBSONIC STREAM

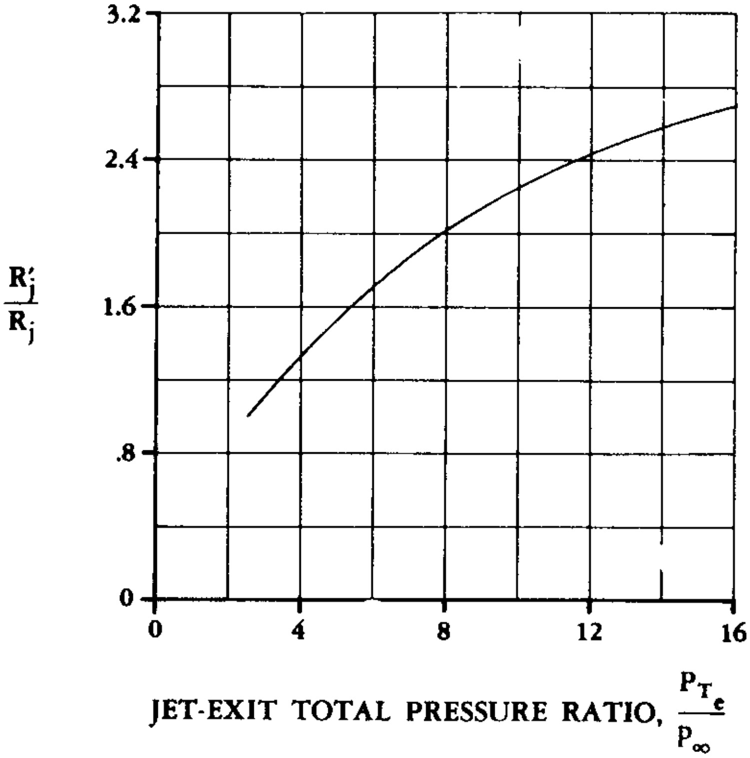

FIGURE 4.6.1-32a EQUIVALENT JET ORIFICE RADIUS FOR SUPERSONIC JET IN A SUBSONIC STREAM

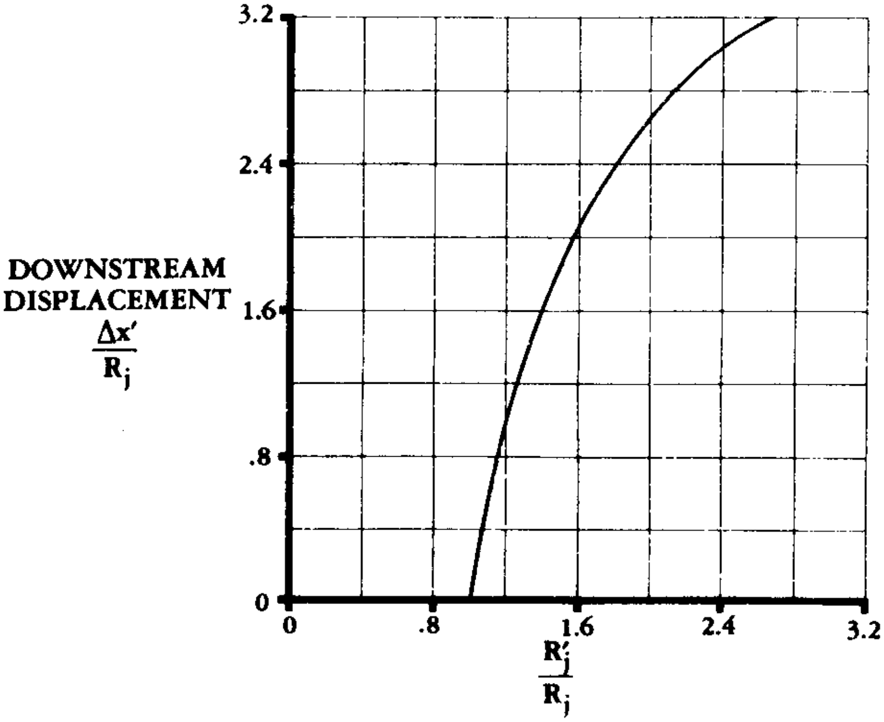

FIGURE 4.6.1-32b DOWNSTREAM DISPLACEMENT OF EQUIVALENT JET ORIFICE LOCATION FOR A SUPERSONIC JET IN A SUBSONIC STREAM

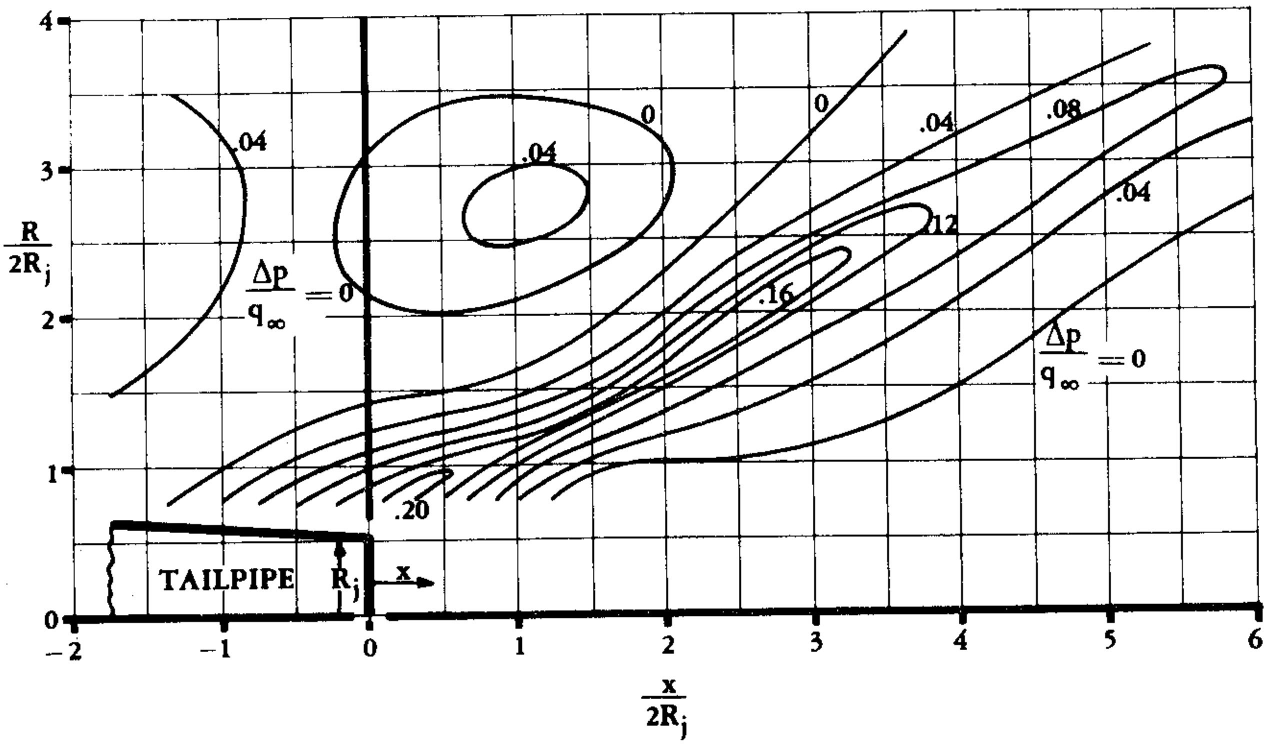

FIGURE 4.6.1-33 PRESSURE FIELD DUE TO JET EXHAUST — M = 2.0 AND $p_{T_e}/p_\infty = 7.0$ (FROM REFERENCE 9)

4.6.2 POWER EFFECTS ON MAXIMUM LIFT

A. PROPELLER POWER EFFECTS ON MAXIMUM LIFT

Over the linear lift-curve-slope range, increases in lift due to propeller power result from the factors discussed in Section 4.6.1, paragraph A. However, near or at maximum lift an additional increase in lift coefficient occurs because the angle of attack for stall increases with power. This effect depends primarily upon the ratio of the immersed wing area to the total wing area. An empirical method,· based on data from references 1 and 2, is presented in this section for estimating the maximum lift increase due to power.

DATCOM METHOD

Step 1. From figure 4.6.2-3 obtain a value for the empirical constant K as a function of the ratio of immersed wing area to total wing area S_i/S_W. (The immersed wing area S_i is calculated in Section 4.6.1.)

Step 2. Calculate the increment in lift due to power $(\Delta C_L)_{\substack{\text{power}\\ \text{on}}}$ at the angle of attack for maximum lift, power off. This value is obtained from equation 4.6.1-w of Section 4.6.1.

Step 3. Calculate the increment of maximum lift due to propeller power by

$$\Delta C_{L_{max}} = K \left(\Delta C_L\right)_{\substack{\text{power}\\ \text{on}}} \qquad 4.6.2\text{-a}$$

The shift in $\alpha_{C_{L_{max}}}$ for the power-on lift curve can only be approximated, based on the shape of the power-off curve. Based on this geometrical approximation, the complete lift curve can then be constructed as shown in sketch (a).

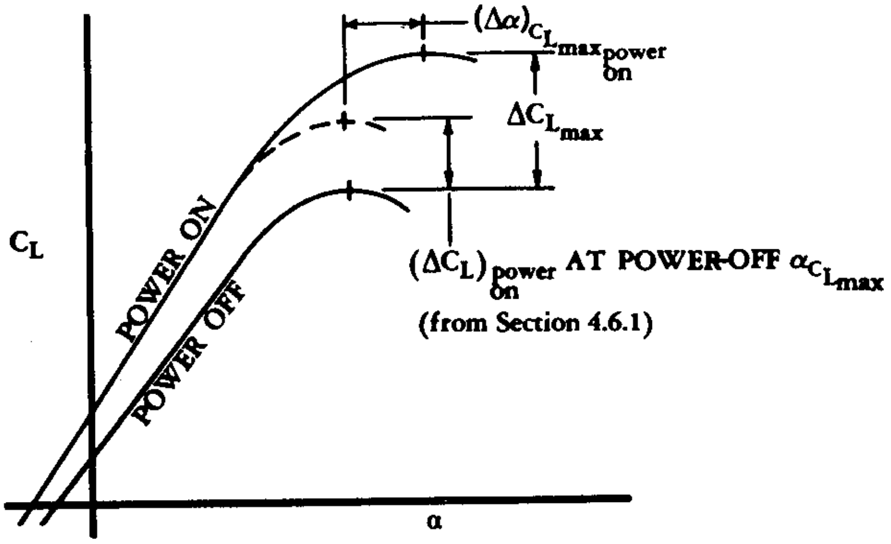

SKETCH (a)

Table 4.6.2-A compares the results obtained by this method with test data.

Sample Problem

Given:

$S_W = 314 \text{ ft}^2$ $\quad T'_c = 0.20$ $\quad \left(\alpha_{stall}\right)_{\substack{power\\off}} = 16°$ (wind-tunnel data)

$\left(\Delta C_L\right)_{\substack{power\\on}} = 0.438$ (Section 4.6.1) $\quad S_i = 114 \text{ ft}^2$ (Section 4.6.1)

Compute:

$$\frac{S_i}{S_W} = \frac{114}{314} = 0.364$$

$K = 1.38$ (figure 4.6.2-3)

$$\Delta C_{L_{max}} = K \left(\Delta C_L\right)_{\substack{power\\on}} \qquad \text{(equation 4.6.2-a)}$$

$$= (1.38)(0.438)$$

$$= 0.604$$

B. JET POWER EFFECTS ON MAXIMUM LIFT

The maximum lift due to jet power is described in Section 4.6.1, paragraph B, since the angle of attack for stall does not exhibit an increase with power as in the case for propellers. The increment in maximum lift is therefore found by calculating the lift increment at the angle of attack for maximum lift, power off, by using the method of Section 4.6.1. The shape of the power-on lift curve near stall is similar to that of the power-off curve determined by using other sections of the Datcom.

REFERENCES

1. Sweberg, H. H., and Dingeldein, R. C.: Summary of Measurements in Langley Full-Scale Tunnel of Maximum Lift Coefficients and Stalling Characteristics of Airplanes. NACA WR L-145, 1945. (U)
2. Anon.: Model C-133A Estimated Basic Stability and Control Data. Douglas Aircraft Company Report LB-21984, 1956. (U)

TABLE 4.6.2-A

LOW-SPEED MAXIMUM-LIFT INCREMENT DUE TO POWER

DATA SUMMARY

Reference	Airplane	T_c	$\frac{S_i}{S_W}$	K	$\left(\Delta C_L\right)_{\substack{power\\on}}$	$\Delta C_{L_{max}}$ Calc	$\Delta C_{L_{max}}$ Test
1	F4U	0.20	0.364	1.38	0.438	0.60	0.64
	Mars	0.13	0.405	1.55	0.123	0.19	0.20
	B-15	0.31	0.500	2.05	0.160	0.33	0.30
	F6F	idle	0.360	1.36	0.101	0.14	0.14
	P-63	idle	0.360	1.36	0.072	0.10	0.08
2	C-133	0.60	0.486	1.97	0.241	0.48	0.56

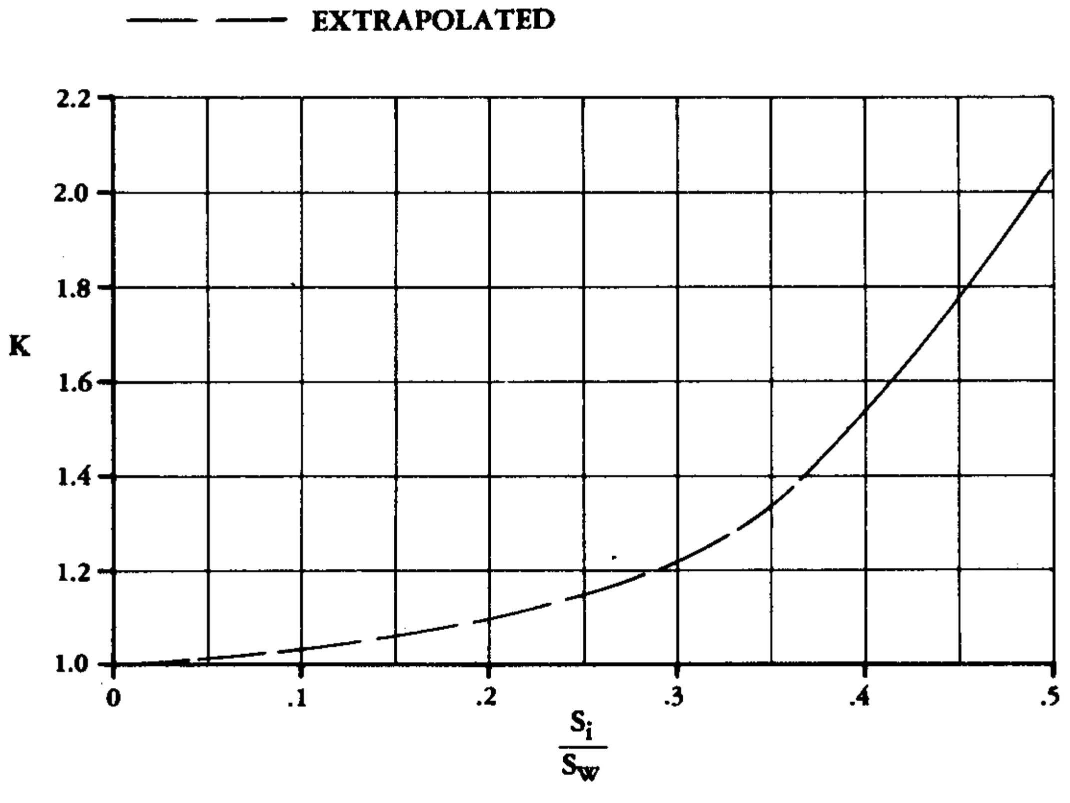

FIGURE 4.6.2-3 CORRECTION FACTOR FOR MAXIMUM LIFT DUE TO POWER

4.6.3 POWER EFFECTS ON PITCHING-MOMENT VARIATION WITH ANGLE OF ATTACK

A. PROPELLER POWER EFFECTS ON PITCHING MOMENT

This section presents a method from references 1 and 2 for estimating the power effects of propellers on the pitching-moment characteristics of a vehicle. Since power effects on pitching-moment characteristics are primarily a result of the increments in lift due to propellers, part A of Section 4.6.1 is directly applicable to this section, and the reader is referred to that discussion for a general description of the fundamental phenomena.

DATCOM METHOD

The Datcom method estimates the power-on pitching-moment curves based on power-off curves, as a function of angle of attack, thrust coefficient, and lift coefficient.

This method analyzes the increments of pitching-moment coefficient due to propeller-power effects in the following order:

1. Offset of the thrust axis from the origin of the axes
2. Propeller normal force due to angle of attack
3. Change in dynamic pressure over the section of the wing in the propeller slipstream
4. Change in lift of the wing caused by power effects
5. Change in dynamic pressure acting on the horizontal tail
6. Change in angle of attack at the horizontal tail

After the above pitching-moment increments for a given angle of attack have been calculated, the accumulated total is then applied to the power-off pitching-moment curve to obtain a point on the power-on pitching-moment curve. After several points have been generated (by considering several angles of attack), the linear section of the power-on pitching-moment curve is obtained for a given thrust coefficient.

All increments of pitching-moment coefficients are nondimensionalized with respect to the product of wing area and wing MAC. Their moment center is at the quarter-chord point of the wing MAC.

Step 1. Calculate the increment in pitching-moment coefficient per engine due to an offset of the thrust axis from the origin of the axes by

$$\left(\Delta C_m\right)_T = T_c' \frac{z_T}{\bar{c}} \qquad \text{4.6.3-a}$$

where the thrust coefficient is a given or chosen quantity. For multiple-engine configurations the total pitching-moment component is found by summing the component due to each engine.

Step 2. Calculate the increment in pitching-moment coefficient due to the propeller normal force by

$$\left(\Delta C_m\right)_{N_p} = \left(\Delta C_L\right)_{N_p} \frac{x_p}{\bar{c}} \frac{\cos i_T}{\cos \alpha_T} \qquad 4.6.3\text{-b}$$

where $(\Delta C_L)_{N_p}$ is obtained from Section 4.6.1 and α_T is given by equation 4.6.1-a, i.e.,

$$\alpha_T = \alpha + i_T$$

Step 3. Calculate the increment in pitching-moment coefficient due to the change in slipstream dynamic pressure acting on the wing as follows:

a. Calculate the zero-lift pitching-moment coefficient $(C_{m_0})_i$ of those components of the tail-off configuration that are immersed in the slipstream by

$$\left(C_{m_0}\right)_i = \left(C_{m_0}\right)_{\text{wing-body}} - \left(C_{m_0}\right)_{\substack{\text{area not}\\ \text{immersed}}} \qquad 4.6.3\text{-c}$$

where $(C_{m_0})_{\text{wing-body}}$ must be obtained from wind-tunnel tests and $(C_{m_0})_{\substack{\text{area not}\\ \text{immersed}}}$ may be obtained from Section 4.1.4.1 and is based on the combined planform area of the wing not immersed in the propeller slipstream.

b. Calculate the change in slipstream dynamic pressure given by equation 4.6.1-r, i.e.,

$$\frac{\Delta q_s}{q_\infty} = \frac{S_W T_c'}{\pi R_p^2}$$

c. Calculate the pitching-moment increment due to the change in slipstream dynamic pressure by

$$\left(\Delta C_m\right)_q = \frac{\Delta q_s}{q_\infty} \left(C_{m_0}\right)_i \qquad 4.6.3\text{-d}$$

Step 4. Calculate the increment in pitching-moment coefficient due to the change in lift of the wing caused by power effects as follows:

a. Calculate the lift increments $(\Delta C_L)_q$ and $(\Delta C_L)_{\Delta\alpha_W}$ by the method in Section 4.6.1.

b. Calculate the pitching-moment increment due to the immersed wing lift increments by

$$\left(\Delta C_m\right)_L = \left[\left(\Delta C_L\right)_q + \left(\Delta C_L\right)_{\Delta\alpha_W}\right] \frac{x_W}{\bar{c}} \qquad 4.6.3\text{-e}$$

where x_W is the longitudinal distance from the aerodynamic center of that portion of the wing immersed in the propeller slipstream to the moment-reference-center location, positive for the aerodynamic center forward of the moment reference center (see Figure 4.6-12).

Step 5. Calculate the increment in pitching-moment coefficient due to the change in dynamic pressure acting on the horizontal tail as follows:

a. Calculate the angle of attack at the horizontal tail α_H by

$$\alpha_H = \alpha + i_H - \left(\epsilon_H\right)_{\substack{\text{power}\\\text{off}}} \qquad 4.6.3\text{-f}$$

where $(\epsilon_H)_{\substack{\text{power}\\\text{off}}}$ is obtained in Section 4.4.1.

b. Obtain a value for the lift-curve slope of the horizontal tail $(C_{L_{\alpha_H}})_{\substack{\text{power}\\\text{off}}}$ from Section 4.1.3.2.

c. Calculate the lift coefficient of the horizontal tail by

$$C_{L_H} = \left(C_{L_{\alpha_H}}\right)_{\substack{\text{power}\\\text{off}}} \alpha_H \qquad 4.6.3\text{-g}$$

d. From figure 4.6.3-14 or 4.6.3-15 obtain a value for the change in downwash at the horizontal tail $\Delta\epsilon_H$ as a function of geometric characteristics, thrust coefficient, and the power-off downwash angle.

e. Calculate the power-on downwash angle at the horizontal tail by

$$\left(\epsilon_H\right)_{\substack{\text{power}\\\text{on}}} = \left(\epsilon_H\right)_{\substack{\text{power}\\\text{off}}} + \Delta\epsilon_H \qquad 4.6.3\text{-h}$$

f. Calculate the geometric distance z_s by equation 4.6.1-n, i.e.

$$z_s = x_p \tan\left(\alpha_T + \epsilon_u - \epsilon_p\right) - z_T$$

g. Calculate the geometric distance $z_{H_{eff}}$ by

$$z_{H_{eff}} = z_s + z_H + \ell_H \tan\left[\alpha_T + \epsilon_u - \epsilon_p - \left(\epsilon_H\right)_{\substack{power\\on}}\right] \qquad 4.6.3\text{-i}$$

h. From figure 4.6.3-16 obtain a value for the change in dynamic pressure $\Delta q_H/q_\infty$ as a function of geometric characteristics and thrust coefficient.

i. Calculate the change in pitching-moment coefficient due to the incremental change in dynamic pressure at the horizontal tail by

$$\left(\Delta C_{m_H}\right)_q = -C_{L_H} \frac{\Delta q_H}{q_\infty} \frac{S_H}{S_W} \frac{\ell_H}{\bar{c}} \qquad 4.6.3\text{-j}$$

Step 6. Calculate the increment in pitching-moment coefficient due to the change in angle of attack of the horizontal tail as follows:

a. Calculate the power-on dynamic-pressure ratio at the horizontal tail by

$$\left(\frac{q_H}{q_\infty}\right)_{\substack{power\\on}} = \left(\frac{q_H}{q_\infty}\right)_{\substack{power\\off}} + \frac{\Delta q_H}{q_\infty} \qquad 4.6.3\text{-k}$$

where $\Delta q_H/q_\infty$ is found in step 5.h and $(q_H/q_\infty)_{\substack{power\\off}}$ is obtained in Section 4.4.1.

b. Calculate the change in pitching-moment coefficient due to the change in angle of attack at the horizontal tail by

$$\left(\Delta C_{m_H}\right)_\epsilon = C_{L_{\alpha_H}} \Delta\epsilon_H \frac{S_H}{S_W} \frac{\ell_H}{\bar{c}} \left(\frac{q_H}{q_\infty}\right)_{\substack{power\\on}} \qquad 4.6.3\text{-}\ell$$

where $\Delta\epsilon_H$ is found in Step 5.d.

Step 7. Calculate the total incremental change in pitching-moment coefficient due to propeller power effects by

$$\left(\Delta C_m\right)_{\substack{power\\on}} = \left(\Delta C_m\right)_T + \left(\Delta C_m\right)_{N_p} + \left(\Delta C_m\right)_q + \left(\Delta C_m\right)_L$$

$$+ \left(\Delta C_{m_H}\right)_q + \left(\Delta C_{m_H}\right)_\epsilon \qquad 4.6.3\text{-m}$$

Sample Problem

The configuration used in this sample problem is the same as that used in the sample problem for propeller effects on lift in Section 4.6.1.

Given:

Wing Parameters:

$S_W = 380 \text{ ft}^2$ $\quad$ $\left.\begin{array}{l} S_i = 117.4 \text{ ft}^2 \\ b_i = 12.8 \text{ ft} \end{array}\right\}$ (calculated in Section 4.6.1)

$$\left.\begin{array}{l} \left(\Delta C_L\right)_{N_p} = 0.00529 \\ \left(\Delta C_L\right)_{\Delta\alpha_W} = -0.0173 \\ \left(\Delta C_L\right)_q = 0.0584 \end{array}\right\} \text{(calculated in Section 4.6.1)}$$

$\bar{c} = 8.17$ ft $\quad$ $\Lambda_{c/4} = 0$ $\quad$ $c_i = 9.17$ ft $\quad$ $\bar{c}_{\substack{\text{area not}\\\text{immersed}}} = 7.50$ ft

$A_{\substack{\text{area not}\\\text{immersed}}} = 4.90$ $\quad$ $\left(c_{m_0}\right)_{\substack{\text{area not}\\\text{immersed}}} = -0.07$ (average value for wing sections not immersed in the slipstream)

$\left(C_{m_0}\right)_{\text{wing-body}} = -0.080$ (tail-off wind-tunnel data) $\quad$ $x_W = 0$

$\alpha = 4.0°$ $\quad$ $\alpha_T = 4.0°$ $\quad$ $\epsilon_u = 1.14°$ $\quad$ $\epsilon_p = 0.59°$

$\epsilon_{\substack{\text{power}\\\text{off}}} = 4.0°$ (wind-tunnel data or Section 4.4.1)

Horizontal-Tail Parameters:

$S_H = 80 \text{ ft}^2$ $\quad$ $\dfrac{S_{H_i}}{S_H} = \dfrac{59}{80} = 0.738$ $\quad$ $i_H = 0$ $\quad$ $A_H = 4.26$

$\lambda_H = 0.59$ $\quad$ $\Lambda_{H_{c/4}} = 0$ $\quad$ $\left(\dfrac{q_H}{q_\infty}\right)_{\substack{\text{power}\\\text{off}}} = 0.9$ $\quad$ (Section 4.4.1)

$C_{L_{\alpha_H}} = 0.057 \quad z_H = -4.10 \text{ ft} \quad z_{H_T} = 3.0 \text{ ft} \quad \ell_H = 20.4 \text{ ft}$

Engine Parameters:

$T'_c = 0.15 \quad R_p = 6.79 \text{ ft} \quad x_p = 10.9 \text{ ft} \quad z_T = -1.10 \text{ ft}$

Compute:

Determine the increment of pitching moment due to an offset of the thrust axis from the origin of the axes

$$\left(\Delta C_m\right)_T = T'_c \frac{z_T}{\bar{c}} \qquad \text{(equation 4.6.3-a)}$$

$$= (0.15) \frac{(-1.10)}{(8.17)} = -0.0202$$

Determine the increment of pitching moment due to the propeller normal force

$$\left(\Delta C_m\right)_{N_p} = \left(\Delta C_L\right)_{N_p} \frac{x_p}{\bar{c}} \frac{1}{\cos \alpha_T} \qquad \text{(equation 4.6.3-b)}$$

$$= (0.00529) \frac{10.9}{8.17} \frac{1}{\cos 4.0^\circ} = 0.00707$$

Determine the increment of pitching moment due to the change in dynamic pressure

$$C_{m_0} = \frac{A \cos \Lambda_{c/4}}{A + 2 \cos \Lambda_{c/4}} \cos \Lambda_{c/4}\, c_{m_0} \qquad \text{(equation 4.1.4.1-a)}$$

where A is the aspect ratio of the combined wing not immersed in the slipstream.

$$C_{m_0} = \frac{4.90}{4.90 + 2} (-0.07)$$

$= -0.05$ (Note: this is based on the wing area not immersed in the slipstream)

$$\left(C_{m_0}\right)_{\substack{\text{area not}\\ \text{immersed}}} = C_{m_0} \left(\frac{S_W - S_i}{S_W}\right) \bar{c}_{\substack{\text{area}\\ \text{immersed}}} \frac{1}{\bar{c}} \qquad \text{(based on } S_W \text{ and } \bar{c}\text{)}$$

$$= (-0.05) \frac{(380 - 117.4)}{380} \frac{(7.50)}{(8.17)} = -0.0317$$

$$\left(C_{m_0}\right)_i = \left(C_{m_0}\right)_{\text{wing-body}} - \left(C_{m_0}\right)_{\substack{\text{area not}\\ \text{immersed}}} \qquad \text{(equation 4.6.3-c)}$$

$$= -0.080 + 0.0317$$

$$= -0.0483$$

$$\frac{\Delta q_s}{q_\infty} = \frac{S_W T'_c}{\pi R_p^2} \qquad \text{(equation 4.6.1-r)}$$

$$= \frac{(380)\,(0.15)}{(3.14)\,(6.79)^2} = 0.394$$

$$\left(\Delta C_m\right)_q = \frac{\Delta q_s}{q_\infty}\left(C_{m_0}\right)_i \qquad \text{(equation 4.6.3-d)}$$

$$= (0.394)\,(-0.0483)$$

$$= -0.019$$

Determine the increment of pitching moment due to the change in lift of the wing

$$\left(\Delta C_m\right)_L = -\left[\left(\Delta C_L\right)_q + \left(\Delta C_L\right)_{\Delta\alpha_W}\right]\frac{x_W}{\bar{c}} \qquad \text{(equation 4.6.3-e)}$$

$$= -\,[0.0584 - 0.0173]\,\frac{0}{8.17}$$

$$= 0$$

Determine the increment of pitching moment due to the change in dynamic pressure on the horizontal tail

$$\alpha_H = \alpha + i_H - \left(\epsilon_H\right)_{\substack{\text{power}\\ \text{off}}} \qquad \text{(equation 4.6.3-f)}$$

$$= 4 + 0 - 4 = 0$$

$$C_{L_H} = \left(C_{L_{\alpha_H}}\right)_{\substack{\text{power}\\ \text{off}}}\alpha_H \qquad \text{(equation 4.6.3-g)}$$

$$= (0.057)\,(0) = 0$$

$$\Delta\epsilon_H = 0.7 \qquad \text{(figure 4.6.3-14)}$$

$$\left(\epsilon_H\right)_{\substack{\text{power}\\ \text{on}}} = \left(\epsilon_H\right)_{\substack{\text{power}\\ \text{off}}} + \Delta\epsilon_H \qquad \text{(equation 4.6.3-h)}$$

$$= 4.0 + 0.7$$

$$= 4.7^\circ$$

$$z_s = x_p \tan\left(\alpha_T + \epsilon_u - \epsilon_p\right) - z_T \qquad \text{(equation 4.6.1-n)}$$

$$= 10.9 \tan (4.0 + 1.14 - 0.59) + 1.10$$

$$= 1.96 \text{ ft}$$

$$z_{H_{eff}} = z_s + z_H + \ell_H \tan\left[\alpha_T + \epsilon_u - \epsilon_p - \left(\epsilon_H\right)_{\substack{\text{power}\\ \text{on}}}\right] \qquad \text{(equation 4.6.3-i)}$$

$$= 1.96 - 4.10 + 20.4 \tan (4 + 1.14 - 0.59 - 4.7)$$

$$= -2.14 + 20.4\,(-0.00262)$$

$$= -2.19 \text{ ft}$$

$$\frac{\Delta q_H}{q_\infty} = 0.14 \qquad \text{(figure 4.6.3-16)}$$

$$\left(\Delta C_{m_H}\right)_q = -C_{L_H} \frac{\Delta q_H}{q_\infty} \frac{S_H}{S_W} \frac{\ell_H}{\bar{c}} \qquad \text{(equation 4.6.3-j)}$$

$$= -(0)\,(0.14)\,\frac{80}{380}\,\frac{20.4}{8.17}$$

$$= 0$$

Determine the increment of pitching moment due to the change in angle of attack at the horizontal tail

$$\left(\frac{q_H}{q_\infty}\right)_{\substack{\text{power}\\ \text{on}}} = \left(\frac{q_H}{q_\infty}\right)_{\substack{\text{power}\\ \text{off}}} + \frac{\Delta q_H}{q_\infty} \qquad \text{(equation 4.6.3-k)}$$

$$= 0.90 + 0.14 = 1.04$$

$$\left(\Delta C_{m_H}\right)_{\epsilon} = C_{L_{\alpha_H}} \Delta\epsilon_H \frac{S_H}{S_W} \frac{\ell_H}{\bar{c}} \left(\frac{q_H}{q_\infty}\right)_{\substack{\text{power}\\\text{on}}} \qquad \text{(equation 4.6.3-}\ell\text{)}$$

$$= (0.057)\,(0.7) \left(\frac{80}{380}\right) \left(\frac{20.4}{8.17}\right) (1.04)$$

$$= 0.0218$$

Determine the total change in pitching moment due to propeller power effects

$$\left(\Delta C_m\right)_{\substack{\text{power}\\\text{on}}} = \left(\Delta C_m\right)_T + \left(\Delta C_m\right)_{N_p} + \left(\Delta C_m\right)_q + \left(\Delta C_m\right)_L$$

$$\left(\Delta C_{m_H}\right)_q + \left(\Delta C_{m_H}\right)_\epsilon \qquad \text{(equation 4.6.3-m)}$$

$$= -0.0202 + 0.00707 - 0.019 + 0 + 0 + 0.0218$$

$$= -0.0103$$

B. JET POWER EFFECTS ON PITCHING MOMENT

This section presents a method from references 1, 3, and 4 for estimating the subsonic jet power effects on pitching moment. The method presented here for estimating the supersonic jet power effects is based on approximate methods developed for the Datcom. Since the power effects on pitching-moment characteristics are primarily a result of the increments in lift due to jet effects, part B of Section 4.6.1 is directly applicable to this section, and the reader is referred to that discussion for a general description of the fundamental phenomena.

DATCOM METHOD

The Datcom method estimates the power-on pitching-moment curves, based on power-off pitching-moment curves, as a function of angle of attack, thrust coefficient, and lift coefficient.

This method analyzes the increments of pitching-moment coefficient due to jet power effects in the following order:

1. Offset of the thrust axis from the origin of the axes

2. Normal force acting at the engine inlet

3. Interference effects

After the above lift increments for a given angle of attack have been calculated, the accumulated total is then applied to the power-off pitching-moment curve to obtain a point on the power-on pitching-moment curve. After several points have been generated (by considering several angles of attack), the linear section of the power-on pitching-moment curve is obtained for a given thrust coefficient. (Refer to figure 4.6-13b for geometrical definitions.)

All increments of pitching-moment coefficients are nondimensionalized with respect to the product of wing area and wing MAC. Their moment center is at the quarter-chord of the wing MAC.

Step 1. Calculate the increment in pitching-moment coefficient per engine due to an offset of the thrust axis from the origin of the axes by

$$\left(\Delta C_m\right)_T = \frac{T_c' z_T}{\bar{c}} \qquad \text{4.6.3-a}$$

where the thrust coefficient is a given or chosen quantity. For multiple-engine configurations the total pitching-moment component is found by summing the single components due to each engine.

Step 2. Calculate the increment in pitching-moment coefficient due to the normal force at the engine inlet as follows:

a. Calculate the inclination of the thrust axis to the oncoming stream α_j at the engine inlet, given by equation 4.6.1-x, i.e.,

$$\alpha_j = \alpha_T + \epsilon_u$$

where the upwash ahead of the wing ϵ_u is obtained from equation 4.6.1-m, i.e.,

$$\epsilon_u = \frac{\partial \epsilon_u}{\partial \alpha}\left(\alpha_W - \alpha_0\right)$$

and the upwash gradient $\partial\epsilon_u/\partial\alpha$ at the engine inlet may be obtained in Section 4.4.1.

b. Calculate the incremental pitching-moment coefficient per engine by

$$\left(\Delta C_m\right)_{N_j} = \frac{2A_I x_I \sin\alpha_j}{S_W \bar{c}} \qquad \text{4.6.3-n}$$

where A_I is the inlet duct area. For multiple-engine configurations the total pitching-moment component is found by summing the single components due to each engine.

Step 3. Calculate the increment in pitching-moment coefficient due to the jet interference effects at the horizontal tail or other surface by

$$\left(\Delta C_m\right)_\epsilon = \left(\Delta C_L\right)_\epsilon \frac{x}{\bar{c}} \qquad \text{4.6.3-o}$$

where $\left(\Delta C_L\right)_\epsilon$ is calculated in Section 4.6.1 and where x is the distance from the moment center to the centroid of the affected area, positive ahead of the moment center (in the case of tail-last configurations x corresponds to the negative value of the tail length ℓ_H).

Step 4. Calculate the total incremental change in pitching-moment coefficient due to jet effects by

$$\left(\Delta C_m\right)_{\substack{\text{power}\\\text{on}}} = \left(\Delta C_m\right)_T + \left(\Delta C_m\right)_{N_j} + \left(\Delta C_m\right)_\epsilon \qquad 4.6.3\text{-p}$$

Sample Problem

The configuration used in this sample problem is the same as that used in the sample problem of Section 4.6.1, paragraph B.

Given:

Engine Parameters:

Outboard Engines (2)

$T_c' = 0.0746$ (per engine) $A_I = 13.64\ \text{ft}^2$ $x_I = 145.2$ in.

$z_T = 53.0$ in. $\alpha_j = 9.87°$ (Section 4.6.1)

Inboard Engines (2)

$T_c' = 0.0746$ (per engine) $A_I = 13.64\ \text{ft}^2$ $x_I = 283.8$ in.

$z_T = 70.8$ in. $\alpha_j = -10.4°$ (Section 4.6.1)

Horizontal-Tail Parameters:

$\left(\Delta C_L\right)_\epsilon = -0.002$ (Section 4.6.1) $\ell_H = 855.0$ in.

Wing Parameters:

$\bar{c} = 272.8$ in. $S_W = 2930\ \text{ft}^2$

Compute:

Determine the increment in pitching-moment coefficient due to an offset of the thrust axis from the origin of the axes by

$$\left(\Delta C_m\right)_T = \frac{T_c' z_T}{\bar{c}} \qquad \text{(equation 4.6.3-a)}$$

Considering the increment in pitching-moment coefficient due to both outboard engines

$$\left[\left(\Delta C_m\right)_T\right]_{\substack{\text{outboard}\\ \text{engines}}} = \frac{(0.0746)\,(53.0)\,(2)}{(272.8)}$$

$$= 0.0290$$

Considering the increment in pitching-moment coefficient due to both inboard engines

$$\left[\left(\Delta C_m\right)_T\right]_{\substack{\text{inboard}\\ \text{engines}}} = \frac{(0.0746)\,(70.8)\,(2)}{(272.8)}$$

$$= 0.0387$$

The total increment in pitching-moment coefficient due to an offset of the thrust axis is

$$\left(\Delta C_m\right)_T = \left[\left(\Delta C_m\right)_T\right]_{\substack{\text{outboard}\\ \text{engines}}} + \left[\left(\Delta C_m\right)_T\right]_{\substack{\text{inboard}\\ \text{engines}}}$$

$$= 0.0290 + 0.0387$$

$$= 0.0677$$

Determine the increment in pitching-moment coefficient due to the normal force at the engine inlets

$$\left(\Delta C_m\right)_{N_j} = \frac{2 A_I x_I \sin \alpha_j}{S_W \bar{c}} \qquad \text{(equation 4.6.3-n)}$$

Considering the increment in pitching-moment coefficient due to both outboard engines

$$\left[\left(\Delta C_m\right)_{N_j}\right]_{\substack{\text{outboard}\\ \text{engines}}} = \frac{(2)\,(2)\,(13.64)\,(145.2)\,(0.1714)}{(2930)\,(272.8)} = 0.00170$$

Considering the increment in pitching-moment coefficient due to both inboard engines

$$\left[\left(\Delta C_m\right)_{N_j}\right]_{\substack{\text{inboard}\\ \text{engines}}} = \frac{(2)\,(2)\,(13.64)\,(283.8)\,(0.1805)}{(2930)\,(272.8)} = 0.00350$$

The total increment in pitching-moment coefficient due to the normal force at the engine inlet is

$$\left(\Delta C_m\right)_{N_j} = \left[\left(\Delta C_m\right)_{N_j}\right]_{\substack{\text{outboard}\\ \text{engines}}} + \left[\left(\Delta C_m\right)_{N_j}\right]_{\substack{\text{inboard}\\ \text{engines}}}$$

$$= 0.00170 + 0.00350$$

$$= 0.00520$$

Determine the increment in pitching-moment coefficient due to the jet interference effects at the horizontal tail

$$\left(\Delta C_m\right)_\epsilon = \left(\Delta C_L\right)_\epsilon \frac{x}{\bar{c}} \qquad \text{(equation 4.6.3-o)}$$

For a tail-last configuration this can be expressed as

$$\left(\Delta C_m\right)_\epsilon = \left(\Delta C_L\right)_\epsilon \frac{(-\ell_H)}{\bar{c}}$$

$$= (-0.002) \frac{(-855.0)}{272.8}$$

$$= 0.00627$$

Determine the total increment of pitching-moment coefficient due to jet power effects

$$\left(\Delta C_m\right)_{\substack{\text{power}\\ \text{on}}} = \left(\Delta C_m\right)_T + \left(\Delta C_m\right)_{N_j} + \left(\Delta C_m\right)_\epsilon \qquad \text{(equation 4.6.3-p)}$$

$$= 0.0677 + 0.0052 + 0.00627$$

$$= 0.079$$

REFERENCES

1. Decker, J., et al: USAF Stability and Control Handbook. M-3671, 1956. (U)
2. Ribner, H. S.: Notes on the Propeller and Slipstream in Relation to Stability. NACA WR L-25, 1944. (U)
3. Squire, H. B., and Trouncer, J.: Round Jets in a General Stream. RAE Report Aero 1974, 1944. (U)
4. Ribner, H. S.: Field of Flow About a Jet and Effect of Jets on Stability of Jet-Propelled Airplanes. NACA WR L-213, 1946. (U)

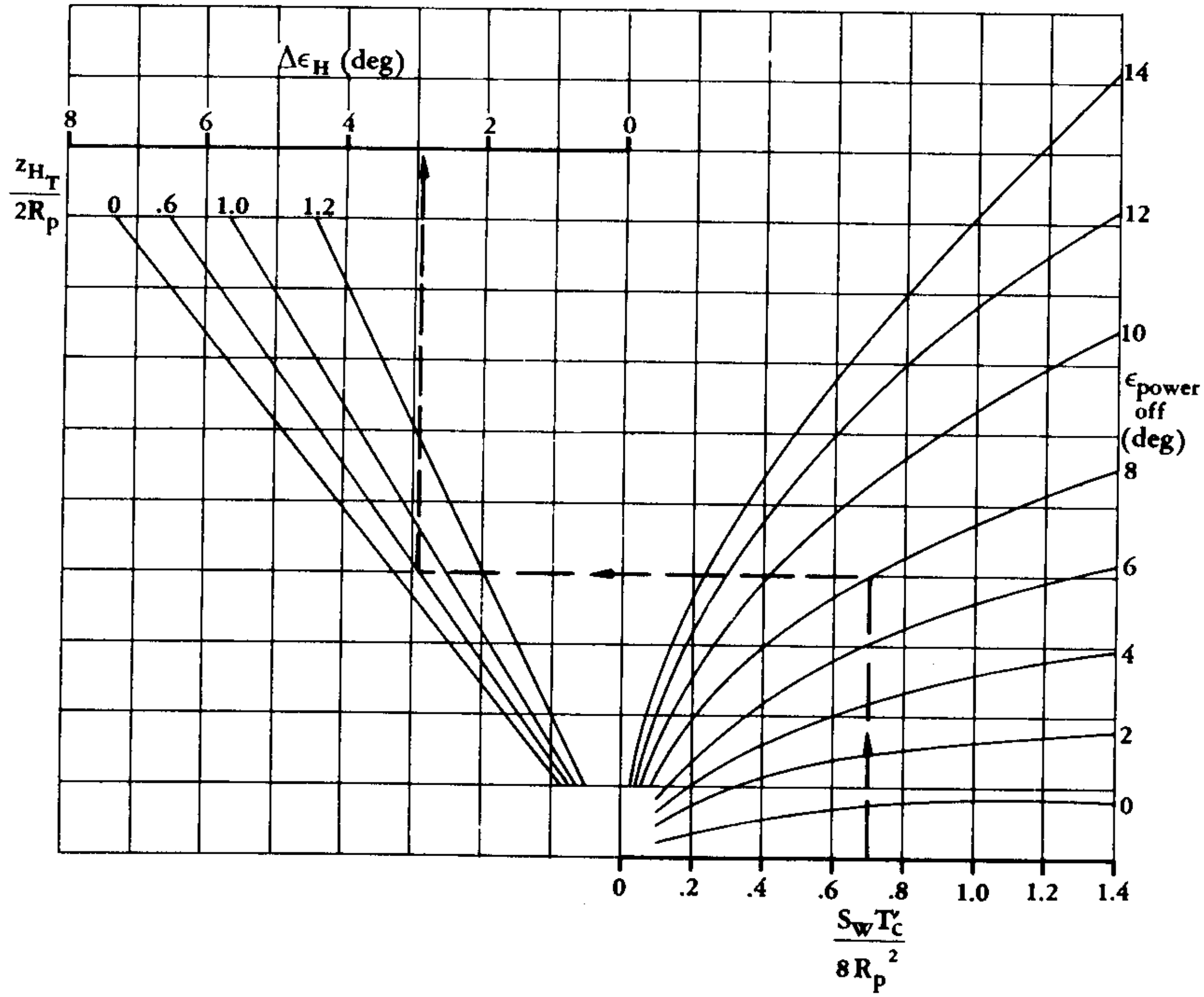

FIGURE 4.6.3-14 INCREMENT IN DOWNWASH DUE TO PROPELLER POWER FOR SINGLE-ENGINE AIRPLANES

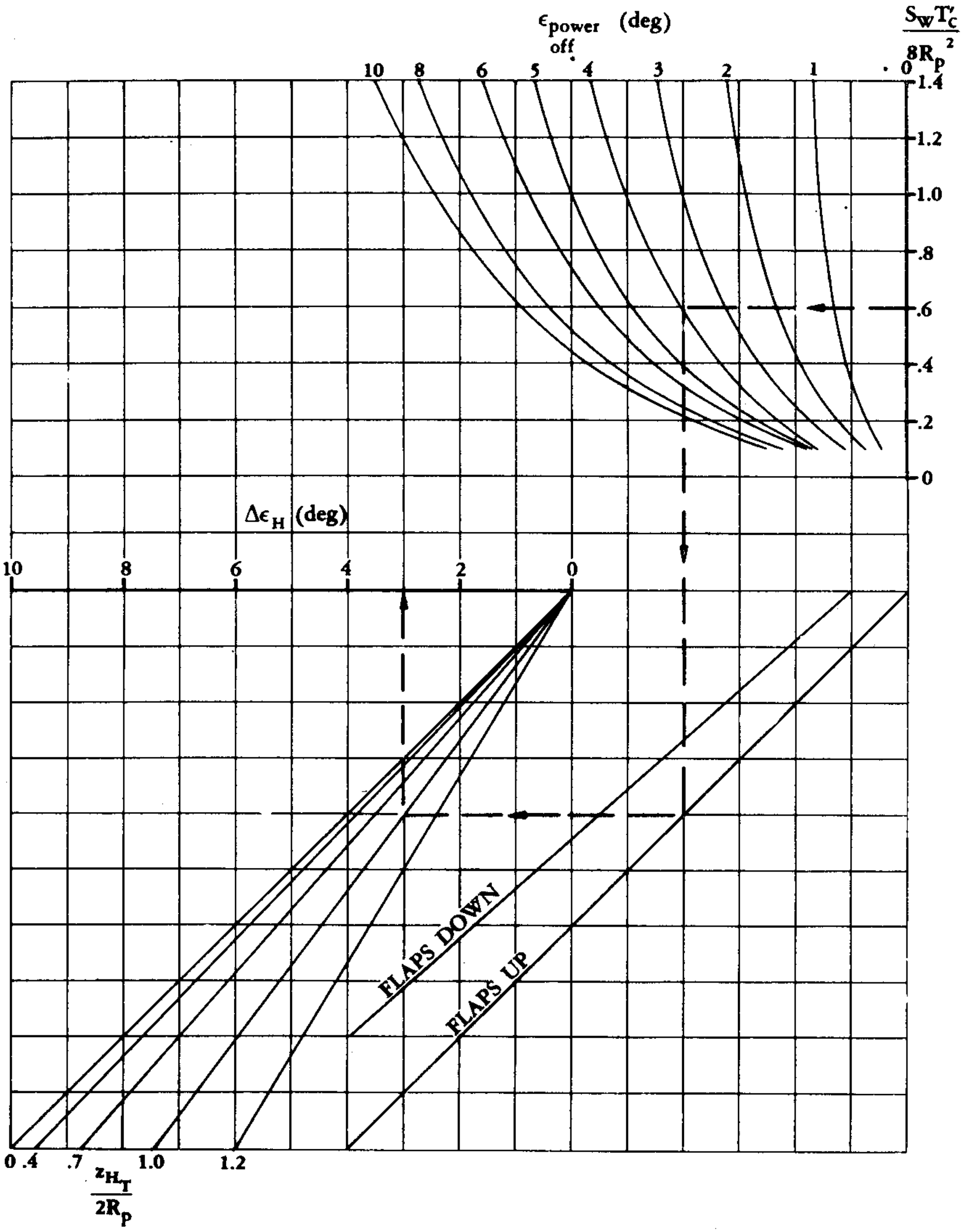

FIGURE 4.6.3-15 INCREMENT IN DOWNWASH DUE TO PROPELLER POWER FOR MULTIENGINE AIRPLANES

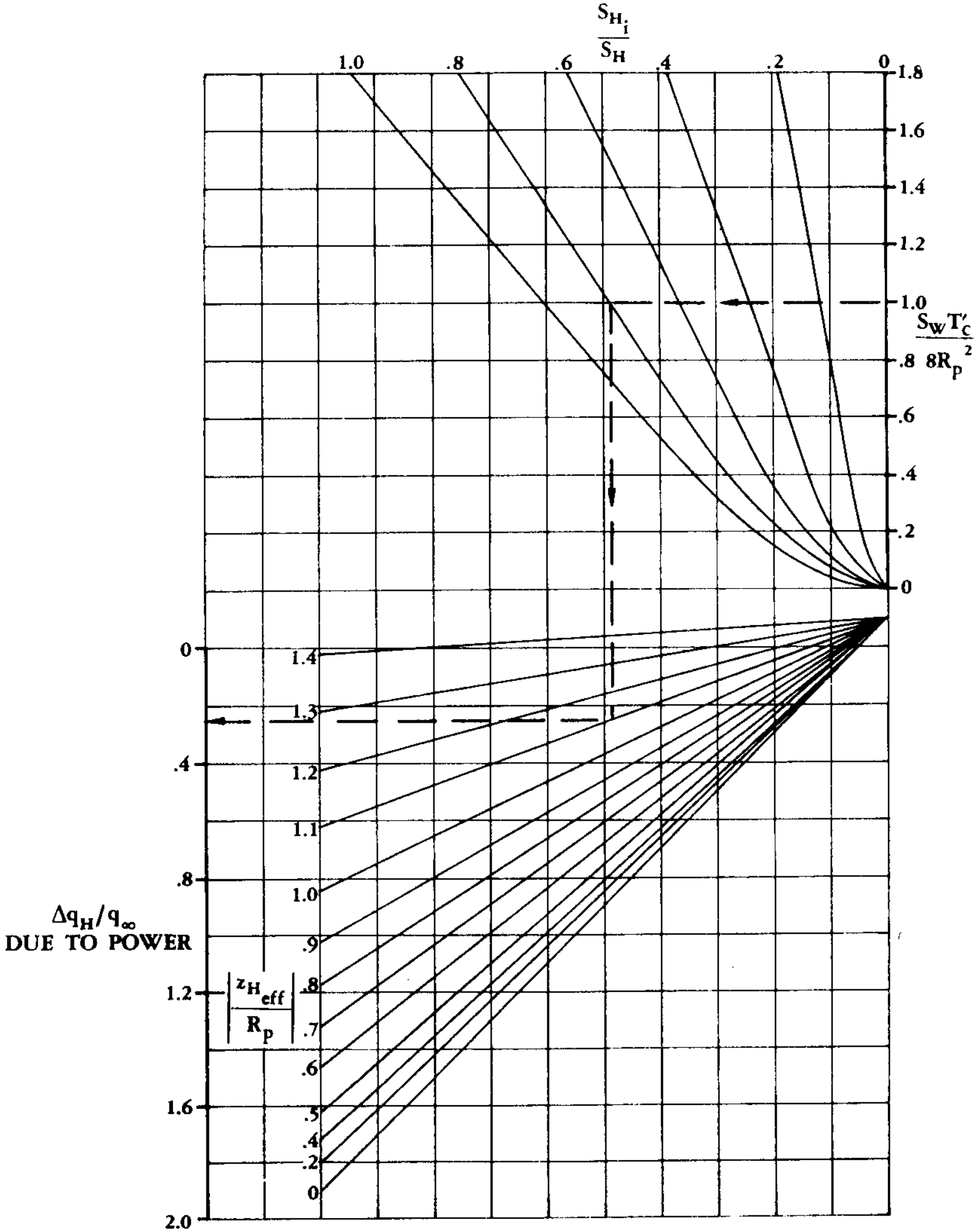

FIGURE 4.6.3-16 EFFECT OF PROPELLER POWER ON DYNAMIC PRESSURE RATIO AT THE HORIZONTAL TAIL

4.6.4 POWER EFFECTS ON DRAG AT ANGLE OF ATTACK

This section presents methods for estimating jet and propeller power effects on the drag of an aircraft. Many of the basic phenomena associated with changes in the drag are discussed in Section 4.6.1, and the reader is referred to that discussion for a more complete description of the fundamental phenomena.

A. PROPELLER POWER EFFECTS ON DRAG

The effects of propeller power on the drag of an airplane require corrections to the zero-lift drag and the lift-dependent drag.

The zero-lift drag is corrected to account for the change in dynamic pressure caused by the propeller slipstream.

The lift-dependent drag of an airplane is affected by propeller power in the following ways:

1. The components of propeller thrust and normal force that are parallel to and have the same direction as the wing lift reduce the wing lift required, thereby reducing the wing drag due to lift.
2. The propeller slipstream modifies the downwash over portions of the wing, thus changing the wing drag due to lift.
3. Propeller thrust is usually assumed to act parallel to the free stream. However, the free-stream component of thrust is really $T \cos \alpha_T$. Therefore, the drag component must include this differential thrust and the propeller normal-force component parallel to the free stream.

DATCOM METHOD

The Datcom method (reference 1) estimates the drag increment due to propeller-thrust effects as a function of angle of attack, thrust coefficient, and propeller normal force.

This method analyzes the increments of drag coefficient due to propeller power effects in the following order:

1. Change in zero-lift drag due to the slipstream dynamic pressure of that portion of the vehicle immersed in the propeller slipstream
2. Change in vehicle drag due to lift as a result of the lift components of propeller thrust and propeller normal force
3. Change in drag due to lift as a result of the change in angle of attack of the wing section immersed in the propeller slipstream

After the above drag increments for a given lift coefficient have been calculated, the accumulated total is then applied to the power-off drag curve to obtain a point on the power-on drag polar. After several points have been generated (by considering several lift coefficients), the power-on drag polar is obtained for a given thrust coefficient.

The above increments in drag can be determined by the following steps. (Reference should be made to figure 4.6-13a for geometric definitions. In all cases the drag increments are based on the wing reference area.)

Step 1. Calculate the zero-lift increment of change in drag coefficient due to propeller-power effects as follows:

a. Calculate the increment of skin-friction drag caused by a higher local dynamic pressure on all surface area immersed in the propeller slipstream S_I by

$$\left(\Delta C_{D_0}\right)_s = \frac{1}{S\,q_\infty} \int_{S_I} C_f \,\Delta q_s \,ds \qquad 4.6.4\text{-a}$$

where C_f is the local skin-friction drag coefficient determined by the methods of Sections 4.1.5.1 and 4.2.3.1. By assuming that q_s and C_f are constant over the area wetted by the slipstream, equation 4.6.4-a may be simplified to

$$\left(\Delta C_{D_0}\right)_s = C_f \frac{S_I}{S} \frac{\Delta q_s}{q_\infty} \qquad 4.6.4\text{-b}$$

where $\Delta q_s/q_\infty$ is determined in Section 4.6.1.

b. Calculate the flap increment of zero-lift drag due to propeller power effects when the wing flaps are extended and are partially or entirely immersed in the propeller slipstream, as follows:

(1) Evaluate the propeller correlation parameter defined as

$$\frac{S_W T_c'}{R_p^2}$$

(2) From figure 4.6.4-12 obtain a value for $T_c' \sqrt{\dfrac{1 + a}{1 + 2a}} \dfrac{S_W}{S_p}$ as a function of of the propeller correlation parameter.

(3) Obtain a value for the power-off drag increment of the deflected flap $\left(\Delta C_{D_0}\right)_{flap}$ from test data if available or from Section 6.1.7.

(4) Calculate the wing planform area S_{W_f} including and directly forward of the flap area.

(5) Calculate the part of S_{W_f} immersed in the propeller slipstream S_i.

(6) Calculate the flap increment of zero-lift drag by

$$\left[\left(\Delta C_{D_0}\right)_{\text{flaps}}\right]_{\substack{\text{power}\\ \text{on}}} = \left(\Delta C_{D_0}\right)_{\text{flaps}} \left(T_c' \sqrt{\frac{1+a}{1+2a}} \frac{S_W}{S_p}\right)\left(\frac{S_i}{S_{W_f}}\right) \qquad 4.6.4\text{-c}$$

c. Calculate the total zero-lift increment of drag due to propeller power effects by

$$\left(\Delta C_{D_0}\right)_{\substack{\text{power}\\ \text{on}}} = \left(\Delta C_{D_0}\right)_s + \left[\left(\Delta C_{D_0}\right)_{\text{flaps}}\right]_{\substack{\text{power}\\ \text{on}}} \qquad 4.6.4\text{-d}$$

When the flaps are retracted the total zero-lift increment is given by equation 4.6.4-b.

Step 2. Calculate the propeller power effects on drag due to lift as follows:

a. Calculate the propeller normal-force coefficient per engine by

$$C_{N_p} = \left(C_{N_\alpha}\right)_p \frac{\alpha_p}{57.3} \frac{S_p}{S_W} \qquad 4.6.4\text{-e}$$

where $\left(C_{N_\alpha}\right)_p$ is obtained from Section 4.6.1.

b. Calculate the angle of attack of the thrust axis α_T measured from the free-stream direction and given by equation 4.6.1-a, i.e.,

$$\alpha_T = \alpha + i_T$$

c. Calculate the thrust coefficient T_c' per engine given by equation 4.6.1-b, i.e.,

$$T_c' = \frac{T}{q_\infty S_W}$$

where the thrust is a given or chosen quantity.

d. Calculate the sum of the propeller lift components by

$$C_{L_p} = T_c' \sin \alpha_T + C_{N_p} \cos \alpha_T \qquad 4.6.4\text{-f}$$

For multiple-engine configurations the total lift component due to propeller forces is found by summing the components due to each engine.

e. Calculate the wing lift coefficient C_L by

$$C_L = \frac{n'W}{q_\infty S_W} \qquad 4.6.4\text{-g}$$

where $n'W$ is the product of load factor and weight.

f. From figure 4.6.4-13a obtain a value for the empirical drag factor K_D as a function of geometry and thrust coefficient.

g. Calculate the wing lift coefficient with power effects C_{L_W} by

$$C_{L_W} = C_L - C_{L_p} \qquad 4.6.4\text{-h}$$

where C_{L_p} is the total lift component due to propeller forces.

h. From figure 4.6.4-13b obtain a value for the ratio of effective downwash to propeller downwash $\bar{\epsilon}/\epsilon_p$ as a function of the propeller correlation parameter and aircraft geometry.

i. Calculate the upwash gradient $\partial\epsilon_p/\partial\alpha_p$ given by equation 4.6.1-j, i.e.,

$$\frac{\partial \epsilon_p}{\partial \alpha_p} = C_1 + C_2 \left(C_{N_\alpha}\right)_p$$

where the constants C_1 and C_2 are obtained from figure 4.6.1-26 as a function of the propeller correlation parameter, and $\left(C_{N_\alpha}\right)_p$ is obtained from Section 4.6.1.

j. Calculate the angle of attack of the propeller plane α_p given by equation 4.6.1-g, i.e.,

$$\alpha_p = \alpha_T + \frac{\partial \epsilon_u}{\partial \alpha} (\alpha_W - \alpha_0)$$

where the upwash gradient $\partial\epsilon_u/\partial\alpha$ at the propeller may be obtained in Section 4.4.1.

k. Calculate the effective downwash over the wing span $\bar{\bar{\epsilon}}$ by

$$\bar{\bar{\epsilon}} = \frac{\bar{\epsilon}}{\epsilon_p} \left(\frac{\partial \epsilon_p}{\partial \alpha_p} \right) \alpha_p \qquad 4.6.4\text{-i}$$

l. Calculate the ratio of the power-on induced drag to the power-off induced drag by

$$\frac{\left(C_{D_L}\right)_{\substack{\text{power}\\ \text{on}}}}{\left(C_{D_L}\right)_{\substack{\text{power}\\ \text{off}}}} = \left(\frac{C_{L_W}}{C_L} \right)^2 \left[1 + \frac{\pi^2 A \bar{\bar{\epsilon}}}{180\, C_{L_W}} \right] + K_D \left[\left(\frac{b}{2R_p} \right) \left(\frac{C_{L_p}}{C_L} \right) \right]^2 \qquad 4.6.4\text{-j}$$

The contribution from the last term in the above equation is generally less than ten percent.

The value for $\left(C_{D_L}\right)_{\substack{\text{power}\\ \text{off}}}$ must be available from wind-tunnel data or may be approximated by the wing-alone value of C_{D_L} obtained by using the method of Section 4.1.5.2.

Step 3. Calculate the total drag of an aircraft including power effects by

$$\left(C_D\right)_{\substack{\text{power}\\ \text{on}}} = \left(C_{D_0}\right)_{\substack{\text{power}\\ \text{on}}} + \left(\Delta C_{D_0}\right)_{\substack{\text{power}\\ \text{on}}} + \left(C_{D_L}\right)_{\substack{\text{power}\\ \text{on}}} \qquad 4.6.4\text{-k}$$

This equation is computed for a range of lift coefficients and thrust coefficients, and the drag-polar curves are constructed. These curves are valid only in the linear-lift region.

Sample Problem

The configuration used in this sample problem is the same as that used in the sample problem for propeller power effects on lift in Section 4.6.1. The quantities listed below are either given or calculated in the sample problem of paragraph A, Section 4.6.1, or assumed.

Given:

Wing Parameters:

$S_W = 380 \text{ ft}^2$ $\qquad \dfrac{S_i}{S_W} = 0.309$ $\qquad A = 6.23$ $\qquad \dfrac{\Delta q_s}{q_\infty} = 0.394$ $\qquad \dfrac{\partial \epsilon_p}{\partial \alpha_p} = 0.115$

$C_L = 0.523$ $\qquad \dfrac{c_f}{c} = 0.20$ $\qquad \delta_f = 30^\circ$ $\qquad \dfrac{S_i}{S_{W_f}} = 0.80$ $\qquad b = 48.65 \text{ ft}$

Engine Parameters:

$\left(C_{N_\alpha}\right)_p = 0.141$ $i_T = 0$ $\alpha_T = 4°$ $R_p = 6.79$ ft $T'_c = 0.150$

$\alpha_p = 5.14°$ $n = 1$

Additional Parameters:

$\alpha = 4.0°$ $n' = 1.0$ $C_f = 0.0040$ $\left(\Delta C_{D_0}\right)_{flap} = 0.040$

$\left(C_{D_L}\right)_{\substack{power\\off}} = 0.0160$ $\left(C_{D_0}\right)_{\substack{power\\off}} = 0.10$

Compute:

Determine the zero-lift increment in drag

$$\left(\Delta C_{D_0}\right)_s = C_f \frac{S_I}{S} \frac{\Delta q_s}{q_\infty} \qquad \text{(equation 4.6.4-b)}$$

$$= (0.0040)\ (0.309)\ (0.394)$$

$$= 0.0005$$

$$\frac{S_W T'_c}{R_p^2} = \frac{(380)\ (0.15)}{(6.79)^2} = 1.236$$

$$T'_c \sqrt{\frac{1+a}{1+2a}}\ \frac{S_W}{S_p} = 0.25 \qquad \text{(figure 4.6.4-12)}$$

$$\left[\left(\Delta C_{D_0}\right)_{flaps}\right]_{\substack{power\\on}} = \left(\Delta C_{D_0}\right)_{flaps} \left(T'_c \sqrt{\frac{1+a}{1+2a}}\ \frac{S_W}{S_p}\right) \left(\frac{S_i}{S_{W_f}}\right)$$

(equation 4.6.4-c)

$$= (0.040)\ (0.25)\ (0.80)$$

$$= 0.0080$$

$$\left(\Delta C_{D_0}\right)_{\substack{\text{power}\\ \text{on}}} = \left(\Delta C_{D_0}\right)_s + \left[\left(\Delta C_{D_0}\right)_{\text{flaps}}\right]_{\substack{\text{power}\\ \text{on}}} \qquad \text{(equation 4.6.4-d)}$$

$$= 0.0005 + 0.0080$$

$$= 0.0085$$

Determine the effects on drag due to lift

$$C_{N_p} = \left(C_{N_\alpha}\right)_p \frac{\alpha_p}{57.3} \frac{S_p}{S_W} \qquad \text{(equation 4.6.4-e)}$$

$$= (0.141) \left(\frac{5.14}{57.3}\right) \frac{(3.14)\,(6.79)^2}{380}$$

$$= 0.0048$$

$$C_{L_p} = T_c' \sin \alpha_T + C_{N_p} \cos \alpha_T \qquad \text{(equation 4.6.4-f)}$$

$$= (0.150)\,(0.0698) + (0.0048)\,(0.998)$$

$$= 0.0105 + 0.0048$$

$$= 0.0153$$

$$K_D = 3.75 \qquad \text{(figure 4.6.4-13a)}$$

$$C_{L_W} = C_L - C_{L_p} \qquad \text{(equation 4.6.4-h)}$$

$$= 0.523 - 0.0153$$

$$= 0.508$$

$$\frac{\bar{\epsilon}}{\epsilon_p} = 0.24 \qquad \text{(figure 4.6.4-13b)}$$

$$\bar{\epsilon} = \frac{\bar{\epsilon}}{\epsilon_p} \left(\frac{\partial \epsilon_p}{\partial \alpha_p}\right) \alpha_p \qquad \text{(equation 4.6.4-i)}$$

$$= (0.24)\,(0.115)\,(5.14^\circ)$$

$$= 0.142^\circ$$

$$\frac{\left(C_{D_L}\right)_{\substack{\text{power}\\ \text{on}}}}{\left(C_{D_L}\right)_{\substack{\text{power}\\ \text{off}}}} = \left(\frac{C_{L_W}}{C_L}\right)^2 \left[1 + \frac{\pi^2 A \bar{\epsilon}}{180\, C_{L_W}}\right] + K_D \left[\left(\frac{b}{2R_p}\right)\left(\frac{C_{L_p}}{C_L}\right)\right]^2$$

(equation 4.6.4-j)

$$= \left(\frac{0.508}{0.523}\right)^2 \left[1 + \frac{(3.14)^2\ (6.23)\ (0.142)}{(180)\ (0.508)}\right] + 3.75 \left[\left(\left(\frac{48.65}{13.58}\right)\ \frac{0.0153}{0.523}\right)\right]^2$$

$$= 0.943\ [1.0954] + 3.75\ [0.01098]$$

$$= 1.074$$

$$\left(C_{D_L}\right)_{\substack{\text{power}\\ \text{on}}} = (1.074)\ (0.016)$$

$$= 0.0172$$

Determine the total drag

$$\left(C_D\right)_{\substack{\text{power}\\ \text{on}}} = \left(C_{D_0}\right)_{\substack{\text{power}\\ \text{off}}} + \left(\Delta C_{D_0}\right)_{\substack{\text{power}\\ \text{on}}} + \left(C_{D_L}\right)_{\substack{\text{power}\\ \text{on}}}$$

(equation 4.6.4-k)

$$= 0.10 + 0.0085 + 0.0172$$

$$= 0.126$$

B. JET POWER EFFECTS ON DRAG

There are three jet power effects on the drag of an airplane. A jet emanating from the rear of a fuselage or nacelle has large effects on both the afterbody drag and the base drag of the fuselage or nacelle. The remaining two jet power effects on drag can be attributed to the lift force of the jet (the vertical component of the thrust) and the inlet normal force. (See Section 4.6.1, paragraph B, for additional discussion.) These lift forces reduce the wing lift and therefore reduce the wing drag due to lift.

Accurate and rapid procedures for estimating the effects of jets on base and afterbody drag are not available. The large number of internal- and external-flow variables and the large number of geometric variables pertaining to the nozzle and the afterbody prevent the prediction of these effects by the use of either simplified theory or empirical correlation of the available test data. Therefore, no Datcom method for treating jet power effects on base and afterbody drag is given. However, a brief discussion is given from references 2 and 3 presenting the salient aspects of the flow elements. The major portion of the discussion is taken from a method for treating transonic and supersonic base drag due to jets from reference 3. (The complexity of the method prevents its formulation into a Datcom method.) Curves are presented that indicate the trends of base pressure with some of the significant variables.

DATCOM METHOD

The Datcom method is composed of two parts. The first part presents a discussion of the jet power effects on base and afterbody drag. The second part presents a method for estimating the jet power effects due to the vertical component of thrust and the inlet normal force.

Jet Power Effects on Base and Afterbody Drag

The mathematical expression for base drag in terms of base pressure may be expressed as

$$C_{D_b} = \frac{1}{q_\infty S} \int_{S_b}\int [p_\infty - p_b(x, y)]\, dx\, dy \qquad 4.6.4\text{-}\ell$$

where S_b is the base area and S is the reference area. The base lies in the XY-plane, and the base pressure p_b may vary over the base. For most cases, p_b is almost constant and equation 4.6.4-ℓ reduces to

$$C_{D_b} = \frac{(p_\infty - p_b)\, S_b}{q_\infty S} \qquad 4.6.4\text{-m}$$

A plot of some of the data of reference 2 is given in figure 4.6.4-14 for the model geometry sketched in the upper part of the figure. The base-pressure coefficient is presented as a function of Mach number for three ratios of jet total pressure to ambient pressure. From figure 4.6.4-14 it can be seen that the highest base-drag conditions occur in the transonic regime.

The geometry and initial-flow parameters for an axially symmetric boattailed afterbody with a nozzle are presented in figure 4.6.4-15. Directly behind the base area is a region of low-velocity air at pressure p_b. The free-stream flow expands to this pressure p_b as it passes the end of the afterbody. The expanded free-stream flow mixes with the low-velocity air along a boundary until it encounters flow from the jet. In similar fashion, flow from the jet expands as it passes through the nozzle exit plane. The flow mixes with the low-velocity air at the base along some boundary. When the external and internal flows meet, each must go through a shock wave that (1) turns the flows until they are parallel, and (2) equalizes the pressures of the two flows. The external flow and the flow from the jet then proceed downstream with a mixing zone lying between them. A flow pattern for the above geometrical description is indicated in figure 4.6.4-16 for a supersonic jet and free stream at a ratio of total pressure to ambient pressure greater than 2.35.

The influence of major design parameters on the base-pressure ratio of axially symmetric afterbodies with jets is presented in figures 4.6.4-17 through 4.6.4-21. The influence of free-stream Mach number on afterbody pressure is given in figure 4.6.4-17 for a convergent nozzle with the indicated geometry and pressure conditions. Figures 4.6.4-18a and 4.6.4-18b present the effects of the ratios of jet total pressure to ambient pressure and of jet diameter to body diameter, respectively, on base pressure. In these two figures the free-stream and exit Mach numbers are constant. For the given free-stream and geometric parameters, divergence of the nozzle significantly increases the base pressure, causing a decrease in base drag. The importance of nozzle divergence angle is shown in figure 4.6.4-19.

The low-speed air at the base of a boattailed afterbody can interact with the boundary layer of the exterior flow. If the jet pressure is sufficiently high, the interaction will increase the pressure in the boundary layer on the rear of the afterbody, decreasing the afterbody drag. Figure 4.6.4-20 presents the probably favorable effects of boattail angle and nozzle divergence angle on both the base pressure and afterbody drag.

The unfavorable effects on base pressure caused by the flaring of an afterbody are presented in figure 4.6.4-21. The flared afterbody is also likely to have more afterbody drag because of its forward-facing slopes.

Jet Power Lift Effects on Drag Due to Lift

The power-on drag due to lift is obtained from the following equation:

$$\left(C_{D_L}\right)_{\substack{\text{power}\\\text{on}}} = \left(C_{D_L}\right)_{\substack{\text{power}\\\text{off}}} \left[\frac{C_L - \left(\Delta C_L\right)_T - \left(\Delta C_L\right)_{N_j}}{C_L}\right]^2 \qquad 4.6.4\text{-n}$$

where C_L is the power-off lift coefficient required for the given flight condition, $\left(C_{D_L}\right)_{\substack{\text{power}\\\text{off}}}$ is the drag due to lift corresponding to C_L obtained by the method of Section 4.1.5.2, $\left(\Delta C_L\right)_T$ and $\left(\Delta C_L\right)_{N_j}$ are found in Section 4.6.1.

Sample Problem

The configuration used in this sample problem is the same as that used in the sample problem of Section 4.6.1, paragraph B.

Given:

$C_L = 0.75$

$$\left.\begin{aligned}\left(\Delta C_L\right)_T &= 0.0446\\ \left(\Delta C_L\right)_{N_j} &= 0.00655\end{aligned}\right\} \text{(Section 4.6.1)}$$

$$\left(C_{D_L}\right)_{\substack{\text{power}\\\text{off}}} = 0.16 \qquad \text{(Section 4.1.5.2)}$$

Compute:

Determine the power-on drag due to lift

$$\left(C_{D_L}\right)_{\substack{\text{power}\\\text{on}}} = \left(C_{D_L}\right)_{\substack{\text{power}\\\text{off}}} \left[\frac{C_L - \left(\Delta C_L\right)_T - \left(\Delta C_L\right)_{N_j}}{C_L}\right]^2 \qquad \text{(equation 4.6.4-n)}$$

$$= 0.16 \left[\frac{0.75 - 0.0446 - 0.00655}{0.75}\right]^2$$

$$= (0.16)\,(0.868)$$

$$= 0.139$$

REFERENCES

1. Decker, J., et al: USAF Stability and Control Handbook. M-3671, 1956. (U)
2. Cubbage, J. M., Jr.: Jet Effects on Base and Afterbody Pressures of a Cylindrical Afterbody at Transonic Speeds. NACA RM L56C21, 1956. (U)
3. Korst, H. H., Chow, W. L., and Zumwalt, G. W.: Research on Transonic and Supersonic Flow of a Real Fluid at Abrupt Increases in Cross Section. Univ. of Ill., Tech. Report. 392-5, 1959. (U)

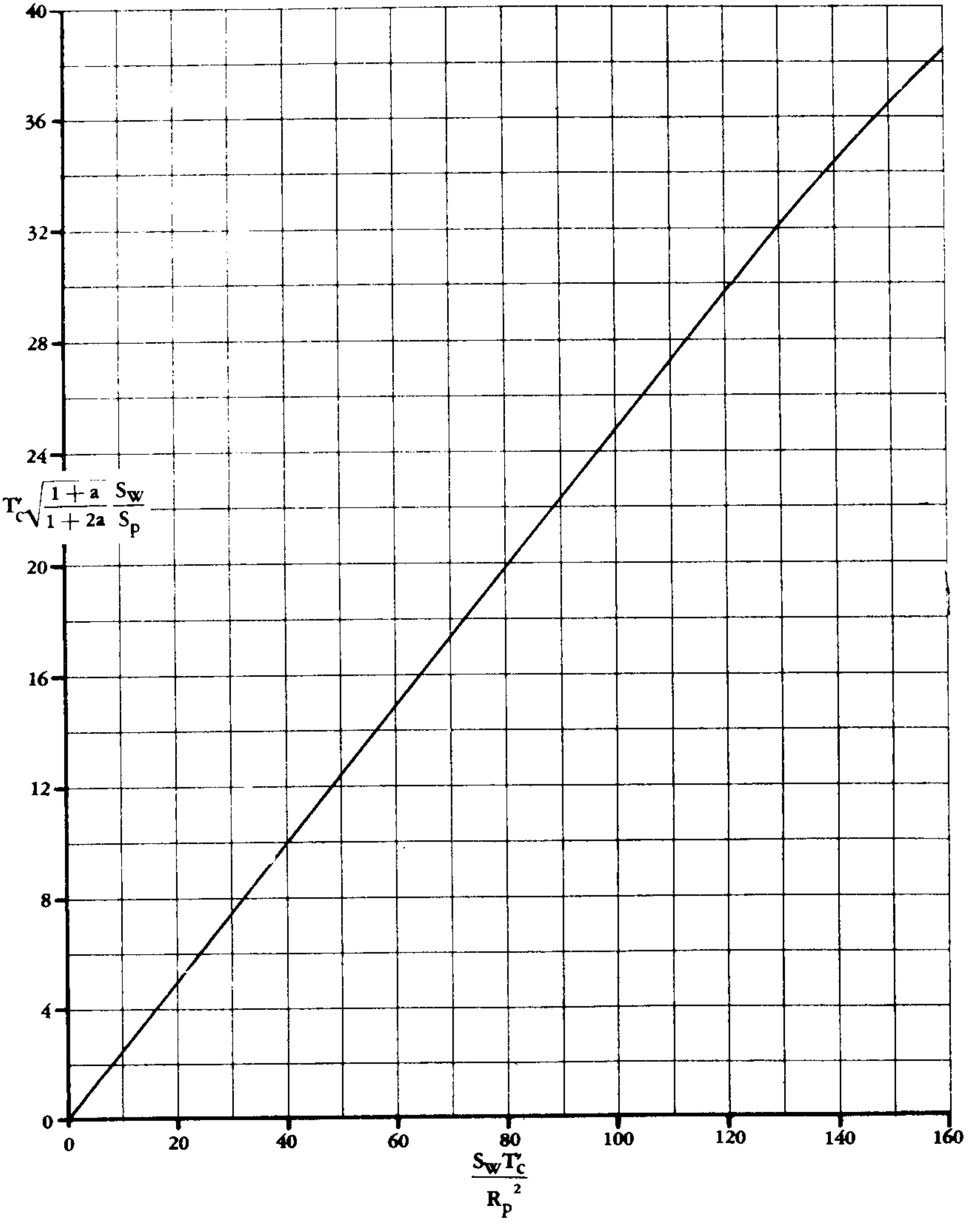

FIGURE 4.6.4-12 THRUST-COEFFICIENT FUNCTION

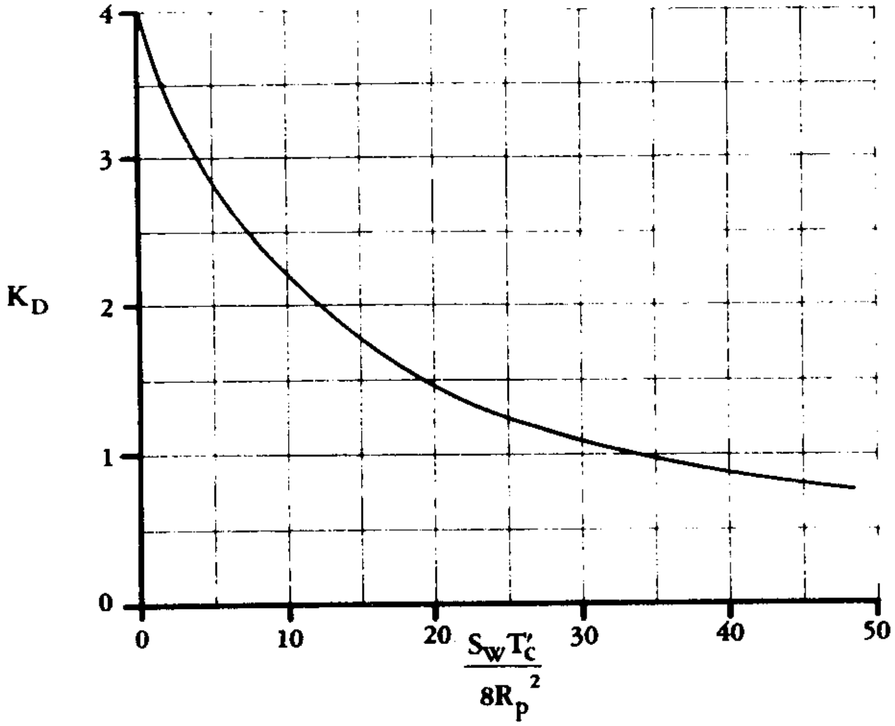

FIGURE 4.6.4-13a PROPELLER DRAG FACTOR

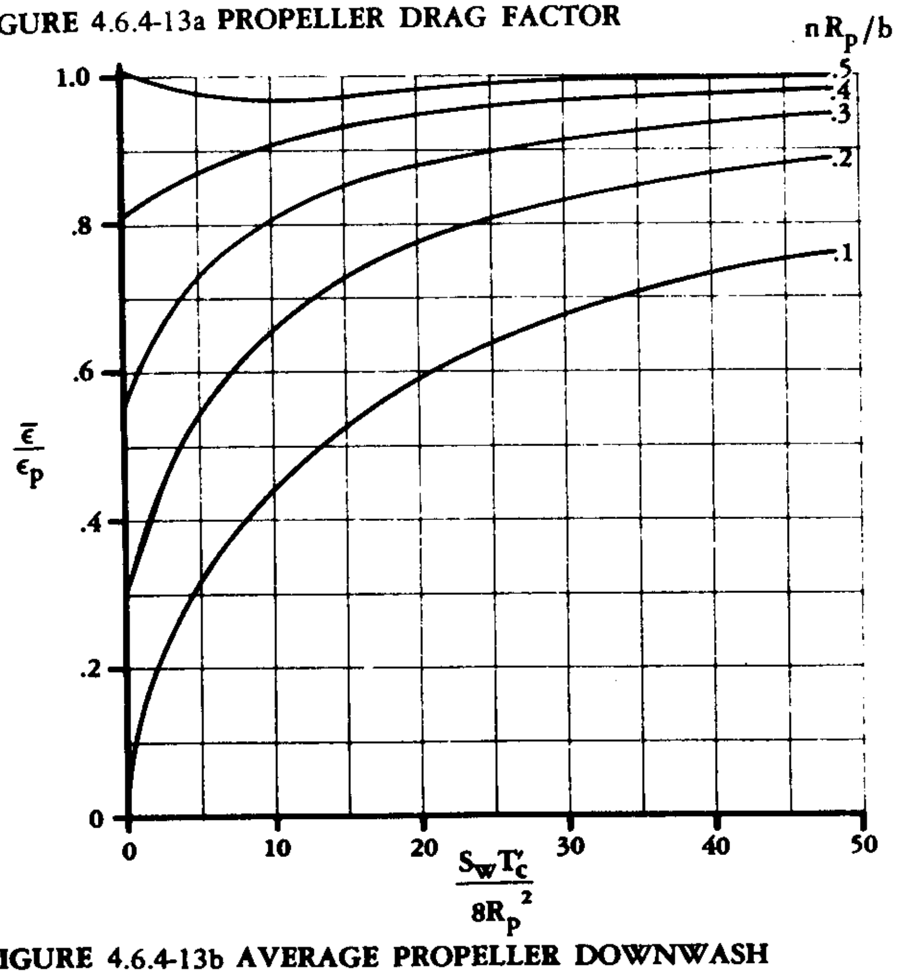

FIGURE 4.6.4-13b AVERAGE PROPELLER DOWNWASH

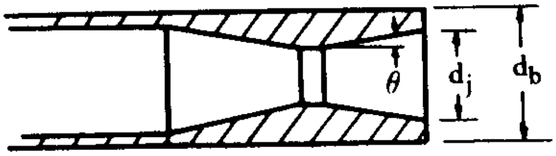

SUPERSONIC NOZZLE
$d_j/d_b = 0.75$
$\theta = 10°$

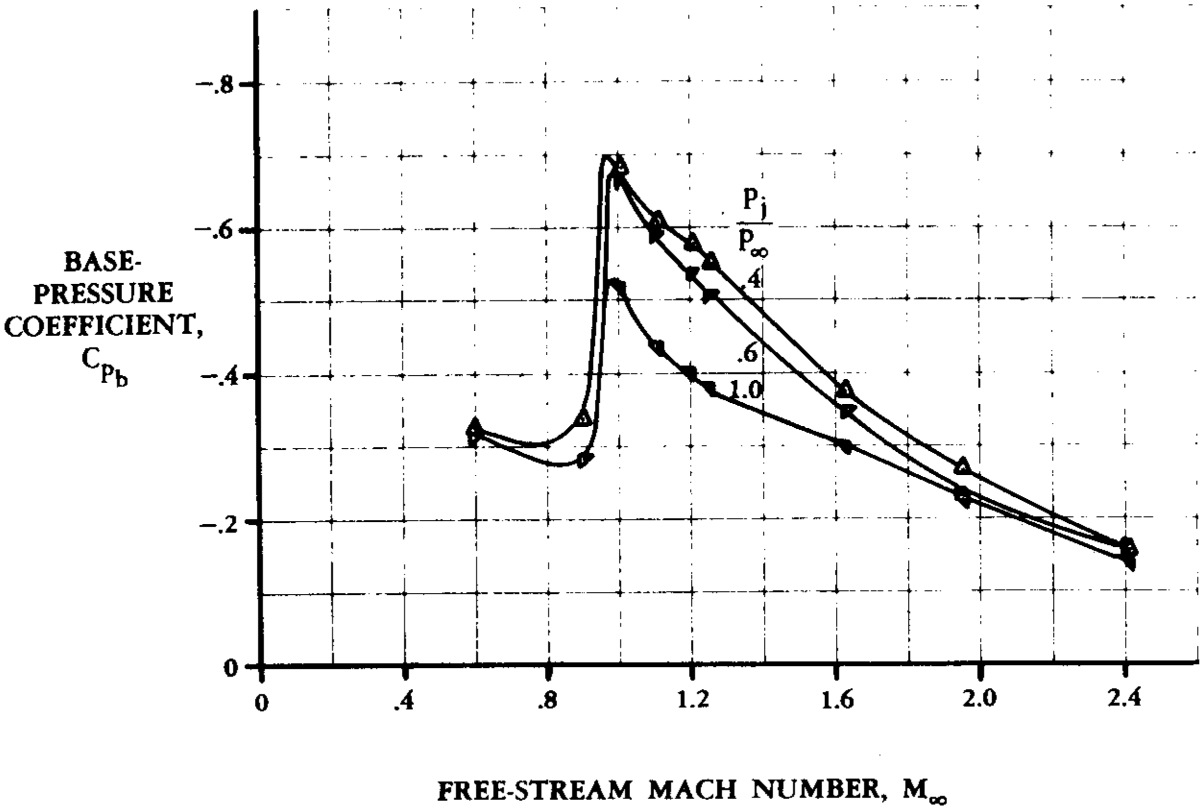

FIGURE 4.6.4-14 EXPERIMENTAL EFFECT OF FREE-STREAM MACH NUMBER ON BASE PRESSURE

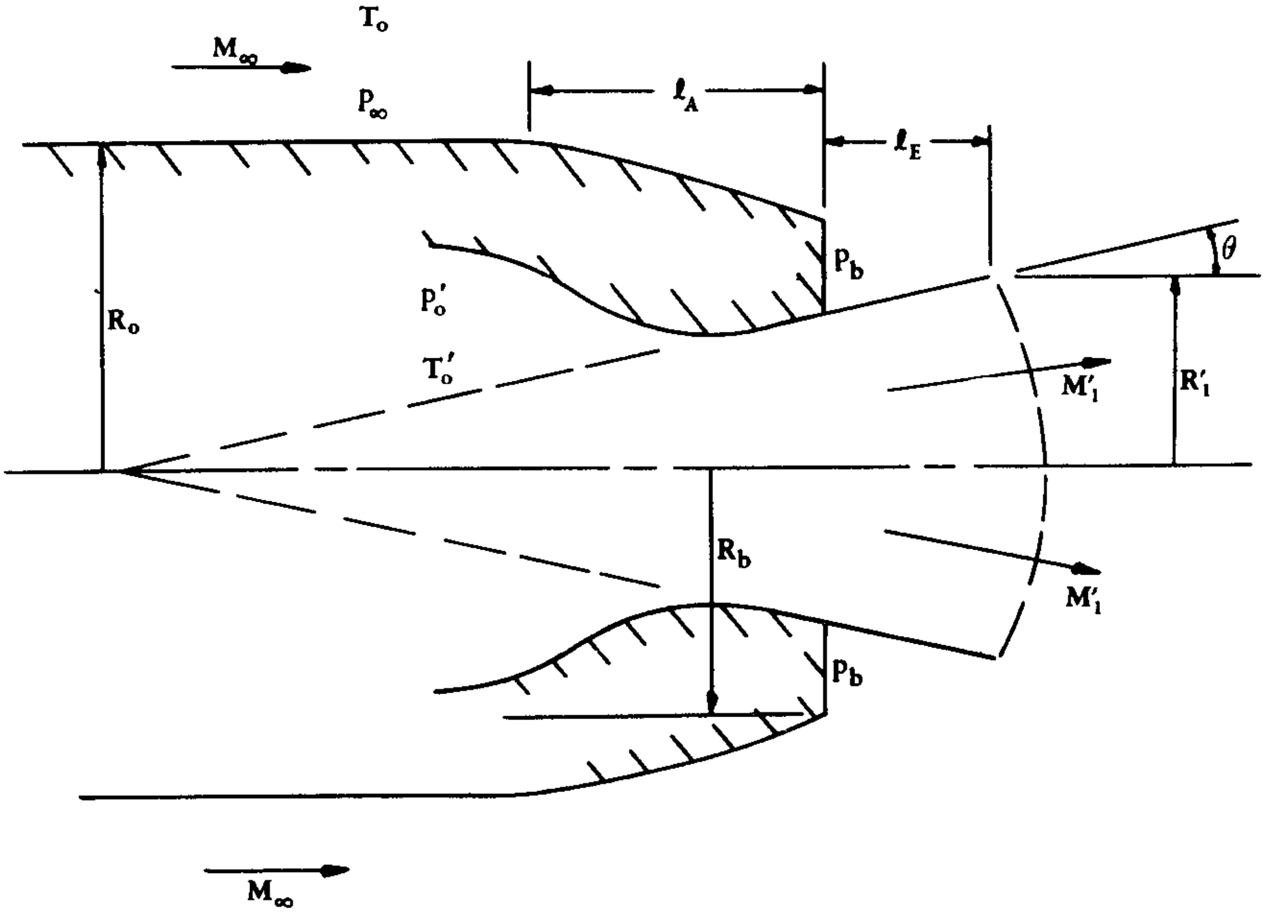

FIGURE 4.6.4-15 GEOMETRY AND INITIAL FLOW PARAMETERS FOR A AXIALLY SYMMETRIC BOATTAILED AFTERBODY WITH A NOZZLE

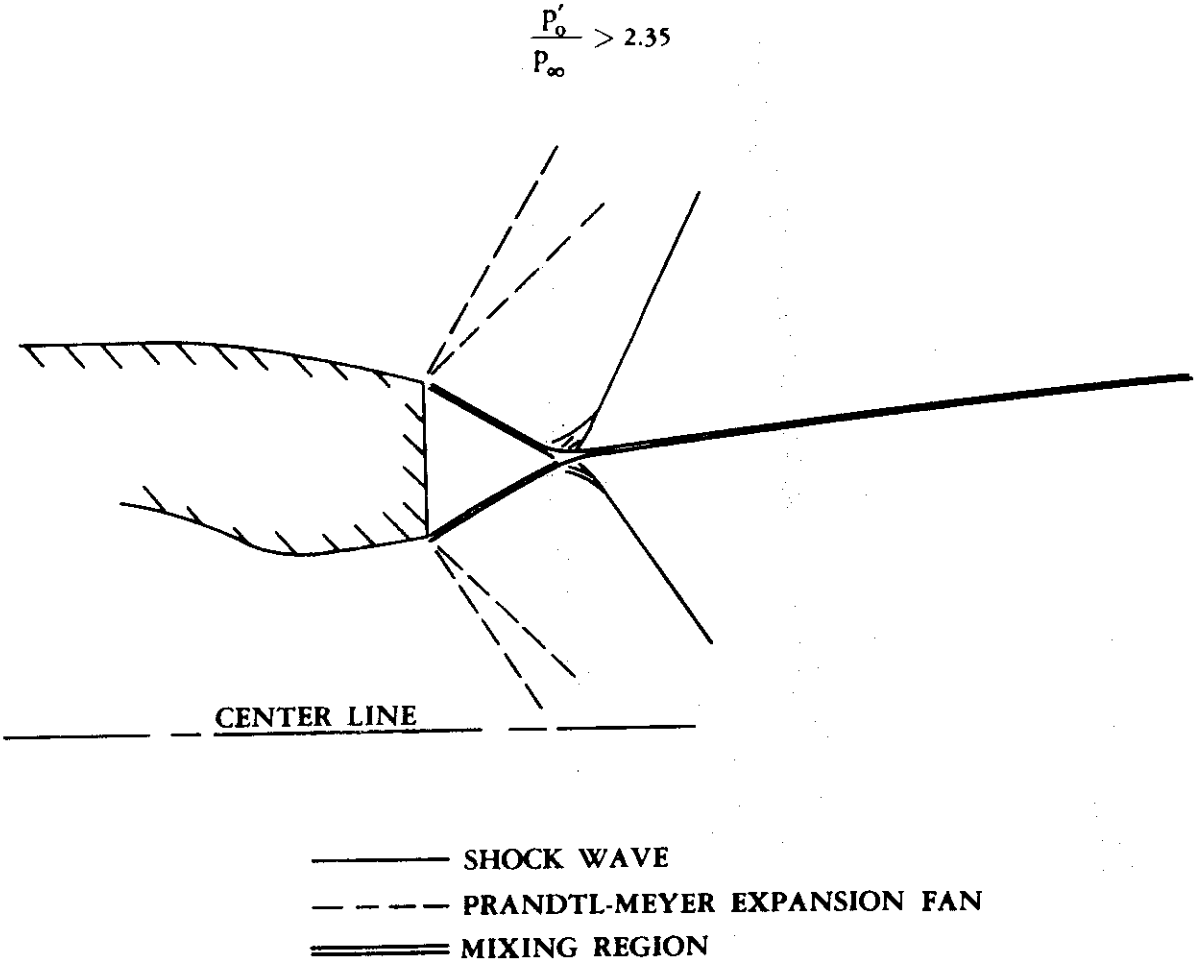

FIGURE 4.6.4-16 TYPICAL FLOW PATTERN

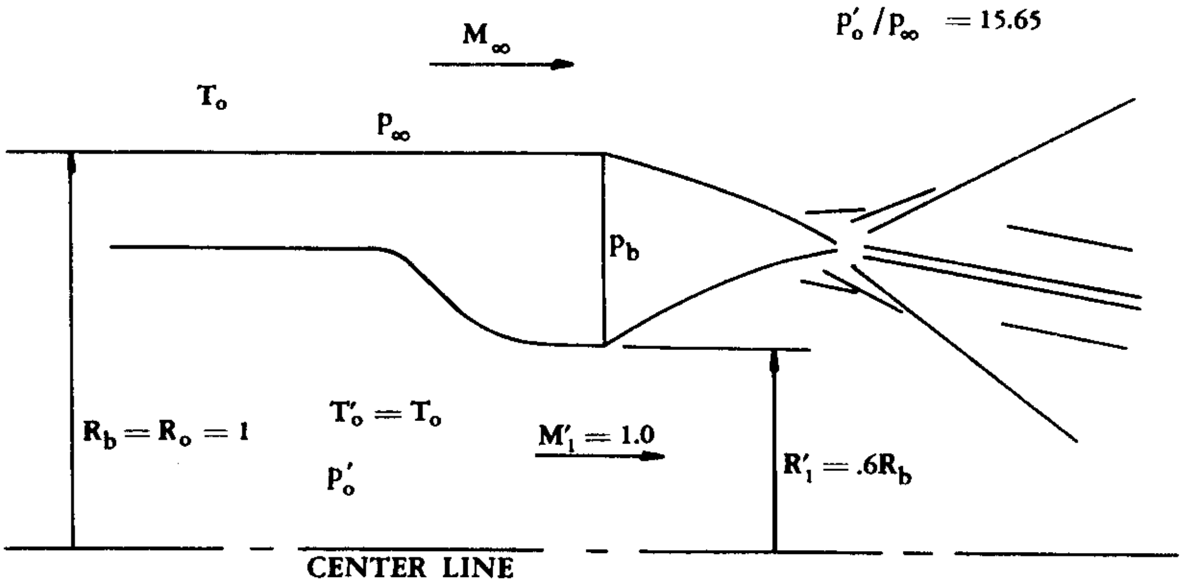

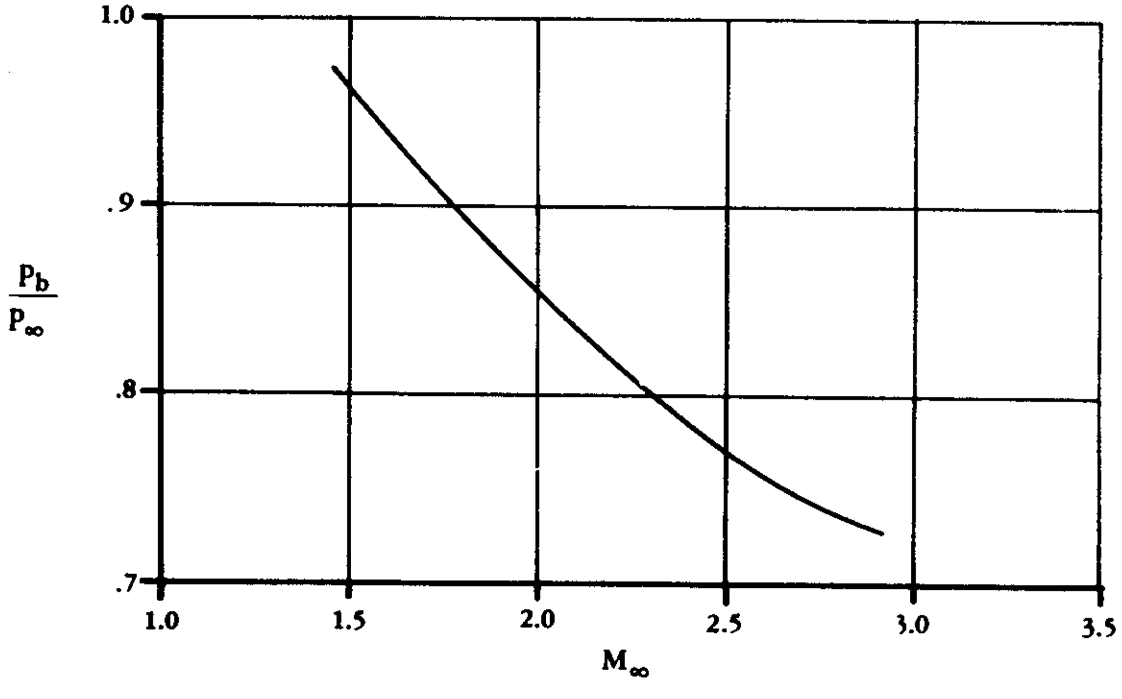

FIGURE 4.6.4-17 INFLUENCE OF FREE-STREAM MACH NUMBER ON BASE-PRESSURE RATIO

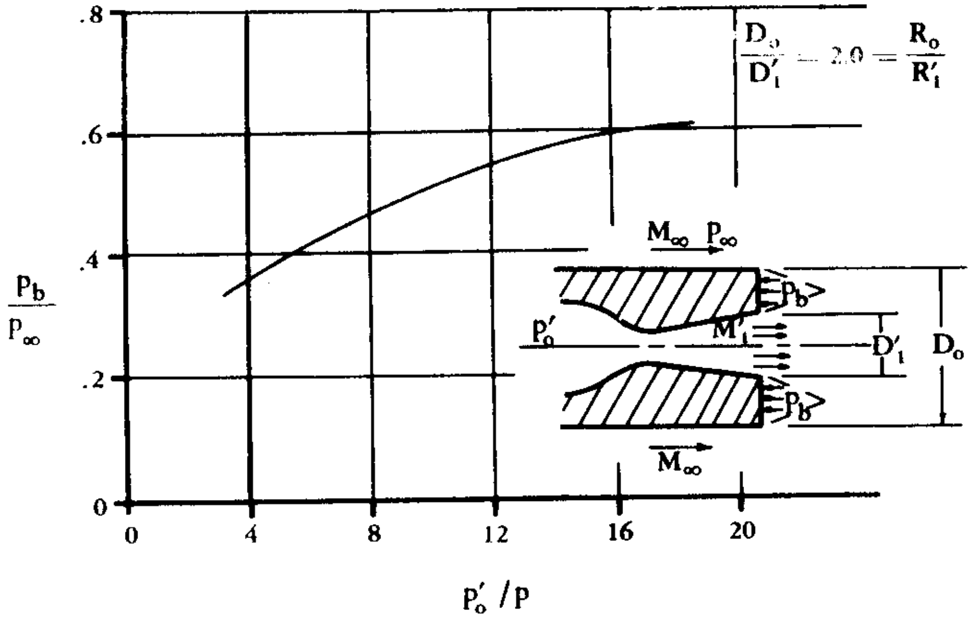

FIGURE 4.6.4-18a EFFECT OF JET-PRESSURE RATIO ON BASE-PRESSURE RATIO

$M_\infty = 2.0$ $M'_1 = 1.5$

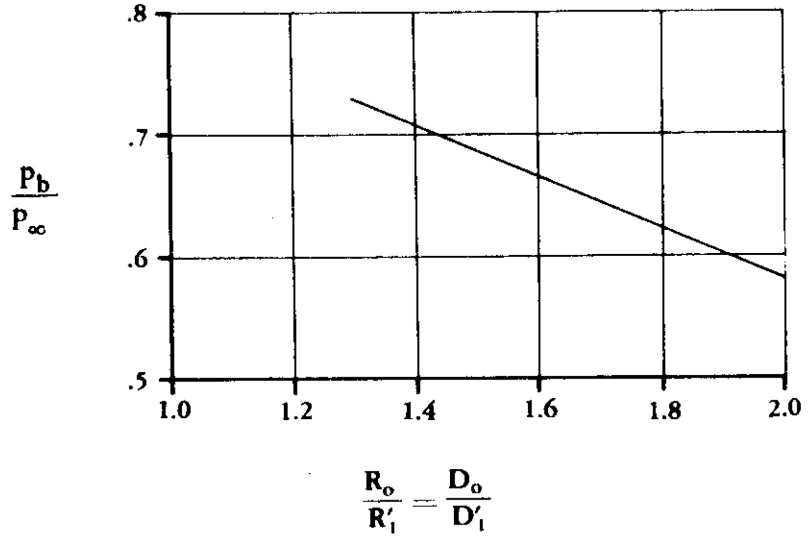

FIGURE 4.6.4-18b EFFECT OF JET-DIAMETER-BODY-DIAMETER RATIO ON BASE-PRESSURE RATIO

$M_\infty = 2.0$ $M'_1 = 1.5$ $p_o/p_\infty = 16$

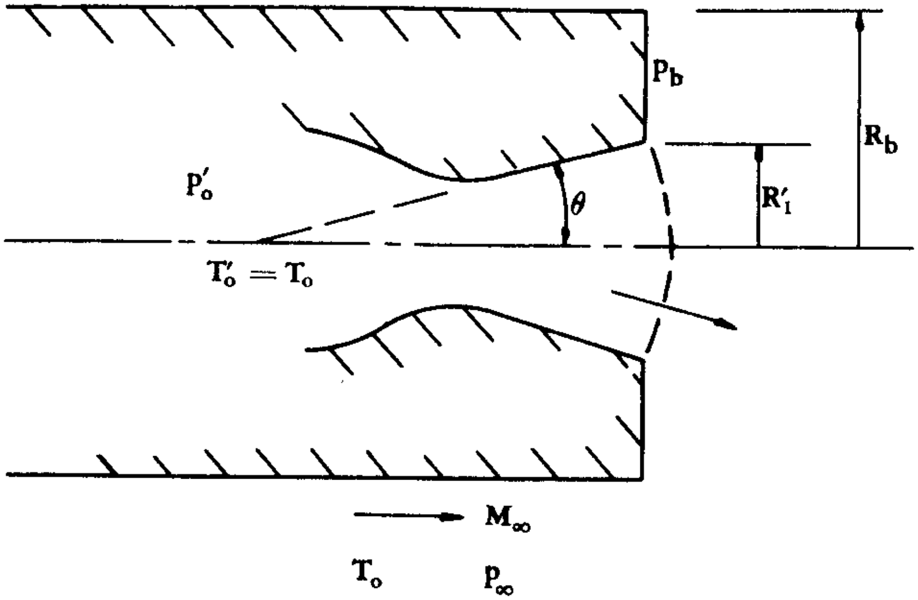

$R'_1/R_1 = .82$
$M_\infty = 2.00$
$M'_1 = 2.54$

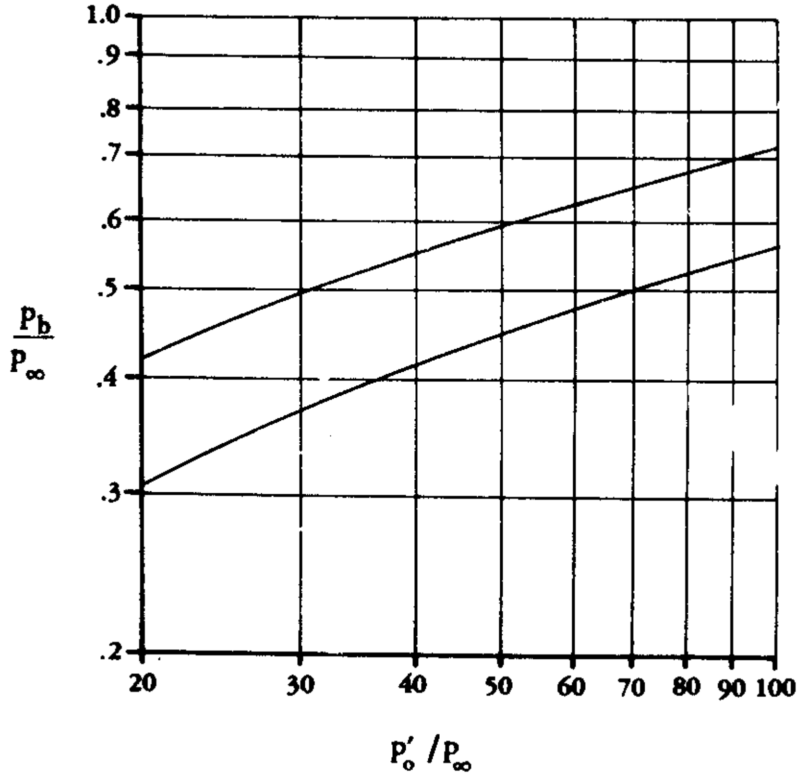

FIGURE 4.6.4-19 EFFECT OF NOZZLE DIVERGENCE ON THE BASE-PRESSURE RATIO

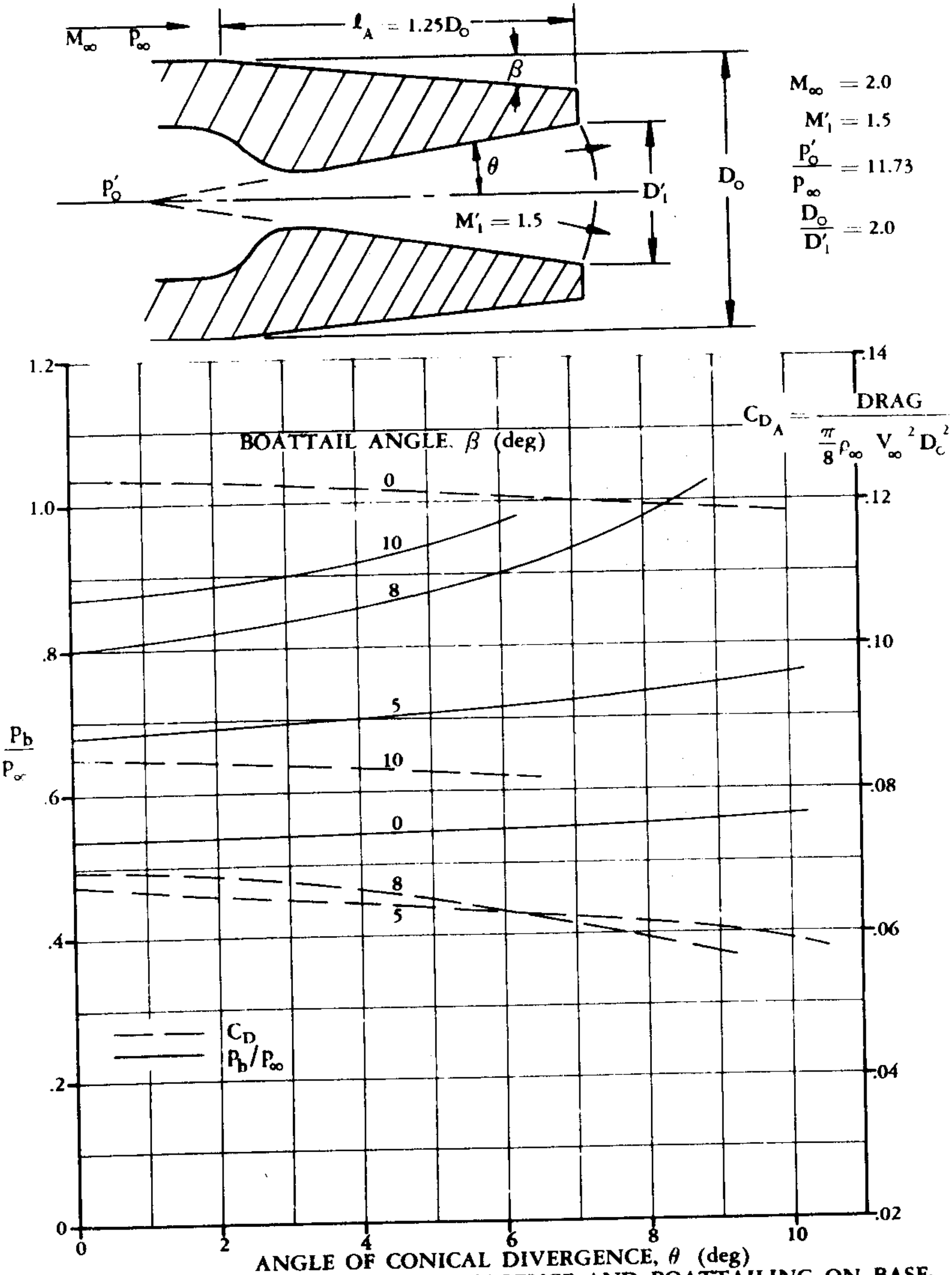

FIGURE 4.6.4-20 EFFECT OF NOZZLE DIVERGENCE AND BOATTAILING ON BASE-PRESSURE RATIO AND AFTERBODY DRAG OF A JET ENGINE

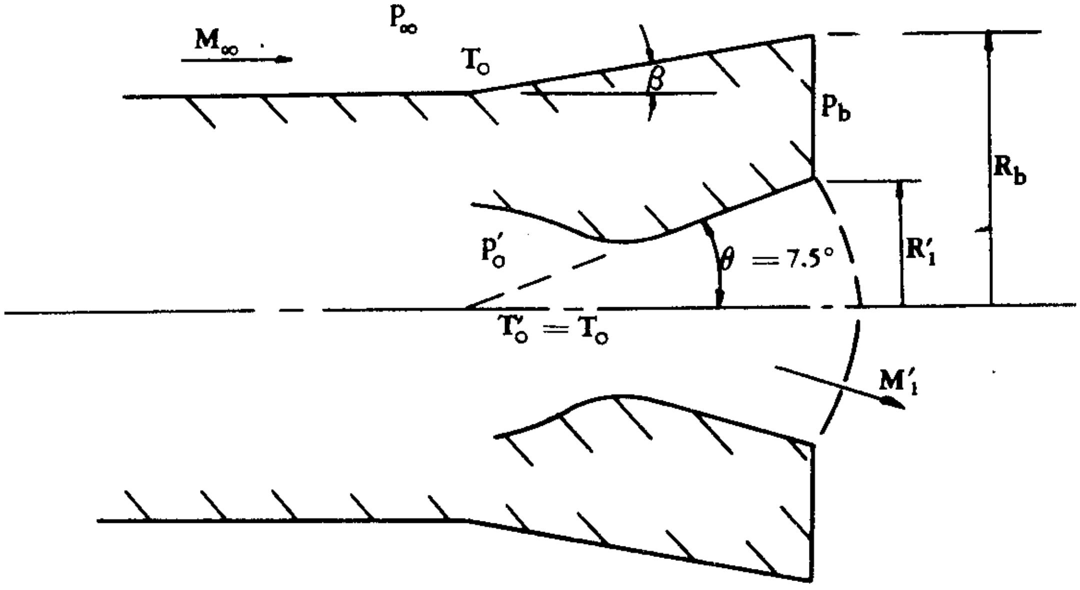

$R'_1/R_1 = .82$

$M_\infty = 2.00$

$M'_1 = 2.54$

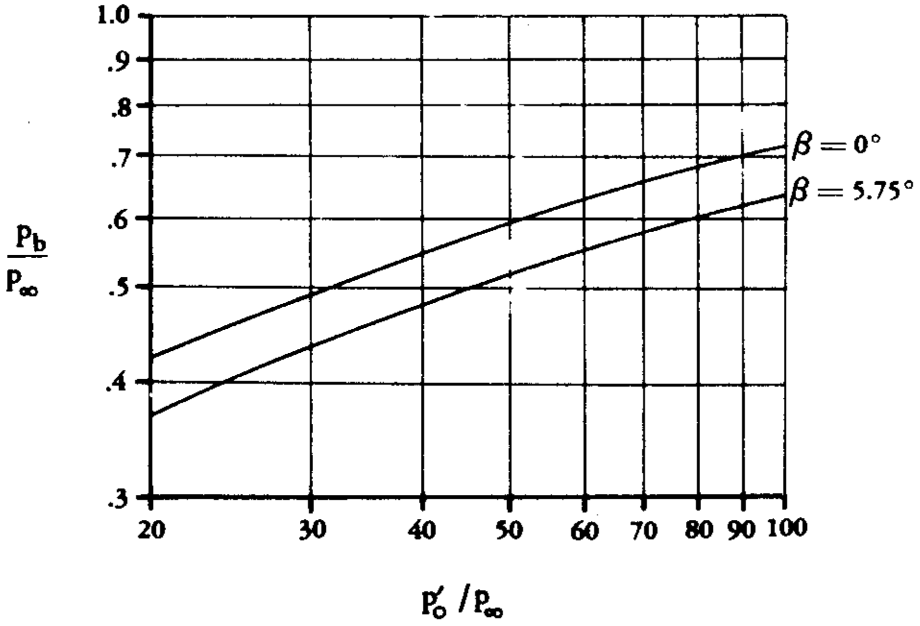

FIGURE 4.6.4-21 EFFECT OF CONICAL FLARING ON THE BASE-PRESSURE RATIO

4.7 GROUND EFFECTS AT ANGLE OF ATTACK

Methods are presented in subsequent sections for estimating ground effects in the linear-lift range on lift, pitching moment, and drag.

In order that the Datcom user may better understand ground effects, a qualitative discussion regarding various aspects of ground effects is presented.

Because of the obvious influence of ground proximity during the takeoff and landing phases, it has been the subject of considerable investigation. However, despite this consideration, an adequate amount of reliable ground-effects data does not appear in the literature. In particular, the prediction of $C_{L_{max}}$, $\alpha_{C_{L_{max}}}$ and pitching moment need additional investigation in ground effects.

The effects of ground proximity generally become measurable at a height above the ground of one wing-span and increase in magnitude as the height above the ground decreases. Both theoretical and experimental investigations indicate that ground proximity produces an increase in the lift-curve slope, a decrease in drag, and a reduction of nose-up pitching moment for most aircraft planforms in the clean configuration. However, high-lift configurations deviate from this trend in that the ground effect tends to reduce the lift-curve slope (Reference 1).

Wind-tunnel investigation of ground effects has been approached by using the following testing techniques: (1) fixed ground plane, (2) moving-belt ground plane, and (3) an image-model aircraft with respect to a fictitious ground. The fixed ground-plane technique provides the most straightforward approach to simulation. However, this approach does not give a true representation of the phenomena because of the lack of relative motion between the ground plane and the model. This lack of motion permits a boundary-layer build-up on the ground plane that introduces an objectionable component into the simulation. Moving-belt ground-plane simulations eliminate this undesirable feature; however, not all wind tunnels offer this capability. The third testing technique, the image-model approach, has the disadvantage of added cost and complexity of constructing and installing a second model in the tunnel to simulate the mirror image of the test model. Most authorities tend to agree on the relative advantages of these different approaches. As might be expected, results from these different testing techniques do not predict identical results for the same configuration. The lack of agreement between various wind-tunnel results is exemplified in the comparisons presented in References 3 and 4. In addition, these wind-tunnel predictions do not compare favorably with the limited flight-test results of References 3 and 4.

The majority of the theoretical approaches analyzing ground effects employ an image-vortex theory to represent the ground plane. The salient aspects of this theory are discussed below.

The lifting wing is represented theoretically by a bound vortex and two trailing vortices. The effect of a ground plane on this "horseshoe" vortex system is represented by placing a mirror image of the vortex system two ground-plane heights below the vortex system representing the wing. The resulting plane of symmetry satisfies the boundary condition of zero vertical velocity at the ground plane. The two vortex systems (the wing-vortex system and the image-vortex system) and the ground plane are illustrated in Sketches (a), (b), and (c).

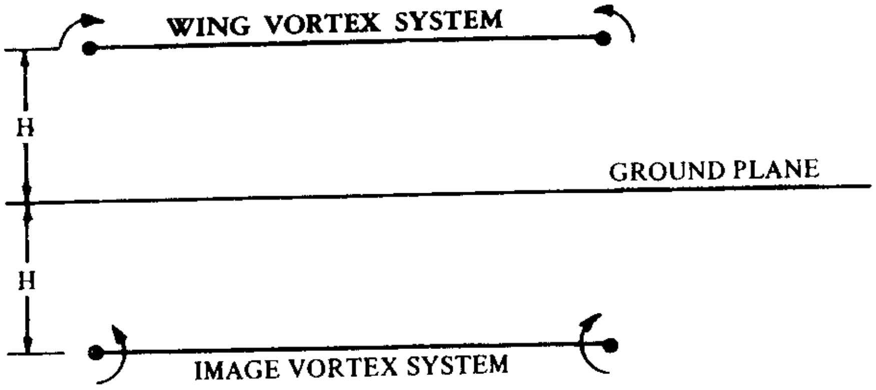

——— Bound vortices

● End view of trailing vortices

(Arrows indicate direction of circulation)

SKETCH (a)

THEORETICAL WING VORTEX SYSTEM, FRONT VIEW

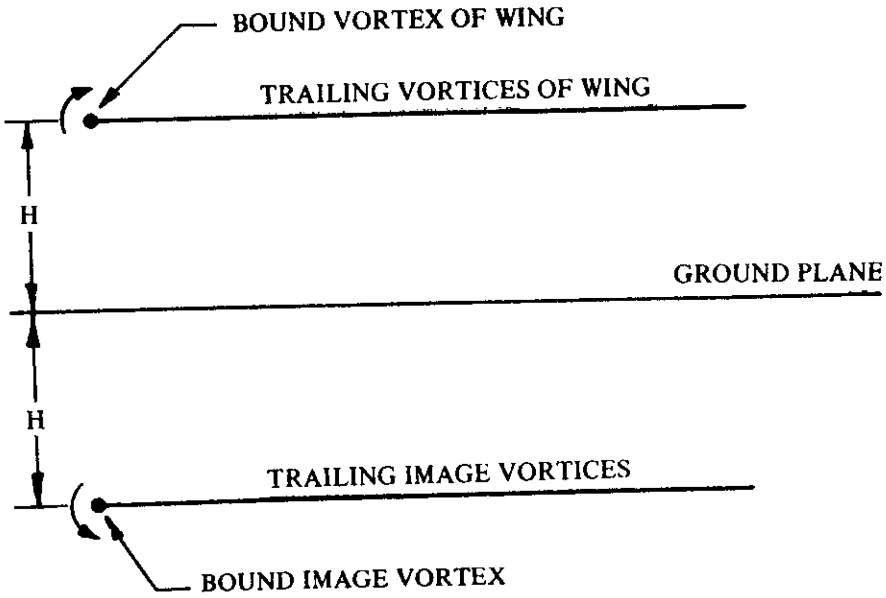

● End view of bound vortices

——— Trailing vortices

(Arrows indicate direction of circulation)

SKETCH (b)

THEORETICAL WING VORTEX SYSTEM, SIDE VIEW

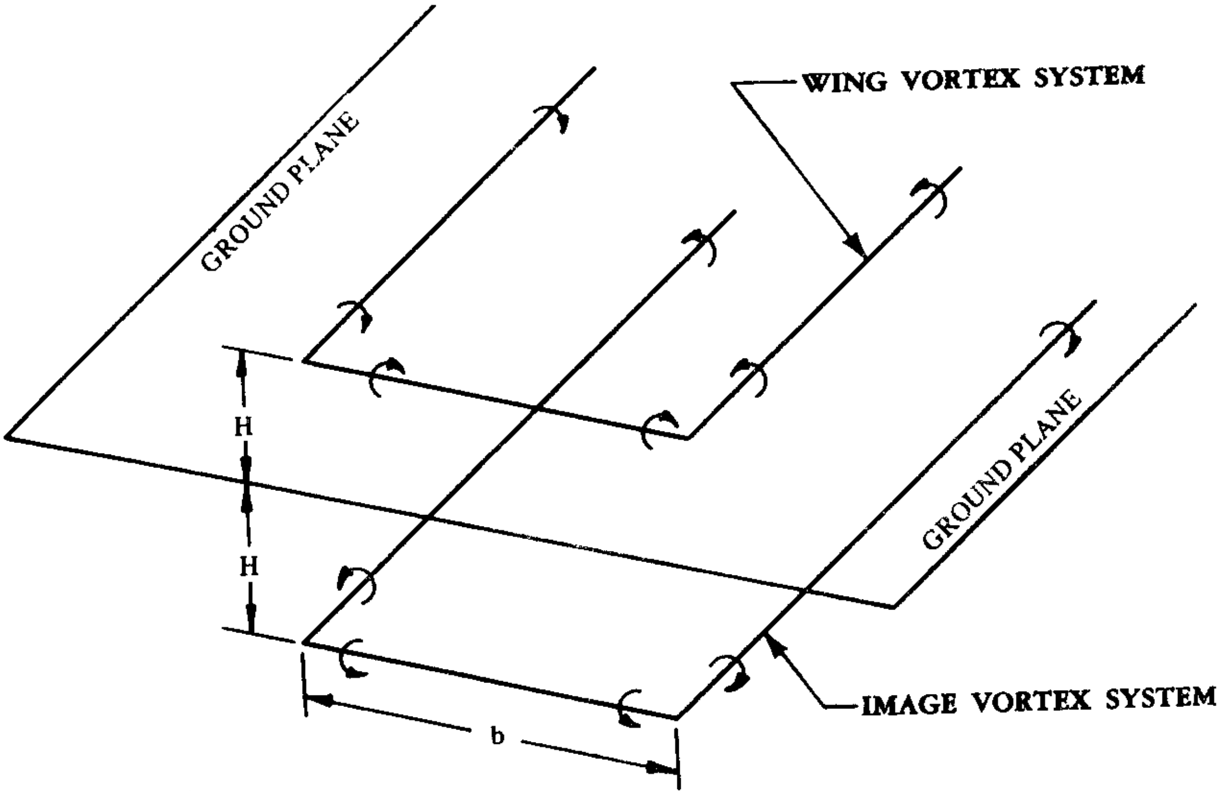

——— Vortex
(Arrows indicate direction of circulation)

SKETCH (c)

Away from the ground plane, the downwash of the two trailing vortices contributes to the wing drag due to lift by rotating the force vector rearward, as shown in Sketch (d). However, near the ground plane, the trailing vortices of the image vortex system have an upwash component, as shown in Sketch (c) and Sketch (e) (Reference 5). This upwash velocity component reduces the downward rotation of the flow direction caused by the wing trailing vortices, thus decreasing the wing drag due

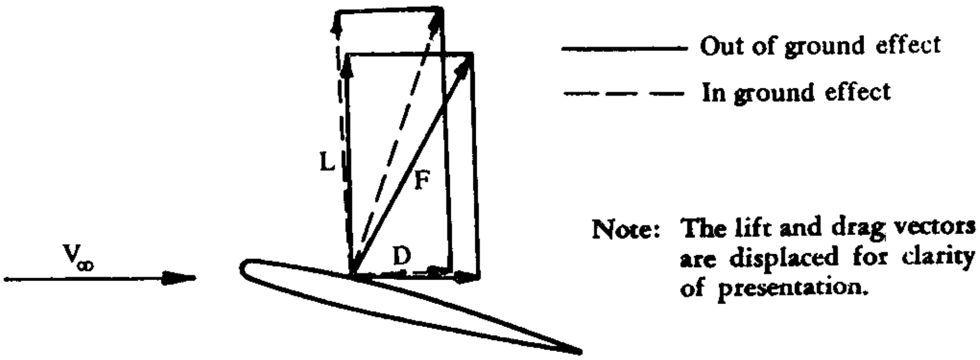

Note: The lift and drag vectors are displaced for clarity of presentation.

SKETCH (d)

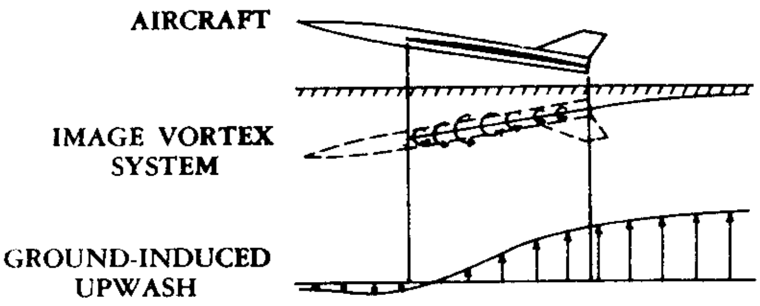

SKETCH (e)
GROUND-INDUCED UPWASH

to lift. The classical treatment of this effect is given by Wieselsberger in Reference 6. Wieselsberger's approach has been extended in Reference 7 by Tani, Taima, and Simidu to consider the induced effects of the image bound vortex. Both of these approaches are summarized in Reference 8. As indicated in the side view of the vortex system presented as Sketch (b), the bound vortex of the image-vortex system will reduce the longitudinal velocity component at the wing bound vortex, thus modifying the circulation of the wing bound vortex. These effects of the image bound-vortex system become more predominant as the height above the ground is reduced.

Improved theoretical analyses of the effects of ground proximity have been formulated using lifting-surface theory. Because of the general nature of lifting-surface theory, computer programs have been generated to facilitate the computations. Reference 9 presents an example of an image-vortex representation using lifting-surface theory, generalized to apply to a straight-tapered wing in nonviscous flow.

The influence of ground effects on the lateral-control characteristics of aircraft has received consideration in References 10 through 12. Results of Reference 10 suggest that ground effects completely alter the basic lateral characteristics of slender aircraft during the period immediately preceding touchdown. As a result, disturbances in bank angle are drastically attenuated just prior to aircraft touchdown.

The influence of wing-tip fairings and wing-tip end plates is examined in References 13 through 15. The general effect of these wing-tip devices is an increase in lift-curve slope and a reduction in induced drag, which generally results in a significant increase in the lift-drag ratio.

The reader is referred to Reference 16 for a comprehensive literature search and survey of the literature available prior to 1966 in the general field of wings operating in ground effect and related phenomena. Comments are included in this reference regarding some of the papers published, along with sketches of the methods of approach taken by the authors. The bibliography presents sources that consider the problem from the theoretical, experimental, and/or applications points of view. Tables are included that provide a convenient breakdown of the various sources, for a quicker method of locating specific references dealing with an area of special interest to the reader.

A list of pertinent references is included at the end of this section, following a list of notation used in subsequent sections.

NOTATION

A	wing aspect ratio
B	parameter accounting for change in circulation
b_{eff}	effective wing span
b'_f	effective span for increment in load due to flaps
b'_W	effective span for unflapped wing
$\bar{c}$	wing mean aerodynamic chord
C_D	wing drag coefficient, $\frac{\text{drag}}{qS}$
C_{D_L}	drag coefficient due to lift
$\left(\Delta C_{D_L}\right)_G$	increment in drag due to lift in the presence of the ground
$C_{D_{WB}}$	wing-body drag coefficient in absence of ground plane
$\left(C_{D_{WB}}\right)_G$	wing-body drag coefficient in the presence of the ground
C_{D_0}	zero-lift drag coefficient
C_L	wing lift coefficient in absence of ground plane
ΔC_{L_f}	increment in lift coefficient due to flaps in absence of ground plane
$\left(C_{L_f}\right)_{WB}$	wing-body lift coefficient including flap effects, out of ground effect
$\Delta\left(\Delta C_L\right)_{flap}$	empirical factor accounting for flap effects in the presence of the ground
$\left(\Delta C_L\right)_G$	increment in lift coefficient in the presence of the ground
$\left(\Delta C_{L_H}\right)_G$	increment in horizontal-tail lift coefficient in the presence of the ground
$C_{L_{max}}$	maximum lift coefficient, $\frac{\text{maximum lift}}{qS}$

$C_{L_{WB}}$	wing-body lift coefficient in absence of ground plane
$\left(\Delta C_{L_{WB}}\right)_G$	increment in wing-body lift coefficient in the presence of the ground
$\left(C_{L_\alpha}\right)_{WB}$	wing-body lift-curve slope
$\left(\Delta C_m\right)_G$	increase in pitching moment in the presence of the ground
$\left(\Delta C_{m_H}\right)_G$	increase in horizontal-tail pitching moment in the presence of the ground
$\left(\Delta C_{m_{WB}}\right)_G$	increase in wing-body pitching moment in the presence of the ground
$\frac{c_r}{b}$	ratio of wing root chord to wing span
H	height of quarter-chord point of wing mean aerodynamic chord above the ground
H_H	height of quarter-chord point of horizontal-tail mean aerodynamic chord above the ground
h	average height above the ground of the quarter-chord point of wing chord at 75-percent semispan and the three-quarter-chord point of the wing root chord (see sketch on Figure 4.7.1-14)
$h_{c_r/4}$	height of the quarter-chord point of the wing root chord above the ground
K	parameter accounting for effective wing thickness
ℓ_H	distance from moment reference center to the quarter-chord point of horizontal-tail MAC, measured parallel to body center line
$\frac{L}{L_o} - 1$	parameter accounting for effect of image bound vortex on lift
n	distance from wing apex to moment reference center measured in wing mean aerodynamic chords, positive aft
$\frac{q_H}{q_\infty}$	effective dynamic-pressure ratio at horizontal tail
r	parameter accounting for effect of finite span
$\frac{S_H}{S_W}$	ratio of area of horizontal tail to wing area

T	parameter accounting for reduction in longitudinal velocity
$\left(\frac{t}{c}\right)_{max}$	ratio of maximum wing thickness to wing chord
x	parameter accounting for effect of image trailing vortex on lift
Δx	the chordwise distance from the quarter-chord point of the 75-percent-semispan chord to the three-quarter-chord point of the wing root chord, positive when the latter is aft of the former (see Figure 4.7.1-14)
$x_{a.c.}$	distance from the wing apex to the wing-body aerodynamic center, positive for a.c. aft of wing apex
$\Delta\alpha$	increment in angle of attack
$\alpha_{C_{L_{max}}}$	wing angle of attack at maximum lift coefficient
$\left(\Delta\alpha\right)_G$	increment in angle of attack at a constant lift coefficient in the presence of the ground
$\left(\Delta\alpha_H\right)_G$	increment in angle of attack of the horizontal tail in the presence of the ground
ϵ	downwash angle out of ground effect
$\left(\Delta\epsilon\right)_G$	increment in downwash due to ground effect in linear-lift range
$\Lambda_{c/4}$	sweep angle of the wing quarter-chord
σ	Prandtl interference coefficient

REFERENCES

1. Recant, I. G.: Wind-Tunnel Investigation of Ground Effect on Wings with Flaps. NACA TN 705, 1939. (U)
2. de Sievers, A.: Wind-Tunnel Tests on the Ground Effect. NASA TT F-11059, 1967. (U)
3. Baker, P. A., Schweikhard, W. G., and Young, W. R.: Flight Evaluation of Ground Effect on Several Low-Aspect-Ratio Airplanes. NASA TN D-6053, 1970. (U)
4. Rolls, L. S., and Koenig, D. G.: Flight-Measured Ground Effect on a Low-Aspect-Ratio Ogee Wing Including a Comparison with Wind-Tunnel Results. NASA TN D-3431, 1966. (U)
5. Kemp, W. B., Jr., Lockwood, V. E., and Phillips, W. P.: Ground Effects Related to Landing of Airplanes with Low-Aspect-Ratio Wings. NASA TN D-3583, 1966. (U)
6. Wieselsberger, C.: Wing Resistance Near the Ground. NACA TM 77, 1922. (U)

7. Tani, I., Taima, M., and Simidu, S.: The Effect of Ground on the Aerodynamic Characteristics of a Monoplane Wing. Tokyo Univ. Aeronautical Research Inst. Report 156, 1937. (U)

8. Wetmore, J. W., and Turner, L. I., Jr.: Determination of Ground Effect from Tests of a Glider in Towed Flight. NACA TR 695, 1940. (U)

9. Kohlman, D. L., and Glatt, C.: A Theoretical Method of Determining the Ground Effect on Lift and Pitching Moment for Wings of Arbitrary Planform. Boeing Airplane Co., D 3-1861, 1958. (U)

10. Pinsker, W. J. G.: The Aerodynamic Effect of Ground Proximity on Lateral Control of Slender Aircraft in the Landing Approach. RAE TR 70079, 1970. (U)

11. Kumar, P. E.: The Lateral Dynamic Stability of a Ground Effect Wing. College of Aeronautics, Cranfield, Gr. Brit., CoA Report Aero 207, 1968. (U)

12. Kumar, P. E.: An Experimental Investigation Into the Aerodynamic Characteristics of a Wing with and without Endplates, in Ground Effect. College of Aeronautics, Cranfield, Gr. Brit., CoA Report Aero 201, 1968. (U)

13. Carter, A. W.: Effect of Ground Proximity on the Aerodynamic Characteristics of Aspect-Ratio-1 Airfoils with and without End Plates. NASA TN D-970, 1961. (U)

14. White, H. E.: Wind-Tunnel Tests of a Low-Aspect-Ratio Wing in Close Proximity to the Ground. DTMB Aero 1056, 1963. (U)

15. Fink, M. P., and Lastinger, J. L.: Aerodynamic Characteristics of Low-Aspect-Ratio Wings in Close Proximity to the Ground. NASA TN D-926, 1961. (U)

16. Foschag, W. F.: Literature Search and Comprehensive Bibliography of Wings in Ground Effect and Related Phenomena. DTMB Aero 1098, 1966. (U)

17. Tani, I., Itokawa, H., and Taima, M.: Further Studies of the Ground Effect on the Aerodynamic Characteristics of an Aeroplane, with Special Reference to Tail Moment. Tokyo Univ. Aeronautical Research Inst. Report 158, 1937. (U)

18. Gersten, K.: Calculation of the Aerodynamic Characteristics of Wings of Finite Span Near the Ground. Abhandlungen der Braunschweigischen Wissenschaftlichen Gesellschaft, XII, 1960, pp. 95-115. (U)

19. Kirkpatrick, D. L. I.: A Method of Correlating the Ground Effects on the Longitudinal Characteristics of Slender Wings. RAE TR 69190, 1969. (U)

20. Thomas, F.: Aerodynamic Properties of Sweptback and Delta Wings Near the Ground. Jahrbuch der Wissenschaftlichen Gesellschaft fur Luftfahrt, E. V., pp. 53-61, 1958. (U)

21. Shen, Y. C.: Theoretical Analysis of Jet-Ground Plane Interaction. IAS Paper 62-144, 1962. (U)

22. Owen, P. R., and Hogg, H.: Ground Effect on Downwash with Slipstream. ARC R&M 2449, 1952. (U)

23. Schweikhard, W.: A Method for In-Flight Measurement of Ground Effect on Fixed-Wing Aircraft. AIAA Paper 66-468 1966. (U)

24. de Sievers, A.: Wind-Tunnel Tests of the Ground Effect on Aircraft Models. NASA TT F-9709, 1965. (U)

25. O'Leary, C. O.: Flight Measurements of Ground Effect on the Lift and Pitching Moment of a Large Transport Aircraft (Comet 3B) and Comparison with Wind Tunnel and Other Data. RAE TR 68158, 1968. (U)

26. Buell, D. A., and Tinling, B. E.: Ground Effects on the Longitudinal Characteristics of Two Models with Wings Having Low Aspect Ratio and Pointed Tips. NACA TN 4044, 1957. (U)

27. Wood, M. N., and Trebble, W. J. G.: Low Speed Tunnel Measurements of the Ground Effect on a 1/5th Scale Model of the Swift. ARC CP 458, 1959. (U)

28. Riebe, J. M., and Graven, J. C., Jr.: Low-Speed Investigation of the Effects of Location of a Delta Horizontal Tail on the Longitudinal Stability and Control of a Fuselage and Thin Delta Wing with Double Slotted Flaps Including the Effects of a Ground Board. NACA RM L53H19a, 1953. (U)

29. Buell, D. A., and Tinling, B. E.: The Static Longitudinal Stability and Control Characteristics in the Presence of the Ground of a Model Having a Triangular Wing and Canard. NASA Memo 3-4-59A, 1959. (U)

30. Bagley, J. A.: Low-Speed Wind Tunnel Tests on a Two-Dimensional Aerofoil with Split Flap Near the Ground. RAE TN Aero 2636, 1961. (U)

31. Bagley, J. A.: The Pressure Distribution on Two-Dimensional Wings Near the Ground. ARC R&M 3238, 1961. (U)

32. Colin, P. E.: Powered Lift Model Testing for Ground Proximity Effects. Training Center for Experimental Aerodynamics, Rhode-Saint-Genese, Belgium, TN 14, 1963. (U)

33. Furlong, G. C., and Bollech, T. V.: Effect of Ground Interference on the Aerodynamic and Flow Characteristics of a 42° Sweptback Wing at Reynolds Numbers up to 6.8×10^6. NACA TR 1218, 1955. (U)

34. Butler, S. F. J., Moy, B. A., and Hutchins, G. D.: Low-Speed Tunnel Tests of an Aspect-Ratio 9 Jet-Flap Model, with Ground Simulation by Moving-Belt Rig. ARC CP 849, 1966. (U)

35. Alexander, A. J.: Experiments on a Jet-Flap Delta Wing in Ground Effect. College of Aeronautics, Cranfield, Gr. Brit., CoA Report Aero 164, 1963. (U)

36. Kumar, P. E.: An Analogue Simulation of the Longitudinal Motion of a Ground Effect Wing. College of Aeronautics, Cranfield, Gr. Brit., CoA Report Aero 208, 1968. (U)

37. Piper, R. W., and Davies, H.: Note on Factors Affecting Trim at Take-off and Landing. Aero. Departmental Note – Wind Tunnel No. 540, 1941. (Unpublished British Paper). (U)

4.7.1 GROUND EFFECTS ON LIFT VARIATION WITH ANGLE OF ATTACK

Methods are presented in this section for estimating the ground effects on lift in the linear-lift region. The reader is referred to Section 4.7 for a basic discussion of various aspects of ground effects.

Representation of the ground plane by an image-vortex system (see Sketches (a), (b), and (c) in Section 4.7) enables the ground effects on lift to be identified (Reference 1) as follows: (1) the decrease in longitudinal velocity at the real wing due to the reflected bound vortex, (2) the change in circulation about the real wing due to the reflected bound vortex, (3) the increase in induced upwash at the real wing due to the reflected trailing vortices, and (4) the change in the flow pattern due to the finite thickness of the wing. The first two effects are opposite and approximately equal, while the effects of wing thickness are generally small. As a result, the ground effects on lift can be approximated by considering only the increase in the upwash. This is the approach taken in the classical theoretical treatment of ground effects by Wieselsberger in Reference 2. Wieselsberger's method of approach has been extended in Reference 3 by Tani, Taima, and Simidu to include the induced effects of the reflected bound vortex and of wing thickness.

The increase in aircraft lift due to ground proximity decreases in magnitude as the height above the ground increases. Flight-test data from Reference 4, showing the increase in lift due to ground effects at a constant angle of attack as a function of ground height, are presented in Sketches (a) and (b) for the F5D-1 and XB-70 airplanes, respectively. These trends are representative of the variation of lift due to ground effects that might be expected from similar aircraft.

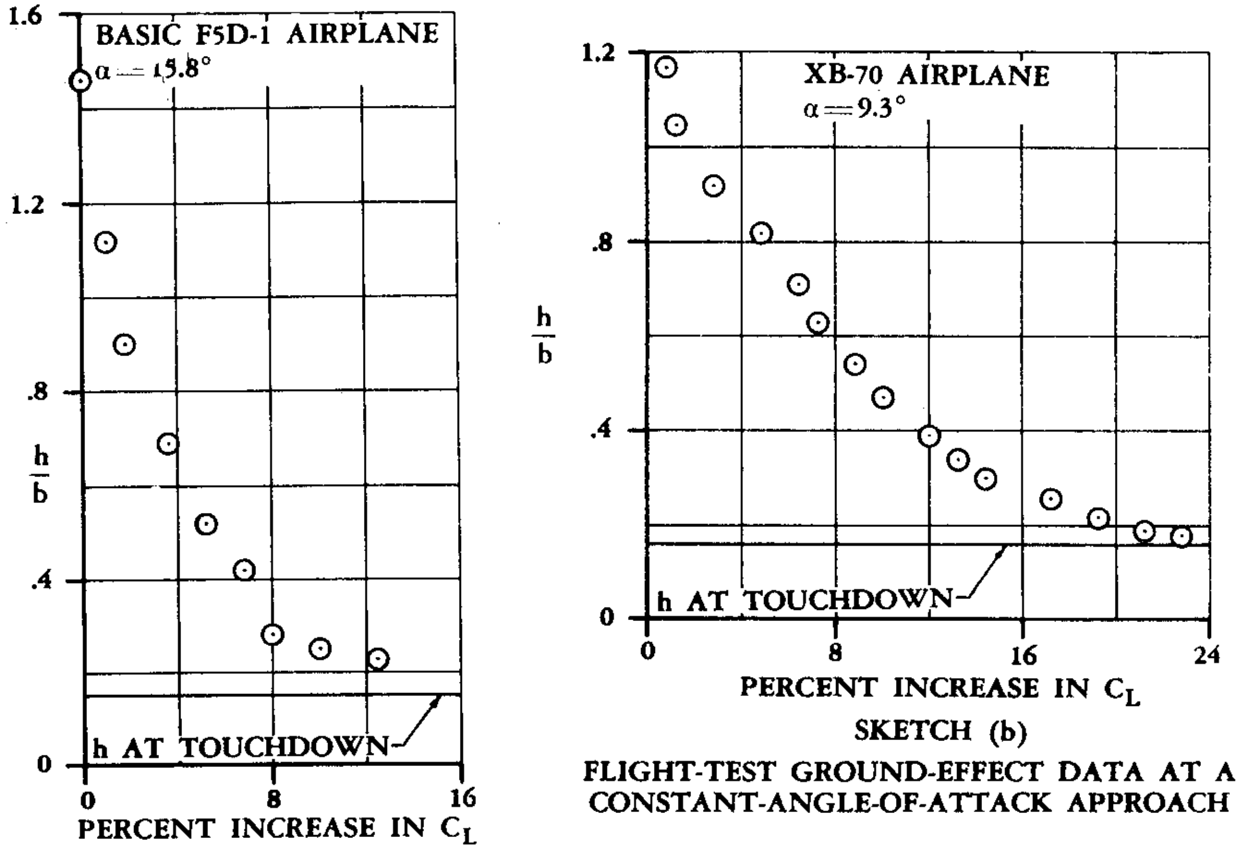

SKETCH (a)

SKETCH (b)

FLIGHT-TEST GROUND-EFFECT DATA AT A CONSTANT-ANGLE-OF-ATTACK APPROACH

Empirical prediction methods have been formulated for low-aspect-ratio delta configurations in References 5, 6, and 7. However, calculated ground effects using these methods do not compare favorably with the flight-test data of Reference 4. The comparisons indicate an inability to predict accurately the variation of ground effect on lift as the height above the ground is varied.

The ground effects on lift are determined somewhat by the planform of the configuration. For low-aspect-ratio delta configurations, the general trend is a constant increase in C_L due to ground effect, as shown in Sketch (c) (Reference 8). However, transport-type configurations show quite a different trend, as presented in Sketch (d) (Reference 8). This trend is dependent upon the type of high-lift system employed. Computer programs utilizing lifting-surface theory are currently the most favorable means of evaluating the effects of various components of high-lift systems on ground effects.

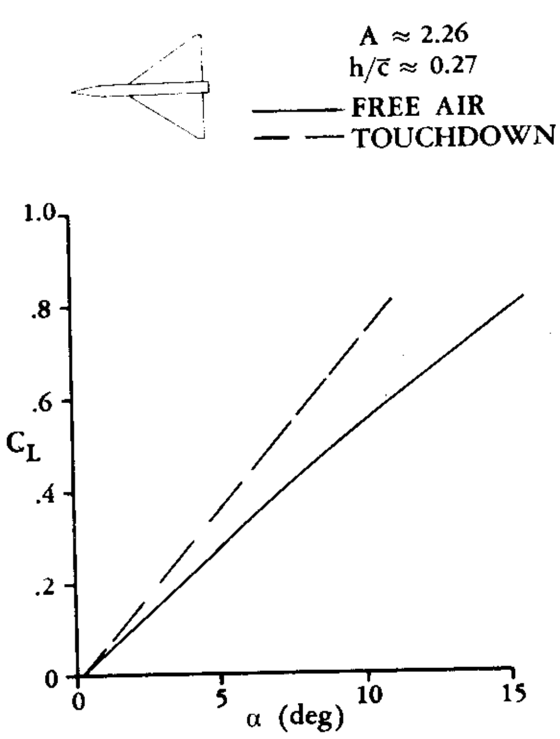

SKETCH (c)
GROUND EFECT ON 55°
DELTA CONFIGURATION

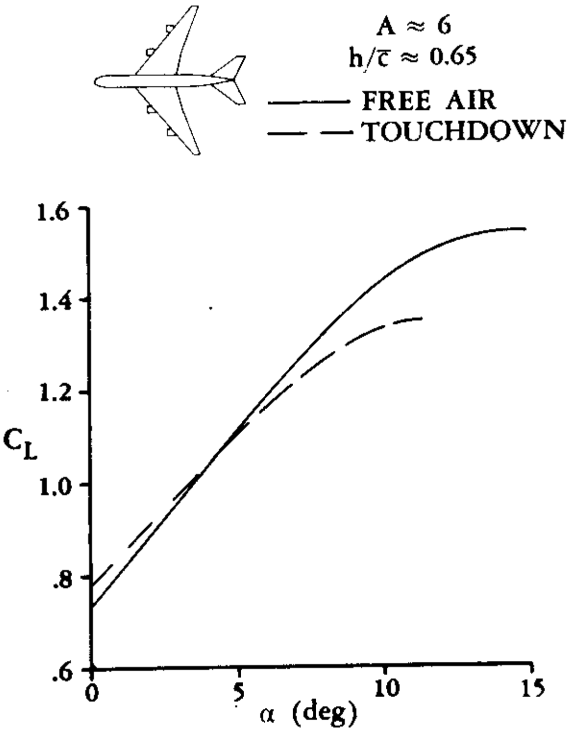

SKETCH (d)
GROUND EFFECT ON A JET
TRANSPORT CONFIGURATION

DATCOM METHODS

For most vehicles, calculating the change in lift due to ground effects consists of evaluating two components:

1. the change in wing-body lift
2. the change in tail-body lift due to the effects of downwash

The change in tail-body lift due to the presence of the ground is generally small in comparison to the downwash effects and is neglected in the Datcom methods. For canard-type configurations the change in downwash due to ground effect should be accounted for in the wing contribution.

Both of the Datcom methods presented require the user to construct wing-body and tail-body lift curves in ground effect based on their corresponding free-air lift curves. Equations are given that calculate the change in angle of attack due to ground effect at a constant lift coefficient. The ground-effect lift curves are then constructed by shifting the free-air lift curves at every C_L by the corresponding increment in angle of attack due to ground effect at constant lift coefficients (see Sketch (e)).

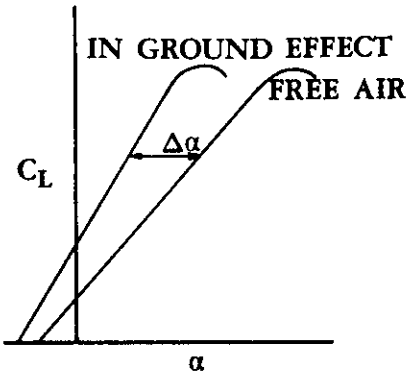

SKETCH (e)

Method 1

This method estimates the ground effects on lift in the linear-lift range for a subsonic transport configuration. The method is an extension of the Tani method of References 3 and 4 and includes the effects of taper ratio, sweep-back, dihedral, and flap deflection, while neglecting the effects of wing thickness since they are generally small. The wing-flap effects are valid only for split and slotted flaps as they are accounted for by empirical curves. The first term in Equation 4.7.1-a accounts for the effects of the trailing vortex, the second term for the effects of the bound vortex, and the third term for wing-flap effects. The method does not account for the effects of wing-leading-edge devices.

The change in wing-body angle of attack at a constant lift coefficient due to ground effect with respect to the out-of-ground-effect lift curve is given by

$$(\Delta\alpha)_G = -\left[\frac{9.12}{A} + 7.16\left(\frac{c_r}{b}\right)\right]\left(C_{L_f}\right)_{WB} x - \frac{A}{2\left(C_{L_\alpha}\right)_{WB}}\left(\frac{c_r}{b}\right)\left(\frac{L}{L_o} - 1\right)\left(C_{L_f}\right)_{WB}{}^{r}$$

$$- \frac{\left(\delta_f/50\right)^2}{\left(C_{L_\alpha}\right)_{WB}}\,\Delta\left(\Delta C_L\right)_{flap} \quad \text{(per deg)} \qquad 4.7.1\text{-a}$$

where

A	is the wing aspect ratio.
$\frac{c_r}{b}$	is the ratio of wing root chord to wing span.
$\left(C_{L_f}\right)_{WB}$	is the wing-body lift coefficient including flap effects, out of ground effect, obtained from test data or Section 4.3.1 and Section 6.1.4.1.
χ	accounts for the effects on lift due to the image trailing vortex and is obtained from Figure 4.7.1-14 as a function of wing geometry and the wing height above the ground.
$\left(C_{L_\alpha}\right)_{WB}$	is the wing-body lift-curve slope, per degree, out of ground effect, obtained from test data or Section 4.3.1.2.
$\frac{L}{L_o} - 1$	accounts for the effects on lift due to the image bound vortex and is obtained from Figure 4.7.1-15 as a function of wing geometry, lift coefficient, and the height of the quarter-chord point of the wing root chord above the ground.
r	accounts for the effect of finite span and is obtained from Figure 4.7.1-16 as a function of wing height above the ground.
$\Delta\left(\Delta C_L\right)_{flap}$	is an empirical factor to account for the effect of flaps and is obtained from Figure 4.7.1-17 as a function of the height of the quarter-chord point of the wing root chord above the ground.

In the linear-lift region, the change in downwash (a decrease) on the tail-body due to ground effects is derived theoretically by representing the ground plane as an image-vortex system. A modification to the method of Reference 9 is given in Reference 10, wherein certain geometric terms are redefined. This modified method is the method presented in the Datcom. The change (a decrease) in tail-body downwash due to ground effects in the linear-lift range is given by

$$(\Delta\epsilon)_G = \epsilon\left[\frac{b_{eff}^2 + 4(H_H - H)^2}{b_{eff}^2 + 4(H_H + H)^2}\right] \qquad 4.7.1\text{-b}$$

where

$(\Delta\epsilon)_G$	is the difference between the downwash in free air and the downwash in ground effect.
ϵ	is the downwash out of ground effect.
H	is the height of $\bar{c}/4$ of the wing above the ground.
H_H	is the height of $\bar{c}/4$ of the horizontal tail above the ground.

b_{eff} is the effective wing span defined as

$$b_{eff} = \frac{C_{L_{WB}} + \Delta C_{L_f}}{\dfrac{C_{L_{WB}}}{b'_W} + \dfrac{\Delta C_{L_f}}{b'_f}} \qquad 4.7.1\text{-c}$$

where

$C_{L_{WB}}$ is the wing-body lift coefficient, flaps retracted, out of ground effect, obtained from test data or Section 4.3.1.

ΔC_{L_f} is the change in lift coefficient due to flaps, out of ground effect, obtained from test data or Section 6.1.4.1.

$$b'_W = \left(\frac{b'_W}{b}\right) b \qquad 4.7.1\text{-d}$$

$$b'_f = \left(\frac{b'_f}{b'_W}\right)\left(\frac{b'_W}{b}\right) b \qquad 4.7.1\text{-e}$$

The ratio $\frac{b'_W}{b}$ is given in Figure 4.7.1-18a as a function of taper ratio and aspect ratio, and $\frac{b'_f}{b'_W}$ is given in Figure 4.7.1-18b as a function of the ratio of flap span to wing span.

The horizontal-tail lift curve in ground effect is constructed by shifting the free-air lift curve at every C_L by the corresponding $-(\Delta\epsilon)_G$, i.e.,

$$(\Delta\alpha_H)_G = -(\Delta\epsilon)_G \qquad 4.7.1\text{-f}$$

Method 2

This method estimates the ground effects on wing-body lift in the linear-lift range for all configurations not included in Method 1. The method is Tani's method from References 3 and 11, modified to include the effects of dihedral. The change in wing-body angle of attack due to ground effects with respect to the out-of-ground-effect lift curve is given by

$$(\Delta\alpha)_G = -18.24 \frac{\left(C_{L_f}\right)_{WB}\sigma}{A} + rT \frac{\left(C_{L_f}\right)^2_{WB}}{57.3\left(C_{L_\alpha}\right)_{WB}} - rB + K\left(\frac{t}{c}\right)_{max} \text{ (per deg)} \qquad 4.7.1\text{-g}$$

where

σ	is Prandtl's interference coefficient from multiplane theory and is obtained from Figure 4.7.1-19 as a function of wing height above the ground.
r	accounts for the effect of finite span and is obtained from Figure 4.7.1-16 as a function of wing height above the ground.
T	accounts for the reduction of the longitudinal velocity and is obtained from Figure 4.7.1-20 as a function of wing height above the ground.
B	accounts for the change in circulation and is obtained from Figure 4.7.1-21 as a function of wing height above the ground.
K	accounts for the effective wing thickness and is obtained from Figure 4.7.1-22 as a function of wing height above the ground.
$\left(C_{L_\alpha}\right)_{WB}$	is the wing-body lift-curve slope, per degree, out of ground effect, obtained from test data or Section 4.3.1.2.
$\left(\frac{t}{c}\right)_{max}$	is the ratio of maximum wing thickness to wing chord.
$\left(C_{L_f}\right)_{WB}$	is the wing-body lift coefficient including flap effects, out of ground effect, obtained from test data or Section 4.3.1 and Section 6.1.4.1.

The change in lift on the horizontal tail due to ground effect is accounted for in the same manner as in Method 1 above.

Sample Problems

1. Method 1

Given: a jet-transport configuration

Wing Characteristics:

$A = 6.8$ $\qquad \frac{c_r}{b} = 0.291$ $\qquad \frac{h_{c_r/4}}{c_r} = 0.29$ $\qquad \Lambda_{c/4} = 35°$

$\lambda = 0.30$ $\qquad b = 1864.4$ in. $\qquad \frac{b_f}{b} = 0.54$ $\qquad \delta_f = 50°$

$H = 158$ in. $\qquad \left(C_{L_\alpha}\right)_{WB} = 0.078$ per deg (test data) $\qquad \frac{h}{b/2} = 0.168$

$\frac{\Delta x}{b/2} = 0.04$ Slotted flaps

From wind-tunnel-test data (out of ground effect):

α (deg)	0	2	4	6	8	10
$\left(C_{L_f}\right)_{WB}$ (with flaps)	1.19	1.35	1.50	1.66	1.82	1.96
$C_{L_{WB}}$ (without flaps)	0.18	0.34	0.49	0.65	0.81	0.97
ΔC_{L_f}	1.01	1.01	1.01	1.01	1.01	0.99

Tail Characteristics:

$A = 3.79$ $\frac{c_r}{b} = 0.386$ $\Lambda_{c/4} = 35°$ $\frac{S_H}{S_W} = 0.377$

$i_H = -6°$ $H_H = 233.7 \cos \alpha - 664.1 \sin \alpha$

From wind-tunnel-test data (out of ground effect):

α (deg)	0	2	4	6	8	10
C_{L_H}	−0.606	−0.535	−0.475	−0.415	−0.360	−0.300
ϵ (deg)	5.1	6.0	6.9	7.8	8.8	9.7

Compute: The change in wing-body lift due to ground effect

$x = 0.56$ (Figure 4.7.1-14)

$$\frac{57.3\, C_L}{2\pi \cos^2 \Lambda_{c/4}} = \frac{57.3\, C_L}{(6.28)\,(0.671)} = 13.6\, C_L$$

α (deg)	$\left(C_{L_f}\right)_{WB}$ (test)	13.6 C_L	$\frac{L}{L_o}-1$ (Fig. 4.7.1-15)
0	1.19	16.2	−0.04
2	1.35	18.4	−0.09
4	1.50	20.4	−0.13
6	1.66	22.6	−0.175
8	1.82	24.8	−0.205
10	1.96	26.7	−0.212

$r = 0.845$ (Figure 4.7.1-16)

$\Delta\left(\Delta C_L\right)_{flap} = -0.083$ (Figure 4.7.1-17)

Solution:

$$(\Delta\alpha)_G = -\left[\frac{9.12}{A} + 7.16\,\frac{c_r}{b}\right]\left(C_{L_f}\right)_{WB} x - \frac{A}{2\left(C_{L_\alpha}\right)_{WB}}\left(\frac{c_r}{b}\right)\left(\frac{L}{L_o} - 1\right)\left(C_{L_f}\right)_{WB} r$$

$$- \frac{\left(\delta_f/50\right)^2}{\left(C_{L_\alpha}\right)_{WB}}\,\Delta\left(\Delta C_L\right)_{flap} \quad \text{(Equation 4.7.1-a)}$$

$$= -\left[\frac{9.12}{6.8} + 7.16(0.291)\right](0.56)\left(C_{L_f}\right)_{WB} - \frac{(6.8)(0.291)(0.845)}{2(0.078)}\left(\frac{L}{L_o} - 1\right)\left(C_{L_f}\right)_{WB}$$

$$- \frac{(50/50)^2}{0.078}\,(-0.083)$$

$$= -1.92\left(C_{L_f}\right)_{WB} - 10.7\left(\frac{L}{L_o} - 1\right)\left(C_{L_f}\right)_{WB} + 1.064$$

α (deg)	$\left(C_{L_f}\right)_{WB}$ (test)	$\frac{L}{L_o}-1$	$(\Delta\alpha)_G$ (deg)
0	1.19	−0.04	−0.71
2	1.35	−0.09	−0.23
4	1.50	−0.13	0.27
6	1.66	−0.175	0.99
8	1.82	−0.205	1.57
10	1.96	−0.212	1.76

The in-ground-effect lift curve can be constructed and is shown in Sketch (f). A comparison of the predicted lift curve to wind-tunnel-test data is shown in Sketch (g).

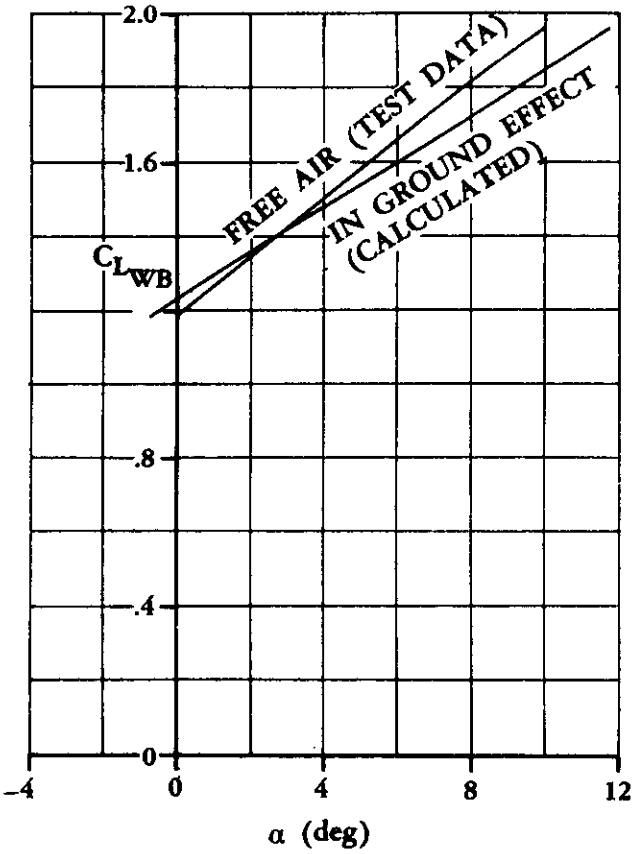

SKETCH (f)

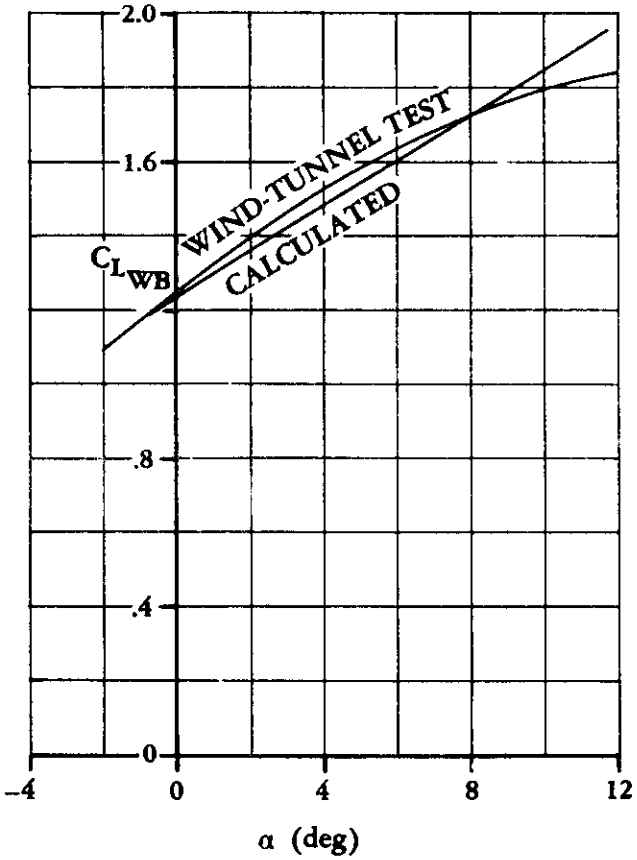

SKETCH (g)

Compute the change in downwash at the horizontal tail due to ground effect

$$\frac{b'_W}{b} = 0.725 \quad \text{(Figure 4.7.1-18a)}$$

$$\frac{b'_f}{b'_W} = 0.70 \quad \text{(Figure 4.7.1-18b)}$$

$$b'_W = \left(\frac{b'_W}{b}\right) b \quad \text{(Equation 4.7.1-d)}$$

$$= (0.725)(1864.4)$$

$$= 1352 \text{ in.}$$

$$b_f = \left(\frac{b'_f}{b'_W}\right)\left(\frac{b'_W}{b}\right) b \quad \text{(Equation 4.7.1-e)}$$

$$= (0.70)(0.725)(1864.4)$$

$$= 946 \text{ in.}$$

$$b_{eff} = \frac{C_{L_{WB}} + \Delta C_{L_f}}{\dfrac{C_{L_{WB}}}{b'_W} + \dfrac{\Delta C_{L_f}}{b'_f}} \quad \text{(Equation 4.7.1-c)}$$

α (deg)	$C_{L_{WB}}$ (test)	ΔC_{L_f} (test)	b_{eff} (in.)
0	0.18	1.01	991
2	0.34	1.01	1023
4	0.49	1.01	1049
6	0.65	1.01	1072
8	0.81	1.01	1092
10	0.97	0.99	1111

The height of the quarter-chord of the horizontal-tail MAC above the ground is calculated by

$$H_H = 233.7 \cos\alpha - 664.1 \sin\alpha$$

α	0	2	4	6	8	10
H_H (in.)	233.7	210.3	186.6	163.1	138.7	114.8

$$(\Delta\epsilon)_G = \epsilon\left[\frac{b_{eff}^2 + 4(H_H - H)^2}{b_{eff}^2 + 4(H_H + H)^2}\right] \quad \text{(Equation 4.7.1-b)}$$

$$(\Delta\alpha_H)_G = -(\Delta\epsilon)_G \quad \text{(Equation 4.7.1-f)}$$

α (deg)	b_{eff} (in.)	H (in.)	H_H (in.)	ϵ (deg)	$(\Delta\epsilon)_G$ (deg)	$(\Delta\alpha_H)_G$ (deg)
0	991	158.0	233.7	5.1	3.21	−3.21
2	1023	158.0	210.3	6.0	3.99	−3.99
4	1049	158.0	186.6	6.9	4.83	−4.83
6	1072	158.0	163.1	7.8	5.74	−5.74
8	1092	158.0	138.7	8.8	6.80	−6.80
10	1111	158.0	114.8	9.7	7.86	−7.86

The in-ground-effect lift curve can be constructed for $i_H = -6^\circ$ and is shown in Sketch (h). No test data are available for comparison.

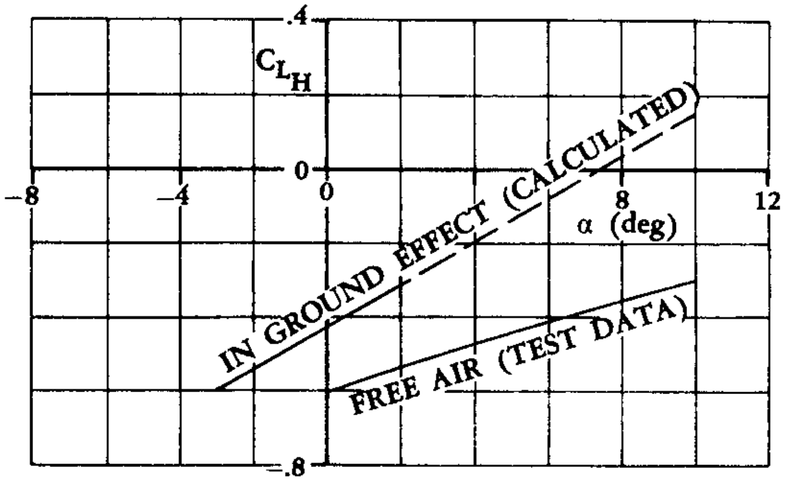

SKETCH (h)

2. Method 2

Given: the F5D-1 aircraft

Wing Characteristics:

$A = 2.02$ $\quad \frac{h}{\bar{c}} = 0.329$ $\quad \frac{h}{b/2} = 0.36$ $\quad \left(C_{L_\alpha}\right)_{WB} = 0.0363$ per degree (test data)

$\left(\frac{t}{c}\right)_{max} = 0.05$

From wind-tunnel-test data:

α (deg)	0	2	4	6	8	10	12	14	16
$C_{L_{WB}}$ (free air)	−0.023	0.048	0.12	0.194	0.267	0.34	0.418	0.495	0.572

Compute:

$\sigma = 0.322$ (Figure 4.7.1-19)

$r = 0.703$ (Figure 4.7.1-16)

$K = 4.6$ (Figure 4.7.1-22)

$T = 6.06$ (Figure 4.7.1-20)

$C_{L_{WB}}$ (test)	−0.023	0.048	0.12	0.194	0.267	0.34	0.418	0.495	0.572
B (deg) (Fig. 4.7.1-21)	–	0.12	0.30	0.50	0.68	0.86	1.04	1.21	1.41

Solution:

$$(\Delta\alpha)_G = -18.24\,\frac{\left(C_{L_f}\right)_{WB}\sigma}{A} + \frac{rT\left(C_{L_f}\right)_{WB}^{2}}{57.3\left(C_{L_\alpha}\right)_{WB}} - rB + K\left(\frac{t}{c}\right)_{max} \qquad \text{(Equation 4.7.1-g)}$$

①	②	③	④	⑤	⑥	⑦
α (deg)	$C_{L_{WB}}$ (test)	$-18.24\,\frac{\left(C_{L_f}\right)_{WB}\sigma}{A}$	$\frac{rT\left(C_{L_f}\right)_{WB}^{2}}{57.3\left(C_{L_\alpha}\right)_{WB}}$	$-rB$	$K\left(\frac{t}{c}\right)_{max}$	$(\Delta\alpha)_G$ (deg) (Eq. 4.7.1-g) ③+④+⑤+⑥
0	−0.023	0.067	0.0011	–	0.23	0.298
2	0.048	−0.140	0.0047	−0.0844	0.23	0.010
4	0.12	−0.349	0.0295	−0.211	0.23	−0.300
6	0.194	−0.564	0.0771	−0.352	0.23	−0.609
8	0.267	−0.776	0.146	−0.478	0.23	−0.878
10	0.34	−0.989	0.237	−0.605	0.23	−1.127
12	0.418	−1.216	0.358	−0.731	0.23	−1.359
14	0.495	−1.440	0.502	−0.851	0.23	−1.559
16	0.572	−1.663	0.670	−0.991	0.23	−1.754

The calculated F5D-1 lift curve in ground effect is now constructed in Sketch (i) by shifting the free-air lift curve at every C_L by the corresponding $(\Delta\alpha)_G$. A comparison of the predicted lift curve to wind-tunnel-test data is shown in Sketch (j).

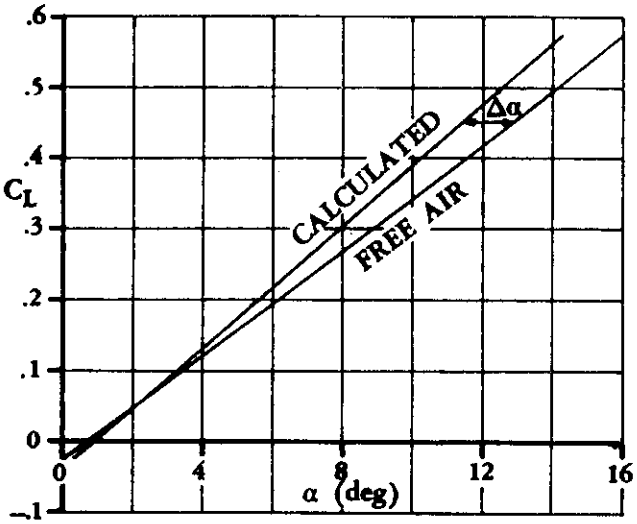

SKETCH (i)

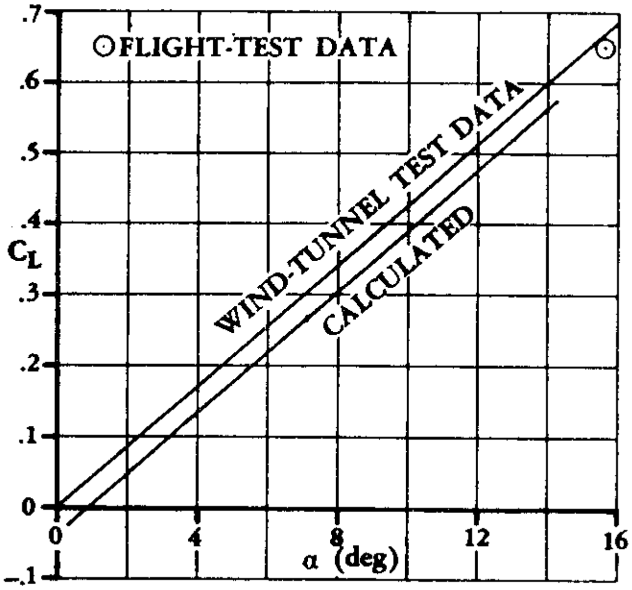

SKETCH (j)

REFERENCES

1. Wetmore, J. W., and Turner, L. I., Jr.: Determination of Ground Effect from Tests of a Glider in Towed Flight. NACA TR 695, 1940. (U)

2. Wieselsberger, C.: Wing Resistance Near the Ground. NACA TM 77, 1922. (U)

3. Tani, I., Taima, M., and Simidu, S.: The Effect of Ground on the Aerodynamic Characteristics of a Monoplane Wing. Tokyo Univ. Aeronautical Research Inst. Report 156, 1937. (U)

4. Baker, P. A., Schweikhard, W. G., and Young, W. R.: Flight Evaluation of Ground Effect on Several Low-Aspect-Ratio Airplanes. NASA TN D-6053, 1970. (U)

5. de Sievers, A.: Wind-Tunnel Tests on the Ground Effect. NASA TT F-11059, 1967. (U)

6. Gersten, K.: Calculation of the Aerodynamic Characteristics of Wings of Finite Span Near the Ground. Abhandlungen der Braunschweigischen Wissenschaftlichen Gesselschaft, XII, 1960, pp. 95-115. (U)

7. Kirkpatrick, D. L. I.: A Method of Correlating the Ground Effects on the Longitudinal Characteristics of Slender Wings. RAE TR 69190, 1969. (U)

8. Kemp, W. B., Jr., Lockwood, V. E., and Phillips, W. P.: Ground Effects Related to Landing of Airplanes with Low-Aspect-Ratio Wings. NASA TN D-3583, 1966. (U)

9. Piper, R. W., and Davies, H.: Note on Factors Affecting Trim at Take-off and Landing. Aero. Departmental Note – Wind Tunnel No. 540, 1941. (Unpublished British Paper). (U)

10. Owen, P. R., and Hogg, H.: Ground Effect on Downwash with Slipstream. ARC R&M 2449, 1952. (U)

11. Tani, I., Itokawa, H., and Taima, M.: Further Studies of the Ground Effect on the Aerodynamic Characteristics of an Aeroplane, with Special Reference to Tail Moment. Tokyo Univ. Aeronautical Research Inst. Report 158, 1937. (U)

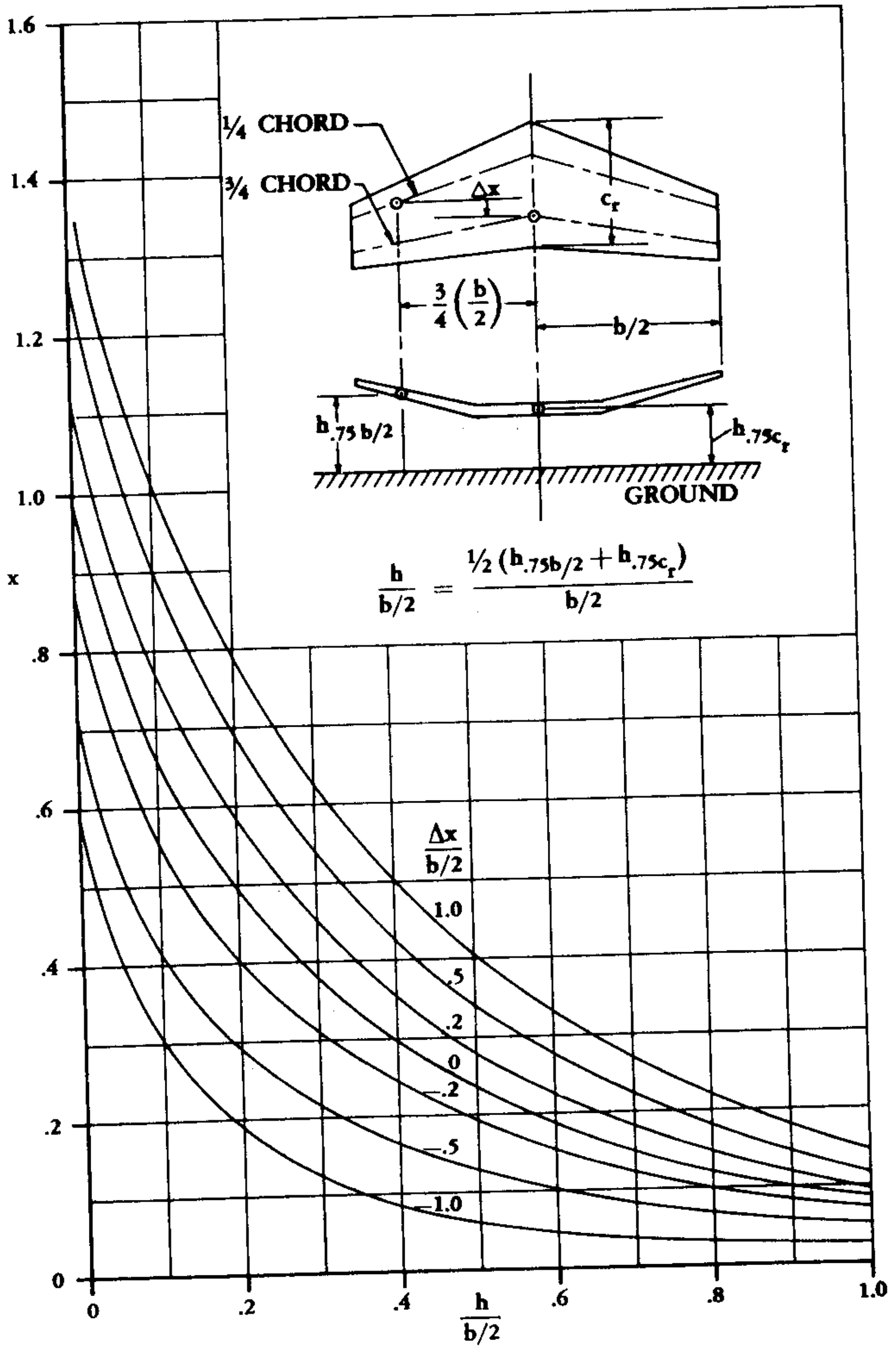

FIGURE 4.7.1-14 PARAMETER ACCOUNTING FOR GROUND EFFECT ON LIFT DUE TO TRAILING VORTICES

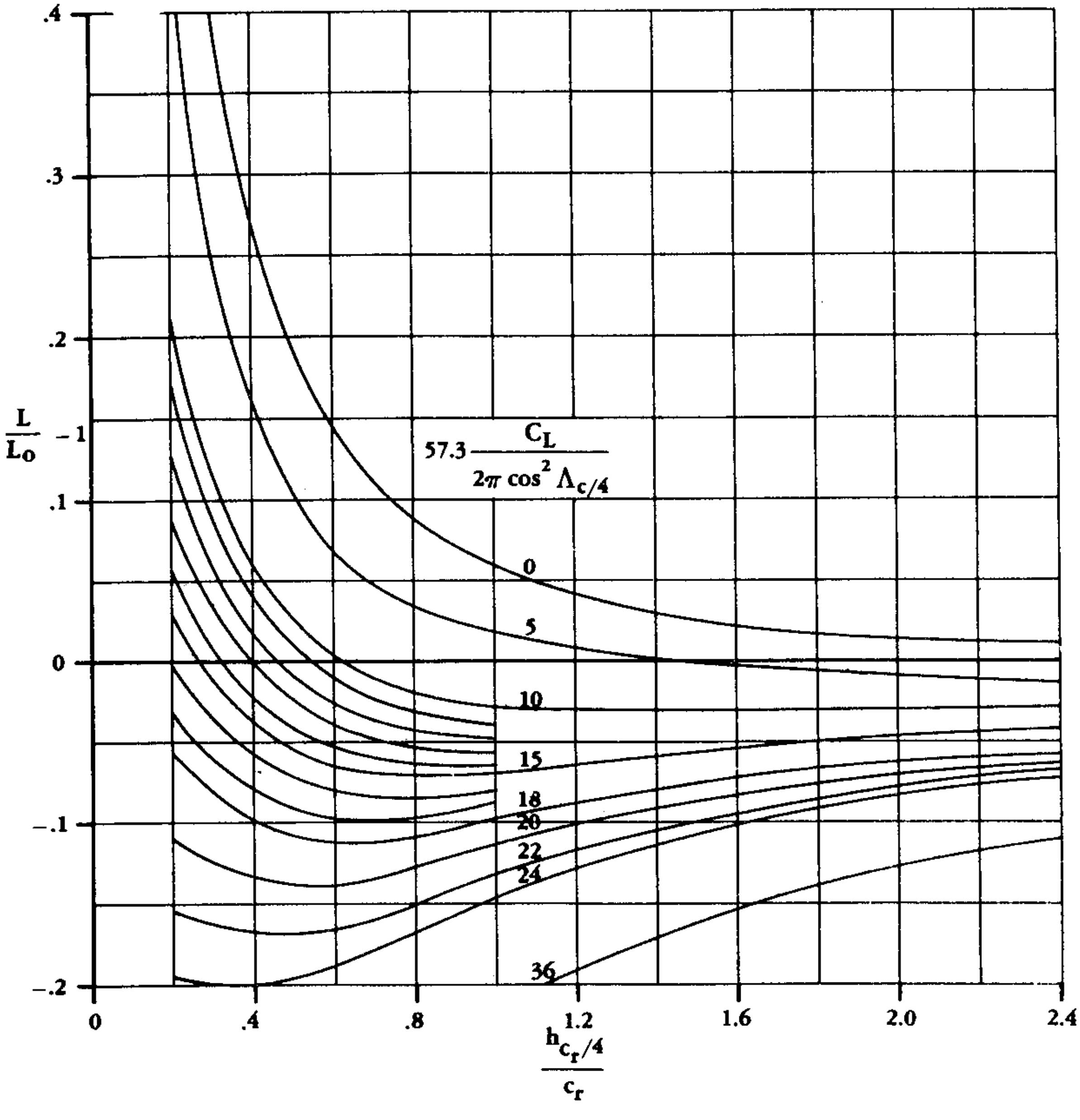

FIGURE 4.7.1-15 PARAMETER ACCOUNTING FOR GROUND EFFECT ON LIFT DUE TO BOUND VORTICES

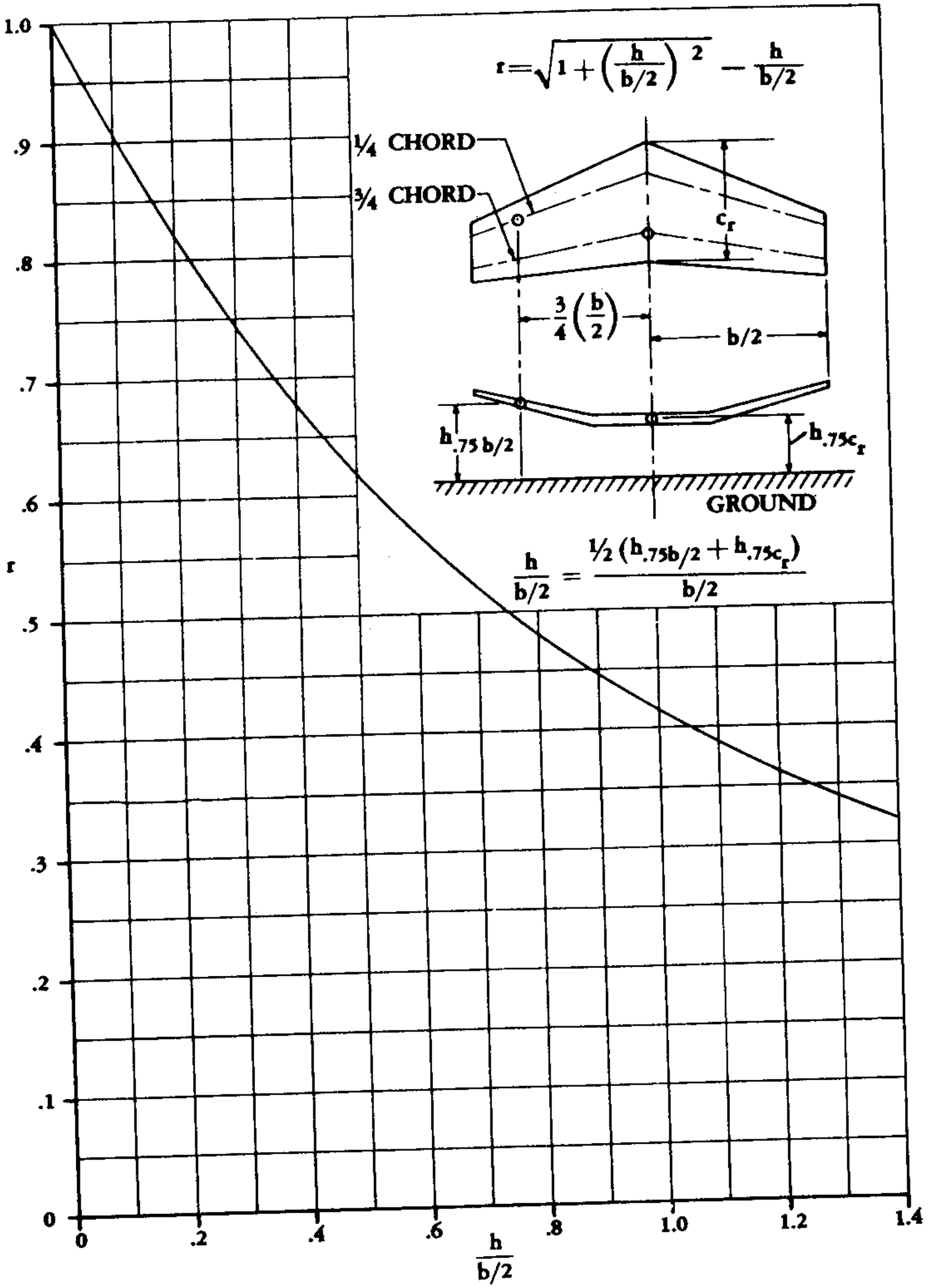

FIGURE 4.7.1-16 FACTOR ACCOUNTING FOR FINITE SPAN IN GROUND EFFECT

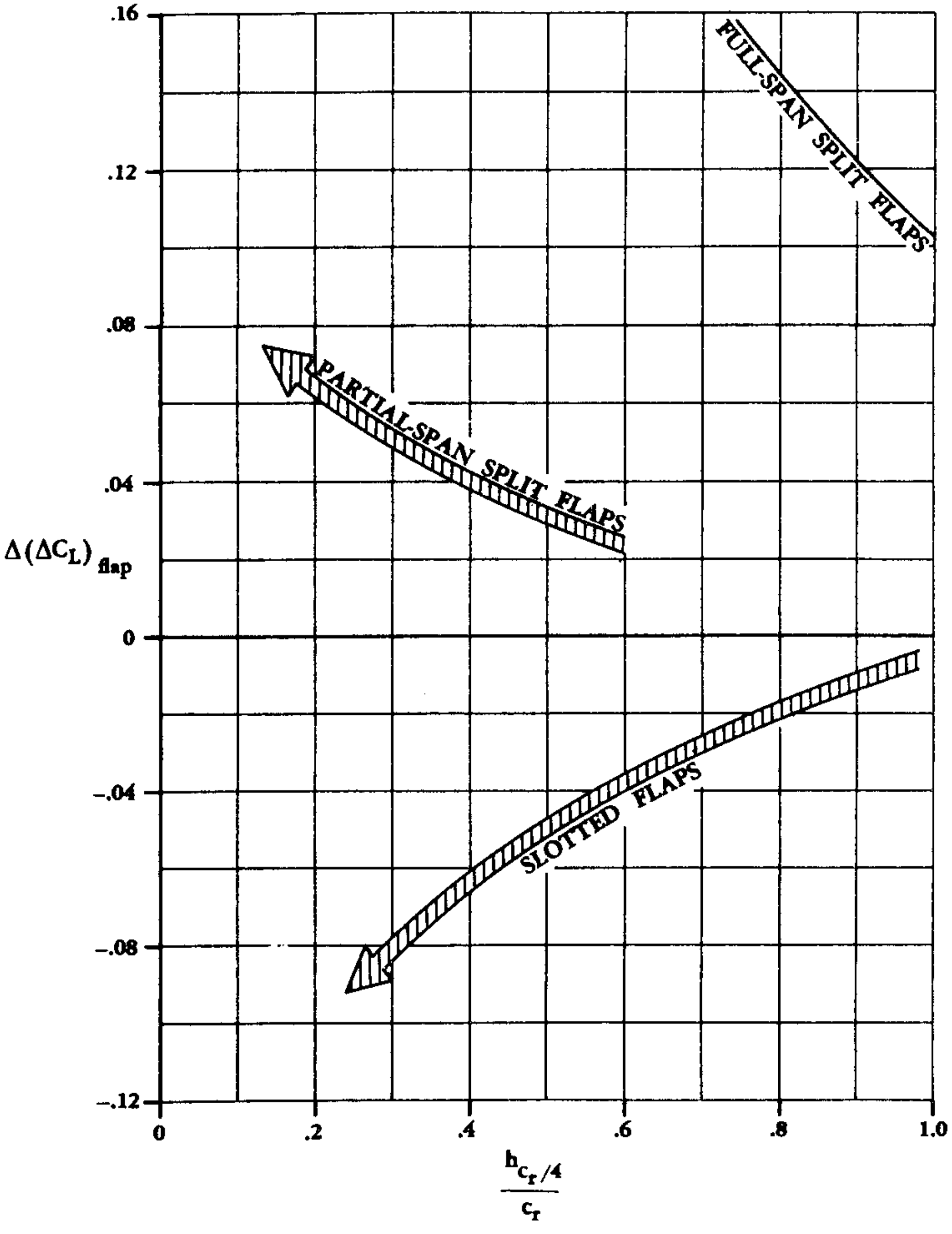

FIGURE 4.7.1-17 EFFECT OF FLAP DEFLECTION ON THE GROUND INFLUENCE ON LIFT

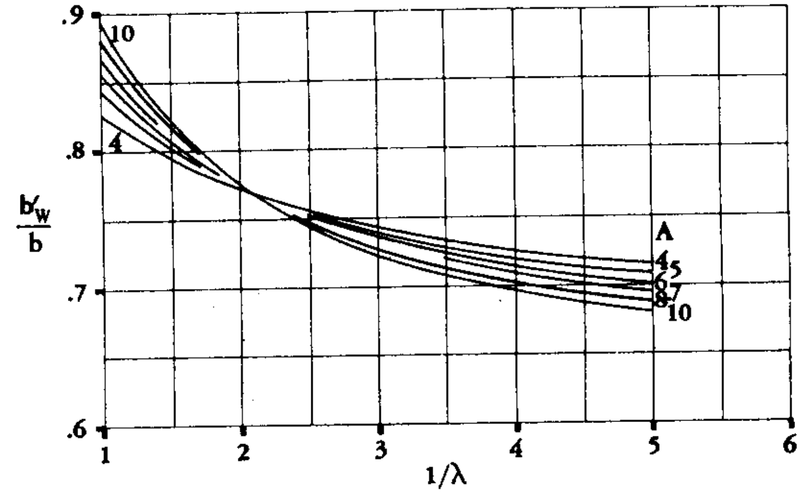

FIGURE 4.7.1-18a EFFECTIVE WING SPAN IN THE PRESENCE OF THE GROUND

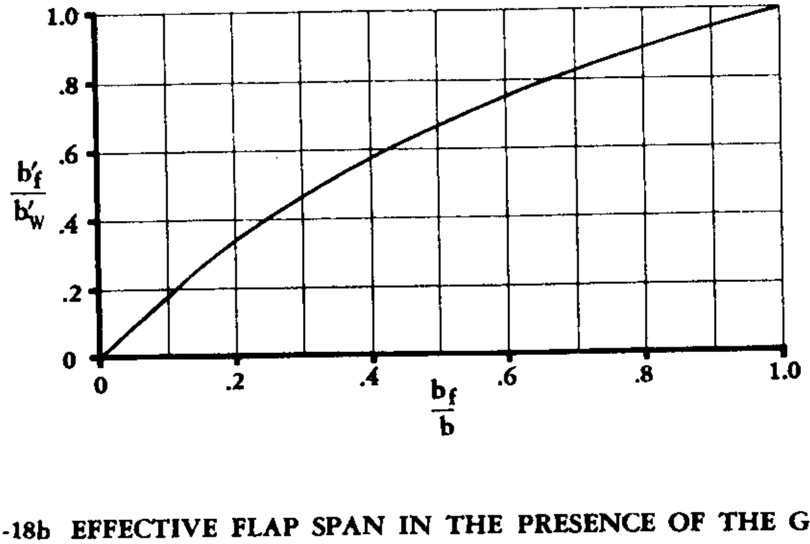

FIGURE 4.7.1-18b EFFECTIVE FLAP SPAN IN THE PRESENCE OF THE GROUND

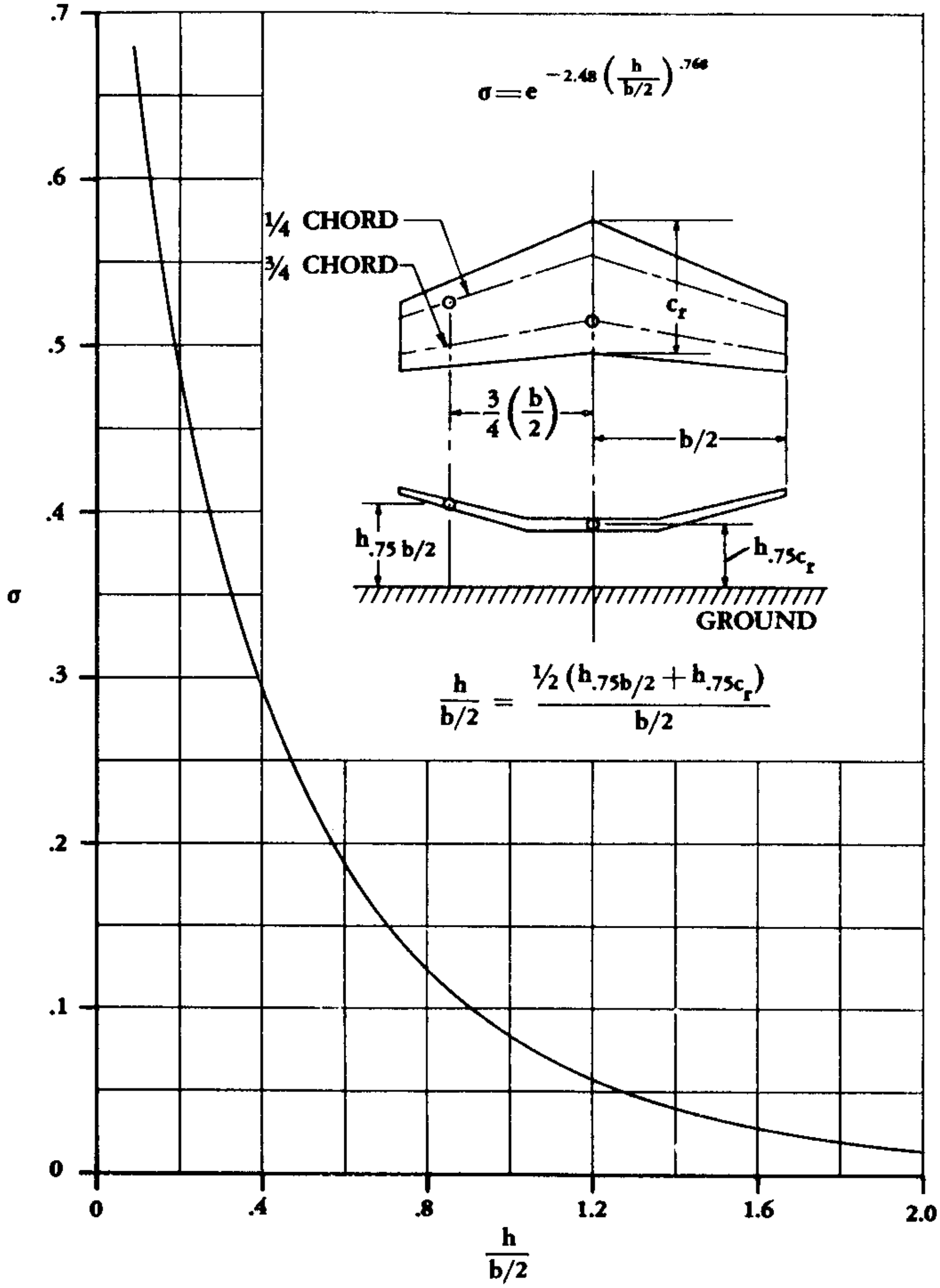

FIGURE 4.7.1-19 PRANDTL'S INTERFERENCE COEFFICIENT — INDICATIVE OF VARIATION IN INDUCED VERTICAL VELOCITY WITH GROUND HEIGHT

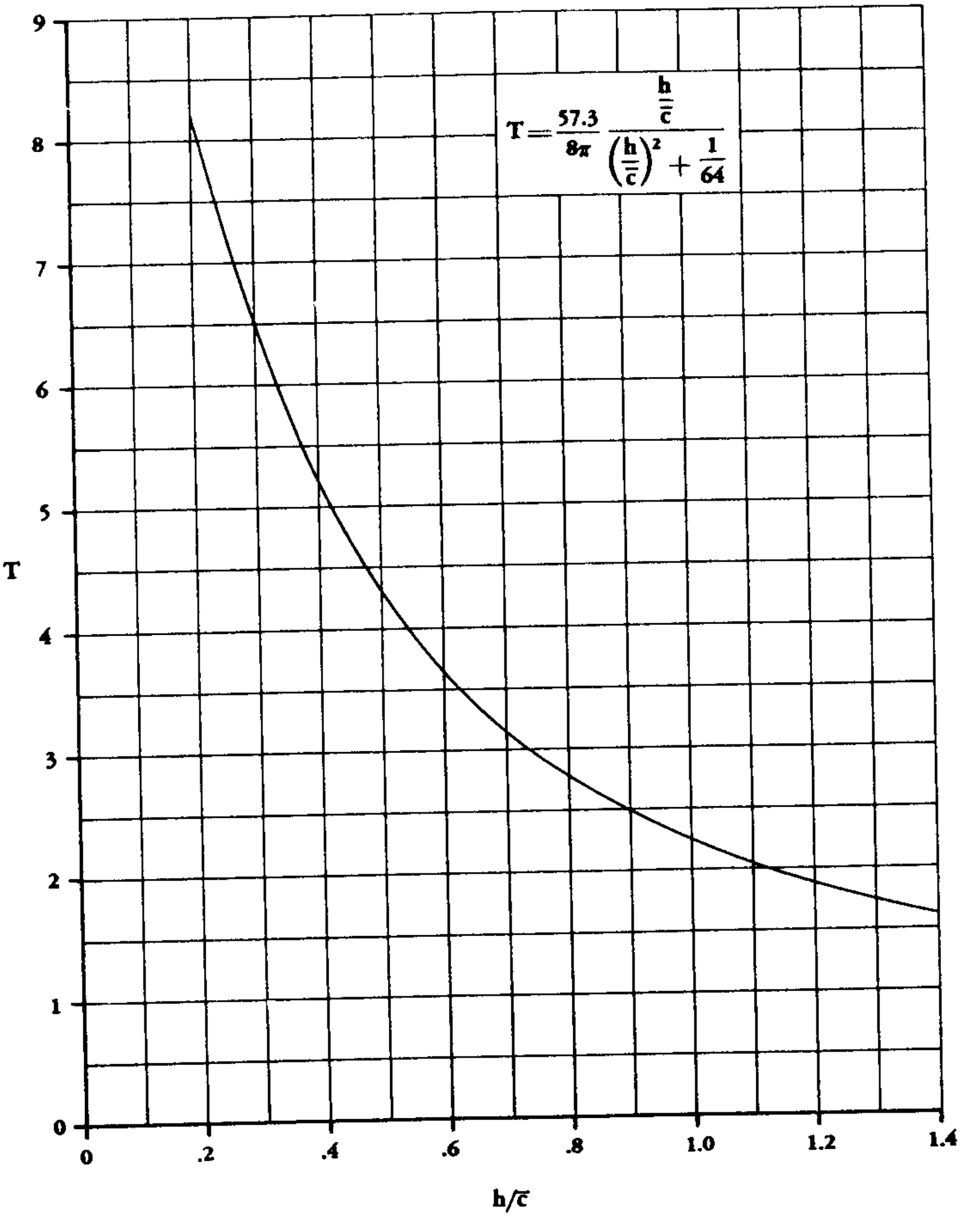

FIGURE 4.7.1-20 PARAMETER ACCOUNTING FOR VARIATION IN LONGITUDINAL VELOCITY WITH GROUND HEIGHT

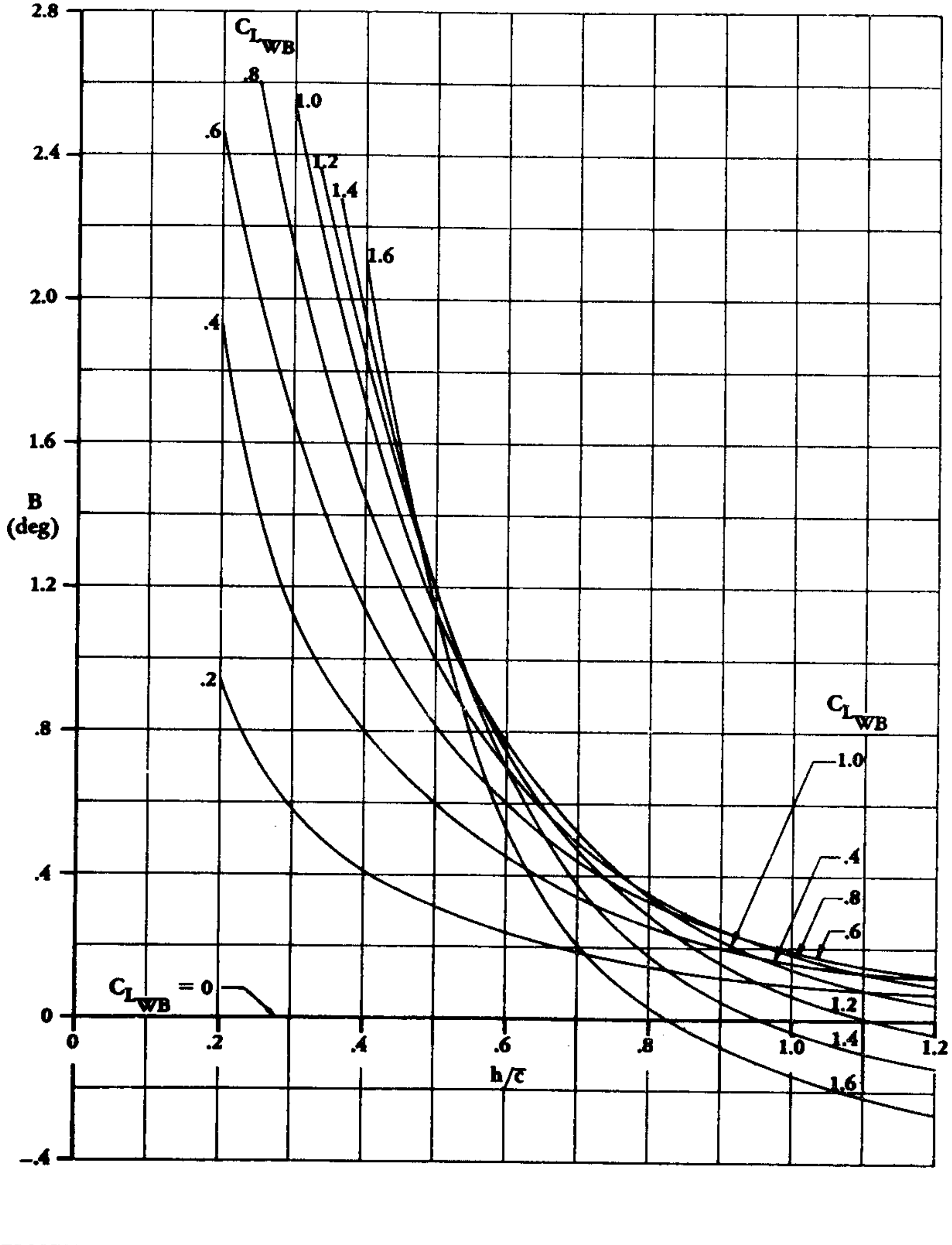

FIGURE 4.7.1-21 PARAMETER ACCOUNTING FOR VARIATION IN CIRCULATION WITH LIFT AND HEIGHT ABOVE GROUND

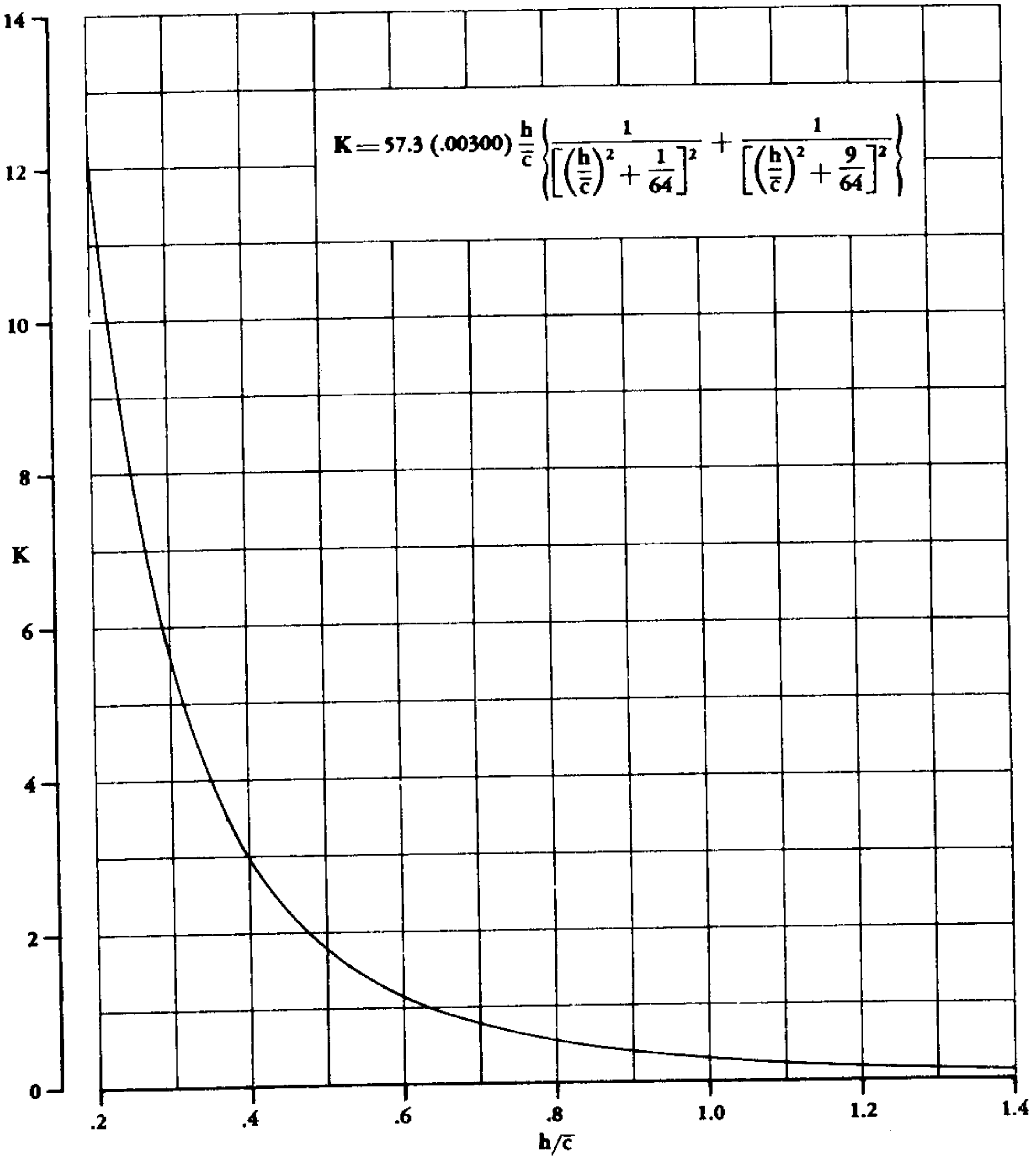

FIGURE 4.7.1-22 PARAMETER ACCOUNTING FOR INFLUENCE OF WING THICKNESS DUE TO HEIGHT ABOVE GROUND

4.7.3 GROUND EFFECTS ON PITCHING-MOMENT VARIATION WITH ANGLE OF ATTACK

A method is presented in this section for estimating the ground effects on pitching moment in the linear-lift region. The reader is referred to Section 4.7 for a basic discussion of various aspects of ground effects.

The change in pitching moment due to ground effects is due primarily to the change in lift on the horizontal tail, which in most cases can be attributed to the change in downwash. An additional pitching-moment increment is produced by the increased lift on the wing and any possible shift in the aerodynamic center due to ground effect.

DATCOM METHOD

The method presented herein is based upon the lift estimates of Section 4.7.1. The method assumes no change in the location of the wing aerodynamic center due to ground effects. The total change in pitching-moment coefficient due to ground effects is the sum of the changes of the horizontal-tail-body and wing-body pitching-moment components, based on the product of wing area and wing MAC, and is expressed as

$$\left(\Delta C_m\right)_G = \left(\Delta C_{m_H}\right)_G + \left(\Delta C_{m_{WB}}\right)_G \tag{4.7.3-a}$$

The change in pitching-moment coefficient of the horizontal-tail-body due to ground effects may be expressed as

$$\left(\Delta C_{m_H}\right)_G = -\left(\Delta C_{L_H}\right)_G \frac{\ell_H}{\bar{c}} \frac{S_H}{S_W} \frac{q_H}{q_\infty} \tag{4.7.3-b}$$

where

$\left(\Delta C_{L_H}\right)_G$	is the change in lift on the horizontal-tail-body at a given angle of attack due to ground effect, based on the horizontal-tail area, and is found from the tail-body lift curves constructed by using Section 4.7.1.
ℓ_H	is the distance from the quarter-chord point of the horizontal-tail MAC to the moment reference center, measured parallel to the body center line.
$\bar{c}$	is the wing mean aerodynamic chord.
$\frac{S_H}{S_W}$	is the ratio of horizontal-tail area to wing area.
$\frac{q_H}{q_\infty}$	is the effective dynamic-pressure ratio at the horizontal tail, obtained from Section 4.4.1.

The change in pitching-moment coefficient of the wing-body due to ground effects may be expressed as

$$\left(\Delta C_{m_{WB}}\right)_G = \left(n - \frac{x_{a.c.}}{\bar{c}}\right)\left(\Delta C_{L_{WB}}\right)_G \qquad 4.7.3\text{-c}$$

where

n	is the distance from the wing apex to the desired moment reference center measured in wing mean aerodynamic chords, positive aft.
$x_{a.c.}$	is the wing-body aerodynamic-center location measured from the wing apex, positive for a.c. aft of wing apex, obtained from Section 4.3.2.2.
$\bar{c}$	is the wing mean aerodynamic chord.
$\left(\Delta C_{L_{WB}}\right)_G$	is the change in lift due to ground effect on the wing-body and is found from the wing-body lift curves constructed by using Section 4.7.1.

Sample Problem

Given: Same jet-transport configuration as Sample Problem 1 of Section 4.7.1.

Wing-Body Characteristics:

$\frac{x_{a.c.}}{\bar{c}} = 1.182$ $\qquad n = 1.242$

From Sample Problem 1 of Section 4.7.1:

α (deg)	0	2	4	6	8	10
$\left(\Delta C_{L_{WB}}\right)_G$	0.04	0.01	−0.025	−0.06	−0.09	−0.11

Tail Characteristics:

$\frac{\ell_H}{\bar{c}} = 2.43$ $\qquad \frac{S_H}{S_W} = 0.377$ $\qquad \frac{q_H}{q_\infty} = 0.95$

From Sample Problem 1 of Section 4.7.1:

α (deg)	0	2	4	6	8	10
$\left(\Delta C_{L_H}\right)_G$	0.255	0.305	0.355	0.415	0.470	0.530

Compute:

$$\left(\Delta C_{m_H}\right)_G = -\left(\Delta C_{L_H}\right)_G \frac{\ell_H}{\bar{c}} \frac{S_H}{S_W} \frac{q_H}{q_\infty} \qquad \text{(Equation 4.7.3-b)}$$

$$= -\left(\Delta C_{L_H}\right)_G (2.43)(0.377)(0.95)$$

$$= -0.870 \left(\Delta C_{L_H}\right)_G$$

α (deg)	0	2	4	6	8	10
$\left(\Delta C_{m_H}\right)_G$	−0.222	−0.265	−0.309	−0.361	−0.409	−0.461

$$\left(\Delta C_{m_{WB}}\right)_G = \left(n - \frac{x_{a.c.}}{\bar{c}}\right) \left(\Delta C_{L_{WB}}\right)_G \qquad \text{(Equation 4.7.3-c)}$$

$$= (1.242 - 1.182) \left(\Delta C_{L_{WB}}\right)_G$$

$$= (0.06) \left(\Delta C_{L_{WB}}\right)_G$$

α (deg)	0	2	4	6	8	10
$\left(\Delta C_{m_{WB}}\right)_G$	0.0024	0.0006	−0.0015	−0.0036	−0.0054	−0.0066

Solution:

$$\left(\Delta C_m\right)_G = \left(\Delta C_{m_H}\right)_G + \left(\Delta C_{m_{WB}}\right)_G \qquad \text{(Equation 4.7.3-a)}$$

α (deg)	0	2	4	6	8	10
$\left(\Delta C_m\right)_G$	−0.220	−0.264	−0.311	−0.365	−0.414	−0.468

No test data are available for comparison.

4.7.4 GROUND EFFECTS ON DRAG AT ANGLE OF ATTACK

In this section, methods are presented for estimating the ground effects on drag in the linear-lift region. The reader is referred to Section 4.7 for a basic discussion of various aspects of ground effects.

The drag of a vehicle in the presence of a ground plane is affected in three ways.

1. The drag due to lift is decreased.
2. A change in the drag at zero lift is also experienced, but is small relative to the change in drag due to lift.
3. The presence of a ground plane introduces a pitching-moment increment (Section 4.7.3), which changes the drag due to lift of the trimmed vehicle.

The second effect is ignored in most calculations and is not presented in the Datcom.

Two methods are presented to determine the reduction in drag due to lift in the presence of the ground. Both methods are based on an image-vortex representation of the ground plane (see Sketches (a), (b), (c), and (d) in Section 4.7). The method of Wieselsberger from Reference 1 considers only the effects of the bound image vortex. However, the method of Tani (References 2 and 3) considers the effects of both the bound and trailing image vortices.

The change in drag due to lift resulting from trimming the pitching-moment increment due to ground effect consists of a synthesis of material presented in other sections.

DATCOM METHODS

Change in Trim Drag Due to Ground Plane

Procedures for calculating the drag increment due to longitudinally trimming a vehicle are presented in Section 4.5.3.2. To determine trim drag in ground effect, the pitching-moment increment due to ground effect $\left(\Delta C_m\right)_G$ of Equation 4.7.3-a is added to the vehicle pitching moment out of ground effect. The combined pitching moment is then used in the standard procedure for determining trim drag out of ground effect (Section 4.5.3.2).

Change, Due to Ground Effect, of Drag Due to Lift of the Wing

According to Reference 3, the two methods presented herein for predicting ground effects on drag due to lift give nearly identical results at moderate to large ground heights. Therefore, Method 1 is preferred for its simplicity. At ground heights within the approximate range $0.3 \geqslant h/b > 0$ however, Method 2 should be used, since its accuracy is significantly better than that of Method 1 in this range. Both methods have been modified slightly to include the effects of wing dihedral.

Neither Method 1 nor Method 2 is very successful in estimating ground effects on drag with flaps down. At low heights above the ground, Method 2 gives results closer to experimental data than does Method 1, although both methods underestimate the reduction of drag in ground effect. At intermediate heights above the ground, the two methods yield nearly equivalent results.

Method 1

The change in wing drag due to lift caused by ground effect as determined by Wieselsberger (Reference 1) is given by

$$\left(\Delta C_{D_L}\right)_G = -\frac{\sigma C_L^2}{\pi A} \qquad 4.7.4\text{-a}$$

where

σ is Prandtl's interference coefficient from multiplane theory and is obtained from Figure 4.7.1-19 as a function of wing height above the ground.

C_L is the lift coefficient of the wing out of ground effect, obtained from test data or estimated by using the method of Section 4.1.3.3.

A is the wing aspect ratio.

The total drag of a wing-body configuration in ground effect is then given by

$$\left(C_{D_{WB}}\right)_G = C_{D_{WB}} + \left(\Delta C_{D_L}\right)_G \qquad 4.7.4\text{-b}$$

where $C_{D_{WB}}$ is the total drag coefficient of the wing-body configuration out of ground effect obtained from test data or Section 4.3.3.2, and $\left(\Delta C_{D_L}\right)_G$ is obtained by using either Method 1 or 2.

Method 2

The reduction in drag due to lift as determined by the method of Tani (References 2 and 3) is given by

$$\left(\Delta C_{D_L}\right)_G = -\frac{\sigma C_L^2}{\pi A} - \left(C_D - \frac{\sigma C_L^2}{\pi A}\right)\frac{rTC_L}{57.3} \qquad 4.7.4\text{-c}$$

where

C_D is the wing-alone drag coefficient corresponding to C_L out of ground effect, obtained from test data or estimated by the method of Section 4.1.5.2, i.e., $\left(C_{D_0} + C_{D_L}\right)$.

r accounts for the condition of finite span and is obtained from Figure 4.7.1-16 as a function of wing height above the ground.

T accounts for the reduction of the longitudinal velocity and is obtained from Figure 4.7.1-20 as a function of wing height above the ground.

All remaining parameters have been defined in Method 1 above.

The total drag of a wing-body configuration in ground effect is calculated by using the procedure in Method 1 above; i.e.,

$$\left(C_{D_{WB}}\right)_G = C_{D_{WB}} + \left(\Delta C_{D_L}\right)_G \qquad 4.7.4\text{-b}$$

The sample problems presented below illustrate the use of both Methods 1 and 2 applied to a wing-alone configuration. It should be noted that, in applying Method 2 to a wing-body configuration, the value of C_D in Equation 4.7.4-c is that of the wing alone. If no test data are available for the particular configuration, the wing drag may be estimated by using the method of Section 4.1.5.2, as noted previously. On the other hand, if only wing-body test data are available, it is suggested that the wing-body result be used instead of attempting to estimate a wing-alone value.

Sample Problems

1. Method 1

Given: The sweptback wing of Reference 4

Wing Characteristics:

$A = 4.01$ $\qquad$ $b = 11.375$ ft $\qquad$ $\bar{c} = 2.89$ ft $\qquad$ $\Lambda_{c/4} = 40°$

Additional Characteristics:

$h = 1.97$ ft

The following drag variation with lift (out of ground effect) from Reference 4:

C_L	0.10	0.20	0.40	0.60	0.70	0.80
C_D Wing Alone	0.0063	0.0093	0.0220	0.0400	0.0500	0.0650

Compute:

$h/(b/2) = (2)(1.97)/11.375 = 0.346$

$\sigma = 0.33$ (Figure 4.7.1-19)

Solution:

$$\left(\Delta C_{D_L}\right)_G = -\frac{\sigma C_L^2}{\pi A} \quad \text{(Equation 4.7.4-a)}$$

$$= -\frac{0.33\, C_L^2}{(3.14)(4.01)}$$

$$= -0.0262\, C_L^2$$

①	②	③
C_L	C_L^2	$\left(\Delta C_{D_L}\right)_G$ (Eq. 4.7.4-a) −0.0262 ②
0.10	0.01	−0.0003
0.20	0.04	−0.0010
0.40	0.16	−0.0042
0.60	0.36	−0.0094
0.70	0.49	−0.0128
0.80	0.64	−0.0168

The calculated results are compared with test values from Reference 4 in Sketch (a).

2. Method 2

Given: The same configuration as that of Sample Problem 1

Compute:

$$\frac{\sigma C_L^2}{\pi A} = 0.0262\, C_L^2 \quad \text{(see Sample Problem 1)}$$

$r = 0.712$ (Figure 4.7.1-16)

$T = 3.24$ (Figure 4.7.1-20)

$rT = (0.712)(3.24) = 2.31$

Solution:

$$\left(\Delta C_{D_L}\right)_G = -\frac{\sigma C_L^2}{\pi A} - \left(C_D - \frac{\sigma C_L^2}{\pi A}\right)\frac{rTC_L}{57.3} \quad \text{(Equation 4.7.4-c)}$$

$$= -0.0262\, C_L{}^2 - \left(C_D - 0.0262\, C_L{}^2\right)(0.0403)\, C_L$$

①	②	③	④	⑤	⑥	⑦
C_L	C_D Wing Alone	$C_L{}^2$	$\frac{\sigma C_L{}^2}{\pi A}$ 0.0262 ③	$\left(C_D - \frac{\sigma C_L{}^2}{\pi A}\right)$ ② − ④	$\left(C_D - \frac{\sigma C_L{}^2}{\pi A}\right)\frac{rTC_L}{57.3}$ 0.0403 ⑤①	$\left(\Delta C_{D_L}\right)_G$ (Eq. 4.7.4-c) − ④ − ⑥
0.10	0.0053	0.01	0.0003	0.0050	0.00002	−0.0003
0.20	0.0093	0.04	0.0010	0.0083	0.0001	−0.0011
0.40	0.0220	0.16	0.0042	0.0178	0.0003	−0.0045
0.60	0.0400	0.36	0.0094	0.0306	0.0007	−0.0101
0.70	0.0500	0.49	0.0128	0.0372	0.0011	−0.0139
0.80	0.0650	0.64	0.0168	0.0482	0.0016	−0.0184

The calculated results are compared with test values from Reference 4 in Sketch (a).

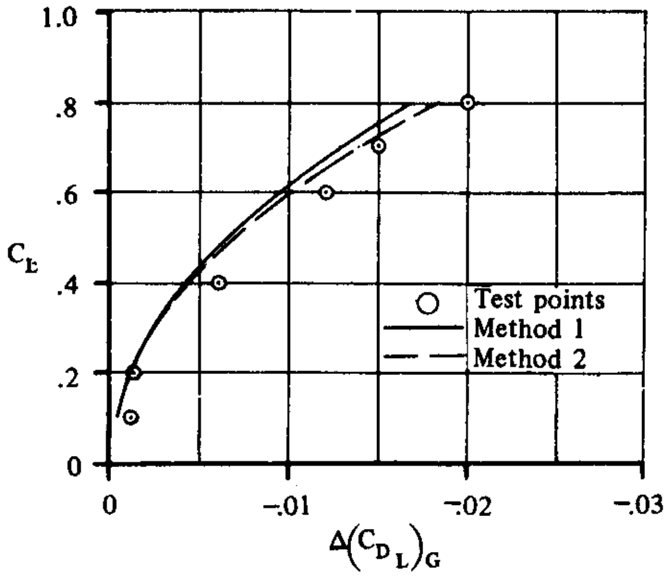

SKETCH (a)

REFERENCES

1. Wieselsberger, C.: Wing Resistance Near the Ground. NACA TM 77, 1922. (U)

2. Tani, I., Taima, M., and Simidu, S.: The Effect of Ground on the Aerodynamic Characteristics of a Monoplane Wing. Tokyo Univ. Aeronautical Research Inst. Report 156, 1937. (U)

3. Tani, I., Itokawa, H., and Taima, M.: Further Studies of the Ground Effect on the Aerodynamic Characteristics of an Aeroplane, with Special Reference to Tail Moment. Tokyo Univ. Aeronautical Research Inst. Report 158, 1937. (U)

4. Furlong, G. C., and Bollech, T. V.: Effect of Ground Interference on the Aerodynamic and Flow Characteristics of a 42° Sweptback Wing at Reynolds Numbers Up to 6.8 x 10^6. NACA TR 1218, 1955. (U)

4.8 LOW-ASPECT-RATIO WINGS AND WING-BODY COMBINATIONS AT ANGLE OF ATTACK

During recent years much work has been done on problems associated with the design and operation of advanced flight vehicles. These vehicles include re-entry configurations and those designed for hypersonic cruise. The requirement that these vehicles operate within the atmosphere at hypersonic speeds necessitates the use of configurations that are not well suited for subsonic flight at low altitudes. The configurations proposed for this type of mission feature, for the most part, extremely low aspect ratios of the order of two or less, and thick, generously-rounded lifting surfaces. These configurations also often have large blunt bases.

The subsonic flow about these vehicles is extremely complex, so much so that in most cases the use of available theoretical methods does not result in satisfactory estimates of the aerodynamic characteristics for this type of vehicle. The methods presented in this section for estimating the aerodynamic characteristics of advanced flight vehicles at subsonic speeds are necessarily semiempirical in nature. The methods are based on test data, which have been correlated with the aid of the extension of available theory. A large portion of the material is related to delta and modified-delta configurations, since a major portion of the pertinent theory and test results relate to these planforms.

In the following group of sections (4.8.1, 4.8.2, and 4.8.3) methods are presented for estimating the normal force, axial force, and pitching moment on specific types of advanced flight vehicles at angles of attack up to 20°.

The aerodynamic forces acting on the vehicle are illustrated in figure 4.8-12. In the lift axis system, the force is resolved into components perpendicular to and parallel to the free stream, called the lift and drag, respectively. In the normal-force axis system, the force is resolved into components perpendicular to and parallel to the zero-normal-force reference plane, called the normal force and axial force, respectively. For unsymmetrical configurations the zero-normal-force reference plane is inclined at some angle α_{N_0} to the body horizontal plane. The body horizontal plane passes through the most forward point on the vehicle nose and its inclination to the free stream defines the angle of attack α in the familiar lift axis system (see figure 4.8-12). The normal-force and axial-force coefficients and the angle of attack of unsymmetrical configurations are designated as $C_N{'}$, $C_X{'}$, and α', respectively. For symmetrical configurations $\alpha_{N_0} = 0$ and $\alpha' = \alpha$, and the zero-normal-force reference plane coincides with the body horizontal plane of symmetry. For symmetrical configurations the normal-force and axial-force ceofficients are designated as C_N and C_X, respectively.

The equations relating lift, drag, normal force, and axial force are as follows:

For unsymmetrical configurations

$$C_{N'} = C_L \cos\alpha' + C_D \sin\alpha'$$

$$C_{X'} = -C_D \cos\alpha' + C_L \sin\alpha'$$

$$C_L = C_{N'} \cos\alpha' + C_{X'} \sin\alpha'$$

$$C_D = -C_{X'} \cos\alpha' + C_{N'} \sin\alpha'$$

For symmetrical configurations (symmetry about the Z = 0 plane)

$$C_N = C_L \cos\alpha + C_D \sin\alpha$$

$$C_X = -C_D \cos\alpha + C_L \sin\alpha$$

$$C_L = C_N \cos\alpha + C_X \sin\alpha$$

$$C_D = -C_X \cos\alpha + C_N \sin\alpha$$

The pitching-moment coefficient at a specified angle is independent of the axis system.

The normal-force axis system is used throughout the following group of sections, since it was found to be more convenient in the correlation of the available test data.

Many of the available test results do not separate the base pressure from other aerodynamic forces. Therefore, the total axial force is analyzed in Section 4.8.2 by separating it into a component produced by base pressure plus a component related to the viscous forces acting on areas other than the base.

A general notation list is included in this section for all sections included under Section 4.8.

Sketches showing planform geometry for nearly all the configurations analyzed in Sections 4.8.1.1 through 4.8.3.2 are presented in table 4.8-A.

NOTATION

SYMBOL	DEFINITION	SECTION
A	aspect ratio of surface	4.8.1.2 4.8.2.2 4.8.3.2
B	blunting parameter, $\dfrac{\tan\theta}{\sqrt{\tan^2\theta + 2}}$	4.8.3.2
b	surface span	4.8.1.2 4.8.2.2 4.8.3.2
b_b	maximum span of base	4.8.2.1 4.8.2.2
c_r	surface root chord	4.8.1.2 4.8.3.2
h_b	maximum height of base	4.8.1.1 4.8.2.1 4.8.2.2

SYMBOL	DEFINITION	SECTION
ℓ_B	total length of body	4.8.1.1 4.8.2.1
M	Mach number	4.8.1.2 4.8.2.2 4.8.3.2
N′	normal force, perpendicular to zero-normal-force reference plane (unsymmetrical configuration)	4.8.2.2
P	perimeter of base (see figure 4.8.2.1-7a)	4.8.2.1
q_∞	free-stream dynamic pressure	4.8.2.2
R_ℓ	Reynolds number	4.8.1.2 4.8.2.2 4.8.3.2
$R_{\frac{1}{3}LE}$	effective radius of round leading-edged wing, perpendicular to leading edge at $c_r/3$ from the nose (see figure 4.8.1.2-11b)	4.8.1.2 4.8.2.2
S	planform area	4.8.1.2 4.8.2.1 4.8.2.2 4.8.3.2
S_b	base area	4.8.2.1 4.8.2.2
S_F	projected frontal area perpendicular to zero-normal-force reference plane	4.8.1.2 4.8.2.2 4.8.3.2
S_{ref}	reference area	4.8.1.2 4.8.2.1 4.8.2.2
S_{wet}	wetted area, excluding base area	4.8.2.1
V_∞	free-stream velocity	4.8.1.1
v	blunting parameter, $\sqrt{1 - \frac{4 \tan \theta}{A}}$	4.8.3.2
X	axial force parallel to zero-normal-force reference plane (unsymmetrical configuration)	4.8.2.2

SYMBOL	DEFINITION	SECTION
$\left[\left(\frac{X'}{N'}\right)_{calc}\right]_{20}$	calculated value of parameter at $\alpha' = 20^{\circ}$	4.8.2.2
$x_{c.p.}$	chordwise distance from the wing apex to the wing center of pressure, positive for c.p. aft of apex	4.8.3.2
$(x_{c.p.})_{\Delta}$	value of parameter for thin, pointed-nose delta wing	4.8.3.2
$\Delta(x_{c.p.})_B$	shift in thin delta wing c.p. due to nose blunting	4.8.3.2
$\Delta(x_{c.p.})_t$	shift in pointed-nose delta wing c.p. due to wing thickness	4.8.3.2
x_m	axial distance from the body nose to the chosen moment center	4.8.3.2
$\bar{z}_{base}$	vertical distance, measured normal to the body horizontal plane, between the centroid of the base area and the body horizontal plane, positive as shown in figure 4.8-12	4.8.1.1
Z	normal-force non-linearity parameter	4.8.1.2
α	angle of attack, positive nose up	4.8.1.1
α_{N_0}	angle of attack at zero normal force	4.8.1.1 4.8.3.1
α'	angle of attack measured from zero-normal-force reference plane, $\alpha - \alpha_{N_0}$ (see figure 4.8-12)	4.8.1.1 4.8.2.2 4.8.3.2
α_0	angle of attack at zero lift	4.8.1.1
$\delta_{\perp}$	total wedge angle of sharp-leading-edged wing, perpendicular to leading edge at $c_r/3$ from nose (see figure 4.8.1.2-11a)	4.8.1.2
$\delta_{e_{\perp}}$	effective wedge angle of sharp-leading-edged wing, perpendicular to leading edge at $c_r/3$ from nose (see figure 4.8.1.2-11a)	4.8.1.2
$\delta_{L_{\perp}}$	average lower-surface angle of sharp leading-edged wing, perpendicular to wing leading edge at $c_r/3$ from nose (see figure 4.8.1.2-11a)	4.8.1.2
δ_L	lower-surface angle of round-leading-edged wing, perpendicular to wing leading edge at $c_r/3$ from nose (see figure 4.8.1.2-11b)	4.8.1.2
θ	wing semiapex angle	4.8.3.2

SYMBOL	DEFINITION	SECTION
Λ_{LE}	sweepback angle of wing leading edge	4.8.1.2 4.8.2.2 4.8.3.2
λ	taper ratio, $\frac{\text{tip chord}}{\text{root chord}}$	4.8.1.2 4.8.2.2 4.8.3.2
C_D	drag coefficient, $\frac{\text{drag}}{qS}$	4.8.1.1
C_f	skin-friction coefficient for incompressible flow	4.8.2.1
ΔC_f	increment in skin-friction coefficient for incompressible flow	4.8.2.1
C_L	lift coefficient, $\frac{\text{lift}}{qS}$	4.8.1.1
C_m	pitching-moment coefficient, $\frac{\text{pitching moment}}{qS\,c_r}$	4.8.3.2
$C_{m_{N_0}}$	pitching-moment coefficient at zero normal force	4.8.3.1 4.8.3.2
C_N	normal-force coefficient, $\frac{N}{qS}$, for a symmetrical configuration	4.8.1.1
$C_{N'}$	normal-force coefficient, $\frac{N'}{qS}$, for an unsymmetrical configuration	4.8.1.1 4.8.1.2 4.8.2.2 4.8.3.2
$(C_{N'})_{20}$	value of coefficient at $\alpha' = 20^\circ$	4.8.1.2
$\left(C_{N'_{calc}}\right)_{20}$	calculated value of coefficient at $\alpha' = 20^\circ$	4.8.1.2
$\left[\frac{C_{N'}}{C_{N'_{calc}}}\right]_{20}$	normal-force-coefficient correlation factor	4.8.1.2
$\left[(C_{N'})_{20}\right]_t$	value of $(C_{N'})_{20}$ corrected for rounded leading edges	4.8.1.2
$\left(C_{N_\alpha}\right)'$	rate of change of normal-force coefficient with angle of attack $\frac{dC_{N'}}{d\alpha'}$	4.8.1.2

SYMBOL	DEFINITION	SECTION
$\left(C_{N_\alpha}\right)'_{N_0}$	value of derivative at zero normal force	4.8.1.2
$\left(C_{N_{\alpha_{calc}}}\right)'_{N_0}$	calculated value of the derivative	4.8.1.2
$\left[\frac{C_{N_\alpha}}{C_{N_{\alpha_{calc}}}}\right]'_{N_0}$	normal-force-curve-slope correlation factor	4.8.1.2
C_{p_b}	base pressure coefficient, $\frac{p_b - p_\infty}{q_\infty}$	4.8.2.1 4.8.2.2
$C_{p_{b_{N_0}}}$	value of coefficient at zero normal force	4.8.2.1 4.8.2.2
$\left(C_{p_b}\right)_{\alpha'}$	value of coefficient at given angle of attack, α'	4.8.2.2
$C_{p_{b_{20}}}$	value of coefficient at $\alpha' = 20^\circ$	4.8.2.2
$\frac{C_{p_{b_{20}}}}{C_{p_{b_{N_0}}}}$	pressure-coefficient-ratio correlation factor	4.8.2.2
C_X	axial-force coefficient, $\frac{X}{qS}$, for a symmetrical configuration	4.8.1.1
$C_{X'}$	axial-force coefficient, $\frac{X'}{qS}$, for an unsymmetrical configuration	4.8.2.2
$\left(C_{X'}\right)_{N_0}$	value of coefficient at zero normal force	4.8.2.1 4.8.2.2
$\Delta C_{X'}$	increment in coefficient due to angle of attack	4.8.2.2
$\Delta C_{X'_{calc}}$	calculated value of the increment	4.8.2.2
$\left[\frac{\Delta C_{X'}}{\Delta C_{X'_{calc}}}\right]_{20}$	axial-force correlation factor at $\alpha' = 20^\circ$	4.8.2.2

SYMBOL	DEFINITION	SECTION
$\Delta C_{X'_b}$	increment in coefficient due to base pressure	4.8.2.1 4.8.2.2
$\Delta C_{X'_{b_{N_0}}}$	value of increment at zero normal force	4.8.2.1
$\left(\Delta C_{X_{b_\alpha}}\right)'$	value of increment at a given angle of attack, α'	4.8.2.2
$\Delta C_{X'_f}$	increment in coefficient due to skin friction	4.8.2.1
$\Delta C_{X'_{f_{N_0}}}$	value of increment at zero normal force	4.8.2.1

REFERENCES

1. Mantz, K., Seager, D. B., and Ross, R.: Tests to Determine Subsonic Aerodynamic Characteristics of Hypersonic Re-Entry Configurations. ASD-TR-61-485, Supplement 1, 1963. (U)
2. Mantz, K., Seager, D. B., and Ross, R.: Tests to Determine Subsonic Pressures, Forces and Moments Acting on a Hypersonic Re-Entry Configuration. ASD-TDR-62-270, Supplement 1, 1963. (U)
3. Mugler, J. P., Jr., and Olstad, W. B.: Static Longitudinal Aerodynamic Characteristics at Transonic Speeds of a Blunted Right Triangular Pyramidal Lifting Re-Entry Configuration for Angles of Attack up to 110°. NASA TN D-797, 1961. (U)
4. Ware, G. M.: Low-Subsonic-Speed Static Stability of Right-Triangular-Pyramid and Half-Cone Lifting Re-Entry Configurations. NASA TN D-646, 1961. (U)
5. Paulson, J. W.: Low-Speed Static Stability and Control Characteristics of a Model of a Right Triangular Pyramid Re-Entry Configuration. NASA Memo 4-11-59L, 1959. (U)
6. Olstad, W. B., Mugler, J. P., Jr., and Cahn, M. S.: Static Longitudinal and Lateral Stability Characteristics of a Right Triangular Pyramidal Lifting Re-Entry Configuration at Transonic Speeds. NASA TN D-655, 1961. (U)
7. Paulson, J. W., and Shanks, R. E.: Investigation of Low-Subsonic Flight Characteristics of a Model of a Hypersonic Boost-Glide Configuration Having a 78° Delta Wing. NASA TN D-894, 1961. (U)
8. Boisseau, P. C.: Investigation of the Low-Subsonic Flight Characteristics of a Model of a Re-Entry Vehicle with a Thick Flat 75° Swept Delta Wing and a Half-Cone Fuselage. NASA TN D-1007, 1962. (U)
9. Shanks, R. E.: Investigation of the Low-Subsonic Flight Characteristics of a Model of an All-Wing Hypersonic Boost-Glide Configuration Having Very High Sweep. NASA TN D-369, 1960. (U)

TABLE 4.8-A
CONFIGURATION SKETCHES

Ref.	Configuration	Sketch
1	D-1	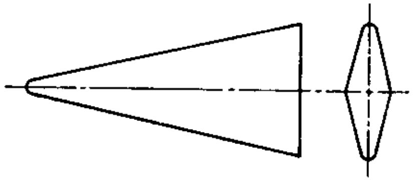
1	D-2	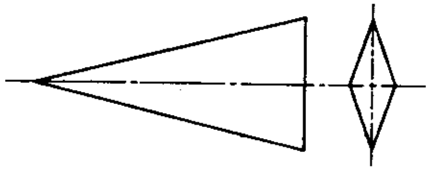
1	D-3	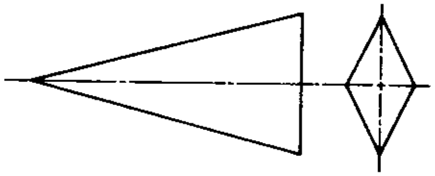
1	D-4	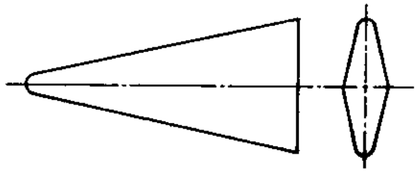
1	D-5	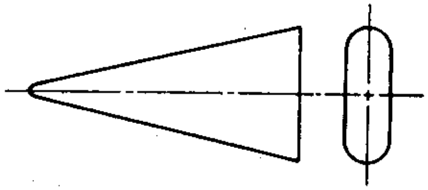
1	D-6	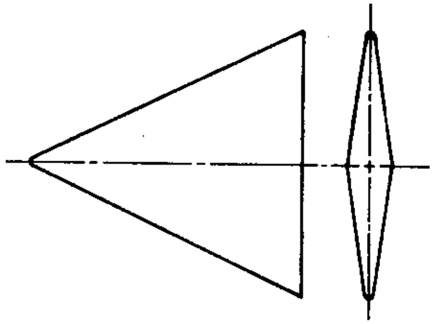
1	D-7	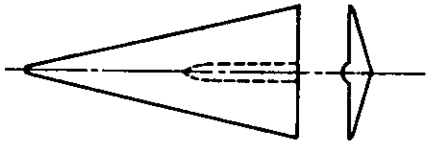
1	D-8	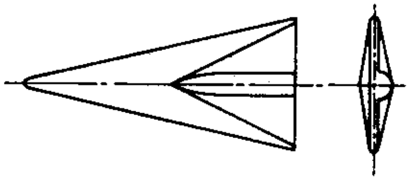

TABLE 4.8-A (CONTD)

Ref.	Configuration	Sketch
1	D-9	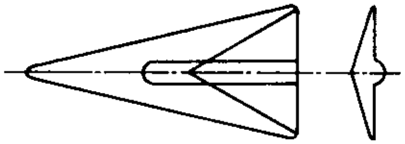
1	D-10	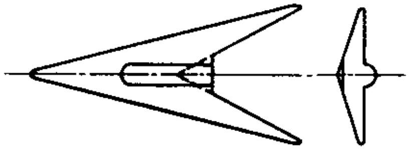
2	D-50	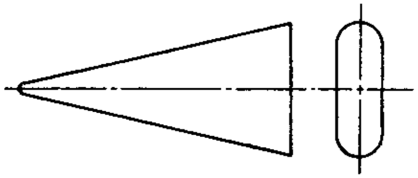
3	Blunted Right Triangular Pyramid	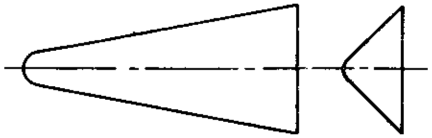
4	a	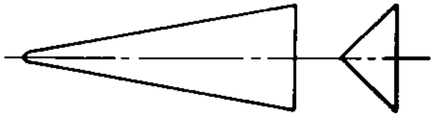
4	b (basic)	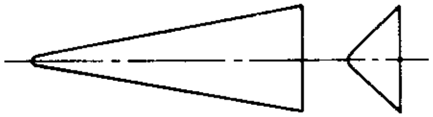
4	c (basic)	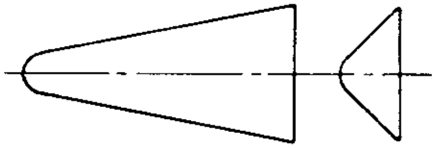
4	c (extended nose)	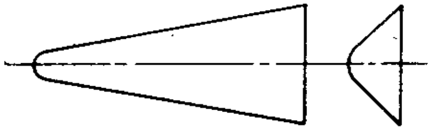
4	d	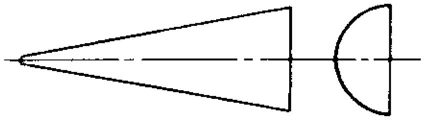
5	Right Triangular Pyramid	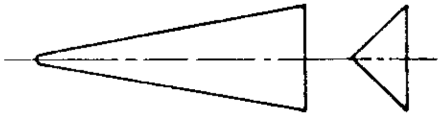

TABLE 4.8-A (CONTD)

Ref.	Configuration	Sketch
6	1	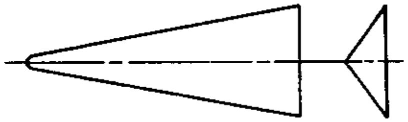
1	WB-1	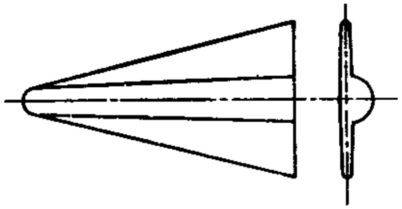
1	WB-2	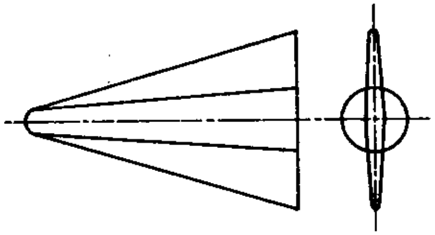
1	WB-3	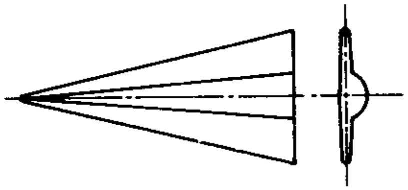
1	WB-4	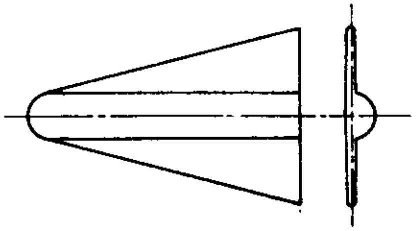
1	WB-5	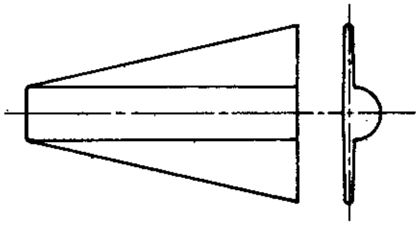
1	WB-6	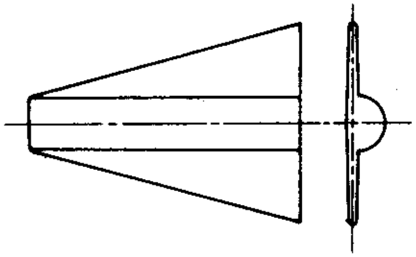
1	WB-7	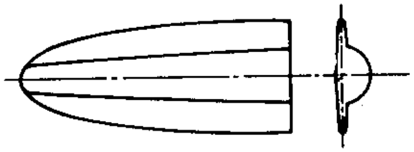

TABLE 4.8-A (CONTD)

Ref.	Configuration	Sketch
1	WB-8	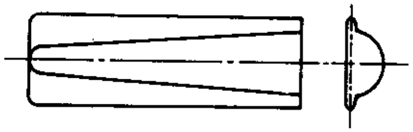
1	WB-9	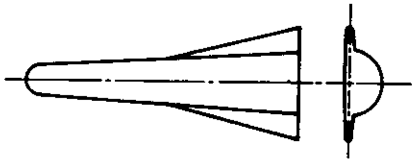
1	WB-10 (0)	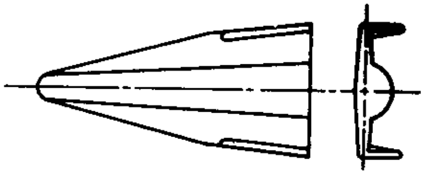
1	R-2	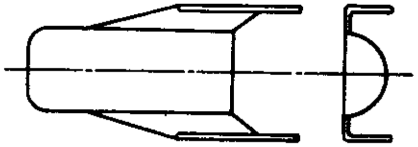
1	R-3	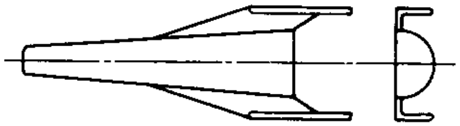
7	Delta Wing Boost-Glide	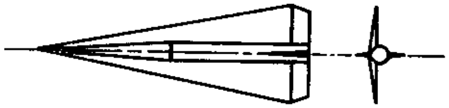
8	Delta Wing With Half-Cone Fuselage	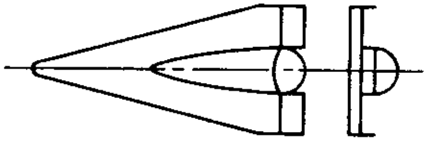
9	All-Wing Boost-Glide	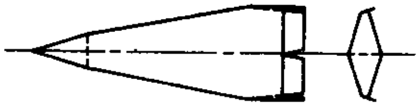

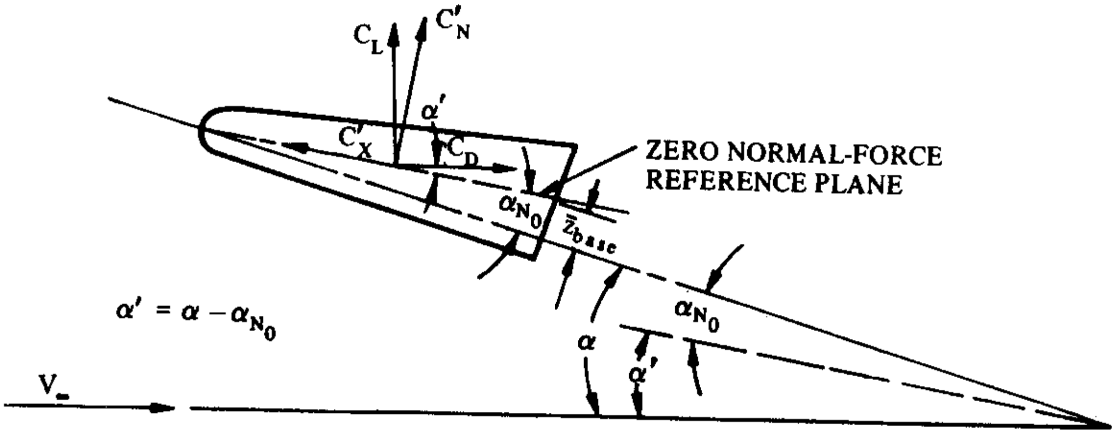

FIGURE 4.8-12 DEFINITION OF REFERENCE-AXIS SYSTEM

4.8.1 WING, WING-BODY NORMAL FORCE

4.8.1.1 WING, WING-BODY ZERO-NORMAL-FORCE ANGLE OF ATTACK

The longitudinal data for the low-aspect-ratio configurations are presented in terms of the normal-force and axial-force coefficients of a normal-force axis system rather than the more common lift and drag coefficients of the lift axis system. The problem arising with the normal-force axis system is that of defining a reference plane for the nonsymmetrical configurations which specifies the direction of the normal force and axial force. This is accomplished by defining a reference axis system which is oriented with respect to the particular configuration so that the normal force is zero at zero angle of attack.

The defined normal-force axis system is illustrated in figure 4.8-12. The normal-force coefficient $C_{N'}$ is perpendicular to and the axial-force coefficient $C_{X'}$ is parallel to a reference plane which passes through the centroid of the base area and the most forward point on the vehicle nose. For symmetrical configurations this is the plane of symmetry.

The zero-normal-force angle of attack α_{N_0} is defined as the angle of attack at which the normal force acting on the body is zero. For a symmetrical configuration, the normal force is zero when the plane of symmetry is parallel to the free stream. Therefore, for symmetrical configurations $\alpha_{N_0} = 0$. For unsymmetrical configurations, α_{N_0} may be related to an arbitrary plane as shown in figure 4.8-12. This arbitrary reference plane is chosen so that its inclination to the free stream defines the angle of attack in the familiar lift axis system. It is referred to as the body horizontal plane.

From the geometry of figure 4.8-12, the angle of attack α' in the defined normal-force axis system is

$$\alpha' = \alpha - \alpha_{N_0} \qquad \text{4.8.1.1-a}$$

where

α is the angle of attack, positive nose-up, measured from the free stream to the body horizontal axis.

α_{N_0} is the zero-normal-force angle of attack, measured between the reference plane and the body horizontal plane, positive as shown in figure 4.8-12.

DATCOM METHOD

The zero-normal-force angle of attack is determined from the configuration geometry as follows:

Step 1. Determine the location of the centroid of the base area and the location of the most forward point on the vehicle nose.

Step 2. Determine α_{N_0} as the angle between the line connecting the centroid of the base and the most forward point on the nose, and the horizontal plane of the body.

Values of the zero-normal-force angle of attack calculated by using this method are compared with test results in table 4.8.1.1-A. Many of the configurations tested were complex re-entry shapes, and the reader should refer to table 4.8-A for a more complete description of the model. Unfortunately, there are not enough data available to illustrate a consistent effect of planform geometry on the zero-normal-force angle of attack.

Sample Problems

1. Given: The right-triangular pyramidal body designated as configuration 1 of reference 6.

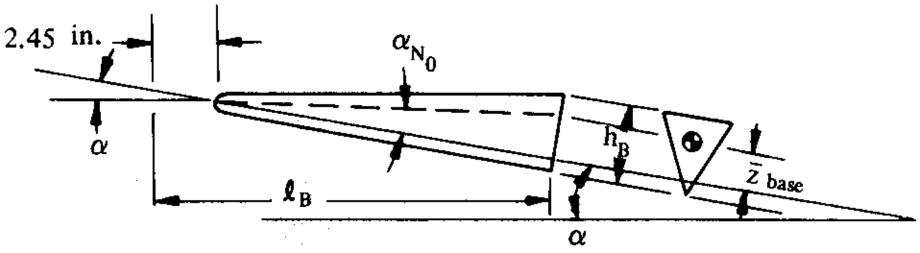

ℓ_B = 31.55 in. Nose radius = 0.1875 in. h_b = 6.44 in.

Compute:

Centroid of base

$$\bar{z}_{base} = \frac{2}{3} h_b - \text{nose radius} = \frac{2}{3}(6.44) - 0.1875 = 4.106 \text{ in.}$$

Solution:

$$\alpha_{N_0} = \tan^{-1} \frac{\bar{z}_{base}}{\ell_B - 2.45} = \tan^{-1} \frac{4.106}{31.55 - 2.45} = \tan^{-1} 0.1412$$

$$= 8.04^{\circ}$$

This compares with a test value of $\alpha_{N_0} = 8.6^{\circ}$ from reference 6.

2. Given: A re-entry configuration of the wing-body group of reference 1 designated WB-10(0). This is a round-nosed, wing-body model of 75° sweep back with a semicircular-body cross section at the point of maximum thickness and with twin vertical tails.

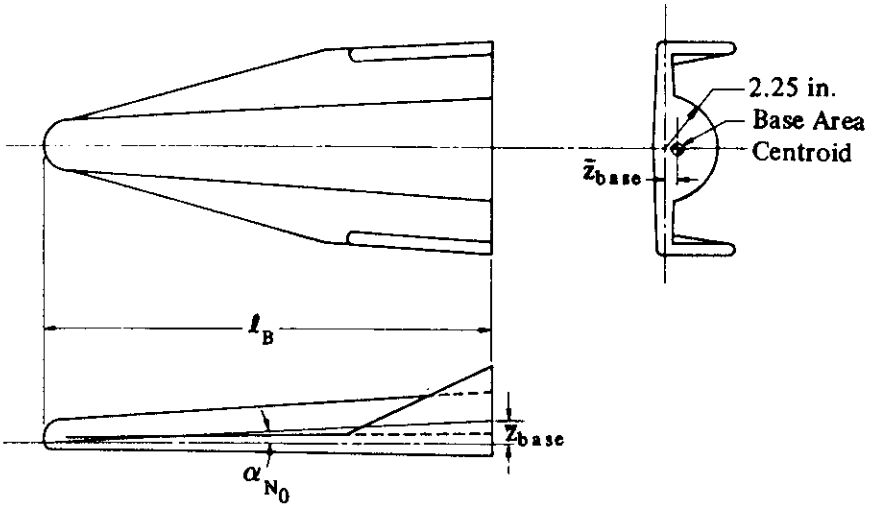

$\ell_B = 20.0$ in. $\bar{z}_{base} = 0.68$ in.

Solution:

$$\alpha_{N_0} = \tan^{-1} \frac{\bar{z}_{base}}{\ell_B} = \tan^{-1} \frac{0.68}{20.0} = \tan^{-1} 0.0340$$

$$= 1.95^{\circ}$$

This compares with a test value of $\alpha_{N_0} = 0.30^{\circ}$ from reference 1.

REFERENCES

1. Mantz, K., Seeger, D. B., and Ross, R.: Tests to Determine Subsonic Aerodynamic Characteristics of Hypersonic Re-Entry Configurations. ASD-TR-61-485, Supplement 1, 1963. (U)

2. Mantz, K., Seeger, D. B., and Ross, R.: Tests to Determine Subsonic Pressures, Forces and Moments Acting on a Hypersonic Re-Entry Configuration. ASD:–TDR-62-270, Supplement 1, 1963. (U)

3. Paulson, J. W.: Low-Speed Static Stability and Control Characteristics of a Right Triangular Pyramid Re-Entry Configuration. NASA Memo 4-11-59L, 1959. (U)

4. Boisseau, P. C.: Investigation of the Low-Subsonic Flight Characteristics of a Model of a Re-Entry Vehicle with a Thick Flat 75° Swept Delta Wing and a Half-Cone Fuselage. NASA TN D-1007, 1962. (U)

5. Ware, G. M.: Low-Subsonic-Speed Static Stability of Right-Triangular-Pyramid and Half-Cone Lifting Re-Entry Configurations. NASA TN D-646, 1961. (U)

6. Olstad, W. B., Mugler, J. P., Jr., and Cahn, M. S.: Static Longitudinal and Lateral Stability Characteristics of a Right Triangular Pyramidal Lifting Re-Entry Configuration at Transonic Speeds. NASA TN D-655, 1961. (U)

7. Mugler, J. P., Jr., and Olstad, W. B.: Static Longitudinal Aerodynamic Characteristics at Transonic Speeds of a Blunted Right Triangular Pyramidal Lifting Re-Entry Configuration for Angles of Attack up to 110°. NASA TN D-797, 1961. (U)

8. Paulson, J. W., and Shanks, R. E.: Investigation of Low-Subsonic Flight Characteristics of a Model of a Hypersonic Boost-Glide Configuration Having a 78° Delta Wing. NASA TN D-894, 1961. (U)

9. Wright Air Development Division: Unpublished data from the 5-foot wind tunnel, 1961. (U)

10. Seeger, D. B., and Meyer, J. E.: An Investigation of the Subsonic Aerodynamic Characteristics and the Landing Flare Maneuver for Hypersonic Re-Entry Configurations. ASD-TDR-62-271, 1962. (C) Title Unclassified

11. Shanks, R. E.: Investigation of the Low-Subsonic Flight Characteristics of a Model of an All-Wing Hypersonic Boost-Glide Configuration Having Very High Sweep. NASA TN D-369, 1960. (U)

TABLE 4.8.1.1-A

SUBSONIC ZERO-NORMAL-FORCE ANGLE OF ATTACK

DATA SUMMARY

Ref.	Configuration	α_{N_0} (deg) Calc.	α_{N_0} (deg) Test	$\Delta\alpha_{N_0}$ (deg) Calc.-Test
1	D-7	-2.15	-2.5	0.35
	D-8	0.20	-0.20	0.40
	D-9	0	2.50	-2.50
	D-10	-1.45	-1.60	0.15
	WB-1	1.35	1.00	0.35
	WB-3	1.46	1.70	-0.24
	WB-4	1.35	-0.30	1.65
	WB-5	1.21	0.70	0.51
	WB-6	1.21	0.70	0.51
	WB-7	1.63	1.20	0.43
	WB-8	1.57	0.90	0.67
	WB-9	2.12	1.90	0.32
	WB-10(0)	1.95	0.30	1.65
	R-2	3.79	2.30	1.49
	R-3	2.62	2.00	0.62
3	Rt. triangular pyramid	7.40	5.20	2.20
4	Delta wing w/half-cone fuselage	0.66	0.40	0.26
5	a	7.23	5.50	1.73
	b (basic)	6.44	6.50	-0.06
	c (basic)	7.15	10.20	-3.05
	d	4.40	4.60	-0.20
6	Rt. triangular pyramid	8.04	8.60	-0.56
7	Blunted right triangular pyramid	6.91	6.30	0.61
8	Delta-wing boost-glide	-0.20	0.60	-0.80
9	W-II E-3	-1.80	-2.00	0.20
	W-III E-3	2.40	1.80	0.60

4.8.1.2 WING, WING-BODY NORMAL-FORCE VARIATION WITH ANGLE OF ATTACK

A. SUBSONIC

This section presents a method for estimating the normal-force variation with angle of attack for a delta- or modified-delta-planform re-entry configuration at subsonic speeds.

The subsonic normal-force characteristics of thin delta wings at small angles of attack can be satisfactorily predicted through the use of linearized theory, which assumes that the flow is unseparated and that the cross-flow components are negligible. At higher angles ($\alpha > 5^{\circ}$, approximately) both cross-flow and separation phenomena become important and these assumptions are no longer valid. The normal force tends to increase more rapidly with angle of attack as the angle is increased.

A major factor influencing the normal-force characteristics of delta wings is leading-edge geometry. Sharp leading edges influence relatively large amounts of air and the corresponding variation of the normal force with angle of attack tends to be high. Rounded leading edges affect a smaller amount of air and the normal-force-curve slope is consequently less.

The method presented herein is taken from reference 1, and is based on a study of test data on low-aspect-ratio delta wings with thick and thin surfaces, with sharp and rounded leading edges, and with varying degrees of nose bluntness. Thin, sharp-leading-edged delta wings were selected as "reference wings," and theoretical relationships were written for the normal-force characteristics of these planforms. The normal-force characteristics of all the test configurations were then calculated by using these "reference wing" relationships, and any deviation between the calculated and the test values was related to the geometry of the wing leading edge. It was found that satisfactory correlation could be obtained by relating the deviation in normal-force characteristics to the leading-edge geometry in a plane normal to the wing leading edge and located one-third the length of the root chord aft of the nose.

Design charts are presented for estimating the normal-force-curve slope at $C_N' = 0$, the value of C_N' at $\alpha' = 20^{\circ}$, and the characteristics of the normal-force variation with angle of attack. The correlation parameters used to develop these charts are leading-edge radius and leading-edge angle for round and sharp leading edges, respectively. It should be noted that as the leading-edge radius approaches zero, the normal-force-curve slope at $C_N' = 0$, the normal force at $\alpha' = 20^{\circ}$, and the normal-force-variation parameter all approach the respective values for a sharp leading edge. Therefore, a configuration with a small leading-edge radius can be analyzed as one having a sharp leading edge.

For configurations with round leading edges, an empirical correction factor is presented to account for the reduction in normal force at higher angles of attack as the wing thickness is increased. This separate correlation is required, since the limited number of test data for very thick delta wings does not correlate well with the thin wing results.

DATCOM METHOD

The normal-force variation with angle of attack for a delta or modified-delta configuration at low speeds, based on the reference area (usually the planform area), is obtained from the procedure outlined in the following steps:

Step 1. Determine the effective leading edge angle. $\delta_{e_\perp}$ for sharp leading edges or the effective leading-edge radius $R_{\frac{1}{3}LE}$ and lower surface angle δ_L for round leading edges. These parameters are functions of the configuration geometry in a plane normal to the leading edge at $\frac{1}{3} c_r$ from the nose. The applicable configuration geometry is illustrated on figures 4.8.1.2-11a and 4.8.1.2-11b.

Step 2. Determine the normal-force-curve slope at zero normal force ($C_{N'} = 0$) by

$$\left(C_{N_\alpha}\right)'_{N_0} = \left(\frac{C_{N_\alpha}}{C_{N_{\alpha_{calc}}}}\right)'_{N_0} \left(C_{N_{\alpha_{calc}}}\right)'_{N_0} \quad \text{(per radian)} \qquad 4.8.1.2\text{-a}$$

where

$\left(C_{N_\alpha}\right)'_{N_0}$ is the normal-force-curve slope at zero normal force $\left(\frac{\partial C_{N'}}{\partial \alpha'}\right)_{N_0}$

$\left[\frac{C_{N_\alpha}}{C_{N_{\alpha_{calc}}}}\right]'_{N_0}$ is the empirical correlation factor of normal-force-curve slope for delta or modified-delta configurations. It is presented as a function of the effective leading-edge angle for configurations with sharp leading edges in figure 4.8.1.2-12a, and as a function of the effective leading-edge radius for configurations with round leading edges in figure 4.8.1.2-12b.

$\left(C_{N_{\alpha_{calc}}}\right)'_{N_0}$ is the calculated normal-force-curve slope at zero normal force, given by

$$\left(C_{N_{\alpha_{calc}}}\right)'_{N_0} = \left(\frac{\pi A}{2} + 2\frac{S_F}{S_{ref}}\right)\frac{4}{4 + A} \quad \text{(per radian)} \qquad 4.8.1.2\text{-b}$$

where

S_{ref} is the reference area.

S_F is the projected frontal area perpendicular to the zero-normal-force reference plane (projected frontal area at $C_{N'} = 0$).

A is the aspect ratio of the surface.

Step 3. Determine the normal-force coefficient at $\alpha' = 20^\circ$ by

$$\left(C_{N'}\right)_{20} = \left[\frac{C_{N'}}{C_{N'_{calc}}}\right]_{20} \left(C_{N'_{calc}}\right)_{20} \qquad 4.8.1.2\text{-c}$$

where

$\left(C_{N'}\right)_{20}$ is the normal-force coefficient at $\alpha' = 20^\circ$.

$\left[\frac{C_{N'}}{C_{N'_{calc}}}\right]_{20}$ is the empirical correlation factor of the normal force for delta and modified-delta configurations. It is presented as a function of the effective leading-edge angle for configurations with sharp leading edges in figure 4.8.1.2-13a, and as a function of the effective leading-edge radius for configurations with round leading edges in figure 4.8.1.2-13b.

$\left(C_{N'_{calc}}\right)_{20}$ is the calculated normal force at $\alpha' = 20^\circ$, given by

$$\left(C_{N'_{calc}}\right)_{20} = 2.195 \left(\frac{A + 0.61}{A + 4.0}\right) \qquad 4.8.1.2\text{-d}$$

Step 4.* Determine the thickness correction to the normal force at $\alpha' = 20^\circ$ for configurations with round leading edges by

$$\left[\left(C_{N'}\right)_{20}\right]_t = \left(\frac{1 + \cos \delta_L}{2}\right) \left(C_{N'}\right)_{20} \qquad 4.8.1.2\text{-e}$$

where δ_L is the lower surface angle from step 1 and $\left(C_{N'}\right)_{20}$ is obtained from step 3.

Step 5. Determine Z, the empirical, nonlinear-normal-force correction factor. This parameter is obtained as a function of the effective leading-edge angle or the effective leading-edge radius for configurations with sharp leading edges or round leading edges, respectively, from figure 4.8.1.2-14.

Step 6. The variation of the normal force with angle of attack is given by:

For round-leading-edged configurations

$$C_{N'} = \left(C_{N_\alpha}\right)'_{N_0} \alpha' + 8.21 \left\{ \left[\left(C_{N'}\right)_{20}\right]_t - 0.349 \left(C_{N_\alpha}\right)'_{N_0} \right\} \left[Z + 2.81(1 - Z)\alpha'\right] \alpha'^2$$

4.8.1.2-f

---

*Step 4 is required only for configurations with round leading edges. For sharp-leading-edged configurations, go to step 5.

For sharp-leading-edged configurations the normal-force coefficient at $\alpha' = 20^\circ$ from step 3 $\left(C_N'\right)_{20}$ is used instead of the term $\left[\left(C_N'\right)_{20}\right]_t$ in the above equation.

α' in the above relation is in radians.

A comparison of the normal-force variation with angle of attack calculated by this method with test results is presented as table 4.8.1.2-A. The Reynolds-number range of the test data is not sufficient to allow analysis of the effect of Reynolds number on the normal force. However, over the angle-of-attack range of this method ($\alpha' \leqslant 20^\circ$), Reynolds-number effects should be negligible even for the thicker configurations.

Sample Problems

1. Round Leading Edge

Given: A delta model with a symmetrical diamond cross section and a blunt trailing edge. This is model D-6 of reference 6.

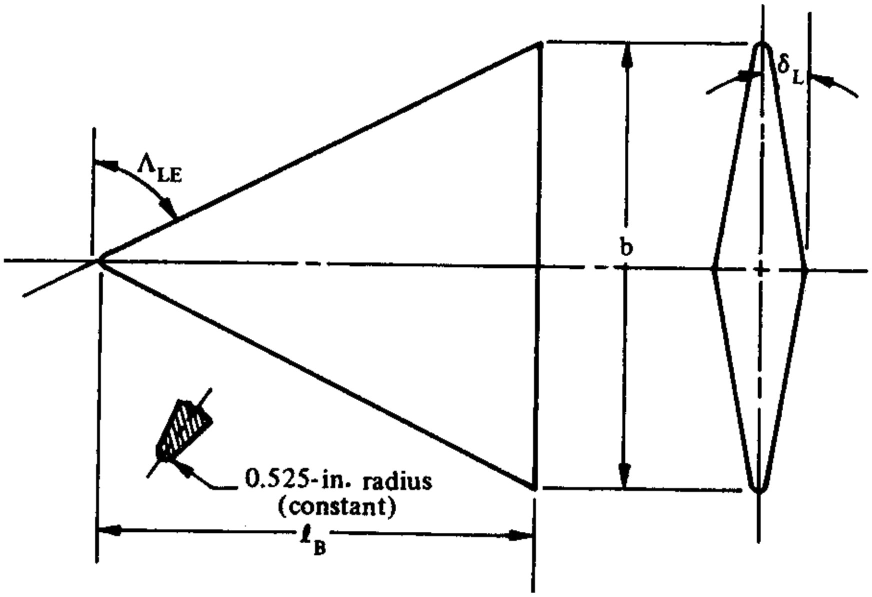

$A = 1.868$ $\quad b = 22.116$ in. $\quad S_{ref} = S = 261.95$ sq in. $\quad \Lambda_{LE} = 65^\circ$

$S_F = 57.42$ sq in. (base area) $\quad \delta_L = 9^\circ$ $\quad R_{\frac{1}{3}LE} = 0.525$ in.

Compute:

Determine the normal-force-curve slope at $C_N' = 0$

$$R_{\frac{1}{3}LE}/b = 0.525/22.116 = 0.0237$$

$$\left[\frac{C_{N_\alpha}}{C_{N_{\alpha_{calc}}}}\right]'_{N_0} = 0.982 \quad \text{(figure 4.8.1.2-12b)}$$

$$\left(C_{N_{\alpha_{calc}}}\right)'_{N_0} = \left(\frac{\pi A}{2} + 2\frac{S_F}{S_{ref}}\right)\frac{4}{4+A} \qquad \text{(equation 4.8.1.2-b)}$$

$$= \left[\frac{\pi(1.868)}{2} + 2\,\frac{57.42}{261.95}\right]\frac{4}{4+1.868}$$

$$= 2.30 \text{ per rad}$$

$$\left(C_N\right)'_{N_0} = \left[\frac{C_{N_\alpha}}{C_{N_{\alpha_{calc}}}}\right]_{N_0} \left(C_{N_{\alpha_{calc}}}\right)'_{N_0} \qquad \text{(equation 4.8.1.2-a)}$$

$$= (0.982)\,(2.30)$$

$$= 2.26 \text{ per rad}$$

Determine the normal-force coefficient at $\alpha' = 20^0$

$$\left[\frac{C_{N'}}{C_{N'_{calc}}}\right]_{20} = 0.935 \quad \text{(figure 4.8.1.2-13b)}$$

$$\left(C_{N'_{calc}}\right)_{20} = 2.195\left(\frac{A + 0.61}{A + 4.0}\right) \qquad \text{(equation 4.8.1.2-d)}$$

$$= 2.195\left(\frac{1.868 + 0.61}{1.868 + 4.0}\right)$$

$$= 0.927$$

$$(C_{N'})_{20} = \left[\frac{C_{N'}}{C_{N'_{calc}}}\right]_{20}\left(C_{N'_{calc}}\right)_{20} \qquad \text{(equation 4.8.1.2-c)}$$

$$= (0.935)\,(0.927)$$

$$= 0.867$$

Determine the thickness correction factor to the normal force at $\alpha' = 20^{\circ}$ (round leading edge)

$$\left[(C_{N}')_{20}\right]_{t} = \left(\frac{1 + \cos \delta_{L}}{2}\right) (C_{N}')_{20} \quad \text{(equation 4.8.1.2-e)}$$

$$= \left(\frac{1 + \cos 9^{\circ}}{2}\right) (0.867)$$

$$= 0.862$$

Determine the empirical, nonlinear-normal-force correction factor

$Z = 0.945$ (figure 4.8.1.2-14)

Solution:

$$C_{N}' = \left(C_{N_{\alpha}}\right)'_{N_0} \alpha' + 8.21 \left\{\left[(C_{N}')_{20}\right]_{t} - 0.349 \left(C_{N_{\alpha}}\right)'_{N_0}\right\} \left[Z + 2.81(1 - Z)\alpha'\right]\alpha'^{2}$$

(equation 4.8.1.2-f)

$$= 2.26\, \alpha' + 8.21 \left\{ 0.862 - 0.349(2.26) \right\} [0.945 + 2.81(1 - 0.945)\alpha']\alpha'^{2}$$

$$= 2.26\, \alpha' + 0.568\, \alpha'^{2} + 0.0930\, \alpha'^{3}$$

①	②	③	④	⑤	⑥	⑦	⑧
α' (deg)	α' (rad)	α'^{2} (rad^{2})	α'^{3} (rad^{3})	$2.26\,\alpha'$ 2.26 ②	$0.568\,\alpha'^{2}$ 0.568 ③	$0.0930\,\alpha'^{3}$ 0.0930 ④	C_{N}' (based on S) (eq. 4.8.1.2-f) ⑤ + ⑥ + ⑦
0	0	0	0	0	0	0	0
5	0.0873	0.00762	0.000665	0.1973	0.00433	0.00006	0.2017
10	0.1745	0.03045	0.005314	0.3944	0.01730	0.00049	0.4122
15	0.2618	0.06854	0.01794	0.5917	0.03893	0.001668	0.6323
20	0.3490	0.12180	0.04251	0.7887	0.06918	0.003953	0.8618

The calculated results are compared with test values from reference 6 in sketch (a) and in table 4.8.1.2-A.

2. Sharp Leading Edge

Given: A delta model with a symmetrical diamond cross section and a blunt trailing edge. This is model D-3 of reference 6.*

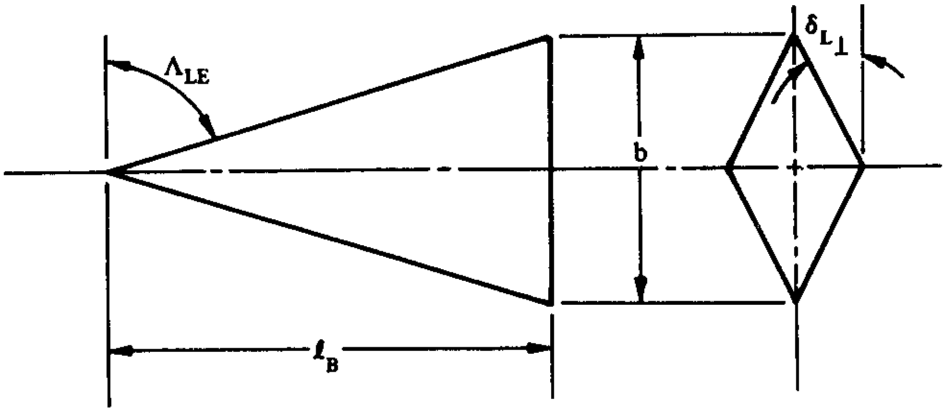

$A = 1.076$ $b = 12.374$ in. $S_{ref} = S = 142.30$ sq in. $\Lambda_{LE} = 75^o$

$S_F = 44.20$ sq in. (base area) $\delta_{L_\perp} = 30^o$ $\delta_\perp = 60^o$ $\delta_{e_\perp} = 90^o$

Compute:

Determine the normal-force-curve slope at $C_{N'} = 0$

$$\left[\frac{C_{N_\alpha}}{C_{N_{\alpha_{calc}}}}\right]'_{N_0} = 0.775 \quad \text{(figure 4.8.1.2-12a)}$$

$$\left(C_{N_{\alpha_{calc}}}\right)'_{N_0} = \left(\frac{\pi A}{2} + 2\frac{S_F}{S_{ref}}\right)\frac{4}{4 + A} \quad \text{(equation 4.8.1.2-b)}$$

$$= \left[\frac{\pi(1.076)}{2} + 2\,\frac{44.20}{142.30}\right]\frac{4}{4 + 1.076}$$

$$= 1.821 \text{ per rad}$$

$$\left(C_{N_\alpha}\right)'_{N_0} = \left[\frac{C_{N_\alpha}}{C_{N_{\alpha_{calc}}}}\right]'_{N_0} \left(C_{N_{\alpha_{calc}}}\right)'_{N_0} \quad \text{(equation 4.8.1.2-a)}$$

$$= (0.775)\,(1.821)$$

$$= 1.411 \text{ per rad}$$

---

*Although this model has a very small nose radius (0.032 in.), it is analyzed as having a sharp leading edge.

Determine the normal-force coefficient at $\alpha' = 20^{o}$

$$\left[\frac{C_{N'}}{C_{N'_{calc}}}\right]_{20} = 0.960 \quad \text{(figure 4.8.1.2-13a)}$$

$$\left(C_{N'_{calc}}\right)_{20} = 2.195 \left(\frac{A + 0.61}{A + 4.0}\right) \quad \text{(equation 4.8.1.2-d)}$$

$$= 2.195 \left(\frac{1.076 + 0.61}{1.076 + 4.0}\right)$$

$$= 0.7291$$

$$\left(C_{N'}\right)_{20} = \left[\frac{C_{N'}}{C_{N'_{calc}}}\right]_{20} \left(C_{N'_{calc}}\right)_{20} \quad \text{(equation 4.8.1.2-c)}$$

$$= (0.960)\,(0.7291) = 0.700$$

Determine the empirical, nonlinear-normal-force correction factor

$$Z = 0.972 \quad \text{(figure 4.8.1.2-14)}$$

Solution:

$$C_{N'} = \left(C_{N_\alpha}\right)'_{N_0} \alpha' + 8.21 \left\{ \left(C_{N'}\right)_{20} - 0.349 \left(C_{N_\alpha}\right)'_{N_0} \right\} \left[Z + 2.81(1 - Z)\, \alpha'\right] \alpha'^{\,2}$$

(equation 4.8.1.2-f, sharp leading edge)

$$= 1.411\ \alpha' + 8.21 \left\{ (0.700) - 0.349(1.411) \right\} \left[0.972 + 2.81(1 - 0.972)\, \alpha'\right] \alpha'^{\,2}$$

$$= 1.411\ \alpha' + 1.656\ \alpha'^{\,2} + 0.134\ \alpha'^{\,3}$$

①	②	③	④	⑤	⑥	⑦	⑧
α' (deg)	α' (rad)	α'^2 (rad^2)	α'^3 (rad^3)	$1.411\,\alpha'$ 1.411 ②	$1.656\,\alpha'^2$ 1.656 ③	$0.134\,\alpha'^3$ 0.134 ④	$C_{N'}$ (based on S) (eq. 4.8.1.2-f) ⑤ + ⑥ + ⑦
0	0	0	0	0	0	0	0
5	0.0873	0.00762	0.000665	0.1232	0.0126	0.00009	0.1359
10	0.1745	0.03045	0.005314	0.2462	0.0504	0.00071	0.2973
15	0.2618	0.06854	0.01794	0.3694	0.1135	0.00240	0.4853
20	0.3490	0.12180	0.04251	0.4924	0.2017	0.00570	0.6998

The calculated results are compared with test values from reference 6 in sketch (a) and in table 4.8.1.2-A.

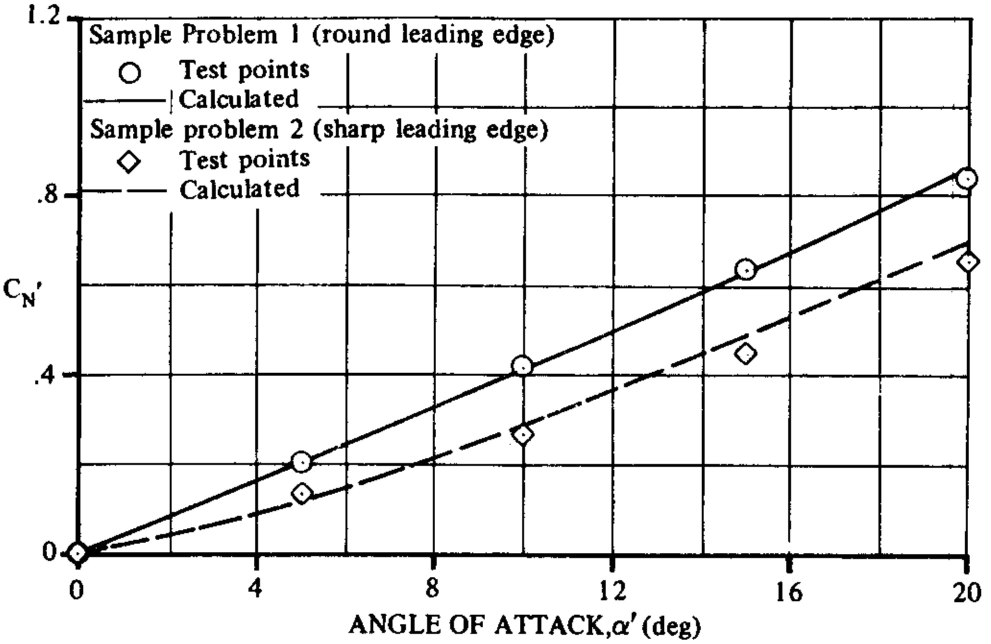

SKETCH (a)

REFERENCES

1. Seeger, D. B., and Meyer, J. E.: An Investigation of the Subsonic Aerodynamic Characteristics and the Landing Flare Maneuver for Hypersonic Re-Entry Configurations. ASD-TDR-62-271, 1962. (C) Title Unclassified

2. Jaquet, B. M., and Brewer, J. D.: Low-Speed Static-Stability and Rolling Characteristics of Low-Aspect-Ratio Wings of Triangular and Modified Triangular Planforms. NACA RM L8L29, 1949. (U)

3. Mugler, J. P., Jr., and Olstad, W. B.: Static Longitudinal Aerodynamic Characteristics at Transonic Speeds of a Blunted Right Triangular Pyramidal Lifting Re-Entry Configuration for Angles of Attack up to 110°. NASA TN D-797, 1961. (U)

4. Paulson, J. W., and Shanks, R. E.: Investigation of Low-Subsonic Flight Characteristics of a Model of a Hypersonic Boost-Glide Configuration Having a 78° Delta Wing. NASA TN D-894, 1961. (U)

5. Ware, G. M.: Low-Subsonic-Speed Static Stability of Right-Triangular-Pyramid and Half-Cone Lifting Re-Entry Configurations. NASA TN D-646, 1961. (U)

6. Mantz, K., Seeger, D. B., and Ross, R.: Tests to Determine Subsonic Aerodynamic Characteristics of Hypersonic Re-Entry Configurations. ASD-TR-61-485, Supplement 1, 1963. (U)

7. Mantz, K., Seeger, D. B., and Ross, R.: Tests to Determine Subsonic Pressures, Forces and Moments Acting on a Hypersonic Re-Entry Configuration. ASD-TDR-62-270, Supplement 1, 1963. (U)

8. Olstad, W. B., Mugler, J. P., Jr., and Cahn, M. S.: Static Longitudinal and Lateral Stability Characteristics of a Right Triangular Pyramidal Lifting Re-Entry Configuration at Transonic Speeds. NASA TN D-655, 1961. (U)

TABLE 4.8.1.2-A

SUBSONIC NORMAL-FORCE VARIATION WITH ANGLE OF ATTACK DELTA PLANFORM CONFIGURATIONS

Ref.	Configuration	A	Λ_{LE} (deg)	b (in.)	$\frac{S_E}{S_{ref}}$	Leading Edge	α' (deg)	C_N' Calc.	C_N' Test	e Percent Error
4	Hypersonic-boost-glide w/out tip cones	0.74	78.0	35.40	0.0497	Sharp	0	0	0	0
						$\delta_{e_\perp} = 26.4°$	5	0.119	0.118	0.8
							10	0.276	0.290	– 4.8
							15	0.471	0.500	– 5.8
							20	0.704	0.707	– 0.4
5	Half-cone cross section	0.783	79.50	21.10	0.307	Round	0	0	0	0
						$R_{\frac{1}{3}LE} = 0.05$ in.	5	0.111	0.098	13.3
						$\delta_L = 0$	10	0.226	0.214	5.6
							15	0.347	0.357	– 2.8
							20	0.476	0.512	– 7.0
6	D-2	1.076	75.0	12.374	0.188	Sharp*	0	0	0	0
						$\delta_{e_\perp} = 58°$	5	0.132	0.124	6.5
							10	0.319	0.303	5.3
							15	0.522	0.525	– 0.6
							20	0.774	0.778	– 0.5
	D-3	1.076	75.0	12.374	0.311	Sharp*	0	0	0	0
						$\delta_{e_\perp} = 90°$	5	0.133	0.116	14.6
							10	0.293	0.267	9.7
							15	0.481	0.445	8.1
							20	0.696	0.700	5.7
	D-6	1.868	65.0	22.116	0.219	Round	0	0	0	0
						$R_{\frac{1}{3}LE} = 0.525$ in.	5	0.202	0.202	0
							10	0.412	0.418	– 1.4
						$\delta_L = 9°$	15	0.630	0.635	– 0.8
							20	0.860	0.835	3.0
	D-5	1.076	75.0	13.13	0.329	Round	0	0	0	0
						$R_{\frac{1}{3}LE} = 1.05$ in.	5	0.128	0.135	– 5.2
							10	0.258	0.263	– 1.9
						$\delta_L = 0$	15	0.390	0.396	– 1.5
							20	0.526	0.535	– 1.7

*Model analyzed as having a sharp leading edge, although LER = 0.032 in.

$$\text{Average Error} = \frac{\Sigma|e|}{n} = 3.4\%$$

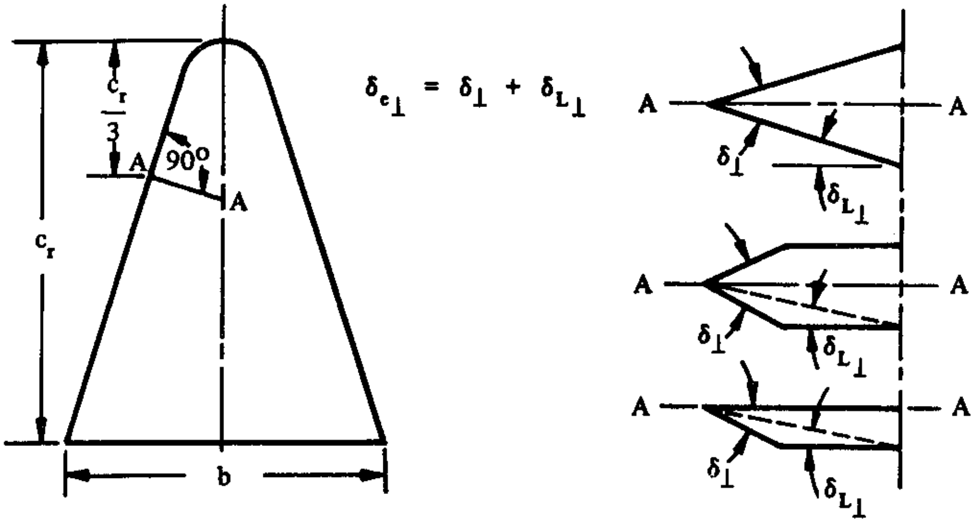

FIGURE 4.8.1.2-11a DEFINITION OF THE EFFECTIVE LEADING-EDGE ANGLE FOR DELTA AND MODIFIED-DELTA CONFIGURATIONS WITH SHARP LEADING EDGES

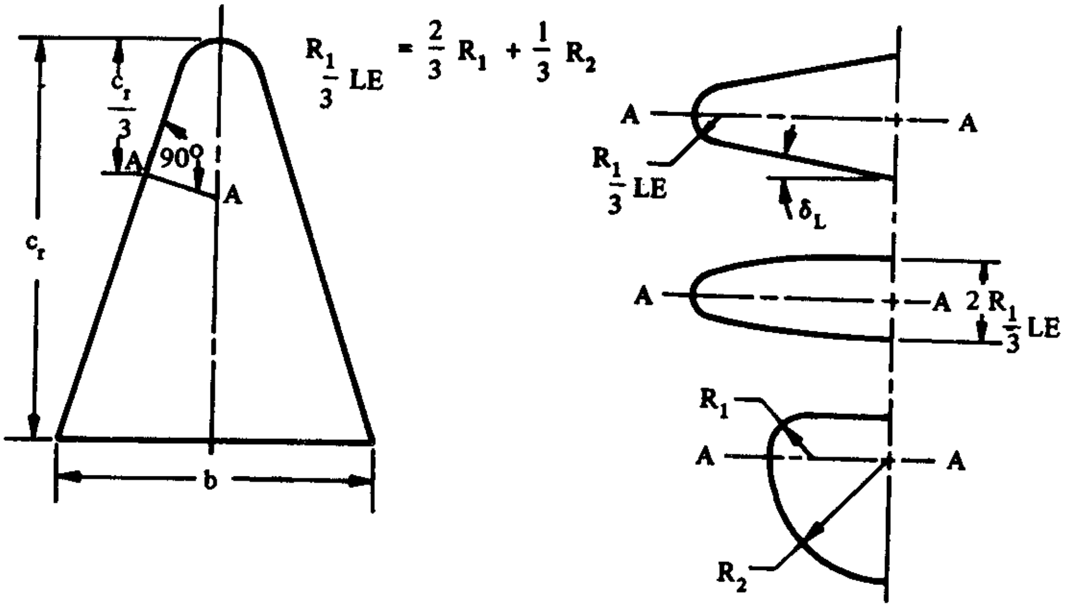

FIGURE 4.8.1.2-11b DEFINITION OF THE EFFECTIVE LEADING-EDGE RADIUS FOR DELTA AND MODIFIED-DELTA CONFIGURATIONS WITH ROUND LEADING EDGES

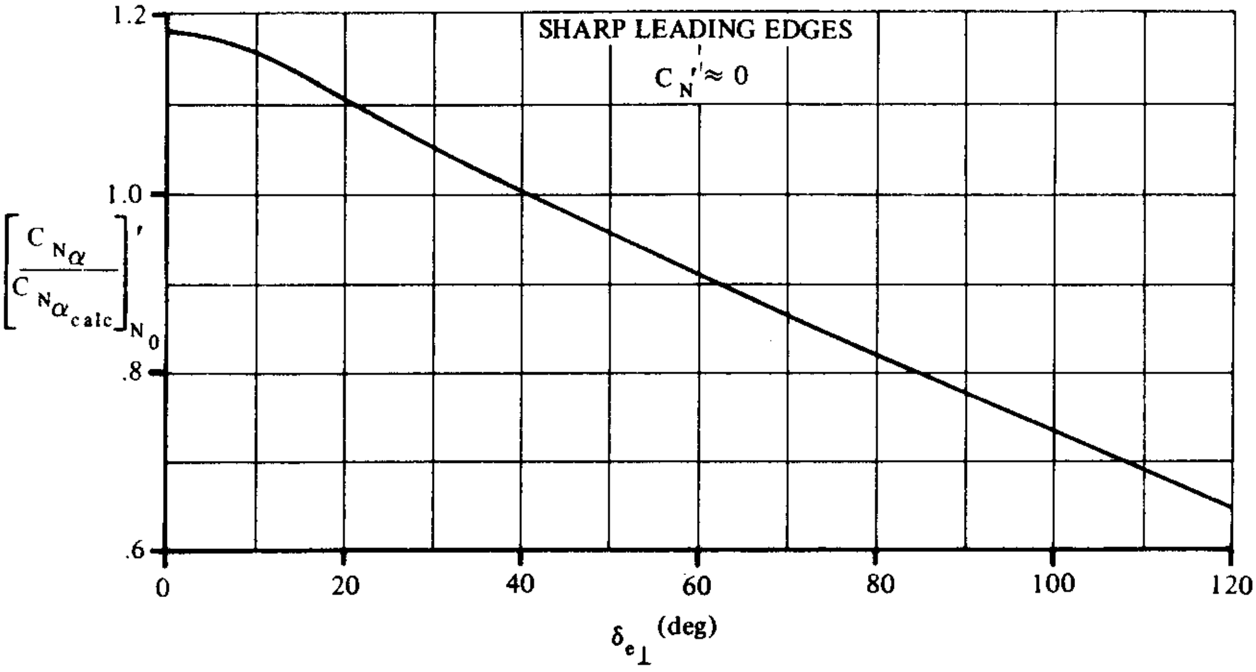

FIGURE 4.8.1.2-12a NORMAL-FORCE-CURVE-SLOPE CORRELATION FACTOR – DELTA AND MODIFIED-DELTA CONFIGURATIONS WITH SHARP LEADING EDGES

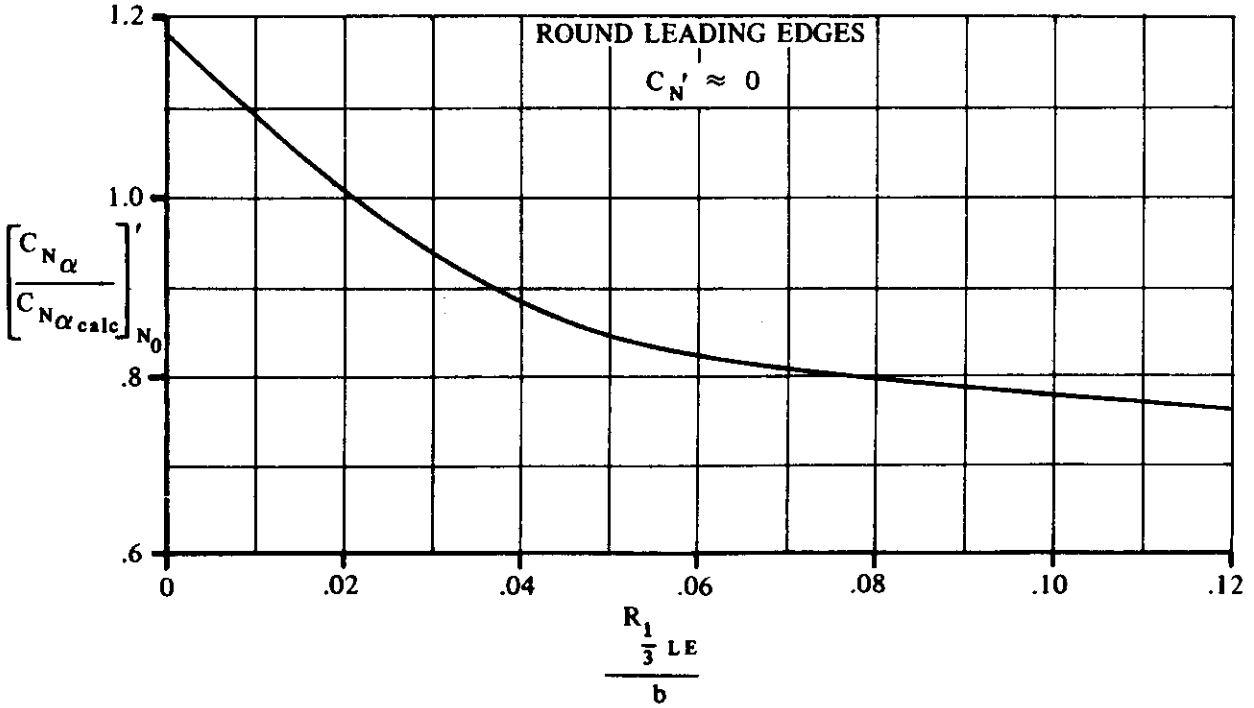

FIGURE 4.8.1.2-12b NORMAL-FORCE-CURVE-SLOPE CORRELATION FACTOR – DELTA AND MODIFIED-DELTA CONFIGURATIONS WITH ROUND LEADING EDGES

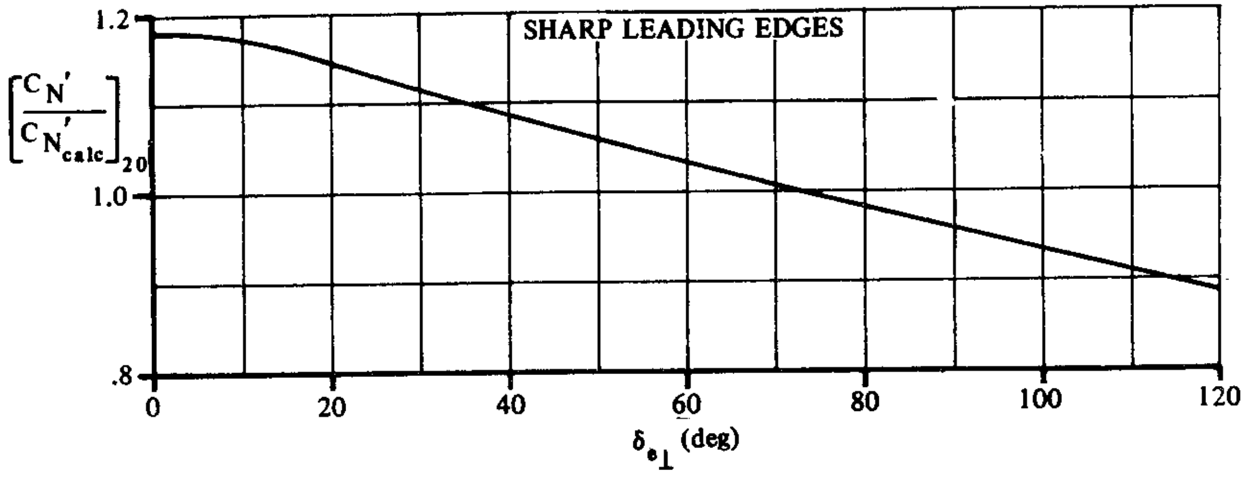

FIGURE 4.8.1.2-13a NORMAL-FORCE-COEFFICIENT CORRELATION FACTOR AT $\alpha' = 20^{\circ}$ – DELTA AND MODIFIED-DELTA CONFIGURATIONS WITH SHARP LEADING EDGES

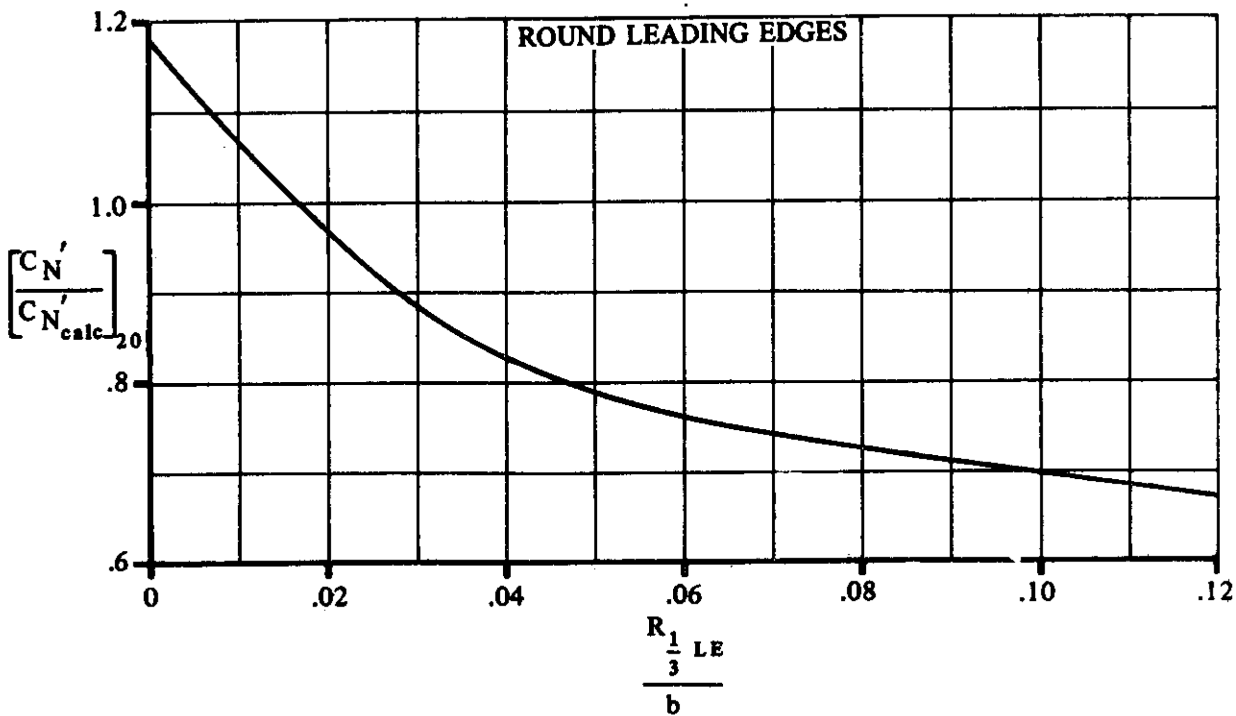

FIGURE 4.8.1.2-13b NORMAL-FORCE-COEFFICIENT CORRELATION FACTOR AT $\alpha' = 20^{\circ}$ – DELTA AND MODIFIED-DELTA CONFIGURATIONS WITH ROUND LEADING EDGES

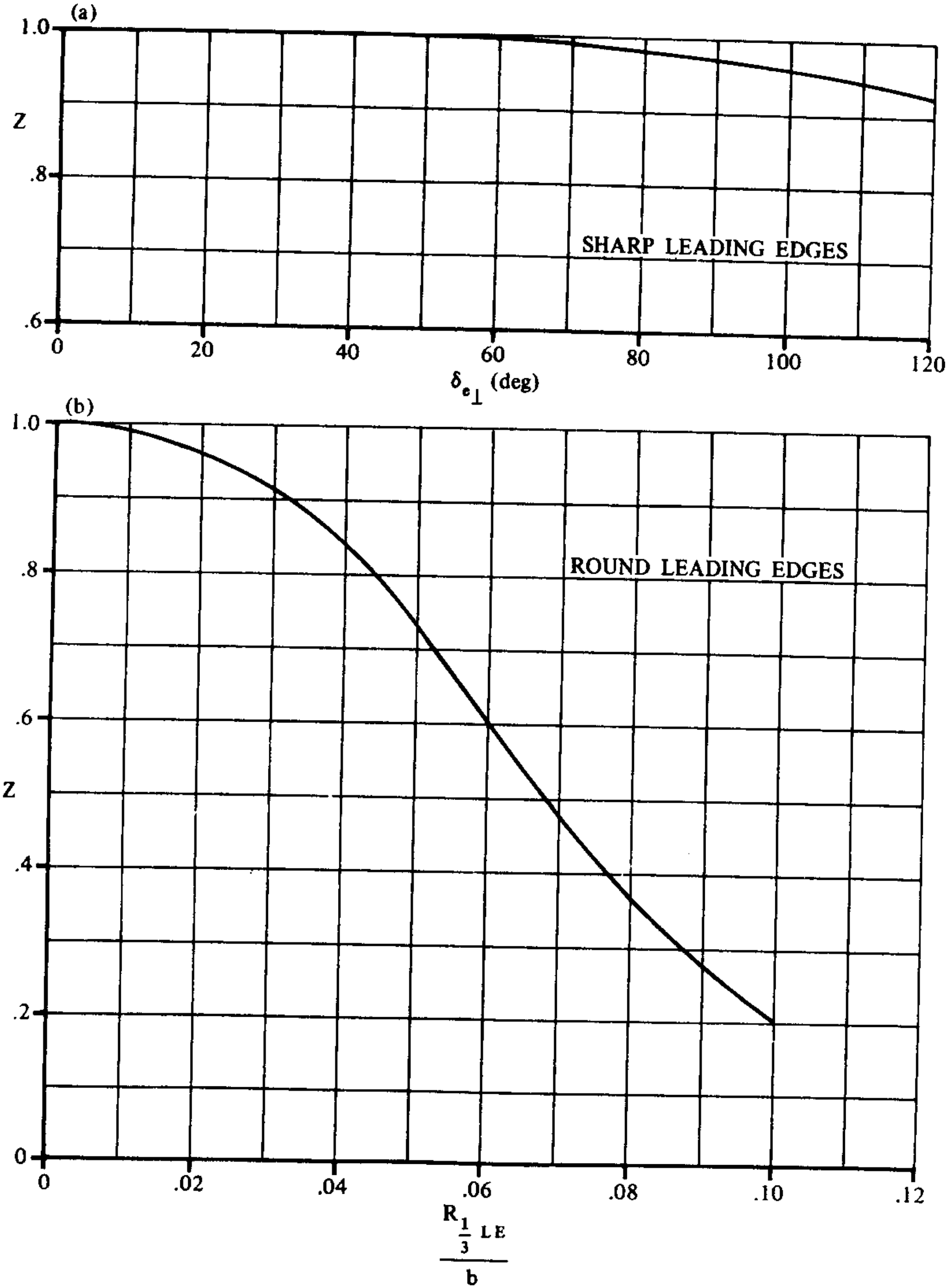

FIGURE 4.8.1.2-14 EFFECT OF LEADING-EDGE GEOMETRY ON THE NORMAL-FORCE COEFFICIENT – DELTA AND MODIFIED DELTA CONFIGURATIONS

4.8.2 WING, WING-BODY AXIAL FORCE

4.8.2.1 WING, WING-BODY ZERO-NORMAL-FORCE AXIAL FORCE

A. SUBSONIC

This section presents a method, taken from reference 1, for estimating the zero-normal-force axial force of advanced flight vehicles at subsonic speeds.

The drag at zero normal force is assumed to be composed of skin-friction drag, base drag, and the pressure drag acting on portions of the configuration other than the base. For most advanced flight vehicles at subsonic speeds, the component of pressure drag acting on portions of the vehicle other than the base is relatively small compared to the sum of the base drag and the skin-friction drag, and it is difficult to isolate. Consequently, in this section it is included as part of an "effective" friction drag.

The "effective" friction drag is determined by multiplying the total wetted area, excluding the base area, by some friction coefficient. For configurations having an average aerodynamic cleanliness, and for thickness ratios not exceeding approximately fifteen to twenty percent, the equivalent friction drag coefficient, based on wetted area, can be assumed to be $C_f = 0.0040$. Of course, this quantity will depend upon such items as surface condition and Reynolds number. Heat and drag loads during re-entry could be such as to roughen the surface and increase surface drag significantly. However, for most configurations of this class, surface drag is a relatively small part of the total drag at most speeds and angles of attack, and it is not considered necessary to go into these effects in greater detail.

Advanced flight vehicles are frequently characterized by large surface areas approximately normal to the direction of flight and facing aft. The "base pressures" acting upon these areas can significantly increase the drag and reduce the maximum lift-drag ratio of these aircraft. For the purpose of definition, "bases" are considered to be those external surface areas which face aft and are approximately perpendicular to the direction of flight; they are formed by the "cutting-off" of some component. The flow ahead of the base should be unseparated and approximately parallel to the free stream, at least near zero lift. In keeping with this definition, bases include the aft facing areas produced by blunting wing trailing edges and by the jet exits of inoperative rocket engines.

The manner in which base drag arises can be visualized by considering the viscous pumping action of the air flowing around the periphery of the base. The viscous forces produced by the external flow tend to drag the air away from the base and consequently reduce the base pressure. In addition, the base pressure would be other than ambient even for a nonviscous flow, since the base would be influenced by the static pressures in the external flow, which are, in general, other than ambient. Consequently, the base pressure would depend both on the magnitude of the pumping, which is related to the ratio of the viscous mixing area to the total base area, and on the shape of the body ahead of the base, which determines the static pressures in the external flow at the boundary of the base.

Because of the complexity of base pressure phenomena at subsonic speeds, it has not been possible theoretically to predict base pressures for even the most simple configurations without entailing complex computational techniques, which nevertheless produce results of doubtful accuracy. Hence, the approach presented in this section is based on semiempirical techniques aimed at isolating the parameters known to be of primary importance.

Factors that might be expected to influence base pressure but which were not isolated in the analysis reported in reference 1 include scale effect and Reynolds number. Available test data show that the variation in Reynolds number produces little effect in base pressure when the flow is turbulent at the base.

DATCOM METHOD

The subsonic axial-force coefficient at zero normal force, based on the reference area (usually the planform area), is obtained from the procedure outlined in the following steps:

Step 1. Determine the increment in axial-force coefficient due to skin friction at zero normal force by

$$\Delta C_{X'_{f_{N_0}}} = -C_f \frac{S_{wet}}{S_{ref}} \qquad 4.8.2.1\text{-a}$$

where

C_f	is the turbulent flat-plate skin-friction coefficient based on the wetted area. It is recommended that a value of $C_f = 0.0040$ be used unless detailed data on surface condition are available. In that case the method of paragraph A of of Section 4.1.5.1 should be used to obtain C_f.
S_{wet}	is the wetted area or surface area of the configuration excluding the base area.
S_{ref}	is the reference area (usually the configuration planform area).

Step 2. Determine the base-pressure coefficient at zero normal force, based on the base area, by

$$C_{p_{b_{N_0}}} = \frac{C_{p_{b_{N_0}}}}{\dfrac{P}{2\sqrt{\pi S_b}}} \; \frac{P}{2\sqrt{\pi S_b}} \qquad 4.8.2.1\text{-b}$$

where

P	is the perimeter of the base of the configuration (see figure 4.8.2.1-7a).
S_b	is the base area of the configuration.

$\dfrac{C_{p_{b_{N_0}}}}{\dfrac{P}{2\sqrt{\pi S_b}}}$ is obtained from figure 4.8.2.1-7b as a function of the shape parameter

$$\frac{2 S_b}{\pi \ell_B (h_b + b_b)} .$$

where

ℓ_B is the total length of the body.

h_b is the maximum height of the base of the configuration (see figure 4.8.2.1-7a).

b_b is the maximum span of the base of the configuration.

Step 3. Determine the increment in axial-force coefficient at zero normal force due to base pressure by

$$\Delta C_{X'_{b_{N_0}}} = C_{p_{b_{N_0}}} \frac{S_b}{S_{ref}} \qquad 4.8.2.1\text{-c}$$

where $C_{p_{b_{N_0}}}$ is obtained from step 2.

Step 4. Determine the axial-force coefficient at zero normal force, based on the reference area, by

$$C_{X'_{N_0}} = \Delta C_{X'_{f_{N_0}}} + \Delta C_{X'_{b_{N_0}}} \qquad 4.8.2.1\text{-d}$$

where $\Delta C_{X'_{f_{N_0}}}$ and $\Delta C_{X'_{b_{N_0}}}$ are obtained from steps 1 and 3, respectively.

Figure 4.8.2.1-7b presents a semiempirical correlation of the base-pressure coefficient at zero normal force. This correlation comprises both a measure of the ratio of the viscous pumping area to the base area, and the effect of the shape of the configuration ahead of the base on the pressures in the external flow.

A comparison of the zero-normal-force axial force calculated by this method with test values is presented as table 4.8.2.1-A.

Sample Problem

Given: The blunted, right-triangular pyramidal lifting body of reference 2.

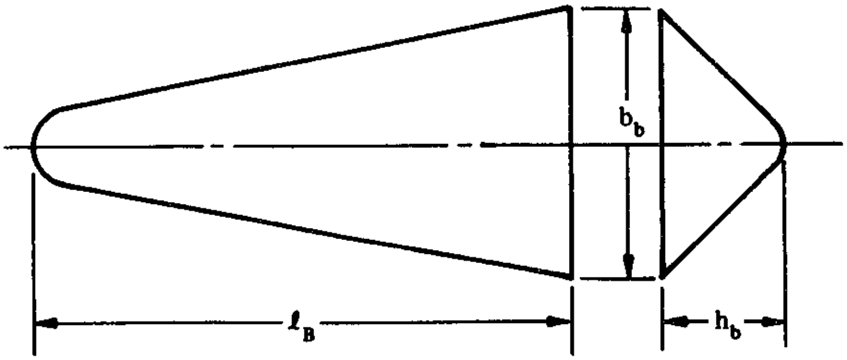

$\ell_B = 19.125$ in. $S_{ref} = S = 104.98$ sq in. $S_b = 21.96$ sq in.

$S_{wet} = 248.83$ sq in. $P = 22.16$ in. $h_b = 4.12$ in. $b_b = 9.08$ in.

Compute:

Determine the increment in axial-force coefficient due to skin friction at zero normal force.

$$C_f = 0.0040$$

$$\Delta C_{X'_{f_{N_0}}} = -C_f \frac{S_{wet}}{S_{ref}} \quad \text{(equation 4.8.2.1-a)}$$

$$= -(0.0040)\left(\frac{248.83}{104.98}\right)$$

$$= -0.00948$$

Determine the base-pressure coefficient at zero normal force

$$\frac{P}{2\sqrt{\pi S_b}} = \frac{22.16}{2\sqrt{\pi(21.96)}} = 1.333$$

$$\frac{2 S_b}{\pi \ell_B (h_b + b_b)} = \frac{2(21.96)}{\pi(19.125)(4.12 + 9.08)} = 0.0554$$

$$\frac{C_{p_{b_{N_0}}}}{\dfrac{P}{2\sqrt{\pi S_b}}} = -0.181 \quad \text{(figure 4.8.2.1-7b)}$$

$$C_{p_{b_{N_0}}} = \frac{C_{p_{b_{N_0}}}}{\dfrac{P}{2\sqrt{\pi S_b}}} \; \frac{P}{2\sqrt{\pi S_b}} \quad \text{(equation 4.8.2.1-b)}$$

$$= (-0.181)(1.333)$$

$$= -0.241 \text{ (based on } S_b\text{)}$$

Determine the increment in axial-force coefficient at zero normal force.

$$\Delta C_{X'_{b_{N_0}}} = C_{p_{b_{N_0}}} \frac{S_b}{S_{ref}} \quad \text{(equation 4.8.2.1-c)}$$

$$= (-0.241)\left(\frac{21.96}{104.98}\right)$$

$$= -0.0504 \text{ (based on } S_{ref}\text{)}$$

Solution:

$$C_{X'_{N_0}} = \Delta C_{X'_{f_{N_0}}} + \Delta C_{X'_{b_{N_0}}} \quad \text{(equation 4.8.2.1-d)}$$

$$= -0.00948 - 0.0504$$

$$= -0.0599 \text{ (based on S)}$$

This compares with a test value of −0.0582 from reference 2.

REFERENCES

1. Seager, D. B., and Meyer, J. E.: An Investigation of the Subsonic Aerodynamic Characteristics and the Landing Flare Maneuver for Hypersonic Re-Entry Configurations. ASD-TDR-62-271, 1962. (C) Title Unclassified
2. Mugler, J. P., Jr., and Olstad, W. B.: Static Longitudinal Aerodynamic Characteristics at Transonic Speeds of a Blunted Right Triangular Pyramidal Lifting Re-Entry Configuration for Angles of Attack up to 110°. NASA TN D-797, 1961. (U)
3. Mantz, K., Seager, D. B., and Ross, R.: Tests to Determine Subsonic Aerodynamic Characteristics of Hypersonic Re-Entry Configurations. ASD-TR-61-485, Supplement 1, 1963. (U)
4. Mantz, K., Seager, D. B., and Ross, R.: Tests to Determine Subsonic Pressures, Forces and Moments Acting on a Hypersonic Re-Entry Configuration. ASD-TDR-62-270, Supplement 1, 1963. (U)
5. Paulson, J. W., and Shanks, R. E.: Investigation of Low-Subsonic Flight Characteristics of a Model of a Hypersonic Boost-Glide Configuration Having a 78° Delta Wing. NASA TN D-894, 1961. (U)
6. Hoerner, S. F.: Fluid Dynamic Drag. Published by author, 1958. (U)
7. Ware, G. M.: Low-Subsonic-Speed Static Stability of Right-Triangular-Pyramid and Half-Cone Lifting Re-Entry Configurations. NASA TN D-646, 1961. (U)
8. Olstad, W. B., Mugler, Jr., J. P., and Cahn, M. S.: Static Longitudinal and Lateral Stability Characteristics of a Right Triangular Pyramidal Lifting Re-Entry Configuration at Transonic Speeds. NASA TN D-655, 1961. (U)
9. Paulson, J. W.: Low-Speed Static Stability and Control Characteristics of a Right Triangular Pyramid Re-Entry Configuration. NASA Memo 4-11-59L, 1959. (U)
10. Boisseau, P. C.: Investigation of the Low-Subsonic Flight Characteristics of a Model of a Re-Entry Vehicle with a Thick Flat 75° Swept Delta Wing and a Half-Cone Fuselage. NASA TN D-1007, 1962. (U)
11. Shanks, R. E.: Investigation of the Low-Subsonic Flight Characteristics of a Model of an All-Wing Hypersonic Boost-Glide Configuration Having Very High Sweep. NASA TN D-369, 1960. (U)
12. Peckham, D. H.: Low-Speed Wind Tunnel Tests on a Series of Uncambered Slender Pointed Wings with Sharp Edges. ARC R&M 3186, 1958. (U)
13. Paulson, J. W., and Shanks, R. E.: Investigation of the Low-Subsonic Stability and Control Characteristics of a Free-Flying Model of a Thick 70° Delta Re-Entry Configuration. NASA TN D-913, 1961. (U)

TABLE 4.8.2.1-A
SUBSONIC ZERO-NORMAL-FORCE AXIAL FORCE
DATA SUMMARY

Ref.	Configuration	S_{ref} (sq in.)	S_b (sq in.)	S_{wet} (sq in.)	ℓ_B (in.)	P (in.)	h_b (in.)	b_b (in.)	$C'_{X_{N_0}}$ Calc.	$C'_{X_{N_0}}$ Test	e Percent Error
2	Blunted right triangular pyramid	104.98	21.96	248.83	19.13	22.16	4.12	9.08	–0.0599	–0.0582	2.9
3	D-1	160.19	33.29	361.73	23.00	28.40	4.32	13.13	–0.0587	–0.0550	6.7
	D-2	142.30	26.98	305.00	23.00	26.54	4.32	12.37	–0.0498	–0.0520	– 4.2
	D-3	142.30	44.36	329.00	23.00	28.58	7.14	12.37	–0.0832	–0.0830	0.2
7	a	570.00	111.30	1251.30	54.00	51.94	10.55	21.10	–0.0480	–0.0480	0
	b (basic)	570.00	109.40	1281.00	54.00	49.65	9.35	21.10	–0.0528	–0.0480	10.0
	c (basic)	1110.00	215.45	2158.00	62.50	70.00	13.50	29.50	–0.0417	–0.0450	– 7.3
	c (extended nose)	1152.00	215.45	2313.00	70.10	70.00	13.50	29.50	–0.0377	–0.0360	4.7
8	1	204.00	41.50	448.50	31.59	31.11	12.89	6.44	–0.0495	–0.0500	– 1.0

$$\text{Average Error} = \frac{\Sigma|e|}{n} = 3.8\%$$

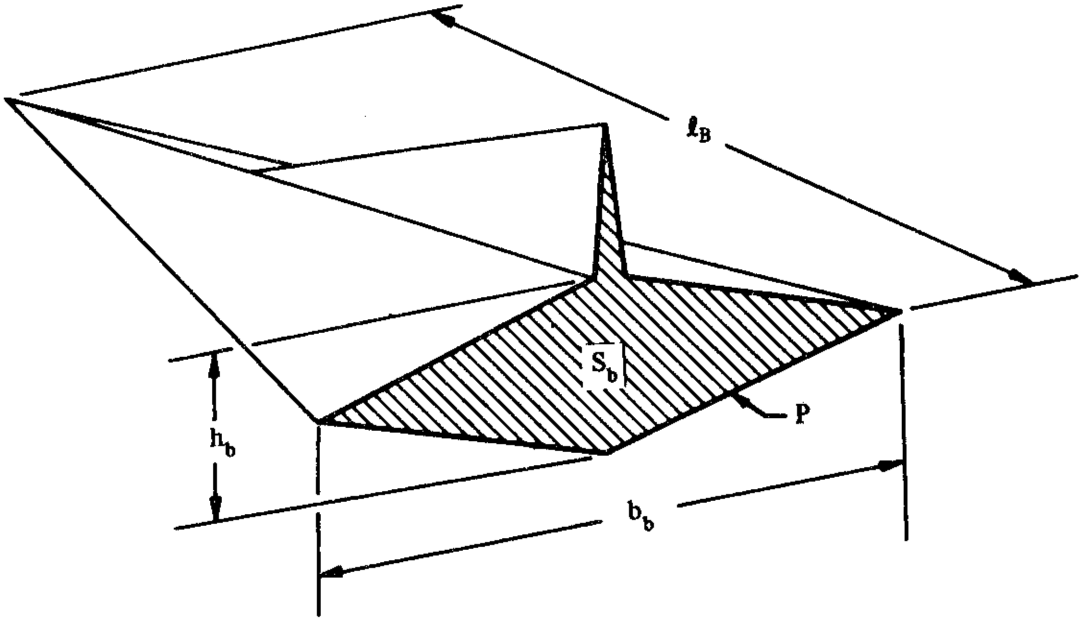

FIGURE 4.8.2.1-7a CONFIGURATION GEOMETRY

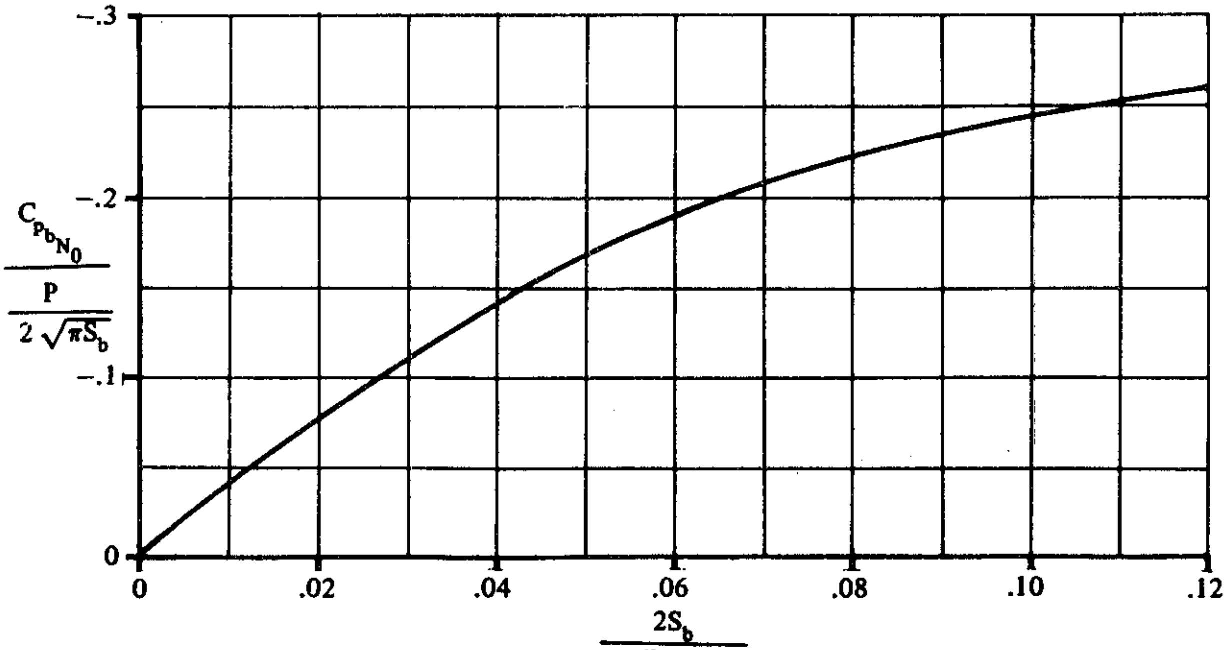

FIGURE 4.8.2.1-7b ZERO-NORMAL-FORCE BASE-PRESSURE COEFFICIENT

4.8.2.2 WING, WING-BODY AXIAL-FORCE VARIATION WITH ANGLE OF ATTACK

A. SUBSONIC

This section presents a method for estimating the axial-force variation with angle of attack for a delta or modified-delta planform re-entry configuration at subsonic speeds.

The method presented herein is taken from reference 1. The total axial force at angle of attack is taken as the sum of that at zero normal force, the increment due to angle of attack, and an increment due to the base pressure at angle of attack.

The axial force at zero normal force is given by the method of Section 4.8.2.1.

The increment of axial force due to angle of attack is obtained by a procedure that closely parallels the one used to obtain the normal-force variation with angle of attack as discussed in Section 4.8.1.2. The method is based on a study of test data on low-aspect-ratio delta wings with thick and thin surfaces, with sharp and rounded leading edges, and with varying degrees of nose bluntness. Thin, sharp-leading-edge delta wings were selected as "reference wings," and theoretical relationships were written for the axial-force characteristics of these planforms. The axial-force characteristics of all the test configurations were then calculated at $\alpha' = 20^\circ$ by using these "reference wing" relationships, and any deviation between the calculated and test values was related to aspect ratio, frontal area, and leading-edge characteristics. The variation of this component of axial force between that at zero normal force and that at $\alpha' = 20^\circ$ is then approximated as a function of the normal-force variation with angle of attack.

In general, the base pressures acting on advanced flight vehicles become less as the angle of attack increases and, consequently, the component of axial force due to base pressure increases negatively as the angle of attack increases. In reference 1 the change in base pressures of the test configurations are correlated with changes in angle of attack by using the base pressures at $\alpha' = 20^\circ$ and at zero normal force as the basis for the correlation.

DATCOM METHOD

The axial-force variation with angle of attack for a delta or modified-delta configuration at low speeds, based on the reference area (usually the planform area), is obtained from the procedure outlined in the following steps:

Step 1. Determine the increment of axial-force coefficient due to angle of attack by

$$\Delta C_{X'} = \left[\left(\frac{X'}{N'}\right)_{calc}\right]_{20} \left[\frac{\Delta C_{X'}}{\Delta C_{X'_{calc}}}\right]_{20} \sqrt{\frac{\alpha'}{20}} \quad C_{N'} \qquad \text{4.8.2.2-a}$$

where

$\left[\left(\frac{X'}{N'}\right)_{calc}\right]_{20}$ is the calcuiated ratio of the axial force to the normal force at $\alpha' = 20^{\circ}$. given by

$$\left[\left(\frac{X'}{N'}\right)_{calc}\right]_{20} = -0.349\left(\frac{A+2}{A+4}\right) \qquad 4.8.2.2\text{-b}$$

$\left[\frac{\Delta C_{X'}}{\Delta C_{X'_{calc}}}\right]_{20}$ is the empirical correlation factor of the axial-force coefficient at $\alpha' = 20^{\circ}$ for delta or modified-delta configurations. This parameter is presented as a function of configuration geometry in figure 4.8.2.2-10. Figure 4.8.2.2-10 is entered with the following geometric parameters:

A	the aspect ratio of the surface
S_F	the projected frontal area perpendicular to the zero-normal-force reference plane (projected frontal area at $C_{N'} = 0$)
S_{ref}	the reference area (usually the configuration planform area)
b	the surface span
$R_{\frac{1}{3}LE}$	the leading-edge radius in a plane normal to the leading edge at $\frac{1}{3}$ c_r from the nose

α' is the angle of attack in degrees.

$$\alpha' = \alpha - \alpha_{N_0}$$

$C_{N'}$ is the normal-force variation with angle of attack obtained by using the method of Section 4.8.1.2.

Step 2. Determine the variation of base pressure with angle of attack by

$$\left(C_{p_b}\right)_{\alpha'} = \left(\frac{C_{p_{b_{20}}}}{C_{p_{b_{N_0}}}} - 1\right)\left(\frac{\alpha}{20}\right)^2 \; C_{p_{b_{N_0}}} \qquad 4.8.2.2\text{-c}$$

where α' is defined above, and

$\frac{C_{p_{b_{20}}}}{C_{p_{b_{N_0}}}}$ is the empirical correlation of the ratio of the pressure coefficient at $\alpha' = 20^{\circ}$ to that at zero normal force. This parameter is obtained from figure 4.8.2.2-11 as a function of the shape parameter

$$\frac{b_b{}^2}{h_b\sqrt{S_b}}$$

where

b_b is the maximum span of the base of the configuration.

h_b is the maximum height of the base of the configuration (see figure 4.8.2.1-7a).

S_b is the base area of the configuration.

The two curves on figure 4.8.2.2-11 refer to two types of re-entry configurations. The upper curve is to be applied to configurations for which the entire base is influenced directly by the primary lifting surface. The lower curve is to be applied to configurations for which portions of the base are aft of nonlifting components, e.g., bodies and vertical surfaces.

$C_{p_{b_{N_0}}}$ is the base pressure coefficient at zero normal force obtained as outlined in step 2 of the Datcom method of Section 4.8.2.1.

Step 3. Determine the variation of the increment of axial-force coefficient due to the base pressure with angle of attack by

$$\left(\Delta C_{X_{b\alpha}}\right) = \left(C_{p_b}\right)_{\alpha'} \frac{S_b}{S_{ref}} \qquad 4.8.2.2\text{-d}$$

where

$\left(C_{p_b}\right)_{\alpha'}$ is the variation of base pressure with angle of attack from step 2.

S_{ref} is the reference area (usually the configuration planform area).

Step 4. Determine the zero-normal-force axial force $C_{X'_{N_0}}$ by using the method of Section 4.8.2.1.

Step 5. The variation of axial force with angle of attack, based on the reference area, is given by

$$C_{X'} = -\Delta C_{X'} + \left(\Delta C_{X_{b\alpha}}\right)' + C_{X'_{N_0}} \qquad 4.8.2.2\text{-e}$$

where $\Delta C_{X'}$, $\left(\Delta C_{X_{b\alpha}}\right)$, and $C_{X'_{N_0}}$ are from steps 1, 3, and 4, respectively.

A comparison of the axial-force variation with angle of attack calculated by this method with test results is presented as table 4.8.2.2-A.

While it is considered that the results presented are satisfactory for use in preliminary design, it should be noted that scale effect and Reynolds number, which might be expected to influence the base pressure, were not isolated in the data correlation reported in reference 1. (Available test data showed, however, that the variation in Reynolds number produced little effect in base pressure when the flow was turbulent at the base.) Furthermore, in many cases the data were not sufficient to accurately define the variation of base pressure over the surface of the base. Consequently, much of the data included in the empirical correlation for axial-force coefficient at $\alpha' = 20^\circ$ (figure 4.8.2.2-10) and in the empirical correlation for the ratio of the pressure coefficient at $\alpha' = 20^\circ$ to that at zero normal force (figure 4.8.2.2-11), are known to be in error.

Sample Problem

Given: A delta model with a symmetrical diamond cross section and a blunt trailing edge. This is model D-3 of reference 3 and is the same configuration as sample problem 2 of Section 4.8.1.2.

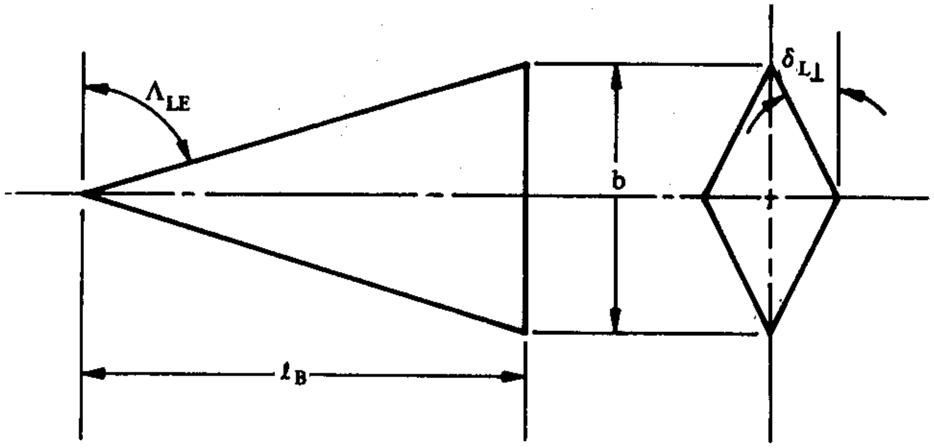

$A = 1.076$ $\quad b = b_b = 12.374$ in. $\quad S_{ref} = S = 142.30$ sq in.

$S_F = S_b = 44.20$ sq in. $\quad S_{wet} = 329.0$ sq in. $\quad h_b = 7.14$ in.

$\ell_B = 23.0$ in. $\quad P = 28.58$ in.

The following variation of $C_{N'}$ with α' from sample problem 2 of Section 4.8.1.2:

α'	0	5	10	15	20
$C_{N'}$	0	0.1359	0.2973	0.4853	0.6998

Compute:

Determine the increment in axial-force coefficient due to angle of attack.

$$\left[\left(\frac{X'}{N'}\right)_{calc}\right]_{20} = -0.349\left(\frac{A+2}{A+4}\right) \quad \text{(equation 4.8.2.2-b)}$$

$$= -0.349\left(\frac{1.076+2}{1.076+4}\right) = -0.2115$$

$$S_F/S_{ref} = 44.20/142.30 = 0.311$$

$$\left[\frac{\Delta C_{X'}}{\Delta C_{X'_{calc}}}\right]_{20} = 0.389 \quad \text{(figure 4.8.2.2-10, sharp leading edge)}$$

$$\Delta C_{X'} = \left[\frac{X'}{N'_{calc}}\right]_{20}\left(\frac{\Delta C_{X'}}{\Delta C_{X'_{calc}}}\right)_{20}\sqrt{\frac{\alpha'}{20}}\; C_{N'} \quad \text{(equation 4.8.2.2-a)}$$

$$= (-0.2115)(0.389)\sqrt{\frac{\alpha'}{20}}\; C_{N'}$$

$$= -0.0823\sqrt{\frac{\alpha'}{20}}\; C_{N'} \quad \text{(see calculation table below)}$$

Determine the variation of base pressure with angle of attack.

$$\frac{b_b^{\,2}}{h_b\sqrt{S_b}} = \frac{(12.374)^2}{7.14\sqrt{44.20}} = 3.226$$

$$\frac{C_{p_{b_{20}}}}{C_{p_{b_{N_0}}}} = 1.42 \quad \text{(figure 4.8.2.2-11, upper curve)}$$

$$\frac{P}{2\sqrt{\pi S_b}} = \frac{28.58}{2\sqrt{\pi\,(44.2)}} = 1.213$$

$$\frac{2\,S_b}{\pi\,\ell_B\,(h_b + b_b)} = \frac{2\,(44.2)}{\pi\,(23.0)\,(7.14 + 12.37)} = 0.0627$$

$$\frac{C_{p_{b_{N_0}}}}{\frac{P}{2\sqrt{\pi S_b}}} = -0.196 \quad \text{(figure 4.8.2.1-7b)}$$

$$C_{p_{b_{N_0}}} = \frac{C_{p_{b_{N_0}}}}{\frac{P}{2\sqrt{\pi S_b}}} \; \frac{P}{2\sqrt{\pi S_b}} \quad \text{(equation 4.8.2.1-b)}$$

$$= (-0.196)\,(1.213)$$

$$= -0.238 \left(\text{This result is also used below in calculating } C_{X'_{N_0}}\right)$$

$$\left(C_{p_b}\right)_{\alpha'} = \left(\frac{C_{p_{b_{20}}}}{C_{p_{b_{N_0}}}} - 1\right)\left(\frac{\alpha'}{20}\right)^2 C_{p_{b_{N_0}}} \quad \text{(equation 4.8.2.2-c)}$$

$$= (1.42 - 1)\left(\frac{\alpha'}{20}\right)^2 (-0.238)$$

$$= -0.100 \left(\frac{\alpha'}{20}\right)^2$$

Determine the variation of the increment of axial-force coefficient due to the base pressure with angle of attack.

$$\left(\Delta C_{X_{b_\alpha}}\right)' = \left(C_{p_b}\right)_{\alpha'} \frac{S_b}{S_{ref}} \quad \text{(equation 4.8.2.2-d)}$$

$$= \left[-0.100\left(\frac{\alpha'}{20}\right)^2\right]\left(\frac{44.20}{142.3}\right)$$

$$= -0.0311 \left(\frac{\alpha'}{20}\right)^2 \quad \text{(see calculation table below)}$$

Determine the zero-normal-force axial force by the method of Section 4.8.2.1.

C_f = 0.0040

$$\Delta C_{X'_{f_{N_0}}} = -C_f \frac{S_{wet}}{S_{ref}} \qquad \text{(equation 4.8.2.1-a)}$$

$$= (-0.0040)\left(\frac{329.0}{142.3}\right)$$

$$= -0.00925$$

$$C_{p_{b_{N_0}}} = -0.238 \text{ (calculated in determining } \left(C_{p_b}\right)_{\alpha'} \text{ above)}$$

$$\Delta C_{X'_{b_{N_0}}} = C_{p_{b_{N_0}}} \frac{S_b}{S_{ref}} \qquad \text{(equation 4.8.2.1-c)}$$

$$= (-0.238)\left(\frac{44.2}{142.3}\right)$$

$$= -0.0739$$

$$C_{X'_{N_0}} = \Delta C_{X'_{f_{N_0}}} + \Delta C_{X'_{b_{N_0}}} \qquad \text{(equation 4.8.2.1-d)}$$

$$= -0.00925 + (-0.0739)$$

$$= -0.0832$$

Solution:

$$C_{X'} = -\Delta C_{X'} + \left(\Delta C_{X_{b\alpha}}\right) + C_{X'_{N_0}} \qquad \text{(equation 4.8.2.2-e)}$$

$$= -(-0.0823)\sqrt{\frac{\alpha'}{20}}\, C_{N'} + (-0.0311)\left(\frac{\alpha'}{20}\right)^2 + (-0.0832)$$

①	②	③	④	⑤
α' (deg)	C_N' (given)	$-0.0823\sqrt{\frac{\alpha'}{20}}\,C_N'$ $-0.0823\sqrt{\frac{①}{20}}$ ②	$-0.0311\left(\frac{\alpha'}{20}\right)^2$ $-0.0311\left(\frac{①}{20}\right)^2$	C_X' (based on S) (eq. 4.8.2.2-e) − ③ + ④ − 0.0832
0	0	0	0	−0.0832
5	0.1359	−0.00559	−0.00194	−0.0796
10	0.2973	−0.01727	−0.00778	−0.0737
15	0.4853	−0.0346	−0.0175	−0.0661
20	0.6998	−0.0576	−0.0311	−0.0567

The calculated results are compared with test values from reference 3 in sketch (a) and in table 4.8.2.2-A.

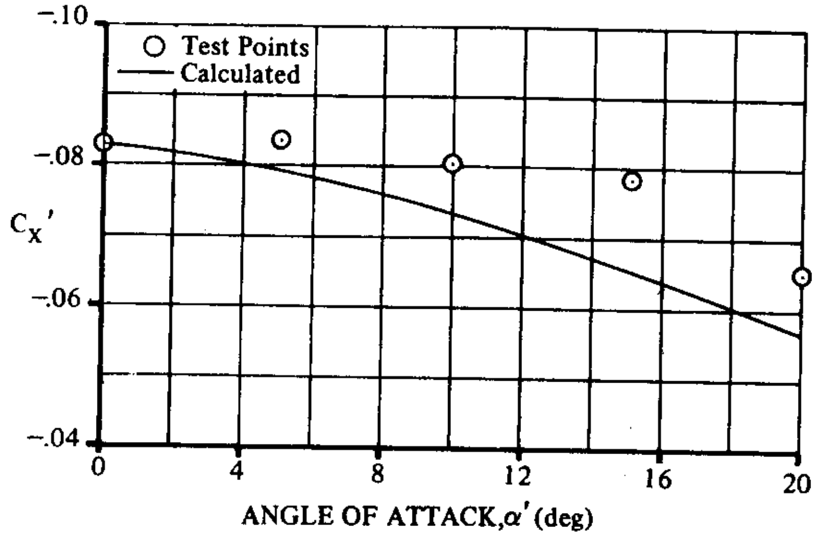

SKETCH (a)

REFERENCES

1. Seeger, D. B., and Meyer, J. E.: An Investigation of the Subsonic Aerodynamic Characteristics and the Landing Flare Maneuver for Hypersonic Re-Entry Configurations. ASD-TDR-62-271, 1962. (C) Title Unclassified
2. Mugler, J. P., Jr., and Olstad, W. B.: Static Longitudinal Aerodynamic Characteristics at Transonic Speeds of a Blunted Right Triangular Pyramidal Lifting Re-Entry Configuration for Angles of Attack up to 110°. NASA TN D-797, 1961. (U)
3. Mantz, K., Seeger, D. B., and Ross, R.: Tests to Determine Subsonic Aerodynamic Characteristics of Hypersonic Re-Entry Configurations. ASD-TR-61-485, Supplement 1, 1963. (U)
4. Mantz, K., Seeger, D. B., and Ross, R.: Tests to Determine Subsonic Pressures, Forces and Moments Acting on a Hypersonic Re-Entry Configuration. ASD-TDR-62-270, Supplement 1, 1963. (U)
5. Paulson, J. W., and Shanks, R. E.: Investigation of Low-Subsonic Flight Characteristics of a Model of a Hypersonic Boost-Glide Configuration Having a 78° Delta Wing. NASA TN D-894, 1961. (U)
6. Jaquet, B. M., and Brewer, J. D.: Low-Speed Static-Stability and Rolling Characteristics of Low-Aspect-Ratio Wings of Triangular and Modified Triangular Planforms. NACA RM L8L29, 1949. (U)
7. Ware, G. M.: Low-Subsonic-Speed Static Stability of Right-Triangular-Pyramid and Half-Cone Lifting Re-Entry Configurations. NASA TN D-646, 1961. (U)
8. Olstad, W. B., Mugler, J. P., Jr., and Cahn, M. S.: Static Longitudinal and Lateral Stability Characteristics of a Right Triangular Pyramidal Lifting Re-Entry Configuration at Transonic Speeds. NASA TN D-655, 1961. (U)
9. Paulson, J. W.: Low-Speed Static Stability and Control Characteristics of a Right Triangular Pyramid Re-Entry Configuration. NASA Memo 4-11-59L, 1959. (U)
10. Boisseau, P. C.: Investigation of the Low-Subsonic Flight Characteristics of a Model of a Re-Entry Vehicle with a Thick Flat 75° Swept Delta Wing and a Half-Cone Fuselage. NASA TN D-1007, 1962. (U)
11. Shanks, R. E.: Investigation of the Low-Subsonic Flight Characteristics of a Model of an All-Wing Hypersonic Boost-Glide Configuration Having Very High Sweep. NASA TN D-369, 1960. (U)
12. Peckham, D. H.: Low-Speed Wind Tunnel Tests on a Series of Uncambered Slender Pointed Wings with Sharp Edges. ARC R&M 3186, 1958. (U)

TABLE 4.8.2.2-A

SUBSONIC AXIAL-FORCE VARIATION WITH ANGLE OF ATTACK
DELTA PLANFORM CONFIGURATIONS

Ref.	Configuration	A	b (in.)	b_b (in.)	h_b (in.)	S_F (sq in.)	S_{ref} (sq in.)	S_b (sq in.)	Leading Edge	α (deg)	$C_X{}'$ Calc.	$C_X{}'$ Test	e Percent Error
2	Blunted right triangular pyramid	0.788	9.08	9.08	4.12	21.96	104.98	21.96	Round	0	−0.0599	−0.0582	2.9
									$R_{\frac{1}{3}LE}$ = .14 in.	5	−0.0564	−0.0575	− 1.9
									δ_L = 45°	10	−0.0517	−0.0540	− 4.3
										15	−0.0471	−0.0470	0.2
										20	−0.0427	−0.0440	− 3.0
3	D-1	1.076	13.13	13.13	4.32	33.29	160.19	33.29	Round	0	−0.0587	−0.0550	6.7
									$R_{\frac{1}{3}LE}$ = .525 in.	5	−0.0535	−0.0564	− 5.1
									δ_L = 15°	10	−0.0461	−0.0630	−13.0
										15	−0.0375	−0.0486	−22.8
										20	−0.0270	−0.0338	−20.1
	D-2	1.076	12.374	12.374	4.32	26.98	142.30	26.98	Sharp*	0	−0.0498	−0.0520	− 4.2
									$\delta_{e_\perp}$ = 58°	5	−0.0475	−0.0544	−12.7
										10	−0.0431	−0.0524	−17.7
										15	−0.0382	−0.0476	−19.7
	D-3	1.076	12.374	12.374	7.14	44.20	142.30	44.20	Sharp*	0	−0.0832	−0.0830	0.2
									$\delta_{e_\perp}$ = 90°	5	−0.0814	−0.0834	− 2.4
										10	−0.0795	−0.0802	− 0.9
										15	−0.0776	−0.0785	− 1.1
										20	−0.0756	−0.0655	15.4
	D-4	1.078	13.934	13.934	4.32	41.44	178.56	41.44	Round	0	−0.0695	−0.0620	12.1
									$R_{\frac{1}{3}LE}$ = 1.05 in.	5	−0.0598	−0.0545	9.7
									δ_L = 10.5°	10	−0.0445	−0.0446	− 0.2
										15	−0.0262	−0.0323	−18.9
8	Right triangular pyramid	0.742	12.89	12.89	6.44	41.40	222.0	41.40	Round	0	−0.0495	−0.0500	− 1.0
									$R_{\frac{1}{3}LE}$ = .187 in.	5	−0.0461	−0.0570	−19.1
									δ_L = 45°	10	−0.0410	−0.0540	−24.1
										15	−0.0362	−0.0430	−18.1

*Model analyzed as having sharp leading edge, although LER = 0.032 in.

$$\text{Average error} = \frac{\Sigma |e|}{n} = 9.5\%$$

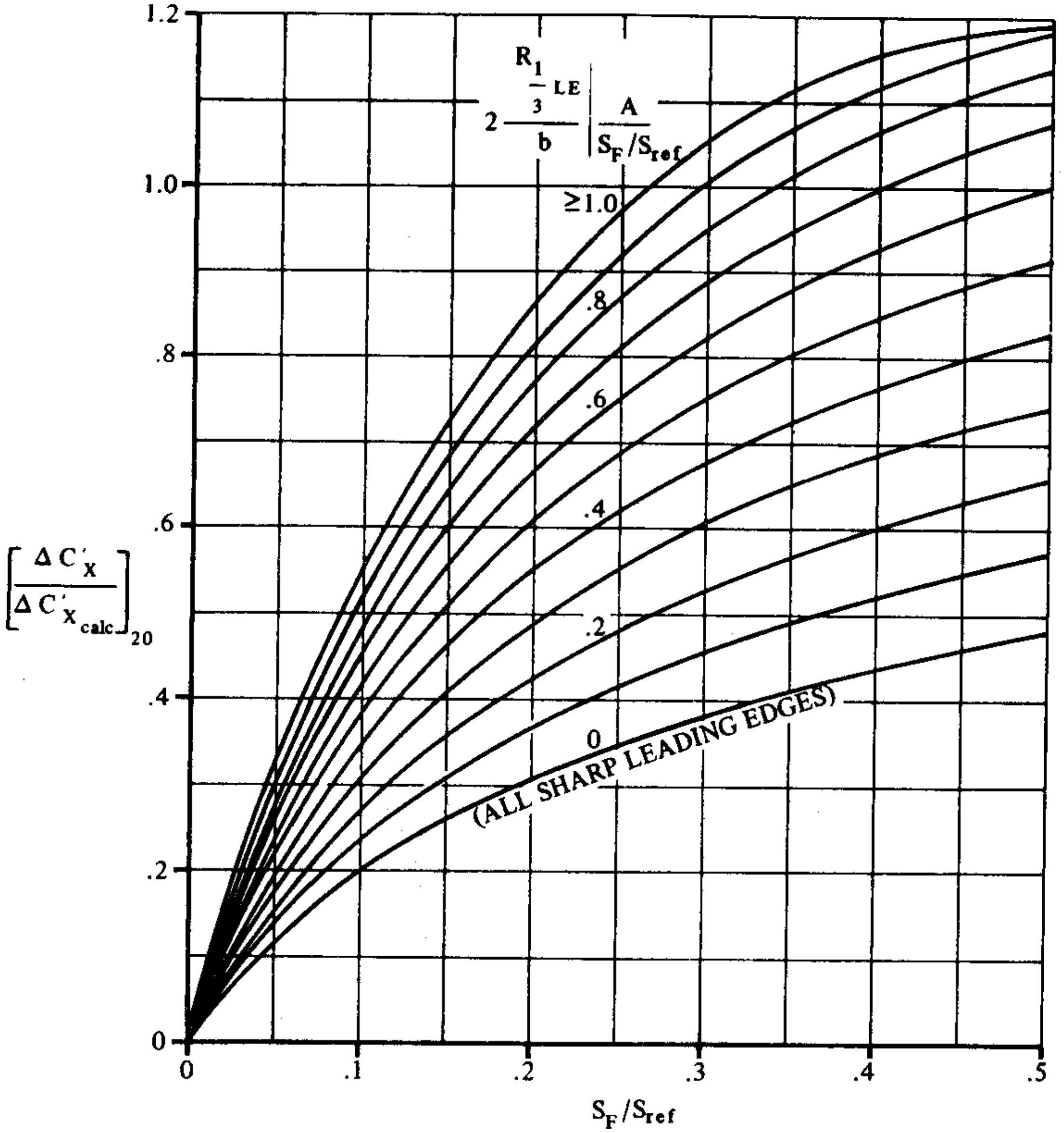

FIGURE 4.8.2.2-10 BASE-PRESSURE-COEFFICIENT CORRELATION FACTOR AT $\alpha' = 20°$ DELTA AND MODIFIED-DELTA CONFIGURATIONS

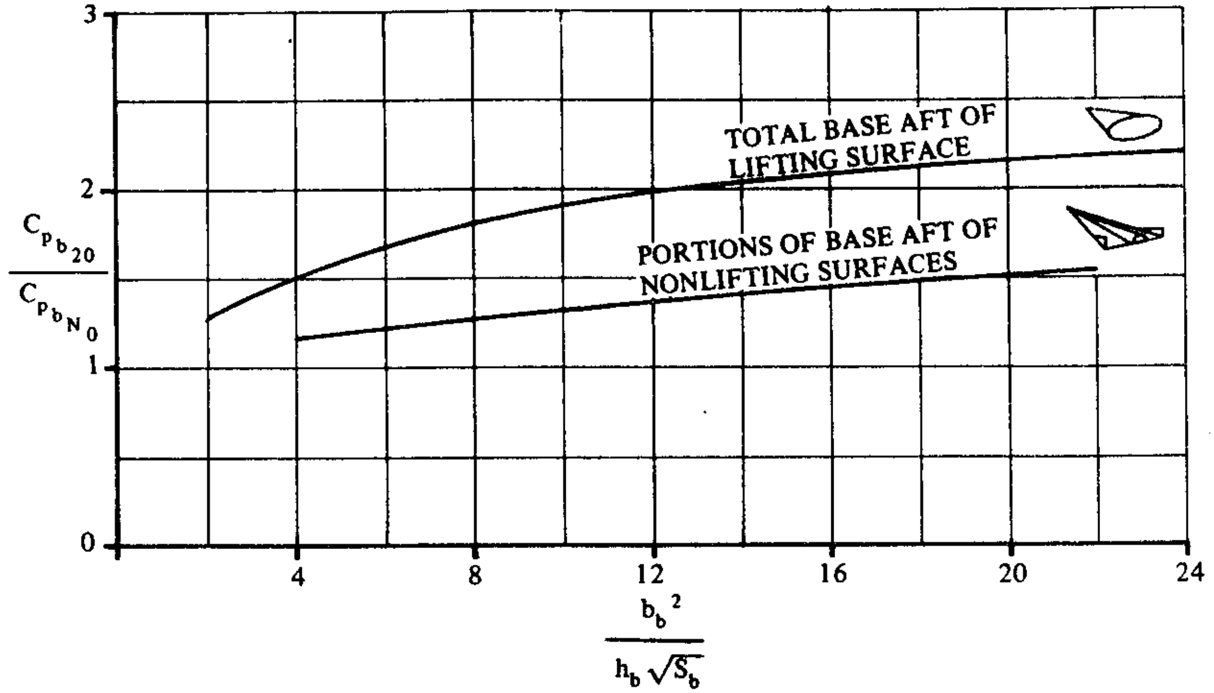

FIGURE 4.8.2.2-11 AXIAL-FORCE-COEFFICIENT CORRELATION FACTOR AT $\alpha' = 20^\circ$ –

4.8.3 WING, WING-BODY PITCHING MOMENT

4.8.3.1 WING, WING-BODY ZERO-NORMAL-FORCE PITCHING MOMENT

A. SUBSONIC

This section presents a design chart, taken from reference 1, to be used in approximating the zero-normal-force pitching-moment coefficient of nonsymmetrical delta-planform configurations with rounded leading edges at low speeds.

The design chart is based on a limited amount of experimental data and, furthermore, does not represent an extensive analysis of the zero-normal-force pitching moment. It is considered to provide only a first-order approximation of $C_{m_{N_0}}$.

DATCOM METHOD

The low-speed zero-normal-force pitching-moment coefficient of a nonsymmetrical delta-planform configuration with rounded leading edges, based on the product of the planform area and root chord Sc_r, is approximated from the procedure outlined in the following steps:

Step 1. Determine the zero-normal-force angle of attack α_{N_0} by using the method of Section 4.8.1.1.

Step 2. Obtain the zero-normal-force pitching-moment coefficient $C_{m_{N_0}}$ from figure 4.8.3.1-4 as a function of α_{N_0} determined in step 1.

Figure 4.8.3.1-4 is not applicable to configurations with sharp leading edges.

A comparison of the zero-normal-force pitching-moment coefficient of unsymmetrical delta-planform configurations calculated by this method with test results is presented as table 4.8.3.1-A. The values of α_{N_0} used in this data summary were calculated by using the method of Section 4.8.1.1.

Sample Problem

Given: The right-triangular pyramidal body designated configuration 1 in reference 7. This is the configuration of sample problem 1 of Section 4.8.1.1.

$\ell_B = 31.55$ in. Nose radius $= 0.1875$ in. $h_b = 6.44$ in.

$\bar{z}_{base} = 4.105$ in.

Compute:

Determine α_{N_0}

$\alpha_{N_0} = 8.04^\circ$ (sample problem 1, Section 4.8.1.1)

Solution:

$$C_{m_{N_0}} = 0.0027 \quad \text{(based on } Sc_r\text{)} \quad \text{(figure 4.8.3.1-4, extrapolated)}$$

The calculated result compares with a test value of 0.0028 from reference 7.

REFERENCES

1. Seager, D. B., and Meyer, J. E.: An Investigation of the Subsonic Aerodynamic Characteristics and the Landing Flare Maneuver for Hypersonic Re-Entry Configurations. ASD-TDR-62-271, 1962. (C) Title Unclassified
2. Mantz, K., Seager, D. B., and Ross, R.: Tests to Determine Subsonic Aerodynamic Characteristics of Hypersonic Re-Entry Configurations. ASD-TR-61-485, Supplement 1, 1963. (U)
3. Mantz, K., Seager, D. B., and Ross, R.: Tests to Determine Subsonic Pressures, Forces and Moments Acting on a Hypersonic Re-Entry Configuration. ASD-TDR-62-270, Supplement 1, 1963. (U)
4. Paulson, J. W.: Low-Speed Static Stability and Control Characteristics of a Right Triangular Pyramid Re-Entry Configuration. NASA Memo 4-11-59L, 1959. (U)
5. Boisseau, P. C.: Investigation of the Low-Subsonic Flight Characteristics of a Model of a Re-Entry Vehicle with a Thick Flat 75° Swept Delta Wing and a Half-Cone Fuselage. NASA TN D-1007, 1962. (U)
6. Ware, G. M.: Low-Subsonic-Speed Static Stability of Right-Triangular-Pyramid and Half-Cone Lifting Re-Entry Configurations. NASA TN D-646, 1961. (U)
7. Olstad, W. B., Mugler, J. P., Jr., and Cahn, M. S.: Static Longitudinal and Lateral Stability Characteristics of a Right Triangular Pyramidal Lifting Re-Entry Configuration at Transonic Speeds. NASA TN D-655, 1961. (U)
8. Mugler, J. P., Jr., and Olstad, W. B.: Static Longitudinal Aerodynamic Characteristics at Transonic Speeds of a Blunted Right Triangular Pyramidal Lifting Re-Entry Configuration for Angles of Attack up to 110°. NASA TN D-797, 1961. (U)
9. Paulson, J. W., and Shanks, R. E.: Investigation of Low-Subsonic Flight Characteristics of a Model of a Hypersonic Boost-Glide Configuration Having a 78° Delta Wing. NASA TN D-894, 1961. (U)
10. Wright Air Development Division: Unpublished data from the 5-foot wind tunnel, 1961. (U)
11. Shanks, R. E.: Investigation of the Low-Subsonic Flight Characteristics of a Model of an All-Wing Hypersonic Boost-Glide Configuration Having Very High Sweep. NASA TN D-369, 1960. (U)

TABLE 4.8.3.1-A

SUBSONIC ZERO-NORMAL-FORCE PITCHING MOMENT DELTA PLANFORM CONFIGURATIONS ROUND LEADING EDGES

DATA SUMMARY

Ref.	Configuration	$\alpha_{N_{0_{calc.}}}$ (Sect 4.8.1.1)	$C_{m_{N_0}}$ Calc.	$C_{m_{N_0}}$ Test
2	D-7	−2.15	−0.0007	−0.002
	D-8	0.20	0.0001	−0.0008
	D-9	0	0	0.0315
	WB-1	1.35	0.00045	0
	WB-3	1.46	0.00048	0
	WB-4	1.35	0.00045	−0.002
	WB-5	1.21	0.0004	−0.004
	WB-6	1.21	0.0004	−0.001
	WB-7	1.63	0.00054	−0.002
	WB-8	1.57	0.00052	0.0015
	WB-9	2.12	0.0007	0.001
	WB-10(0)	1.95	0.00065	−0.004
	R-2	3.79	0.00126	−0.009
	R-3	2.62	0.00087	−0.001
4	Right triangular pyramid	7.40	0.00246	0.002
5	Delta wing with half-cone fuselage	0.66	0.00022	−0.0123
6	a	7.23	0.00244	0.00133
	b(basic)	6.44	0.00214	−0.00133
	c(basic)	7.15	0.00214	0.00622
	d	4.40	0.0015	0
7	1	8.04	0.0027	0.0028
8	Blunted right triangular pyramid	6.91	0.0023	0.0023
9	Delta-wing boost-glide	−0.20	−0.0001	−0.0067
10	W-II E-3	−1.80	−0.0006	0.0100
11	All-wing boost-glide	−2.1	−0.0007	−0.00146

ROUND LEADING EDGES

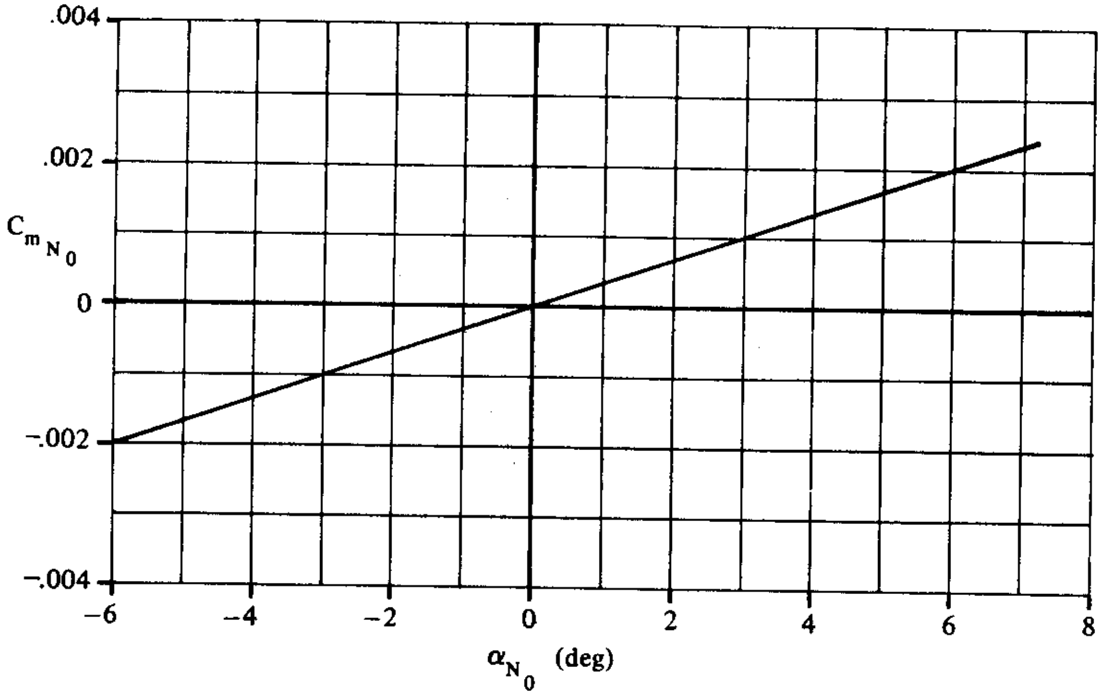

FIGURE 4.8.3.1-4 VARIATION OF ZERO-NORMAL-FORCE PITCHING-MOMENT COEFFICIENT WITH CAMBER – DELTA AND MODIFIED DELTA CONFIGURATIONS

4.8.3.2 WING, WING-BODY PITCHING-MOMENT VARIATION WITH ANGLE OF ATTACK

A. SUBSONIC

This section presents a method for estimating the variation of pitching-moment coefficient with angle of attack for delta or modified-delta planform re-entry configurations at subsonic speeds.

The design charts are given in terms of the center-of-pressure location. The following equation is used to find the pitching-moment coefficient, based on the product of the planform area and root chord Sc_r:

$$C_m = C_{m_{N_0}} + \left(\frac{x_m}{c_r} - \frac{x_{c.p.}}{c_r} \right) C_N{}' \qquad \text{4.8.3.2-a}$$

where

$\left(\frac{x_m}{c_r}\right)$ is the distance from the nose of the configuration to the desired moment reference center measured in root chords, positive aft.

$\left(\frac{x_{c.p.}}{c_r}\right)$ is the distance from the nose of the configuration to the center of pressure measured in root chords, positive aft.

$C_N{}'$ is the normal-force variation with angle of attack obtained by using the method of Section 4.8.1.2.

$C_{m_{N_0}}$ is the zero-normal-force pitching-moment coefficient obtained by using the method of Section 4.8.3.1. For symmetrical configurations $C_{m_{N_0}} = 0$.

The method for estimating the center-of-pressure location is taken from reference 1. A theoretical variation of center-of-pressure location with aspect ratio (or semiapex angle) from reference 2 was corrected to provide center-of-pressure estimates for thin, pointed-nose, symmetrical delta configurations. This result was then corrected to account for the effects of nose blunting and finite thickness.

The effect of nose blunting on delta wings was evaluated by assuming that the normal force acting on a pure delta wing can be divided into two components. One of these components is distributed uniformly over the planform and the other is concentrated at the leading edge. The strength of the concentrated component has a magnitude at any spanwise station proportional to the local chord. In accordance with this concept, the resultant of the uniform load acts 1/3 of the root chord forward of the trailing edge and the resultant of the leading-edge component acts 2/3 of the root chord forward of the trailing edge for a pure delta wing. The nose-blunting effects were then determined by assuming that the pitching moment depends only on normal force and by analyzing a simplified situation where a part of the nose of a pure delta wing is removed by a straight cut normal to the root chord. The center-of-pressure movement predicted in this manner is different from experimental results, since actual nose blunting usually consists of a rounding of the forward part of the wing rather than a sharp cut-off. Therefore, an empirical factor was applied, based on the results of reference 3, to compensate for this difference.

Finite thickness modifies the center-of-pressure location because of the contribution of axial force to pitching moment. The axial force produces a nose-down pitching moment at positive lifts as a result of the negative pressures on the upper surface of the wing and the positive pressures on the lower surface. An empirical correction for this effect, taken from reference 1, is presented in the Datcom method.

The Datcom method is applicable for angles of attack up to 20°.

DATCOM METHOD

The center-of-pressure location of delta or modified-delta configurations is given by

$$\frac{x_{c.p.}}{c_r} = \left(\frac{x_{c.p.}}{c_r}\right)_\Delta + \Delta\left(\frac{x_{c.p.}}{c_r}\right)_B + \Delta\left(\frac{x_{c.p.}}{c_r}\right)_t \qquad 4.8.3.2\text{-b}$$

where

$\left(\frac{x_{c.p.}}{c_r}\right)_\Delta$ is the distance from the wing apex to the center-of-pressure location, measured in root chords, of thin, pointed-nose, symmetrical delta configurations. This parameter is obtained from figure 4.8.3.2-6b as a function of the wing semiapex angle θ. The semiapex angle is measured as illustrated on figure 4.8.3.2-6a.

$\Delta\left(\frac{x_{c.p.}}{c_r}\right)_B$ is the increment in the center-of-pressure location, measured in root chords, due to nose blunting. This parameter is obtained from figure 4.8.3.2-7a as a function of the configuration semiapex angle θ and aspect ratio. The aspect ratio is that of the blunt-nose configuration.

$\Delta\left(\frac{x_{c.p.}}{c_r}\right)_t$ is the increment in the center-of-pressure location, measured in root chords, due to finite thickness. This parameter is obtained from figure 4.8.3.2-7b as a function of the ratio of the projected frontal area to the planform area S_F/S.

Figure 4.8.3.2-6a illustrates the configuration geometry used in this method.

A comparison of the center-of-pressure location calculated by this method with test results is presented as table 4.8.3.2-A. It should be noted that Reynolds-number effects might be expected to influence the pitching-moment characteristics of these configurations as the angle of attack and normal-force coefficients increase. However, the limited Reynolds-number range of the test data precluded isolation of Reynolds-number effects during the data correlation reported in reference 1.

Sample Problem

Given: A blunt-nose delta-wing model with a symmetrical diamond cross section and a blunt trailing edge. This is model D-4 of reference 5.

$A = 1.087$ $b = 13.934$ in. $S = 178.56$ sq in. $S_F = 41.44$ in.

$\theta = 15°$ $c_r = 23.0$ in.

Compute:

$$\left(\frac{x_{c.p.}}{c_r}\right)_{\Delta} = 0.60 \quad \text{(figure 4.8.3.2-6b)}$$

$$1 - \frac{4 \tan \theta}{A} = 1 - \frac{4 \tan 15^{\circ}}{1.087} = 0.0140$$

$$\Delta\left(\frac{x_{c.p.}}{c_r}\right)_{B} = -0.049 \quad \text{(figure 4.8.3.2-7a)}$$

$$S_F/S = 41.44/178.56 = 0.232$$

$$\Delta\left(\frac{x_{c.p.}}{c_r}\right)_{t} = 0.0238 \quad \text{(figure 4.8.3.2-7b)}$$

Solution:

$$\frac{x_{c.p.}}{c_r} = \left(\frac{x_{c.p.}}{c_r}\right)_{\Delta} + \Delta\left(\frac{x_{c.p.}}{c_r}\right)_{B} + \Delta\left(\frac{x_{c.p.}}{c_r}\right)_{t} \quad \text{(equation 4.8.3.2-b)}$$

$$= 0.600 - 0.049 + 0.0238$$

$$= 0.5748$$

This compares with a test value of 0.582 from reference 5.

REFERENCES

1. Seager, D. B., and Meyer, J. E.: An Investigation of the Subsonic Aerodynamic Characteristics and the Landing Flare Maneuver for Hypersonic Re-Entry Configurations. ASD-TDR-62-271, 1962. (C) Title Unclassified

2. Holmboe, V.: The Center of Pressure Position at Low Speeds and Small Angles of Attack for a Certain Type of Delta Wings. SAAB TN 13, 1952. (U)

3. Edwards, G. G., and Savage, H. F.: The Subsonic Aerodynamic Characteristics of Some Blunt Delta Configurations with 75° Sweepback. NASA TM X-581, 1961. (C) Title Unclassified

4. Mugler, J. P., Jr., and Olstad, W. B.: Static Longitudinal Aerodynamic Characteristics at Transonic Speeds of a Blunted Right Triangular Pyramidal Lifting Re-Entry Configuration for Angles of Attack up to 110°. NASA TN D-797, 1961. (U)

5. Mantz, K., Seager, D. B., and Ross, R.: Tests to Determine Subsonic Aerodynamic Characteristics of Hypersonic Re-Entry Configurations. ASD-TR-61-485, Supplement 1, 1963. (U)

6. Mantz, K., Seager, D. B., and Ross, R.: Tests to Determine Subsonic Pressures, Forces and Moments Acting on a Hypersonic Re-Entry Configuration. ASD-TDR-62-270, Supplement 1, 1963. (U)

7. De Young, J., and Harper, C. W.: Theoretical Span Loading at Subsonic Speeds for Wings Having Arbitrary Planform. NACA TR 921, 1948. (U)

8. Paulson, J. W., and Shanks, R. E.: Investigation of Low-Subsonic Flight Characteristics of a Model of a Hypersonic Boost-Glide Configuration Having a 78° Delta Wing. NASA TN D-894, 1961. (U)

9. Wright Air Development Division: Unpublished data from the 5-foot wind tunnel, 1961. (U)

10. Shanks, R. E.: Investigation of the Low-Subsonic Flight Characteristics of a Model of an All-Wing Hypersonic Boost-Glide Configuration Having Very High Sweep. NASA TN D-369, 1960. (U)

11 Paulson, J. W.: Low-Speed Static Stability and Control Characteristics of a Right Triangular Pyramid Re-Entry Configuration. NASA Memo 4-11-59L, 1959. (U)

12 Boisseau, P. C.: Investigation of the Low-Subsonic Flight Characteristics of a Model of a Re-Entry Vehicle with a Thick Flat 75° Swept Delta Wing and a Half-Cone Fuselage. NASA TN D-1007, 1962. (U)

13. Ware, G. M.: Low-Subsonic-Speed Static Stability of Right-Triangular-Pyramid and Half-Cone Lifting Re-Entry Configurations. NASA TN D-646, 1961. (U)

14. Olstad, W. B., Mugler, J. P., Jr., and Cahn, M. S.: Static Longitudinal and Lateral Stability Characteristics of a Right Triangular Pyramidal Lifting Re-Entry Configuration at Transonic Speeds. NASA TN D-655, 1961. (U)

15. Jaquet, B. M., and Brewer, J. D.: Low-Speed Static-Stability and Rolling Characteristics of Low-Aspect-Ratio Wings of Triangular and Modified Triangular Planforms. NACA RM L8L29, 1949. (U)

TABLE 4.8.3.2-A

SUBSONIC CENTER-OF-PRESSURE LOCATION DELTA PLANFORM CONFIGURATIONS

DATA SUMMARY

Ref.	Configuration	A	θ (deg)	$\frac{S_F}{S}$	Nose Configuration	$\frac{x_{c.p.}}{c_r}$ Calc.	$\frac{x_{c.p.}}{c_r}$ Test	e Percent Error
4	Blunted right triangular pyramid	0.788	10.5	0.208	blunt	0.548	0.529	3.6
5	D-1	1.076	15.0	0.208	blunt	0.594	0.595	−0.2
↓	D-2	1.075	↓	0.190	sharp	0.619	0.612	1.1
↓	D-3	1.076	↓	0.312	sharp	0.631	0.626	0.8
↓	D-4	1.087	↓	0.232	blunt	0.575	0.582	−1.2
↓	D-5	1.076	↓	0.329	blunt	0.607	0.608	−0.2
↓	D-6	1.868	25.0	0.219	blunt	0.586	0.594	−1.3
↓	WB-2	1.094	15.0	0.161	blunt	0.560	0.577	−2.9
↓	WB-3	1.074	↓	0.150	blunt	0.601	0.582	3.3
6	D-50	1.076	15.0	0.329	blunt	0.607	0.609	−0.3
8	Delta-wing boost-glide	0.74	12.0	0.050	sharp	0.613	0.625	−1.9
9	W-III E-3	1.07	15.0	0.029	blunt	0.583	0.578	0.9
11	Rt. triangular pyramid	0.78	10.6	0.203	blunt	0.547	0.618	−11.5
12	Delta wing with half-cone fuselage	0.77	15.0	0.484	blunt	0.598	0.568	5.3
13	b(basic)	0.783	10.5	0.201	blunt	0.551	0.575	−4.2
↓	c(basic)	0.787	↓	0.371	blunt	0.566	0.591	−4.2
↓	d	0.783	↓	0.291	blunt	0.560	0.553	1.3
14	1	0.742	10.5	0.186	blunt	0.632	0.560	12.9
15	2	2.31	30.0	0.120	sharp	0.583	0.539	8.2
	4	1.07	15.0	↓	sharp	0.613	0.534	14.8
	7	4.00	45.0	↓	sharp	0.559	0.548	2.0

$$\text{Average Error} = \frac{\Sigma|e|}{n} = 3.9\%$$

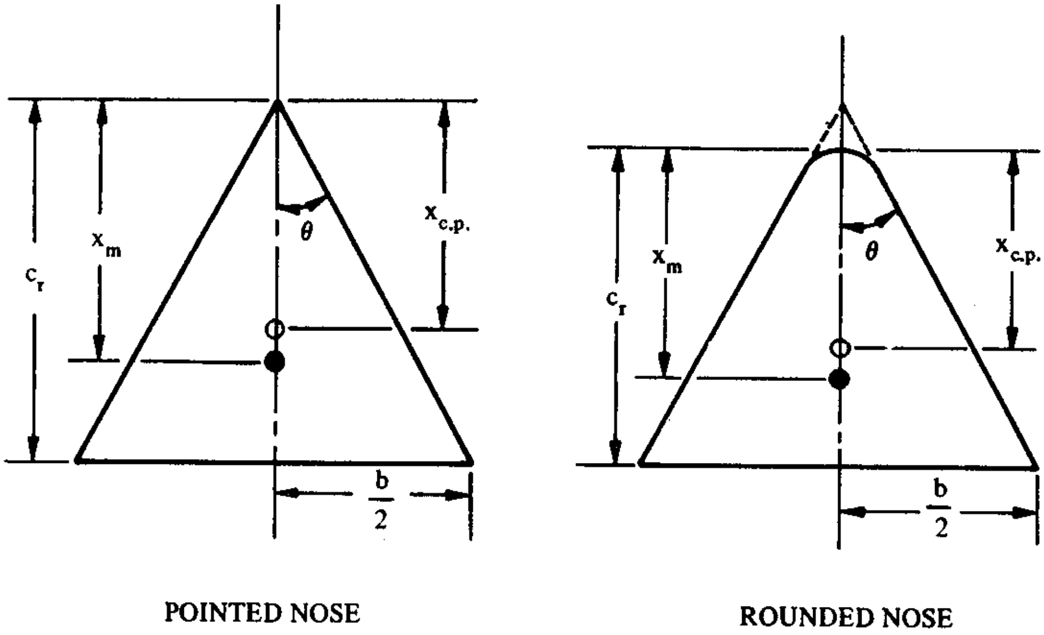

FIGURE 4.8.3.2- 6a CONFIGURATION GEOMETRY

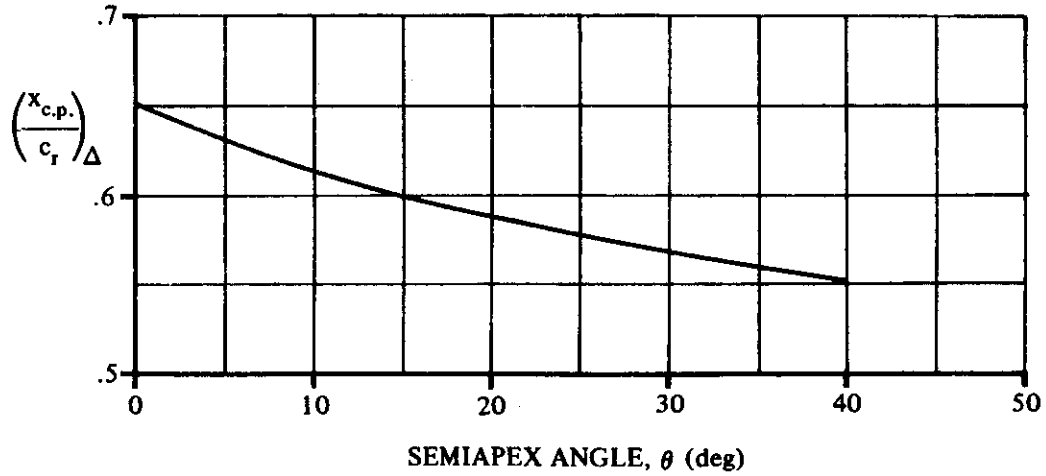

FIGURE 4.8.3.2- 6b CENTER OF PRESSURE FOR THIN, POINTED-NOSED, SYMMETRICAL DELTA CONFIGURATIONS

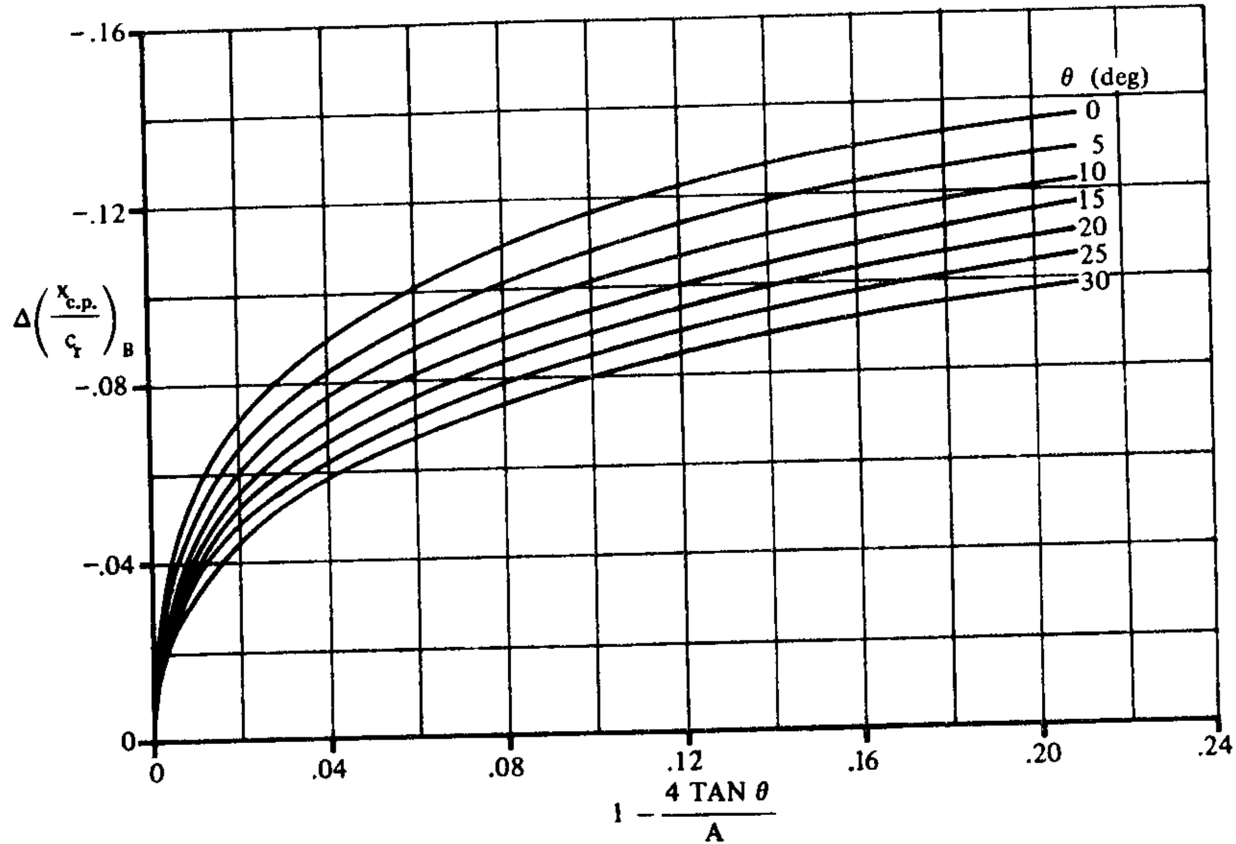

FIGURE 4.8.3.2-7a EFFECTS OF NOSE BLUNTING ON CENTER OF PRESSURE FOR DELTA AND MODIFIED-DELTA CONFIGURATIONS

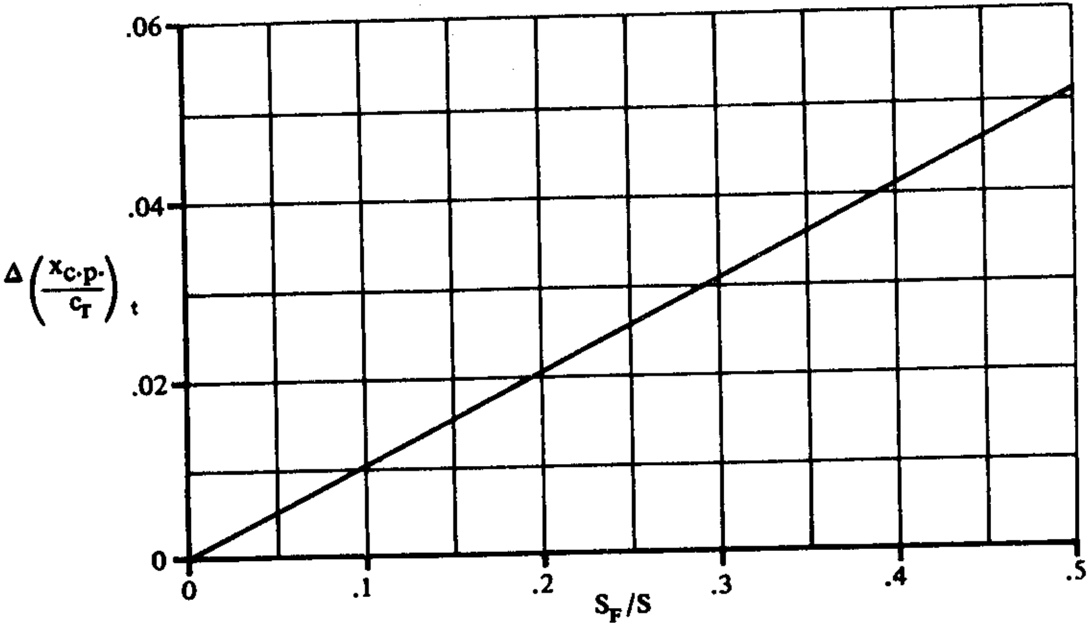

FIGURE 4.8.3.2-7b EFFECTS OF CONFIGURATION THICKNESS ON CENTER OF PRESSURE FOR DELTA AND MODIFIED-DELTA CONFIGURATIONS